

**DESIGN OF A MICRO-MACHINED CANTILEVER APPARATUS SUITABLE
FOR TESTING MODIFIED NEWTONIAN DYNAMICS**

BRADEN T. WIENS
Bachelor of Science, University of Lethbridge, 2015

A Thesis
Submitted to the School of Graduate Studies
of the University of Lethbridge
in Partial Fulfillment of the
Requirements for the Degree

MASTER OF SCIENCE

Department of Physics and Astronomy
University of Lethbridge
LETHBRIDGE, ALBERTA, CANADA

© Braden T. Wiens, 2018

DESIGN OF A MICRO-MACHINED CANTILEVER APPARATUS SUITABLE FOR
TESTING MODIFIED NEWTONIAN DYNAMICS

BRADEN T. WIENS

Date of Defense: September 6, 2018

Dr. S. Patitsas Co-Supervisor	Associate Professor	Ph.D.
Dr. S. Das Co-Supervisor	Professor	Ph.D.
Dr. L. Spencer Committee Member	Associate Professor	Ph.D.
Dr. M. Walton Committee Member	Professor	Ph.D.
Dr. B. Mahmoud Chair, Thesis Examination Com- mittee Member	Associate Professor	Ph.D.

Abstract

Micro-cantilevers have been used for Atomic Force Microscopy to obtain topographic images of surfaces. The resolution of these images allows for individual atoms to be resolved. In this work micro-cantilevers were studied to determine their noise spectrum. A theoretical model was derived using the Euler-Bernoulli beam equation, hydrodynamics and thermodynamics to ascertain the expected power spectral density of a micro-cantilever in a fluid due to thermal energy. Experimental data was collected with a lock-in amplifier to measure noise vs frequency to compare with the theoretical model. The data was used to determine the expected uncertainty of measurements due to noise to determine if measurements can be made in the Modified Newtonian Dynamics (MOND) regime. These results will be used to determine the viability of using a micro-cantilever for an Earth based experiment to test MOND.

Contents

Contents	iv
List of Tables	vii
List of Figures	viii
1 Introduction	1
1.1 Introduction	1
1.2 Micro-Machined Cantilevers	2
1.3 Modified Newtonian Dynamics and Dark Matter	3
1.4 Previous Tests of Modified Newtonian Dynamics	6
1.5 MOND Experiment	7
1.6 Conclusion	8
2 Vibrations of a Beam: A) without Dissipation	10
2.1 Overview	10
2.2 Euler-Bernoulli Beam Equation	10
2.2.1 Geometry and Coordinates of a Deflected Beam	11
2.2.2 Bending Moments and Shear Forces	12
2.3 The Wave Equation for a String	19
2.4 Potential Energy of a Beam	21
2.5 Fixed-Free Boundary Conditions	23
2.6 Fixed-Fixed Boundary Conditions	26
2.7 Conclusion	30
3 Vibrations of a Beam: B) with Dissipation	31
3.1 Introduction	31
3.2 Hydrodynamic Load	32
3.3 Damped and Driven Beams	44
3.4 Green's Function Solution	46
3.5 Frequency Response of the Beam	49
3.6 Power Spectral Density for Fluctuating Loads	52
3.7 Cantilever Motion from Forces	55
3.8 Conclusion	57

4	Vibrations of a Beam: C) with Prescribed Driving Forces	58
4.1	Introduction	58
4.2	Green's Function Solution	58
4.3	Uniform Loads	66
4.4	Point Loads	67
4.5	Laser Load	68
4.6	Conclusion	69
5	Damped Harmonic Oscillator Model	71
5.1	Overview	71
5.2	Damped Harmonic Oscillator	71
5.3	Small Dissipative Effects Model	74
5.4	DHO Model Application	76
5.5	Cantilever Calibration using the DHO Model	81
5.6	Fluid Effects	82
5.7	Conclusion	92
6	Experimental Apparatus	94
6.1	Overview	94
6.2	Equipment Overview	95
6.3	Cantilevers	97
6.3.1	Ideal and Guaranteed Dimensions	99
6.3.2	Variation of Dimensions	101
6.4	Detector	105
6.5	Detection Laser	107
6.6	Driving Laser	108
6.7	Equipment Mounts	109
6.8	Lock-In Amplifier	112
6.8.1	Phase Sensitive Detector	113
6.8.2	Low Pass Filter	114
6.8.3	Synchronous Filters	118
6.8.4	Lock-In Amplifier Output Channels	118
6.9	Conclusion	119
7	Response Analysis	120
7.1	Overview	120
7.2	Detector Output Model	120
7.3	Noise Calculation	127
7.4	Acceleration Calculation	131
7.5	Conclusion	133
8	Experimental Results	135
8.1	Overview	135
8.2	Harmonic Noise	136
8.3	Detector Model Factors	139

8.4	Driving Laser Calibration	141
8.5	Common Mode Noise and Photon Shot Noise	143
8.6	Cantilever Dimension Estimates	144
8.7	Fluid Effects	148
8.8	Effects of Varying the Detection Point	150
8.9	Instrument Noise	160
8.10	Cantilever Noise Results	164
	8.10.1 500 μm Cantilever	164
	8.10.2 225 μm Cantilever	166
8.11	Noise in the Cantilever's Slope	168
8.12	Cantilever Acceleration Noise Spectral Density	170
8.13	Rms Acceleration Noise	172
8.14	Driven Acceleration Results	175
	8.14.1 500 μm Cantilever	175
	8.14.2 225 μm Cantilever	177
8.15	Conclusion	179
9	Future MOND Experiments	182
	9.1 Overview	182
	9.2 Evaluation of RMS Acceleration	182
	9.3 Differentiating forms of $\mu(x)$	186
	9.4 Conclusion	187
10	Conclusion	188
	Bibliography	194

List of Tables

2.1	The first four mode shapes and corresponding values for C_n for the cantilever. The striped end plate represents the rigid mount that the cantilever extends out from.	26
2.2	The first four mode shapes and corresponding values for C_n for the bridge beam. The striped end plates represents the rigid mounts that the bridge extends between.	30
5.1	Quantitative comparison of the the Euler-Bernoulli beam equation (EBBE) model, using values obtained using the Damped Harmonic Oscillator (DHO) fit, and the Small Dissipative Effects (SDE) model.	80
6.1	Manufacturer specified values for the 225 μm and 500 μm cantilevers. . . .	100
6.2	Equivalent noise bandwidth and required wait time based on the filter pole order and time constant, τ [s] [1].	117
8.1	Calculated values for the 225 μm and 500 μm cantilevers based on DHO fits. The thickness of the 225 μm and 500 μm cantilevers were calculated using the values of the quality factor and resonant frequency from the DHO fit of the first resonant peak for each cantilever. The columns indicating with or without a coating allow the thickness of each cantilever to be calculated with the added mass of the coating. The EBBE thickness is the required thickness for the EBBE model to fit the data that was used for the DHO fit. .	148
8.2	Summary of the properties of the 225 μm and 500 μm cantilevers. The values for for Q and ω_f were obtained from the DHO fits from Figures 8.9 and 8.8. ρ_{cant} is calculated using Eq. (6.1) and values provided in this section. Calculated values for \overline{Re} and \overline{T} , Eq. (5.25), for the 225 μm and 500 μm cantilevers. The values of these parameters determine how the motion of the beam will be affected by the fluid the beam is submerged in.	149
8.3	Equivalent Noise Bandwidth (ENBW) for measurements using a 0.003 s, 1 s and 1000 s time constant, each using a 4 th order pole	168
8.4	Comparison of the frequency where acceleration noise is equal to a_0 and $0.1a_0$ for the 225 μm and 500 μm cantilevers. The results are presented for a Low Pass Filter (LPF) using a 4 th order pole filter and time constants of 0.03 s, 1 s and 1000 s. The frequency for $0.1a_0$ for the 500 μm cantilever has not been included as the data does not extend to a low enough frequency. 175	

List of Figures

2.1	Schematic depicting the required coordinate systems for Euler-Bernoulli equation derivation. The black dashed line represents the neutral axis of the cantilever which remains a constant length during deflection and the grey dashed line represents the x-axis.	12
2.2	Part a) shows a cantilever which has a force, L , applied at $x = l$ and the resulting deflection. Part b) shows the same cantilever and force. The beam is considered as two pieces in this case so that the right portion of the beam can be considered to determine the bending moment, M , and shear force, V , as a result of the applied force.	13
2.3	Schematic illustrating pertinent geometry of a small section of the beam during deflection. dx is the length of the neutral axis and δx is the change of length at the radius r due to expansion or compression. A positive δx indicates an increase of length due to expansion. R is the radius of curvature for this element of the beam and r is the distance from the neutral plane to the narrow strip of interest of the beam.	14
2.4	Schematic depicting the shear forces and bending moments for some small section of the cantilever that results from deflection.	16
2.5	Diagram showing a deflected string segment and the resulting tension. . . .	19
2.6	Diagram depicting the radius of curvature, R , for a deflected beam. Δs is the length of the neutral axis while Δs_0 is the length of a cord of the beam located at a distance r from the neutral axis. If the beam were not deflected then $\Delta s = \Delta s_0$	22
2.7	Cantilever deflection from a relaxed state along the x-axis is given by $w(x, t)$.	24
3.1	The coordinate system used for the derivation of the hydrodynamic function for a cylindrical beam with a diameter of b	35
3.2	The spring constant of a beam is calculated based on the required force that must be applied to the beam such that it is deflected by a displacement of Δy .	51
4.1	Plot of the Green's function. The axes for x and x' have been normalized such that $x = x' = 1$ corresponds to $x = x' = l$	63
4.2	Plot of the first derivative of the Green's function with respect to x . The axes for x and x' have been normalized such that $x = x' = 1$ corresponds to $x = x' = l$	63
4.3	Plot of the second derivative of the Green's function with respect to x . The axes for x and x' have been normalized such that $x = x' = 1$ corresponds to $x = x' = l$	64

4.4	Plot of the third derivative of the Green's function with respect to x . The axes for x and x' have been normalized such that $x = x' = 1$ corresponds to $x = x' = l$	65
4.5	ζ describes the ratio of the slope of the cantilever at x with the displacement of the free end.	67
5.1	Plot of the Noise Amplitude Spectral Density (NASD) of the slope as calculated by EBBE model and DHO fits for 3 resonant peaks for a large frequency, ω , range. The solid blue line shows the results for the EBBE model as calculated for a $500 \mu\text{m}$ cantilever with ideal dimensions in air. The three other plots are results for the DHO fit of the first, dashed green line, second, dot dash red line, and third, dotted black line, peaks. See Table 5.1 for a summary of these results.	78
5.2	Plot of the NASD of the slope as calculated by the EBBE, blue solid line, and SDE, red dot dash line, models. The solid blue line is the EBBE model for a $500 \mu\text{m}$ cantilever with ideal dimensions. The dot dash red line shows the SDE model for the same cantilever. The SDE model can be seen as having larger deviations from the EBBE model as the peak number increases. See Table 5.1 for a summary of these results.	79
5.3	Normalized thermal displacement NASD $H = \sqrt{J_w(1 \omega)k\omega_{vac,1}/(2k_bT)}$ for the fundamental mode of a cantilever in a gas. The expected resonance frequency as calculated by the inviscid model, Eq. (5.27), is indicated by the black vertical line. The quality factor for each plot is shown with its respective line. The plots are generated using $\overline{Re} = 0.1$ (blue solid line), $\overline{Re} = 1$ (green dot dash line), $\overline{Re} = 4.4$ (red dotted line) and, $\overline{Re} = 10$ (teal dashed line). Part a) is plotted using $\overline{T} = 0.0059$ and part b) $\overline{T} = 0.049$	84
5.4	Normalized thermal displacement NASD $H = \sqrt{J_w(1 \omega)k\omega_{vac,1}/(2k_bT)}$ for the first two modes of a cantilever in a liquid. The expected resonance frequencies as calculated by the inviscid model, Eq. (5.27), are indicated by the black vertical lines. The quality factor for each plot is shown with its respective line. The plots are generated using $\overline{Re} = 1$ (blue solid line), $\overline{Re} = 10$ (green dot dash line) and, $\overline{Re} = 100$ (red dotted line). Part a) is plotted using $\overline{T} = 5$ and part b) $\overline{T} = 20$	87
5.5	Plot demonstrating fluid effects on the quality factor the fundamental resonant peak, as calculated by Eq. (5.29). Plot a) generated using $\overline{T} = 0.0059$ (solid blue line), $\overline{T} = 0.02$ (green dashed line) and, $\overline{T} = 0.049$ (red dotted line). Plot b) generated using $\overline{T} = 5$ (solid blue line), $\overline{T} = 20$ (green dashed line) and, $\overline{T} = 45$ (red dotted line).	88
5.6	Relative fundamental resonance frequencies with respect to $\omega_{vac,1}$ for a broad range of \overline{Re} . Plot a) generated using $\overline{T} = 0.0059$ (solid blue line), $\overline{T} = 0.02$ (green dashed line) and, $\overline{T} = 0.049$ (red dotted line). Plot b) generated using $\overline{T} = 5$ (solid blue line), $\overline{T} = 20$ (green dashed line) and, $\overline{T} = 45$ (red dotted line).	89

5.7 Normalized thermal displacement $NASD H = |J_w(1|\omega)|^2 k \omega_{vac,1} / (2k_b T)$, square root of Eq. (3.115), for the fundamental mode of a cantilever. Plot a) generated using $\bar{T} = 0.0059$ (solid blue line), $\bar{T} = 0.02$ (green dashed line) and, $\bar{T} = 0.049$ (red dotted line). Plot b) generated using $\bar{T} = 5$ (solid blue line), $\bar{T} = 20$ (green dashed line) and, $\bar{T} = 45$ (red dotted line). 90

5.8 The EBBE model (solid blue line), square root of Eq. (3.115), is presented here using a normalized amplitude with respect to unity, $\bar{R}e = 10$ and $\bar{T} = 15$. The DHO model, square root of Eq. (5.10), is fit to this data (dashed green line). 92

6.1 Schematic of equipment for the cantilever, driving and detection lasers and detector. 96

6.2 Cross-sectional schematic of cantilever. The cantilevers are manufactured such that they are slightly wider at the top where the detection laser is reflected off as compared to the sample side. This causes an increase of up to 30% of the reflecting surface, increasing the amount of the incident beam that is reflected toward the detector. 98

6.3 Zoomed in photograph of the 500 μm cantilever. This image shows the pointed tip which causes the last 10% of the tip to deviate from the expected rectangular shape. 101

6.4 EBBE model results demonstrating the effects of varying the 500 μm cantilever's dimension on the fundamental resonant peak. Each subplot varies a different dimension as labelled on the subplot. The blue dashed line corresponds to the minimum guaranteed value, the solid green line is the ideal value and the red dotted line is the maximum guaranteed value. All values are based on Tab. 6.1. 103

6.5 EBBE model results demonstrating the effects of varying the 225 μm cantilever's dimension on the fundamental resonant peak. Each subplot varies a different dimension as labelled on the subplot. The blue dashed line corresponds to the minimum guaranteed value, the solid green line is the ideal value and the red dotted line is the maximum guaranteed value. All values are based on Tab. 6.1. 104

6.6 a) Diagram demonstrating the silicon gap between quadrants of the detector and its correlation to the detection point at x. As the cantilever moves the reflected beam will shift across the detector. The only portion of the reflected beam that transfers from a quadrant is the portion at the silicon gap. Any portion of the beam that strikes one quadrant and does not leave that quadrant due to laser shifting does not affect the output of the detector. b) Diagram showing the quadrant nature of the detector. Measurements for the displacement of the cantilever are collected from the left-minus-right output or $(A+B)-(C+D)$ 112

6.7	Plot showing the response of an arbitrary low pass filter, $G(\omega)$. LPF have minimal attenuation at low frequencies and completely pass DC signals. As the frequency increases the signal becomes attenuated. At the frequency ω_{co} the filter attenuates the signal to -3 dB, symbolized by the green dash line.	114
6.8	Theoretical low pass filter gain for multiple pole orders. The purple line corresponds to -3 dB.	118
7.1	A schematic diagram showing the geometry and the various coordinate systems being employed. The u -coordinate system describes the incident beam, the x -coordinate system describes the cantilever and finally the u' -coordinate system describes the detector surface. θ_0 is the angle between the norm of the cantilever and the incident beam or the norm of the detector. ϕ is equal to the angle of deflection caused by the motion of the cantilever bending from center.	121
7.2	Diagram showing single light ray response to cantilever motion.	133
8.1	Noise Measurements of a 50 ohm resistor for different filter pole orders and using a time constant of 30 ms. Noise measurements were obtained using a 10 s time constant has been included to show what is the expected noise at frequencies below 1 krad/s.	137
8.2	Noise Measurements of a 50 ohm resistor for different filter pole orders and using a time constant of 1 s. Noise measurements were obtained using a 10 s time constant has been included to show what is the expected noise at frequencies below 1 krad/s.	137
8.3	Comparison of the measured noise of a 50 ohm resistor with the synchronous filter on, green, or off, blue, with time constant of 30 ms and a 4 th order pole. Measurements were made from 1 to 1000 rad/s with a time constant of 3 second and 4 th order pole, red, to determine the expected noise at lower frequencies.	138
8.4	Experimental results for determining voltage to displacement factor for a cantilever.	140
8.5	A selected portion of the voltage to displacement factor data (dots) and the resulting linear fit (line).	141
8.6	Driving laser output response to power supply voltage. Calibration of the driving laser was performed by measuring the laser's power output, blue dots, over a range of voltages. The marked off region, two black bars, indicate the region where the laser has a linear response to the supply voltage. The red line is a linear fit to this region.	142
8.7	Effective NASD of the slope for the detection laser aimed directly at the detector. Detection laser noise centered (blue) is where the difference output reads 0 volts and 0.25 mm (orange) is the average of the noise when the laser is shifted 0.25 mm either left or right of centered. The same is true for the 0.50 mm (green), 0.75 mm (red) and, 1.00 mm (purple) results. The black line indicates the expected shot noise of the laser.	143

8.8 Fit of the DHO model to experimental data collected for the 500 μm cantilever. The values required to calculate the thickness of the cantilever are the resonant frequency, ω_f , and the quality factor, Q . Fit results for Q and ω_f were 22.09 ± 0.06 and $(23894.843 \pm 0.0007) \text{ rad s}^{-1}$ respectively. 145

8.9 Fit of the DHO model to experimental data collected for the 225 μm cantilever. The values required to calculate the thickness of the cantilever are the resonant frequency, ω_f , and the quality factor, Q . Fit results for Q and ω_f were 180.0 ± 0.4 and $(341999.0 \pm 0.01) \text{ rad s}^{-1}$ respectively. 146

8.10 Diagram of the normalized deflection for the first mode of a cantilever (blue line) with length l and the normalized slope of the first mode (black dashed line). Calculated using Eq. 2.42. 151

8.11 Diagram of the normalized deflection for the second mode of a cantilever with length l (blue line) and the normalized slope of the second mode (black dashed line). The green dashed vertical line at $0.47l$ indicates where the slope is 0 and the red dot-dashed vertical line at $0.78l$ indicates where the deflection of the cantilever is 0. 152

8.12 NASD of the slope of the beam. EBBE model prediction for the measured noise of the second mode of a cantilever beam (blue line). The green dashed line and red dot-dashed line correlate to those in Fig. 8.11 indicating where the slope and displacement are 0 respectively. 153

8.13 Measured noise of the 500 μm cantilever when the detection point is approximately at $0.8l$ where $\zeta(x) = 1.32$. Plot a) shows the measured noise across the full range of 0.16 rad s^{-1} to 628 krad s^{-1} . Plot b) shows a zoomed in image of the second harmonic peak. The second resonance peak is easily found in both plot a) and b) without the EBBE model showing where it is located. 154

8.14 Measured noise of the 500 μm cantilever when the detection point is approximately at $0.78l$ where $\zeta(x) = 1.32$. Plot a) shows the measured noise across the full range of 0.16 rad s^{-1} to 628 krad s^{-1} . The resonance peak for the first mode is easily detected and there is a notable data point where the second resonance peak is expected to be. The displacement of the beam at this point is 0 while the slope is not. Plot b) shows a zoomed in image of the second harmonic peak. The location of the second resonance peak can only be found using the EBBE model and could easily be mistaken for a random, high noise data point. The location of the peak is indicated by a single data point as the peak is largely hidden by the noise of the system. 155

8.15 Measured noise of the 500 μm cantilever when the detection point is approximately at $0.47l$ where $\zeta(x) = 1.13$. Plot a) shows the measured noise across the full range of 0.16 rad s^{-1} to 628 krad s^{-1} . Plot b) shows a zoomed in image of the second harmonic peak. The slope of the second mode is 0 at this point while the displacement is not. The location of the second resonance peak is indicated by the EBBE model but the peak is not notable as it is completely hidden by the noise of the rest of the system. 156

8.16 Measured noise of the 500 μm cantilever when the detection point is approximately at $0.45l$ where $\zeta(x) = 1.11$. Plot a) shows the measured noise across the full range of 0.16 rad s^{-1} to 628 krads^{-1} . The amplitude of the resonance peak, as calculated using the EBBE model, for the first mode is about the same as the second mode's peak. Plot b) shows a zoomed in image of the second harmonic peak. The amplitude of the noise peak for the second mode has increased from the previous plot as the slope is greater, despite the fact that the displacement is smaller. 157

8.17 Diagram of the normalized deflection for the second mode of a bridge beam with length l (blue line) and the normalized slope of the first mode (black dashed line). The green dashed vertical line at $0.5l$ indicates where the slope is 0 and the red dot-dashed vertical lines at $0.224l$ and $0.776l$ indicates where the deflection of the cantilever is 0. 159

8.18 NASD of the slope of the beam. EBBE model prediction for the measured noise of the first mode of a bridge beam (blue line). The green dashed line and red dot-dashed lines correlate to those in Fig. 8.17 indicating where the slope and displacement are 0 respectively. 160

8.19 Effective NASD of the slope noise for the Lock-In Amplifier (LIA), detector and detection laser. The noise of the LIA (cyan stars), detector (black dashes) and detection laser (blue pluses). These results show that the LIA, connected to a 50 Ohm resistor, generates less noise than any other piece of equipment. The detection laser also generates more noise than the LIA and detector combined and thus only the laser needs to be considered for future analysis. 162

8.20 NASD comparisons for the detection laser (blue pluses), the 225 μm cantilever (red x) and the 500 μm cantilever (green dots). The detection laser was measured using the difference output of the detector using an alignment that gave the same sum and difference output as that with the 500 μm cantilever. 163

8.21 NASD of the slope of the 500 μm cantilever with the theoretical EBBE model (blue line) and experimental results (green dots). The theoretical model does not account for any noise sources except for the expected cantilever noise. This data was collected using a detection point of $0.75l$ 165

8.22 NASD of the slope of the 225 μm cantilever with the theoretical EBBE model (blue line) and experimental results (green dots). This data was collected using a detection point of $0.25l$ 166

8.23 Plot of the theoretical (blue line) and experimental (green dots) NASD of the slope of the 225 μm cantilever. This data was collected using a detection point of $0.25l$ 167

8.24 Contribution of the noise to a measurement of the slope of the beam for the 500 μm cantilever using three different time constants, each using a 4th order pole. The time constants are: 0.03 second time constant (data: blue dots, model: blue dot dash line), 1 second (data: green x's, model: green dashed line), and 1000 seconds (data: red pluses, model: red dotted line). . 169

8.25 Plot of the theoretical (blue line) and experimental (green dots) acceleration NASD of the 500 μm cantilever. 170

8.26 Plot of the theoretical (blue line) and experimental (green dots) acceleration NASD of the 225 μm cantilever. 171

8.27 Contribution of the noise to a measurement of the acceleration of the 500 μm cantilever using three different time constants, each using a 4th order pole. The time constants are: 0.03 second time constant (data: blue dots, model: blue dot dash line), 1 second (data: green x's, model: green dashed line), and 1000 seconds (data: red pluses, model: red dotted line). The solid, black, horizontal line indicates a_0 and the black, dashed, vertical line indicates 10 rad/s. 173

8.28 Contribution of the noise to a measurement of the acceleration of the 225 μm cantilever using three different time constants, each using a 4th order pole. The time constants are: 0.03 second time constant (data: blue dots, model: blue dot dash line), 1 second (data: green x's, model: green dashed line), and 1000 seconds (data: red pluses, model: red dotted line). The solid, black, horizontal line indicates a_0 and the black, dashed, vertical line indicates 55 rad/s. 174

8.29 Plot of the experimental acceleration of the 500 μm cantilever driven by a laser. These results were obtained with the cantilever driven at 25 rad/s, using a 3 second time constant and 4th order pole filter. The error of the laser load is 0.1%. 176

8.30 Plot of the experimental acceleration of the 225 μm cantilever driven by a laser. These results were obtained with the cantilever driven at 25 rad/s, using a 3 second time constant and 4th order pole filter. The error of the laser load is 0.1%. 177

8.31 Plot of the experimental acceleration of the 225 μm cantilever driven by a laser. These results show the driven acceleration level of the cantilever to be within the MOND regime. The error of the laser load is 0.1%. 178

9.1 A comparison of the expected acceleration for the Newtonian regime, blue line, and the MOND regime using $\mu_1(x)$, red dot dash line, and $\mu_2(x)$, black dash line. 187

List of Acronyms

AFM Atomic Force Microscopy.

DHO Damped Harmonic Oscillator.

EBBE Euler-Bernoulli beam equation.

EFE External Field Effect.

ENBW Equivalent Noise Bandwidth.

LHS Left Hand Side.

LIA Lock-In Amplifier.

LPF Low Pass Filter.

MOND Modified Newtonian Dynamics.

NASD Noise Amplitude Spectral Density.

NSD Noise Spectral Density.

PSD Power Spectral Density.

RHS Right Hand Side.

RMS Root Mean Square.

SDE Small Dissipative Effects.

SNR Signal-to-Noise Ratio.

STM Scanning Tunnelling Microscope.

VTD Voltage To Displacement.

Chapter 1

Introduction

1.1 Introduction

As early as 1922 it was found by Jacobus Kapteyn [2] that the measured mass within galaxies was insufficient to support radial velocities of stars at large distances from the galactic core. A suggestion that he provided and was later developed by Fritz Zwicky [3] was dark matter. Alternative theories have also been developed to help solve this observational discrepancy like Modified Newtonian Dynamics (MOND) by Mordehai Milgrom [4]. MOND is a theory that postulates that Newton's 2nd Law is inaccurate at very small acceleration levels, below $\sim 1.2 \times 10^{-10} \text{ m/s}^2$.

Experimental tests of MOND are difficult to perform as the acceleration experienced by the equipment is influenced by the Earth and the Sun. Experiments could be performed using satellites where the equipment is in free fall; however, the technical requirements and costs of such endeavours are significantly increased.

This work will explore the possibility of using an Atomic Force Microscopy (AFM) cantilever for an Earth-based experiment to test MOND. AFM is a field of study which uses micro-cantilevers to study the surface of materials. This equipment is sensitive to very small deflections of the beam and can be used to create images with resolution sufficient to identify individual atoms [5]. To determine if an AFM cantilever can be used in such a manner a theoretical model of the noise of a cantilever are developed, Chapters 2 to 4. Chapter 5 will compare the theoretical model with a model for the Damped Harmonic Oscillator (DHO) and determine the effects of a fluid on the motion of a beam. Chapters 6 and 7 dis-

cusses the equipment that is used for data acquisition, its layout, some important features of the equipment and how the data must be processed for it to be fit with the theoretical model. Chapter 8 considers the experimental results for the measurements of important model factors, the noise of the equipment and the cantilevers and, the calculated acceleration noise. Finally, chapters 9 and 10 will derive equations to determine the expected uncertainty of acceleration measurements and the potential of a MOND experiment here on Earth.

1.2 Micro-Machined Cantilevers

The AFM was developed by Binnig, Quate and Gerber in 1985, followed by a paper discussing their work in 1986 [6]. For their work developing the AFM, Binnig and Rohrer won the 1986 Nobel Prize in Physics [7].

The first AFM was designed with the intent to overcome an issue with the Scanning Tunnelling Microscope (STM) which was only capable of making surface measurements of conductors. The AFM uses a fine tip that extends down from the free end of the beam that interacts with the inter-atomic forces to deflect a cantilever. The cantilever is moved about the x- and y-axes in a raster pattern while the cantilever's deflection in the z-direction is recorded with a resolution of about 1 Å. The deflection of the cantilever at positions around the sample are measured and the results are computationally analyzed to obtain an image of the surface of the material [5].

There are several different methods that can be used to measure the deflection of the cantilever. The first AFM built used the then well known scanning tunnelling microscope. The STM was positioned, stationary, above the cantilever and the sample was moved around underneath the cantilever. The STM was then used to measure the displacement of the cantilever [6, 5]. A second method, which simplifies the detection equipment, was developed by Meyer and Amer in their 1988 paper [8]. In their study they proposed and successfully tested what is referred to as the optical level method. The process involves reflecting a laser off the back of the cantilever to a photosensitive detector. The deflection of the cantilever

can then be determined based on the motion of the laser across the detector. This is the detection system that is employed in the experimental work of this thesis.

1.3 Modified Newtonian Dynamics and Dark Matter

The first mention of dark matter as a concept applying to the rotation curves of a galaxy was by Jacobus Kapteyn in his 1922 paper [2, 9]. During his work studying the motion of stars in the Milky Way, he discovered that the linear velocity at distances of 2 kpc from the center of the galaxies neared a constant value around 19.5 km/s. In a subsection labelled “Remark. Dark Matter.,” Kapteyn proposed a simple method to measure the dark, unaccounted for matter by considering the required mass for a given system and then dividing that by the number of luminous stars [2]. This ratio is similar to what is used in cosmology currently, the mass per luminosity, M/L .

The methods for determining the masses of clusters and nebulae used observations of the luminosities and the internal rotations of those clusters and nebulae [10]. Fritz Zwicky found that these methods were unreliable and at best could be used to determine the minimum mass of those bodies. He concluded nebulae and clusters required more mass to remain stable. Zwicky introduces the term *dunkele (kalte) materie* [(cold) dark matter] in 1933 [3, 11]. He later uses this term in response to his studies of the Coma Cluster using the 18-inch Schmidt telescope on Mount Palomar. The excess mass, dark matter, that he considered in this case were “cool and cold stars, macroscopic and microscopic solid bodies and gases” [10].

From the time of Zwicky until the late 1960s and early 1970s, the issue of the missing matter was largely misjudged. This was partially caused by the difficulty in analyzing the data. The analysis process would employ one of several different Keplerian models. Through the choice of which model was used and manipulation of parameters, different astronomy groups obtained widely varying results [12]. An example of this is the comparison of the results found for the rotation curve of the galaxy M31 between a Cambridge

group, who found no issues between the model and data and thus required no dark matter, [13, 14, 15, 16] and a separate group whose results were in direct contradiction [17].

There was a wide range of solutions suggested ranging from ionized hydrogen gas [18], changes to the law of gravity [19, 20, 21], cosmologically created black holes [22], the presence of massive neutrinos [23] and, observational errors [24], as summarized in [12]. While many of these possibilities have been eliminated, the search for dark matter continues.

As time progressed it seemed that the two best options to solve the missing mass problem were: dark matter that could not, or simply has not yet, been directly detected as the source of the excess mass or that Newtonian gravity was not sufficient to describe galaxies and clusters [25]. One of the most dominant alternatives to Newtonian gravity was suggested by Milgrom who considered “the time is ripe for considering alternatives to the hidden mass hypothesis.” Milgrom proposed a theory called MOND which introduced a function, $\mu(a/a_0)$, to Newton’s law of gravity such that it took the form

$$a\mu(a/a_0) = \frac{GM}{r^2} \tag{1.1}$$

If the particle’s actual acceleration, a , is greater than an acceleration constant, a_0 , then $\mu(a/a_0) \approx 1$, and if $a < a_0$ then $\mu(a/a_0) \approx a_0/a$. Through analysis of galaxies the value of a_0 was determined to be $\sim 1.2 \times 10^{-10} \text{ m/s}^2$ [26]. This result can be solved in the deep MOND regime, $a < a_0$, for circular motion to obtain a relation which resembles the baryonic Tully-Fisher relation,

$$v^4 = GMa_0. \tag{1.2}$$

Milgrom found that the use of this modified law eliminated the need for dark matter in galaxies [26]. One of the benefits of MOND, versus previous models that had been used, is that a_0 is a constant and thus was not a fitting parameter. Once a_0 is determined for a range of galaxies it should be applied to future analysis with that value, reducing the number of

fitting parameters and the possibility of variations between different groups [25].

MOND has had success with determining the rotation curves of spiral galaxies from just the detected matter [27] as well as galaxies scaling relations for spirals and ellipticals [28, 29]. The theory works well to determine the rotation curves using only the mass that is detected; that is, stars, brown dwarfs, Jupiters and clouds [9]. It is capable to solve not only the general trends of the rotation curves, for example the approach to asymptotic velocities are large radii, but also the specific details of individual galaxies. Sanders and McGaugh use MOND to analysis roughly 100 different galaxies and their results found that MOND is not significantly different from observations in over 90% of those galaxies. For some galaxies, there is so much observational data and the model is accurate enough that they completely overlap and the MOND model is hidden by the data [25]. In the case of some tidal dwarf galaxies, results show MOND can describe the rotation curves better than the cold dark matter model [30, 31].

The success of MOND also extends to small groups of galaxies and some super-clusters like the Perseus-Pisces filament. MOND's ability to explain these kinematics is thanks to the low acceleration rates which can be as small as a few percent of a_0 [32]. MOND's success with clusters, and not simply individual galaxies, lends support to the idea of considering alternatives to the dark matter theory [33].

Gerbai et al. [34] found there is a mass discrepancy based on observations of 8 X-ray emitting clusters, specifically when dealing with the cores. Aguirre et al. [35] found the same issue for a sample of galaxy clusters and Ly α absorbers. A challenge for MOND when dealing with rich clusters, especially in the core, is that the acceleration rates are in excess of a_0 and thus they are not in the MOND regime [28, 29]. Supporters of MOND, like Sanders [33], have stated that if the value of a_0 is increased by a factor of 3 or 4 larger than is required for galaxies, the amount of missing matter is significantly reduced for X-ray emitting clusters. While the required mass is reduced there can still be some missing mass and Sanders notes that this is not strictly a contradiction or falsification of MOND as

MOND does not strictly prohibit the use of unseen matter; it works to reduce the amount of required unseen matter. The necessity of extra matter can be seen in X-ray and weak-lensing observations, as found by Clowe et al. [36] and Angus et al. [37]; the latter suggests the potential for a theory using a combination of MOND and dark matter.

1.4 Previous Tests of Modified Newtonian Dynamics

At the time of writing the author is aware of only three experiments which have been conducted with the express intent of testing MOND. A brief discussion of each experiment in order of decreasing acceleration levels will follow.

The first experiment was performed by Meyer et al. [38] in 2012 using a resonance cavity. The experiment used a microwave resonator where the two ends of the resonator were independent of each other and suspended by wires. Mobile masses were then introduced to the system to cause small accelerations of the resonator ends by gravitation. The change in distance between the resonator ends caused a shift in the resonance frequency which could be used to determine the position of the ends. Ultimately, this experiment was not able to probe significantly below a_0 but it was able to test six different previously proposed forms for $\mu(a/a_0)$. They found that one form was incompatible with their results and that two others were “slightly disfavoured.” The remaining three forms were found to fit the data and are candidates for $\mu(a/a_0)$.

Abramovici and Vager published a paper in 1986 [39] detailing the results of an experiment to test MOND using a modified interferometer and pendulum mass that was accelerated using an applied electric field. The lowest measurable acceleration was $3 \times 10^{-11} \text{ m/s}^2$ and results showed the pendulum’s motion were well described by Newtonian physics.

Results for the experiment with the lowest acceleration were published by Gundlach et al. [40] in 2007. Measurements of a large, rotational pendulum were used to determine the period and acceleration. These results showed that the rotation of the pendulum fit the Newtonian expectation down to acceleration levels of $5 \times 10^{-14} \text{ m/s}^2$.

One of the challenges of these experiments, and a major reason why they are not considered conclusive, is due to the presence of accelerations other than the Earth's gravitational field, this is referred to as the External Field Effect (EFE) [41]. In a 2007 study [42], Ignatiev showed that experiments of MOND in a non-inertial reference frame of a laboratory cannot, in general, be done due to the EFE. Using considerations of the Earth's motion around the Sun and galaxy, Ignatiev calculates a window where the cumulative effects cancel each other and accelerations due to the EFE are within the MOND regime. This window is about 1 s long and would work at a specific location on Earth with a surface area of approximately 7 cm by 40 cm. In 2010, Lorenc et al. [43] proposed an idea to make it possible to cancel the EFE at any location on Earth at any time through the use of a gyroscope like apparatus. Their results concluded that the apparatus would create conditions favourable to testing MOND for a space of up to 10^{-8} m^2 and a time duration of approximately 10^{-6} s .

1.5 MOND Experiment

The goal of this thesis is to determine the potential of an experiment in an Earth based laboratory which is detailed by Das and Patitsas [44]. The potential experiment, hereby referred to as “the MOND experiment”, uses measurements of the acceleration of an AFM cantilever that is driven by a laser. The cantilever is to be mounted on a platform that is repetitively either dropped some height or tossed up and then caught in an evacuated drop tube. The small size of the AFM cantilevers and detector sensitivity allows for very small deflections to be measured. It may be possible to drive the cantilever with such small accelerations that, when in free fall, the dominant acceleration will be within the MOND regime. The experiment must be performed in a vacuum as the acceleration of the cantilever must be within the MOND regime for deviations from Newtonian dynamics to potentially occur. If the experimental apparatus is dropped while in a fluid, like the atmosphere, the drag force will cause the acceleration levels to exceed the MOND regime.

This experiment has the potential to shed more light on the premise of MOND. A satellite based experiment would allow the experiment to run over extended durations of time. However, the cost of such an endeavour is prohibitive and finding a satellite with open space and ideal for the experiment is challenging at best. The process of repetitive dropping or tossing on Earth allows for a large data set to be collected. If the noise of the system is louder than the required measurement, a large number of iterations can be used to reduce the uncertainty to within acceptable limits. Finally, Earth based experiments also have the great advantage of not requiring any special design considerations for vibrations during rocket launching and any issue with the equipment can be dealt with by a human without the need for extra-vehicular activity.

1.6 Conclusion

The process to determine the potential use of cantilevers for use in a MOND experiment will require several topics to be studied. The Euler-Bernoulli beam equation will be derived to describe the motion of a cantilever beam in both a vacuum and a fluid. This equation will be derived from first principles and use the vacuum results to derive the result for a fluid. This derivation will make use of the Navier-Stokes equation to derive the hydrodynamic function. Two results that will be obtained for a fluid will give the spectral density for the cantilever's position and slope. Experimental data will be collected over a broad range of frequencies for the purposes of comparing with the model results and further analysis. Comparisons of the model and the experimental data will provide insight as to how the equipment used for data acquisition and the cantilever are performing. These results will determine if there is a component that is under-performing and should be replaced by a better system. These results will also be used to determine if measurements can be obtained in the MOND regime with small enough uncertainty that MOND can be tested. This will consider a variety of conditions ranging from small vacuum tubes or drop tubes to aircraft and satellites. Finally, attempts will be made to determine if the cantilever can be driven

at acceleration levels in the MOND regime in the lab. This will be a practical test with the apparatus sitting on a table to determine if this is possible, before attempts may be made with the equipment in free fall in the future.

The cantilever's motion will be measured during an experiment where it is driven by a laser. The results for both the noise and driven experiments will be used to consider the possibility of using an AFM cantilever for an experiment to test MOND. The potential experiment will be considered in three different environments; in an evacuated chamber where the experiment is tossed up and caught repeatedly, in an evacuated chamber where the equipment can be dropped repeatedly or, in space upon a satellite where the experiment can be left running for an extended duration of time.

Chapter 2

Vibrations of a Beam: A) without Dissipation

2.1 Overview

The motion of a cantilever with small deflections can be determined through the use of the Euler-Bernoulli beam equation (EBBE). This equation will be derived in this chapter from first principles. The EBBE will also be solved for two different types of beams that are applicable to this project. These beams are the cantilever which is rigidly mounted on one end and free at the other end and the other is a bridge beam which is rigidly mounted at both ends. The solution of the EBBE equation will be solved in the time domain for a freely vibrating beam as this process is simple to complete and the result is required for more complicated situations.

The equation of a wave along a string will also be derived. This result will be used as a comparison to the EBBE to demonstrate why the EBBE is a 4th order differential equation. The second part of the derivation includes the material properties to determine the resulting forces internal to the beam as a result of its deflection. The result that is obtained at this stage is for an ideal beam that is located in a vacuum.

2.2 Euler-Bernoulli Beam Equation

Derivation of the EBBE deals with two different parts. The first part is concerned with the deflection of the beam from an unloaded position and the resulting geometry while the second part deals with the forces in the beam itself due to deflection from its resting

position. Let us first consider the beam's deflection and how it is described.

2.2.1 Geometry and Coordinates of a Deflected Beam

Let there be an axis that runs down the length of the beam that is defined as x and has its origin located at a rigid mount of the beam, as shown in Fig. 2.1. The length of the beam is parallel to this axis. In the case of a cantilever the point $x = l$ will be located at the free end, for a bridge beam $x = l$ will indicate the second rigid mount. A second axis that is orthogonal to x and in the direction of vibration for the cantilever will be defined as y . The height of the beam is parallel to this axis. A final third axis will be the z -axis, perpendicular to the x and y axes and parallel to the width of the beam.

When the beam is deflected, one side of the beam will be compressed and the other stretched. Between these two regions will be a neutral axis whose length remains constant during deflection. The neutral axis will be defined as lying on the x -axis when there is no forces applied to the beam and it is at rest. If the cantilever experiences any deflection, a measure from the neutral axis of the deflected beam to the x -axis is the magnitude of the beam's deflection. Figure 2.1 shows these coordinates and a black dashed line which represents the neutral axis and a grey dashed line as the x -axis. It is convenient to have this displacement described by some function of x and t , specifically $w(x,t)$. Using this coordinate system it can be seen that the slope of the cantilever at any point x is simply $\partial w(x,t)/\partial x$. A third axis, the z -axis, is perpendicular to both the x -axis and y -axis and the width of the cantilever is along this axis. No vibrations along this axis will be considered and as a result in most figures it will be ignored.

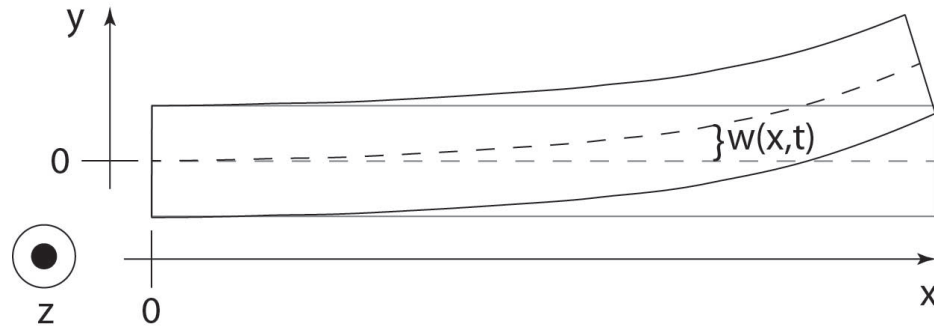


Figure 2.1: Schematic depicting the required coordinate systems for Euler-Bernoulli equation derivation. The black dashed line represents the neutral axis of the cantilever which remains a constant length during deflection and the grey dashed line represents the x -axis.

2.2.2 Bending Moments and Shear Forces

It will be shown that the EBBE equation is dependent upon the force per unit length, referred to as a load, that is applied to a beam. However, to solve for the forces in the beam as a result of deflection this definition must be accepted now.

Consider a beam that has a load, L , applied at $x = l$ and is in static equilibrium. This load pulls at $x = l$ parallel to the y -axis, as depicted in Fig. 2.2a. To gain an understanding of the forces and moments within the cantilever as a result of the applied load, the cantilever will now be considered in two parts, the section on the left which is mounted to the base and the section on the right that the load is applied to, Fig. 2.2b. This allows the right portion of the beam to be analyzed using a free body diagram.

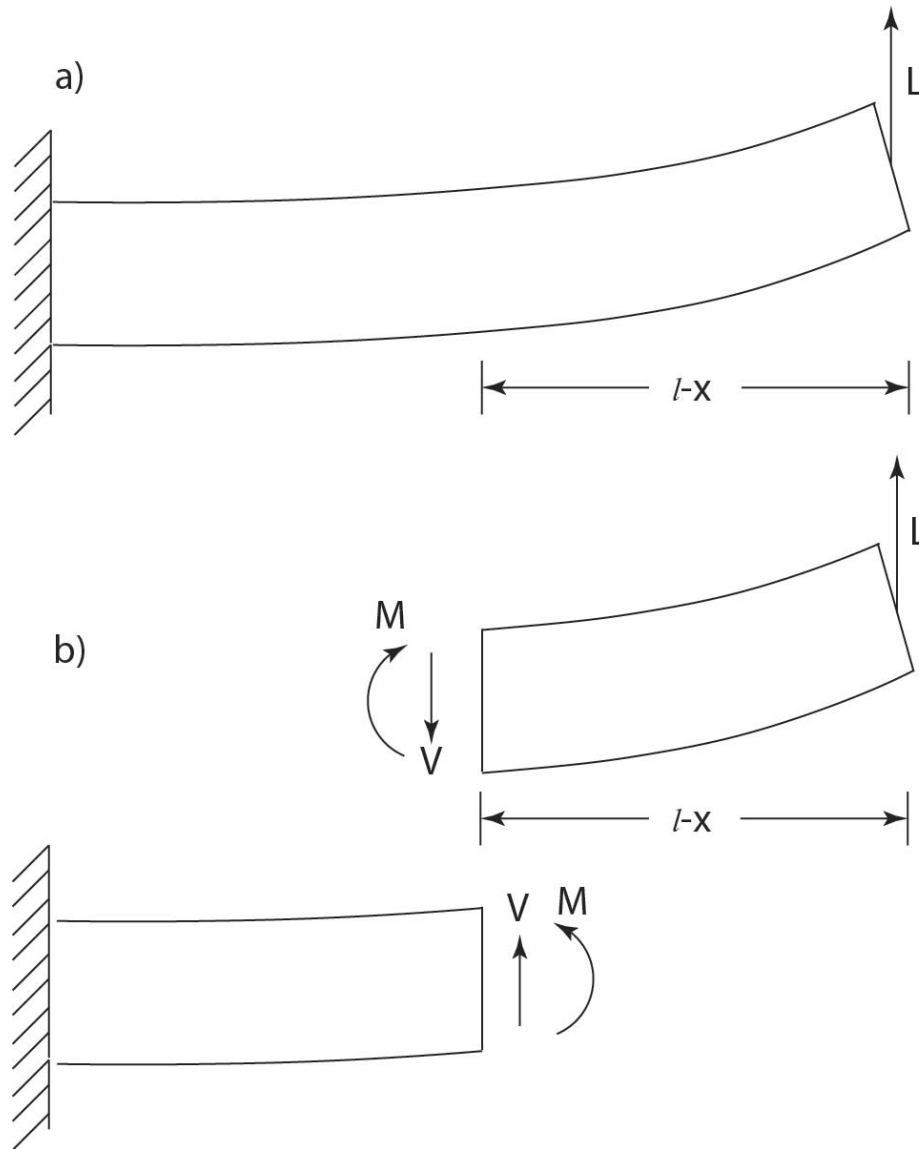


Figure 2.2: Part a) shows a cantilever which has a force, L , applied at $x = l$ and the resulting deflection. Part b) shows the same cantilever and force. The beam is considered as two pieces in this case so that the right portion of the beam can be considered to determine the bending moment, M , and shear force, V , as a result of the applied force.

As a result of the applied load, the beam develops a bending moment M , which acts about the axis of rotation, and a shear force V , which acts parallel to the cross section of the beam.

For a beam that is deflected in the $+y$ -direction, as in Fig. 2.1, the section of the beam above the neutral plane will experience compression while the section of the beam below the neutral plane will experience stretching. Let the absolute distance a particle in the

cantilever is displaced due to stretching or compression be defined as δx (see Fig. 2.3). When some load L is applied perpendicular to the length of the beam causing it to deflect from rest, the original point at x will be displaced to a new located at $x + \delta x$. Using this definition then a positive δx means the beam has been stretched out while a negative δx indicates compression.

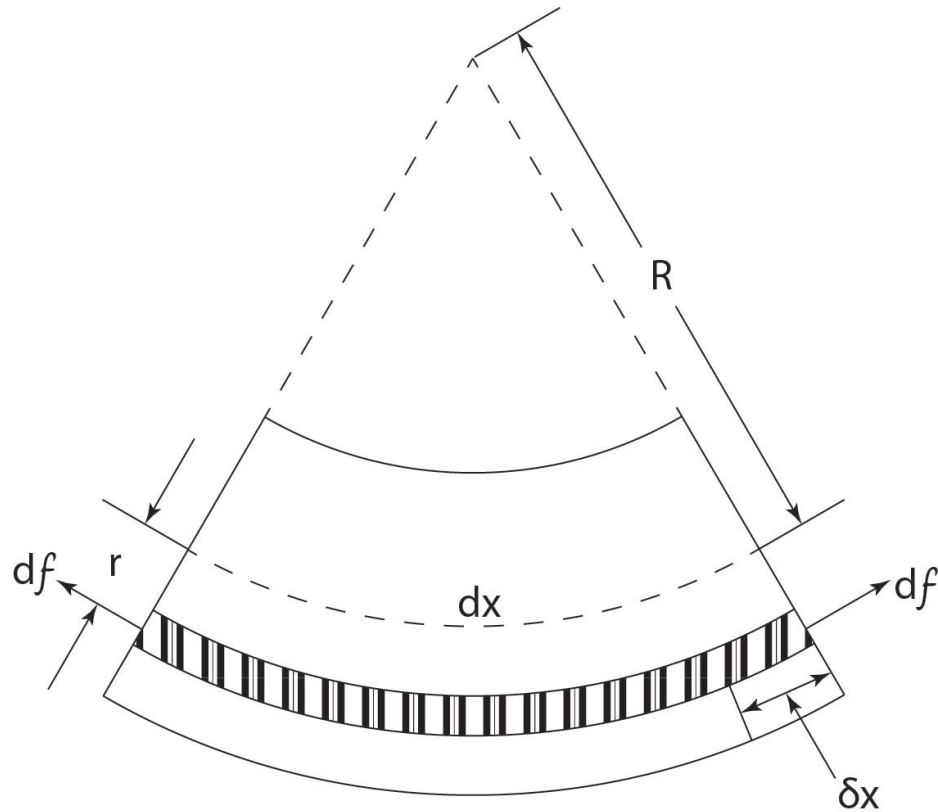


Figure 2.3: Schematic illustrating pertinent geometry of a small section of the beam during deflection. dx is the length of the neutral axis and δx is the change of length at the radius r due to expansion or compression. A positive δx indicates an increase of length due to expansion. R is the radius of curvature for this element of the beam and r is the distance from the neutral plane to the narrow strip of interest of the beam.

The restoring force f due to strain can be calculated using Hooke's Law. If we make the assumption that the strain is small then Hooke's Law can be written as

$$f = -ES \frac{\delta x}{\partial x} \quad (2.1)$$

where S is the cross sectional area of the element of interest and E is the Young's modulus

of the material. For the case of a deflected cantilever where $\delta x/\partial x$ is not a constant across the height of the cantilever this becomes [45]

$$df = -E \frac{\delta x}{\partial x} dS. \quad (2.2)$$

A beam can be considered as small segments from a position x to $x + dx$. The neutral axis of a deflected beam can be extended out such that it forms a circle. The radius of this circle is called the radius of curvature, R , and is illustrated in Fig. 2.3. For some narrow strip that runs along the length of the small segment, parallel to and a distance of r from the neutral axis, it can be seen that $(dx + \delta x)/(R + r) = dx/R$ which can be simplified to find $\delta x/dx = r/R$. This relation can be substituted into Eq. 2.2 to obtain

$$df = \frac{-Er}{R} dS. \quad (2.3)$$

For the case of the deflected beam considered here, there are positive forces above the neutral plane and negative forces below. Due to the deflection and the distribution of forces there is a bending moment, M , present. Specifically, using Eq. 2.3:

$$M = \int r df = \frac{-E}{R} \int r^2 dS. \quad (2.4)$$

The equation for M can be simplified by noting that the area moment of inertia for a beam is $I = \int r^2 dS$ and thus $M = -EI/R$. This integral is performed from r_0 , the point of the beam that we are interested in finding the moment at, out to r_f , the location of the applied load. The moment for some point along the beam will be affected by all loads between that point and the end of the beam. As a result of this the base of a cantilever will be affected by all applied loads while the moment at a point near the free end will only be affected by loads applied between that point and the free end. This model assumes that the beam is rectangular in nature but it can be seen that the base and main portion of the body adhering to this assumption is more important than the free end. It should be noted at this point the

current derivation is using the assumption that both E and I are constant along the length of the beam.

From the geometry of the beam it can be determined that the inverse of the radius of curvature is [46]

$$\frac{1}{R} = \frac{\partial^2 w(x,t)/\partial x^2}{[1 + (\partial w(x,t)/\partial x)^2]^{3/2}} \simeq \frac{\partial^2 w(x,t)}{\partial x^2}. \quad (2.5)$$

This result can then be substituted into Eq. (2.4) to obtain

$$M(x) = -EI \frac{\partial^2 y}{\partial x^2}. \quad (2.6)$$

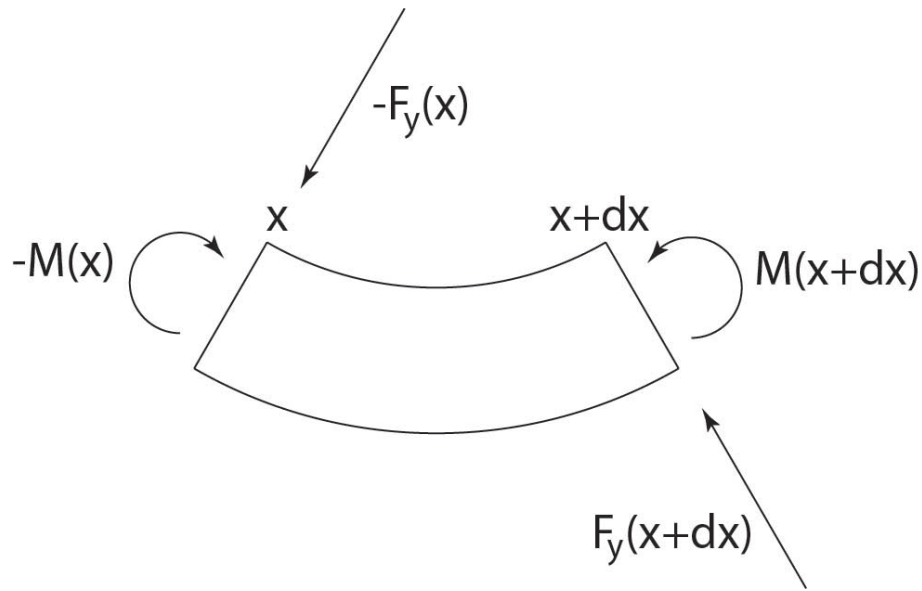


Figure 2.4: Schematic depicting the shear forces and bending moments for some small section of the cantilever that results from deflection.

Bending moments are related to shear forces. Consider some shear force in the beam at x of magnitude $F_y(x)$ and a second at $x + dx$ of $F_y(x + dx)$. These two forces will cause the beam to bend and create an internal bending moment. The relationship between the shearing force and the bending moment of a static beam can be determined by summing all of the moments acting on the beam about the point $x + dx$. For a static beam this is

$$M(x+dx) - M(x) - F_y(x)dx = 0. \quad (2.7)$$

This can be solved for $F_y(x)$ by using Eq. (2.6) to find

$$F_y(x) = \frac{\partial M(x)}{\partial x} = -EI \frac{\partial^3 w(x,t)}{\partial x^3}. \quad (2.8)$$

For the cantilever to have motion there must be a load that is acting upon it. The load can be external, F_{ext} , or internal created by the compression and expansion of the material the beam is composed of. The case of an external load will be considered in a later section. The internal load case can be determined through the use of shear forces. That is, if there is some force dF_y in the cantilever acting on the slice from x to $x+dx$ then the resulting slice will have some acceleration. Mathematically this force is described by

$$dF_y = F_y(x+dx) - F_y(x) = \frac{\partial F_y(x)}{\partial x} dx = -EI \frac{\partial^4 w(x,t)}{\partial x^4} dx, \quad (2.9)$$

where Eq. (2.8) was used.

For a cantilever that is in motion we can employ Newton's 2nd law where the acceleration of the cantilever is $\partial^2 w(x,t)/\partial t^2$ and the mass of a thin element of the cantilever is μdx . Newton's 2nd law, $ma = \sum_i F_i$, can now be used to obtain the result

$$\mu dx \frac{\partial^2 w(x,t)}{\partial t^2} = -EI \frac{\partial^4 w(x,t)}{\partial x^4} dx + F_{ext}(x,t) dx. \quad (2.10)$$

This result can be simplified to obtain the EBBE,

$$EI \frac{\partial^4 w(x,t)}{\partial x^4} + \mu \frac{\partial^2 w(x,t)}{\partial t^2} = F_{ext}(x,t). \quad (2.11)$$

$F_{ext}(x,t)$ is a force per unit length and can be integrated to obtain the total force that is applied to the cantilever is $F_{total} = \int_0^l F_{ext}(x,t) dx$.

The phase speed of a wave through a beam can be calculated using Eq. (2.11) where

we assume that there is no external load. This equation can be simplified to become

$$\frac{\partial^4 w(x,t)}{\partial x^4} + \frac{EI}{\mu} \frac{\partial^2 w(x,t)}{\partial t^2} = 0. \quad (2.12)$$

Consider a simple harmonic wave travelling along the beam of the form

$$w(x,t) = Ce^{i(kx-\omega t)} \quad (2.13)$$

where C is the waves amplitude, k is the wave number and ω is the frequency of the wave. Substituting Eq. (2.13) into Eq. (2.12) and evaluating we obtain

$$k^4 - \frac{EI\omega^2}{\mu} = 0. \quad (2.14)$$

Given that the frequency cannot be negative, the positive root solution for the frequency is

$$\omega = k^2 \sqrt{\frac{\mu}{EI}}. \quad (2.15)$$

The relationship between ω and k is not proportional as is normally found for mechanic waves. The relationship here is similar to that of a free particle in quantum mechanics, $\omega = \hbar k^2 / 2m$. The phase speed, c , of a wave is

$$c = \frac{\omega}{k}. \quad (2.16)$$

Taking the positive root of Eq. (2.15) and substituting this result into Eq. (2.16), the phase speed of a wave through a beam can be determined to be

$$c = \left(\frac{EI\omega^2}{\mu} \right)^{1/4}. \quad (2.17)$$

The phase speed is dependent upon $\sqrt{\omega}$, causing waves of different frequencies to travel down the beam at different velocities. A direct result of this is that the shape of the wave packet will change as it propagates.

2.3 The Wave Equation for a String

A common equation in physics that deals with the motion of a linear body is the one dimensional wave equation. This equation describes transverse displacements of a string as a wave travels down it. This equation will be derived from first principles and then compared with the EBBE. Undergraduate students are taught the wave equation for a string. This result is found to be a second order differential equation. The derivation is provided here as a comparison to that of the EBBE derivation to help demonstrate the complexities of the beam system and why it is a fourth order differential equation.

Let us consider some small segment of a string that is stretched between two points with some tension T . If no external forces are applied to the string and it is simply left at rest the string will connect the two end points by a straight line. This will be referred to as the neutral axis, the x -axis.

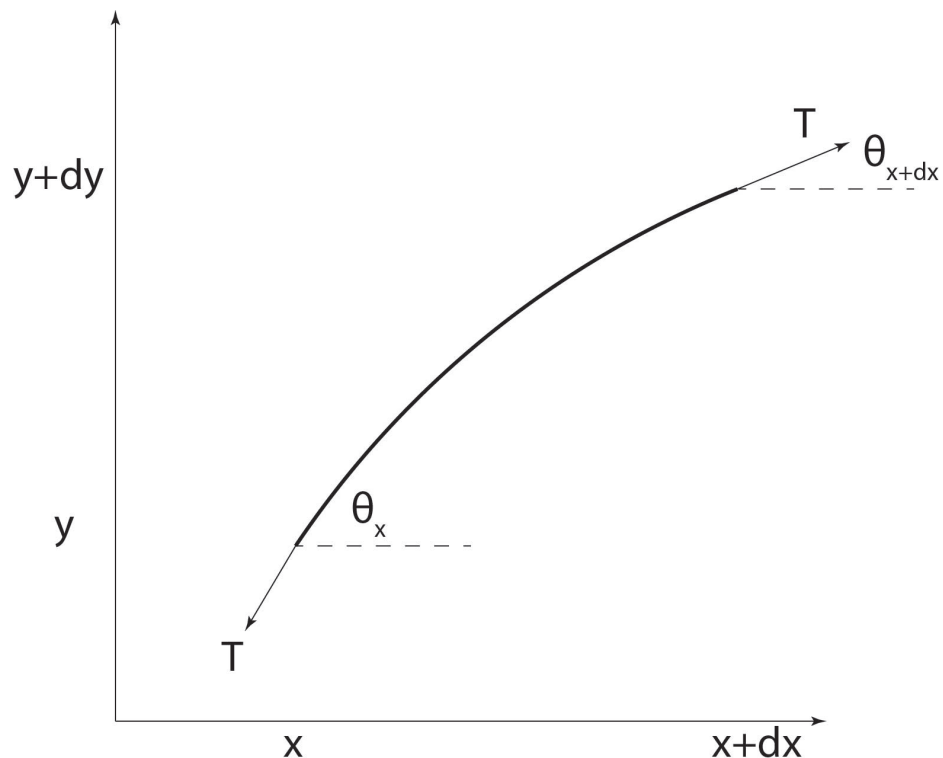


Figure 2.5: Diagram showing a deflected string segment and the resulting tension.

The tension within a small segment of the string is inline with the tangent of that seg-

ment. When the string is at rest the tension will be applied directly along the length of the string and there will be no y-component. If the string is deflected off of the x-axis it is possible that the tension will have a y-component. If the segment of the string makes a small angle, θ , with respect to the x-axis then the y-component of the tension within the string that is acting upon the segment is

$$df_y(x) = (T \sin(\theta_{x+dx})) - (T \sin(\theta_x)) \quad (2.18)$$

The first term on the Right Hand Side (RHS) can be expanded using a Taylor series to obtain

$$\begin{aligned} df_y(x) &= [(T \sin(\theta_x)) + \frac{\partial(T \sin(\theta_x))}{\partial x} dx + \dots] - (T \sin(\theta_x)) \\ &= \frac{\partial(T \sin(\theta_x))}{\partial x} dx. \end{aligned} \quad (2.19)$$

The second line of the equation was found by making the assumption that the displacement of the string and θ will be small and thus it is reasonable to keep only the first two leading terms. Given that θ is small we can use the small angle approximation and rewrite θ as $\frac{\partial y}{\partial x}$. Making this substitution into the previous equation, the net force that is applied to the small segment of the string becomes

$$df_y(x) = T \frac{\partial^2 y}{\partial x^2} dx. \quad (2.20)$$

Newton's 2nd law can now be applied in the y-direction to determine the motion of the string. The mass of the segment of the string is μdx where μ is the linear mass density of the string. Substituting Eq. (2.20) into Newton's 2nd law gives the result

$$T \frac{\partial^2 y}{\partial x^2} dx = \mu dx \frac{\partial^2 y}{\partial t^2}. \quad (2.21)$$

This result can be simplified by using the term $c = \sqrt{\frac{T}{\mu}}$, the phase speed of the wave, to obtain

$$\frac{\partial^2 y}{\partial x^2} = \frac{1}{c^2} \frac{\partial^2 y}{\partial t^2}. \quad (2.22)$$

For the case of a deflected string, the restoring force that pulls on the string is the result of the tension of the string as shown by Eq. (2.20). For some small segment of the string this force is dependent on the second derivative of the string and thus the wave equation is second order.

From the derivation of the EBBE it was found that the restoring force was the shear force within the beam (see Eq. (2.9)). Hooke's Law, Eq. (2.1), can be used to determine the force that acts along the length of the beam. This force created a bending moment within the beam which, using a result from the geometry section, determined the moment to be dependent upon the second derivative of the beam. The derivative of the bending moment provides the result for the shear force in the beam, dependent upon the 3rd derivative. It is this shear force that causes the beam to move. Finally, to determine the shear force acting upon some small segment of the beam the derivative of the shear force is taken and multiplied by the length of the segment. The length was found to cancel out when Newton's 2nd law was applied and thus the EBBE became a 4th order differential equation.

2.4 Potential Energy of a Beam

The total energy that is stored in a beam as a result of deformation is called strain energy. For the case of a simple beam that experiences deflection in only one direction this is [47]

$$U = \frac{1}{2} \int_V \sigma \epsilon dV \quad (2.23)$$

where σ is the stress and ϵ strain caused by the deflection. Both the stress and strain are the result of compression or expansion of the beam due to deflection and can be solved for from the geometry of the beam. The stress within the cantilever is directly related to the strain, that is

$$\sigma = E\varepsilon. \quad (2.24)$$

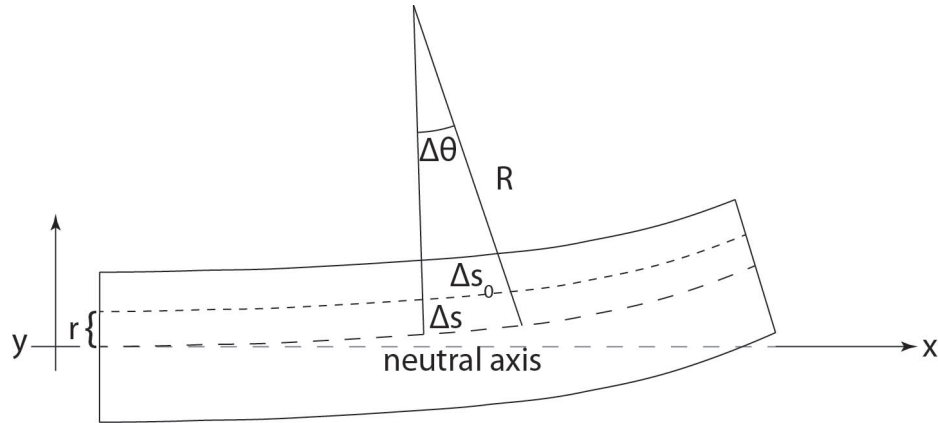


Figure 2.6: Diagram depicting the radius of curvature, R , for a deflected beam. Δs is the length of the neutral axis while Δs_0 is the length of a cord of the beam located at a distance r from the neutral axis. If the beam were not deflected then $\Delta s = \Delta s_0$.

Consider a thin cord that runs along the length of cantilever at some distance r from the neutral axis, as shown in Fig. 2.6. As a result of deflection, the cantilever has a radius of curvature R , the cord will have a length of Δs and the corresponding cord along the neutral axis will have a length of Δs_0 . The strain that the cord experiences is [47]

$$\varepsilon = \frac{\Delta s - \Delta s_0}{\Delta s_0}. \quad (2.25)$$

An assumption that is used for this analysis is that the deflection of the cantilever is small such that the small angle approximation can be used which makes $\Delta s_0 = R\theta$ and $\Delta s = (R - r)\theta$. Substituting this into the previous equation and using the result of Eq. (2.5), the strain in the beam is

$$\varepsilon = \frac{(R - r)\theta - R\theta}{R\theta} = \frac{-r}{R} = -r \frac{\partial^2 w(x, t)}{\partial x^2}. \quad (2.26)$$

Substituting the results of Eqs 2.24 and 2.26 into Eq. 2.23 we obtain

$$U = \frac{1}{2} \int_V E r^2 \left(\frac{\partial^2 w(x,t)}{\partial x^2} \right) dV. \quad (2.27)$$

This integral is simplified by the fact that the area moment of inertia is

$$I = \int \int r^2 dy dz. \quad (2.28)$$

Finally, the potential energy stored in a beam due to a deflection is

$$U(t) = \frac{EI}{2} \int_0^l \left(\frac{\partial^2 w(x,t)}{\partial x^2} \right)^2 dx. \quad (2.29)$$

2.5 Fixed-Free Boundary Conditions

The simple, free motion of a cantilever is much easier to derive than one which is damped in a fluid and driven by thermal energy. The solution to the simple case is also beneficial as it provides the equation that describes the modes of the cantilever as well as the frequency equation, both of which are important to the more complicated system.

The properties of the two ends of the beam are required to define the boundary conditions [45]. Let the beam be defined to be mounted at $x = 0$ and free at $x = l$ where l is the length of the beam (see Fig. 2.7). Due to the beam being rigidly mounted at $x = 0$, it can have neither a displacement nor a slope, that is

$$w(x,t)|_{x=0} = 0 \quad \text{and} \quad \left. \frac{\partial w(x,t)}{\partial x} \right|_{x=0} = 0. \quad (2.30)$$

The free end of the of cantilever at $x = l$ is free to have motion and thus can have both a displacement and slope. As there is nothing to act upon the free end of the cantilever it does not experience any bending moment nor shear force causing the boundary conditions to be

$$\left. \frac{\partial^2 w(x,t)}{\partial x^2} \right|_{x=l} = 0 \quad \text{and} \quad \left. \frac{\partial^3 w(x,t)}{\partial x^3} \right|_{x=l} = 0. \quad (2.31)$$

The EBBE, Eq. (2.11), where there are no external forces is

$$EI \frac{\partial^4 w(x,t)}{\partial x^4} + \mu \frac{d^2 w(x,t)}{dt^2} = 0. \quad (2.32)$$

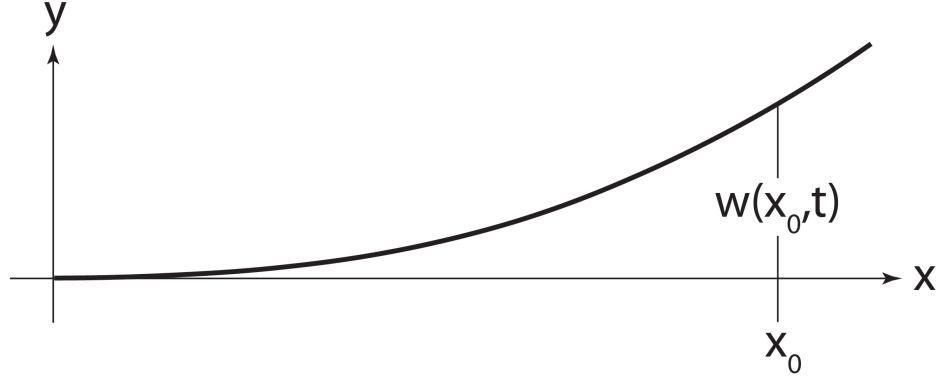


Figure 2.7: Cantilever deflection from a relaxed state along the x -axis is given by $w(x,t)$.

We can assume a solution using separation of variables; Then $w(x,t)$ is of the form,

$$w(x,t) = \sin(\omega t + \theta) \phi(x) \quad (2.33)$$

where the sine term allows the function to evolve over time and the function $\phi(x)$ describes the shape of each mode of the cantilever. Substituting $w(x,t)$ of this form into Eq. (2.32) and moving the constants to the RHS results in

$$\frac{\partial^4 \phi(x)}{\partial x^4} = \frac{-\mu \omega^2}{EI} \phi(x). \quad (2.34)$$

The general solution for this differential is

$$\phi(x) = D_1 \cos(\kappa x) + D_2 \sin(\kappa x) + D_3 \cosh(\kappa x) + D_4 \sinh(\kappa x) \quad (2.35)$$

where D_n are constants, x ranges from 0 to l and

$$\kappa = \left(\frac{\mu \omega^2}{EI} \right)^{1/4}. \quad (2.36)$$

Using the boundary conditions for $x = 0$ it can be determined that $D_3 = -D_1$ and $D_4 = -D_2$. Using these relations Eq. (2.35) becomes

$$\phi(x) = D_1 (\cos(\kappa x) - \cosh(\kappa x)) + D_2 (\sin(\kappa x) - \sinh(\kappa x)). \quad (2.37)$$

Using the boundary conditions for $x = l$, a matrix with the form $\mathbf{AC} = \mathbf{0}$, can be made,

$$\begin{bmatrix} (\cos(\kappa l) + \cosh(\kappa l)) & (\sin(\kappa l) + \sinh(\kappa l)) \\ (\sinh(\kappa l) - \sin(\kappa l)) & (\cos(\kappa l) + \cosh(\kappa l)) \end{bmatrix} \begin{bmatrix} D_1 \\ D_2 \end{bmatrix} = \begin{bmatrix} 0 \\ 0 \end{bmatrix}. \quad (2.38)$$

For Eq. 2.38 to be true and the result to be non-trivial, that is D_1 and D_2 not equal to zero, it is required that $\det|\mathbf{A}| = 0$ [48]. This result is called the frequency equation and for a cantilever beam it is

$$1 + \cos(\kappa l) \cosh(\kappa l) = 0. \quad (2.39)$$

The roots of the frequency equation can be used to determine the fundamental resonance frequencies of the cantilever in a vacuum. Let the n^{th} root of the frequency equation to be C_n , where the roots are in ascending order and $n = 1$ corresponds to the smallest, non-trivial positive root. Then, using Eq. 2.36, the roots are

$$C_n = l \left(\frac{\mu \omega_n^2}{EI} \right)^{1/4}. \quad (2.40)$$

The resonance frequency for the n^{th} mode of the cantilever in a vacuum is

$$\omega_{vac,n} = \frac{C_n^2}{l^2} \sqrt{\frac{EI}{\mu}}. \quad (2.41)$$

The boundary condition $d^3\phi(l)/dx^3 = 0$ can be used to obtain the relation between D_1 and D_2 . The solution for the n^{th} mode, which can be substituted into Eq. (2.33) for the position of the cantilever, is

$$\begin{aligned} \phi_n(x) = & (\cos(C_n x/l) - \cosh(C_n x/l)) \\ & + \frac{(\cos(C_n) + \cosh(C_n))}{(\sin(C_n) + \sinh(C_n))} \times (\sinh(C_n x/l) - \sin(C_n x/l)). \end{aligned} \quad (2.42)$$

The previous result uses $D_1 = 1$ such that

$$\int_0^l \phi_n^2(x) dx = l. \quad (2.43)$$

Equation (2.42) can be substituted back into Eq. (2.33) for a solution to the EBBE for a cantilever in a vacuum.

Table 2.1: The first four mode shapes and corresponding values for C_n for the cantilever. The striped end plate represents the rigid mount that the cantilever extends out from.

n	C_n	$\phi_n(x)$
1	1.875104	
2	4.69409	
3	7.8547574	
4	10.99554	

2.6 Fixed-Fixed Boundary Conditions

The free vibrations of a simple bridge beam will be considered in this section. A bridge beam is one that is rigidly mounted at both ends, as opposed to just one end like the cantilever beam. While all experiments were performed using a cantilever, the bridge will be considered theoretically to determine if the cantilever was the best choice. The cantilever

beam will be studied experimentally in later chapters. The inclusion of the bridge beam is for theoretical purposes only. The EBBE model will be solved for the bridge beam and these theoretical results will be compared with the theoretical model of the cantilever. This will determine which beam produces the least amount of noise and if the bridge beam should be considered for the MOND experiment. Other types of beam mounting are possible; like free ends, which the cantilever has one free end, or mounting using a mechanism, like a pin, that allows the beam to freely rotate about a point. Beams that are held without a rigid mount like a pin, unlike what the bridge and cantilever use, are challenging to work with as they are free to rotate about the pin that holds them in place causing difficulties when trying to determine if the measured deflection is due to beam deflection or simply the whole beam rotating around the pin. The use of pins also introduces manufacturing challenges on such small scales while rigid mounts are much easier to create. The free beam which uses no mounts allows the beam to rotate and move freely around. Due to the freedom of this beam it will fall to the ground in a gravitational field. Due to these varying challenges in the manufacturing, mounting, and measurement processes, the only viable alternative to the cantilever beam is the doubly, rigidly mounted bridge.

Unlike the cantilever, the bridge has both ends rigidly mounted to the base. As both ends use the same mounting style they are both subject to the same boundary conditions. A rigidly mounted beam end can have no displacement nor rotation making the boundary conditions at $x = 0$ and $x = l$ to be

$$\begin{aligned}
 w(0,t) = 0 \quad \text{and} \quad \frac{\partial w(0,t)}{\partial x} = 0 \\
 \text{and} \\
 w(l,t) = 0 \quad \text{and} \quad \frac{\partial w(l,t)}{\partial x} = 0.
 \end{aligned}
 \tag{2.44}$$

The bridge is required to satisfy the same equation as the cantilever, Eq. (2.32). Separation of variables, Eq. (2.33), can be used and the resulting differential equation that must be solved is

$$\frac{\partial^4 \phi(x)}{\partial x^4} = \frac{-\mu\omega^2}{EI} \phi(x). \quad (2.45)$$

The general solution for this differential is

$$\phi(x) = D_1 \cos(\kappa x) + D_2 \sin(\kappa x) + D_3 \cosh(\kappa x) + D_4 \sinh(\kappa x) \quad (2.46)$$

where D_n are constants, x ranges from 0 to l and

$$\kappa = \left(\frac{\mu\omega^2}{EI} \right)^{1/4}. \quad (2.47)$$

To solve the differential equation using the boundary condition we require Eq. (2.46) along with it's derivative,

$$\frac{d\phi(x)}{dx} = -D_1 \kappa \sin(\kappa x) + D_2 \kappa \cos(\kappa x) + D_3 \kappa \sinh(\kappa x) + D_4 \kappa \cosh(\kappa x). \quad (2.48)$$

Applying the boundary conditions for $x = 0$ we find that $D_4 = -D_2$ and $D_3 = -D_1$. Making the appropriate substitutions ϕ and $d\phi/dx$ become

$$\phi(x) = D_1 (\cos(\kappa x) - \cosh(\kappa x)) + D_2 (\sin(\kappa x) - \sinh(\kappa x)) \quad (2.49)$$

and

$$\frac{d\phi(x)}{dx} = -D_1 \kappa (\sin(\kappa x) + \sinh(\kappa x)) + D_2 \kappa (\cos(\kappa x) - \cosh(\kappa x)). \quad (2.50)$$

The previous two results can be used to create the matrix equation

$$\begin{bmatrix} (\cos(\kappa l) - \cosh(\kappa l)) & (\sin(\kappa l) - \sinh(\kappa l)) \\ -(\sinh(\kappa l) + \sin(\kappa l)) & (\cos(\kappa l) - \cosh(\kappa l)) \end{bmatrix} \begin{bmatrix} D_1 \\ D_2 \end{bmatrix} = \begin{bmatrix} 0 \\ 0 \end{bmatrix}. \quad (2.51)$$

In the same fashion that the frequency equation was calculated for the cantilever beam, the frequency equation for the bridge beam is determined by finding the non-trivial solutions to Eq. 2.51. These solutions can be found by setting the determinant of \mathbf{A} to zero. From this process it is found that the frequency equation is

$$1 - \cos(\kappa l) \cosh(\kappa l) = 0. \quad (2.52)$$

As with the cantilever, the roots of this equation can be used to determine the resonance frequency for the n^{th} mode. Let the n^{th} root be C_n where $n = 1$ corresponds to the smallest, non-trivial positive root. Using Eq. (2.47) the roots are

$$C_n = l \left(\frac{\mu \omega_n^2}{EI} \right)^{1/4}. \quad (2.53)$$

The resonance frequency for the n^{th} mode of the bridge beam in a vacuum is

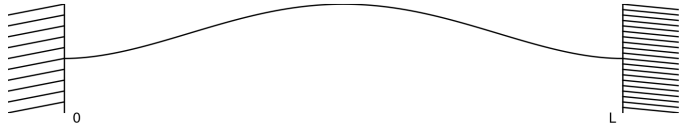
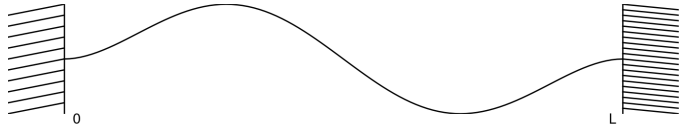
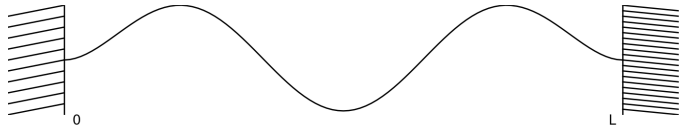
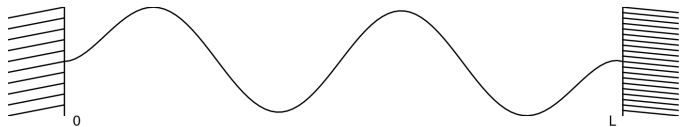
$$\omega_{vac,n} = \frac{C_n^2}{l^2} \sqrt{\frac{EI}{\mu}}. \quad (2.54)$$

The relationship between D_1 and D_2 can be found using the boundary condition $\phi(l) = 0$ to obtain

$$\begin{aligned} \phi_n(x) &= (\cos(C_n x/l) - \cosh(C_n x/l)) \\ &\quad - \frac{(\cos(C_n) - \cosh(C_n))}{(\sin(C_n) - \sinh(C_n))} (\sin(C_n x/l) - \sinh(C_n x/l)) \end{aligned} \quad (2.55)$$

As with the cantilever, D_1 was set to 1. This result can be substituted back into Eq. (2.33) for a solution to the EBBE for a beam in a vacuum.

Table 2.2: The first four mode shapes and corresponding values for C_n for the bridge beam. The striped end plates represents the rigid mounts that the bridge extends between.

n	C_n	$\phi_n(x)$
1	4.7300408	
2	7.8532046	
3	10.9956075	
4	14.31371655	

2.7 Conclusion

The theory starts with the derivation of the differential equation that describes the motion of a beam, the EBBE equation. This process uses a simple coordinate system to describe the deflection of a beam and the bending moments and shear forces can be used to determine the resulting acceleration of the beam from an arbitrary load. This chapter derived the EBBE equation that describes the motion of a beam. This result is used to solve for the free motion of a cantilever and a bridge beam in a vacuum. Beams are often submerged in a fluid and the results obtained here for a vacuum are not adequate in that case. However, the mode shapes of the beams that were obtained here do apply to the more complicated system of a beam in a fluid.

Chapter 3

Vibrations of a Beam: B) with Dissipation

3.1 Introduction

It is common that a beam will be submerged in a fluid of some sort, be that a liquid or gas. The effects of a fluid on a beam's motion are determined using the hydrodynamic load. The hydrodynamics will be derived using Stokes' equation for a circular beam. Finally, as the beam has a non-zero temperature it will have energy and will fluctuate. Thermodynamics will be employed to determine the motion of the beam as a result of the beam having thermal energy. The results that are obtained will apply to both the cantilever and the bridge beam.

The EBBE that was derived was for the time domain. However, the derivation to determine the effects of a fluid on a beam in motion is most easily completed in the frequency domain. As a result, a Fourier transform will be used such that the EBBE will be in the frequency domain as well. This will prove beneficial as later analysis will be considering the cantilever's Power Spectral Density (PSD).

The PSD of the cantilever can be used to determine the expected uncertainty of a measurement. The MOND experiment requires very small accelerations to be accurately measured. The expected uncertainty can be used to determine the limits for how small of a measurement can be obtained. Later analysis will use the cantilever's PSD to determine what the requirements will be for MOND experiment.

3.2 Hydrodynamic Load

In this section the effects of a fluid on a submerged beam which is in motion are considered. The hydrodynamic force was first derived by Stokes in 1901 [49]. This derivation has been repeated by Magrab [47] with modern notation and the following section is based on his outline.

The properties of the fluid must be considered to help define the required boundary conditions. It will be assumed that the fluid has no motion of its own beyond that created by the beam. For the simplicity of the mathematics it will be assumed that the box that contains the beam will be infinitely large. This allows the fluid that is infinitely far away from the beam to have zero velocity. As a direct result of the small size of the beam it is expected that it will have a very small displacement allowing the beam's effects on the fluid to dissipate very quickly.

The Navier-Stokes equation is

$$\frac{D\vec{u}}{Dt} = \frac{-\vec{\nabla}p}{\rho_f} + \nu\nabla^2\vec{u} \quad (3.1)$$

where the introduced variables are: \vec{u} describes the velocity of the fluid, p is the pressure within the fluid, ρ_f is the density of the fluid, $\nu = \eta_f/\rho_f$ is the kinematic viscosity of the fluid, and η_f is the dynamic viscosity. The “substantial differential” is defined as [52]

$$\frac{D}{Dt} \equiv \frac{\partial}{\partial t} + u_i \frac{\partial}{\partial x_i} \quad (3.2)$$

where u_i are the velocity components and x_i are the coordinates of the system.

There are two assumptions that can be made to simplify this derivation, and that are reasonable as the displacement of the beam is small. First, let us assume that the magnitude of oscillations is small compared to the diameter of the beam, then the linearized form of the Navier-Stokes equations can be used [50]. This assumption allows the non-linear convective terms to be ignored. This assumption allows the non-linear convective terms to

be ignored,

$$\frac{D\vec{u}}{Dt} \simeq \frac{\partial\vec{u}}{\partial t}. \quad (3.3)$$

Secondly, let it be assumed that the fluid is incompressible. This assumption is permissible so long as the wavelength of the vibrations are much larger than the dominant length scale of the beam in the flow, b , and this length scale is much larger than the amplitude of the vibrations of the beam. This assumption can be extended to gases as well so long as the dominant length scale is much greater than the mean free path of the gas [51]. This is a common assumption to use and is employed by Stokes when calculating the drag on a sphere [49]. In the case where this is not true and the fluid does compress, acoustic radiation dampening effects will need to be accounted for as a source of drag. Using this assumption, it can be stated that

$$\vec{\nabla} \cdot \vec{u} = 0. \quad (3.4)$$

Let the coordinate system be Cartesian with the x -axis running along the length of the beam and the direction of oscillation of the beam be along the y -axis. In this case the oscillation of the beam can be described by $\vec{q} = q_0 e^{i\omega t} \hat{j}$. Employing the previous assumptions Eq. (3.1) can be rewritten as

$$\frac{\partial\vec{u}}{\partial t} = \frac{-\vec{\nabla}p}{\rho_f} + \nu\nabla^2\vec{u}. \quad (3.5)$$

The curl of a gradient field is zero, $\vec{\nabla} \times \vec{\nabla}p = 0$. As a result of this, the curl of the Navier-Stokes equation is

$$\frac{\partial}{\partial t} \vec{\nabla} \times \vec{u} = \nu \vec{\nabla} \times (\nabla^2 \vec{u}). \quad (3.6)$$

The assumption that the fluid is incompressible allows for the use of the streamline

concept allowing \vec{u} to be written as

$$\vec{u} = \vec{\nabla}\psi \times \vec{\nabla}x = \vec{\nabla}\psi \times \hat{i} \quad (3.7)$$

where ψ is a streamline [52]. A streamline is a curve of constant value that is tangent to the direction of flow of the fluid.

The vorticity, $\vec{\sigma}$, of a fluid is

$$\begin{aligned} 2\vec{\sigma} &\equiv \vec{\nabla} \times \vec{u} = \vec{\nabla} \times (\vec{\nabla}\psi \times \hat{i}) \\ &= (\hat{i} \cdot \vec{\nabla})\vec{\nabla}\psi - \hat{i}\vec{\nabla} \cdot (\vec{\nabla}\psi) = -\hat{i} \left(\frac{\partial^2\psi}{\partial y^2} + \frac{\partial^2\psi}{\partial z^2} \right). \end{aligned} \quad (3.8)$$

The only non-trivial term is σ_x and thus the vorticity is

$$\sigma \hat{i} = \frac{1}{2} \vec{\nabla} \times \vec{u} = -\frac{1}{2} \nabla^2 \psi \hat{i}. \quad (3.9)$$

The previous result can be used to simplify Eq. (3.6). The Left Hand Side (LHS) of Eq. (3.6) becomes

$$\frac{\partial}{\partial t} \vec{\nabla} \times \vec{u} = \frac{\partial}{\partial t} (-\hat{i} \nabla^2 \psi). \quad (3.10)$$

To simplify the RHS of Eq. (3.6) will require the curl of the Laplacian of a vector field,

$$\nabla \times \nabla^2 \vec{u} = \nabla \times \nabla(\nabla \cdot \vec{u}) - \nabla \times \nabla \times (\nabla \times \vec{u}). \quad (3.11)$$

When $\nabla \times \nabla(\nabla \cdot \vec{u})$ is evaluated it is determined to be 0 as the curl of a gradient is 0. Now the RHS of Eq. (3.6) can be rewritten as

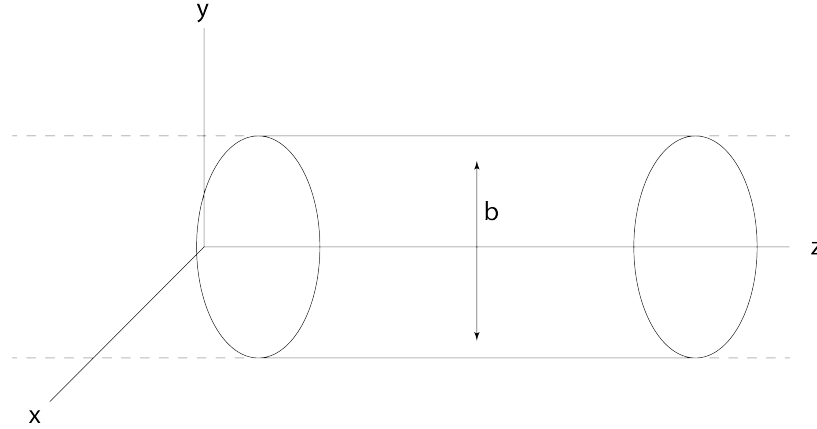


Figure 3.1: The coordinate system used for the derivation of the hydrodynamic function for a cylindrical beam with a diameter of b .

$$\begin{aligned}
 \nu \vec{\nabla} \times (\nabla^2 \vec{u}) &= -\nu \vec{\nabla} \times (\vec{\nabla} \times \vec{\nabla} \times \vec{u}) \\
 &= 2\nu \vec{\nabla} \times (\vec{\nabla} \times \hat{\sigma} \hat{i}) \\
 &= 2\nu \vec{\nabla} \times (-\hat{i} \times \vec{\nabla} \sigma) \\
 &= -2\nabla^2 \sigma \hat{i} \\
 &= \nu \nabla^4 \psi \hat{i}
 \end{aligned} \tag{3.12}$$

Substituting the results of Eq. (3.10) and Eq. (3.12) back into Eq. (3.5) we find that the streamline function must satisfy

$$\nabla^2 \left(\nabla^2 \psi - \frac{\rho_f}{\eta_f} \frac{\partial \psi}{\partial t} \right) = 0. \tag{3.13}$$

For some small element of the beam that is very close to $x = 0$ or $x = l$ it is obvious that the fluid flow will vary from that of the fluid that is around the central portion of the beam. Thus this derivation will use the assumption that the diameter of the beam is small compared to the length of the beam and that the beam is infinite, making the errors introduced at the ends small.

Thanks to the assumption that the beam is infinitely long it is easiest to solve this portion of the problem using cylindrical co-ordinates. The beam will be considered cylindrical in

nature with a diameter of b . This result will later be used to determine the hydrodynamic function for a beam with a rectangular cross section using a correction function. The z -axis will be defined as running along the axis of the beam when it is at rest such that the origin of the polar coordinate system is at the center of the beam, Fig. 3.1. The r -coordinate will extend out from the z -axis and the θ -coordinate will extend around the beam. Using this coordinate system and the infinite beam assumption, there will be symmetry along the length of the z -axis and as a result this term will be dropped leaving the polar coordinate system defined by r and θ . For cylindrical coordinates, the equation that the streamline function must satisfy, Eq. (3.13) will use

$$\nabla^2 = \frac{\partial^2}{\partial r^2} + \frac{1}{r} \frac{\partial}{\partial r} + \frac{1}{r^2} \frac{\partial^2}{\partial \theta^2}. \quad (3.14)$$

Equation (3.13) can be solved using a sum of solutions, $\psi = \psi_1 + \psi_2$, where ψ_1 and ψ_2 are, respectively, solutions to

$$\begin{aligned} \nabla^2 \psi_1 &= 0 \\ \nabla^2 \psi_2 - \frac{\rho_f}{\eta_f} \frac{\partial \psi_2}{\partial t} &= 0. \end{aligned} \quad (3.15)$$

The two components of the velocity of the fluid as it flows around the beam are

$$\begin{aligned} u_r &= \frac{1}{r} \frac{\partial \psi}{\partial \theta} \hat{r} \\ u_\theta &= -\frac{\partial \psi}{\partial r} \hat{\theta}. \end{aligned} \quad (3.16)$$

The boundary conditions for the fluid can be defined at two different locations, the surface of the beam and at a distance infinitely far away from the beam. Let us assume that the beam is being driven as a forced harmonic oscillator at a frequency ω and the magnitude of the velocity is u_0 . The boundary conditions for the fluid at the surface of the beam will be

$$u_r(b/2, \theta, t) = u_0 \cos(\theta) e^{i\omega t},$$

and

$$(3.17)$$

$$u_\theta(b/2, \theta, t) = -u_0 \sin(\theta) e^{i\theta t}.$$

It will be assumed that the space containing the beam was infinitely large and is stationary except for the fluid motion caused by the cantilever. Consequently, the boundary condition for the fluid at an infinite distance away from the beam is that as $r \rightarrow \infty$, $u_r \rightarrow 0$ and $u_\theta \rightarrow 0$.

From these boundary conditions we can assume the form of the solutions to Eq. (3.15) will be

$$\Psi_k = \Psi_k(r) \sin(\theta) e^{i\omega t} \quad k = 1, 2. \quad (3.18)$$

This solution can be substituted back into Eq. (3.15) to obtain

$$\nabla_r^2 \Psi_1 = 0 \quad (3.19)$$

and

$$\nabla_r^2 \Psi_2 - \frac{i\omega \rho_f}{\eta_f} \Psi_2 = 0 \quad (3.20)$$

where

$$\nabla_r^2 = \frac{\partial^2}{\partial r^2} + \frac{1}{r} \frac{\partial}{\partial r} - \frac{1}{r^2}. \quad (3.21)$$

Equation (3.19) has a solution of the form

$$\Psi_1 = \frac{C_1}{r} + C_2 r. \quad (3.22)$$

For this solution to satisfy the boundary conditions at $r \rightarrow \infty$, C_2 must be 0. Thus Ψ_1 is

$$\psi_1 = \frac{C_1}{r}. \quad (3.23)$$

The solution to Eq. (3.20) can be solved by first expanding it using Eq. (3.14) to obtain

$$r^2 \frac{\partial^2 \psi_2}{\partial r^2} + r \frac{\partial \psi_2}{\partial r} - \left(\left(\frac{2\lambda r}{b} \right)^2 + 1 \right) \psi_2 = 0 \quad (3.24)$$

where

$$\begin{aligned} \lambda &= \sqrt{iRe} \\ Re &= \frac{\rho_f \omega b^2}{4\eta_f}. \end{aligned} \quad (3.25)$$

The solution to this equation is [47]

$$\psi_2 = C_3 I_1(2\lambda r/b) + C_4 K_1(2\lambda r/b) \quad (3.26)$$

where $I_1(x)$ is the modified Bessel function of the first kind of order 1 and $K_1(x)$ is the modified Bessel function of the second kind of order 1. $I_1(x)$ is divergent as $x \rightarrow \infty$ so by the boundary condition where $r \rightarrow \infty$, C_3 must be 0. Thus ψ_2 becomes

$$\psi_2 = C_4 K_1(2\lambda r/b). \quad (3.27)$$

Using the results from Eqs. (3.23) and (3.27), ψ can be rewritten as

$$\begin{aligned} \psi &= \Psi(r) \sin(\theta) e^{i\omega t} = (\Psi_1 + \Psi_2) \sin(\theta) e^{i\omega t} \\ &= \left(\frac{C_1}{r} + C_4 K_1(2\lambda r/b) \right) \sin(\theta) e^{i\omega t}. \end{aligned} \quad (3.28)$$

This result can now be substituted back into Eq. (3.16) to obtain

$$\begin{aligned}
 u_r &= \frac{1}{r} \left(\frac{C_1}{r} + C_4 K_1(2\lambda r/b) \right) \cos(\theta) e^{i\omega t} \\
 u_\theta &= \left(\frac{C_1}{r^2} + \frac{2\lambda C_4}{b} \left[\frac{b}{2\lambda r} K_1(2\lambda r/b) + K_0(2\lambda r/b) \right] \right) \sin(\theta) e^{i\omega t}.
 \end{aligned} \tag{3.29}$$

C_1 and C_2 can be determined by evaluating the previous equation using the boundary conditions at the surface of the beam, Eq. (3.17). Computing this evaluation gives

$$\begin{aligned}
 u_0 &= \frac{4C_1}{b^2} + \frac{2}{b} C_4 K_1(\lambda) \\
 -u_0 &= \frac{4C_1}{b^2} + \frac{2\lambda C_4}{b} \left[\frac{1}{\lambda} K_1(\lambda) + K_0(\lambda) \right].
 \end{aligned} \tag{3.30}$$

This result can then be solved for the coefficients to obtain

$$\begin{aligned}
 C_1 &= \frac{u_0 b^2}{4} \left(\frac{2 K_1(\lambda)}{\lambda K_0(\lambda)} + 1 \right) \\
 C_4 &= -\frac{u_0 b}{\lambda K_0(\lambda)}.
 \end{aligned} \tag{3.31}$$

Substituting the coefficients back into ψ_1 and ψ_2 we obtain

$$\psi_1 = \frac{u_0 b^2}{4r} \left(\frac{K_1(\lambda)}{K_0(\lambda)} + 1 \right) \tag{3.32}$$

and

$$\psi_2 = \frac{-u_0 b}{\lambda} \frac{K_1(2\lambda r/b)}{K_0(\lambda)}. \tag{3.33}$$

The total force applied to a section of the beam of length L against the direction of travel of the beam is calculated using

$$F = L \frac{b}{2} \int_0^{2\pi} (P_r \cos(\theta) - P_\theta \sin(\theta)) d\theta \tag{3.34}$$

where P_r and P_θ are stress components within the fluid. These are calculated by

$$P_r = -p|_{r=b/2} + 2\eta_f \left. \frac{\partial u_r}{\partial r} \right|_{r=b/2}$$

and

$$P_\theta = \eta_f \left[\frac{1}{r} \frac{\partial u_r}{\partial \theta} + \frac{\partial u_\theta}{\partial r} - \frac{u_\theta}{r} \right] \Big|_{r=b/2}$$

where pressure of the fluid is p . The various derivatives of the previous results can be solved using the velocity relations in Eq. (3.16) and the boundary conditions of Eq. (3.17). The two derivatives of u_r are

$$\begin{aligned} \left. \frac{\partial u_r}{\partial r} \right|_{r=b/2} &= \left[\frac{1}{r} \left(-\frac{\partial \psi}{\partial \theta} + \frac{\partial^2 \psi}{\partial r \partial \theta} \right) \right] \Big|_{r=b/2} = \left[\frac{1}{r} \left(-u_r - \frac{\partial u_\theta}{\partial \theta} \right) \right] \Big|_{r=b/2} \\ &= \frac{2}{b} \left(-u_0 \cos(\theta) e^{i\omega t} + u_0 \frac{\partial}{\partial \theta} \sin(\theta) e^{i\omega t} \right) = 0 \\ \left. \frac{1}{r} \frac{\partial u_r}{\partial \theta} \right|_{r=b/2} &= \frac{1}{r^2} \frac{\partial^2 \psi}{\partial \theta^2} \Big|_{r=b/2} = \frac{2}{b} \frac{\partial}{\partial \theta} u_0 \cos(\theta) e^{i\omega t} \\ &= -\frac{2}{b} u_0 \sin(\theta) e^{i\omega t} = \left. \frac{u_\theta}{r} \right|_{r=b/2}. \end{aligned} \quad (3.36)$$

The derivative $\left. \frac{\partial u_\theta}{\partial r} \right|_{r=b/2}$ can also be solved using previous results. First the result of Eq. (3.16) must be substituted into the derivative to obtain

$$\left. \frac{\partial u_\theta}{\partial r} \right|_{r=b/2} = - \left. \frac{\partial^2 \psi}{\partial r^2} \right|_{r=b/2}. \quad (3.37)$$

Given that the two parts of Eq. (3.15) are both equal to 0, set part b equal to the negative of part a and then move all terms to the right hand side and simplify in terms of ψ to find

$$\nabla^2 \psi_1 + \nabla^2 \psi_2 - \frac{\rho_f}{\eta_f} \frac{\partial \psi_2}{\partial t} = \nabla^2 \psi - \frac{\rho_f}{\eta_f} \frac{\partial \psi}{\partial t}. \quad (3.38)$$

This result can be expanded using the definition provided in Eq. (3.14) and then solved to obtain

$$-\frac{\partial^2 \psi}{\partial r^2} = \frac{1}{r} \frac{\partial \psi}{\partial r} + \frac{1}{r^2} \frac{\partial^2 \psi}{\partial \theta^2} - \frac{\rho_f}{\eta_f} \frac{\partial \psi_2}{\partial t}. \quad (3.39)$$

Substituting this result back into Eq. (3.37) gives

$$\left. \frac{\partial u_\theta}{\partial r} \right|_{r=b/2} = \left. \frac{1}{r} \frac{\partial \psi}{\partial r} \right|_{r=b/2} + \left. \frac{1}{r^2} \frac{\partial^2 \psi}{\partial \theta^2} \right|_{r=b/2} - \frac{\rho_f}{\eta_f} \frac{\partial \psi_2}{\partial t}. \quad (3.40)$$

Finally, using a result from the second part of Eq. (3.36) and using the boundary conditions in Eq. (3.17) it can be found that

$$\begin{aligned} \left. \frac{\partial u_\theta}{\partial r} \right|_{r=b/2} &= -\left. \frac{u_\theta}{r} \right|_{r=b/2} + \left. \frac{u_\theta}{r} \right|_{r=b/2} - \frac{\rho_f}{\eta_f} \frac{\partial \psi_2}{\partial t} \\ &= -\frac{\rho_f}{\eta_f} \frac{\partial \psi_2}{\partial t}. \end{aligned} \quad (3.41)$$

The results of Eqs. (3.36) and (3.41) can now be used to simplify Eq. (3.35) to

$$\begin{aligned} P_r &= -p|_{r=b/2} \\ P_\theta &= -\rho_f \frac{\partial \psi_2}{\partial t}. \end{aligned} \quad (3.42)$$

This can be substituted into Eq. (3.34) to find

$$F = -L \frac{b}{2} \int_0^{2\pi} p|_{r=b/2} \cos(\theta) d\theta + L \rho_f \frac{b}{2} \int_0^{2\pi} \left. \frac{\partial \psi_2}{\partial t} \right|_{r=b/2} \sin(\theta) d\theta. \quad (3.43)$$

To simplify the solution let us break the previous result into F_1 for the first integral and F_2 for the second integral. The integral of F_1 can be solved using integration by parts,

$$\begin{aligned} F_1 &= -L \frac{b}{2} \left[\sin(\theta) \Big|_0^{2\pi} - \int_0^{2\pi} \left. \frac{dp}{d\theta} \right|_{r=b/2} \sin(\theta) d\theta \right] \\ &= L \frac{b}{2} \int_0^{2\pi} \left. \frac{dp}{d\theta} \right|_{r=b/2} \sin(\theta) d\theta. \end{aligned} \quad (3.44)$$

A result from Stokes [49] is

$$\frac{\partial p}{\partial \theta} = \rho_f \frac{\partial}{\partial t} \left(r \frac{\partial \Psi_1}{\partial r} \right). \quad (3.45)$$

This result can be substituted into Eq. (3.44) to find

$$F_1 = L \rho_f \frac{b}{2} \int_0^{2\pi} \frac{\partial}{\partial t} r \frac{\partial \Psi_1}{\partial r} \Big|_{r=b/2} \sin(\theta) d\theta. \quad (3.46)$$

Using this result, Eq. (3.34) becomes

$$F = L \rho_f \frac{b}{2} \frac{\partial}{\partial t} \int_0^{2\pi} \left(r \frac{\partial \Psi_r}{\partial r} + \Psi_2 \right) \Big|_{r=b/2} \sin(\theta) d\theta. \quad (3.47)$$

Evaluation of this integral is easily computed using Eq. (3.18) to be

$$\begin{aligned} F &= i\omega L \rho_f e^{i\omega t} \frac{b}{2} \int_0^{2\pi} \left(r \frac{\partial \Psi_1}{\partial r} + \Psi_2 \right) \Big|_{r=b/2} \sin^2(\theta) d\theta \\ &= i\omega L \rho_f \pi e^{i\omega t} \frac{b}{2} \left(r \frac{\partial \Psi_1}{\partial r} + \Psi_2 \right) \Big|_{r=b/2}. \end{aligned} \quad (3.48)$$

This can be simplified by using the results for Ψ_1 and Ψ_2 from Eqs. (3.23) and (3.27), respectively, to obtain

$$\begin{aligned} F &= -i\omega u_0 L \rho_f \pi e^{i\omega t} \frac{b^2}{2} \left(\frac{b}{4r} \left(\frac{2 K_1(\lambda)}{\lambda K_0(\lambda)} + 1 \right) + \frac{K_1(2\lambda r/b)}{\lambda K_0(\lambda)} \right) \Big|_{r=b/2} \\ &= -i\omega u_0 e^{i\omega t} M_f \Gamma_{circ}(\omega) \end{aligned} \quad (3.49)$$

where

$$M_f = \rho_f \pi \frac{b^2}{4} L \quad (3.50)$$

and

$$\Gamma_{circ}(\omega) = \left(1 + \frac{4 K_1(\lambda)}{\lambda K_0(\lambda)} \right). \quad (3.51)$$

The two introduced quantities are M_f which is the mass of fluid displaced by the beam and contributes to the inertial effects which will be discussed later and $\Gamma_{circ}(\omega)$ is complex and is referred to as the hydrodynamic function. $\Gamma_{circ}(\omega)$ is the function that determines both the inertial effects and dissipative effects. These two effects and the complex nature of $\Gamma_{circ}(\omega)$ causes the motion of the beam to become out of phase with the driving forces.

Γ_{circ} applies to beams that have a circular profile. Sader et al. [51] provides a function $\Omega(\omega)$ that can be applied to obtain $\Gamma_{rect}(\omega)$ for rectangular beams. $\Omega(\omega)$ was obtained by fitting experimental data and was found to be accurate to within 0.1% across the range $Re \in [10^{-6}, 10^4]$. The real and imaginary components of $\Omega(\omega)$, respectively, are

$$\begin{aligned} \Omega_r(\omega) = & (0.91324 - 0.48274\tau + 0.46842\tau^2 - 0.12886\tau^3 \\ & + 0.044055\tau^4 - 0.0035117\tau^5 + 0.00069085\tau^6) \\ & \times (1 - 0.56964\tau + 0.48690\tau^2 - 0.13444\tau^3 \\ & + 0.045155\tau^4 - 0.0035862\tau^5 + 0.00069085\tau^6)^{-1} \end{aligned} \quad (3.52)$$

and

$$\begin{aligned} \Omega_i(\omega) = & (-0.024134 - 0.029256\tau + 0.016294\tau^2 \\ & - 0.00010961\tau^3 + 0.000064577\tau^4 \\ & - 0.000044510\tau^5) (1 - 0.59702\tau + 0.55182\tau^2 \\ & - 0.18357\tau^3 + 0.079156\tau^4 - 0.014369\tau^5 \\ & + 0.0028361\tau^6)^{-1} \end{aligned} \quad (3.53)$$

where

$$\tau = \log_{10}(Re). \quad (3.54)$$

Using this correction function, $\Gamma_{rect}(\omega)$ is then

$$\Gamma_{rect}(\omega) = \Omega(\omega)\Gamma_{circ}(\omega). \quad (3.55)$$

$\Gamma(\omega)$ can now take the form of $\Gamma_{circ}(\omega)$ or $\Gamma_{rect}(\omega)$ depending on if the beam has a circular or rectangular profile respectively.

$F_{hydro}(x|\omega)$ is the magnitude of the load applied to the beam at some frequency ω . For a harmonic oscillator the magnitude of the velocity is $u_0 = \omega W(x|\omega)$. This result can be substituted into Eq. (3.49) to obtain

$$F = -i\omega^2 e^{i\omega t} M_f \Gamma(\omega) W(x|\omega). \quad (3.56)$$

Finally, substituting in M_f and dividing the magnitude of the real part of this result by the length of the beam gives

$$F_{hydro}(x|\omega) = \frac{\pi}{4} \rho_f \omega^2 b^2 \Gamma(\omega) W(x|\omega). \quad (3.57)$$

3.3 Damped and Driven Beams

The thermal motion of the cantilever is solved for by incorporating the thermal effects as an external force in the EBBE, Eq. 2.11, which is

$$EI \frac{\partial^4 w(x,t)}{\partial x^4} + \mu \frac{\partial^2 w(x,t)}{\partial t^2} = F_{net}(x,t) \quad (3.58)$$

where $F_{net}(x,t)$ is related to the external forces applied to the cantilever. Specifically $F_{net}(x,t)$ is a force per unit length and quantities of this nature will be referred to as loads.

The Fourier transform for any function $x(t)$ is

$$\hat{X}(\omega) = \int_{-\infty}^{\infty} x(t) e^{-i\omega t} dt. \quad (3.59)$$

To determine the frequency response of the cantilever, the Fourier transform of Eq. (3.58)

is computed to obtain

$$EI \frac{d^4 \hat{W}(x|\omega)}{dx^4} - \mu \omega^2 \hat{W}(x|\omega) = \hat{F}_{net}(x|\omega). \quad (3.60)$$

For the cantilever system that is being tested $F_{net}(x, t)$ must be expanded to incorporate all the loads that will be applied to the cantilever. Loads of this nature, like forces, can simply be summed together allowing $F_{net}(x, t)$ to be written as

$$\hat{F}_{net}(x|\omega) = \hat{F}(x|\omega) + \hat{F}_{hydro}(x|\omega) \quad (3.61)$$

where

$$\hat{F}(x|\omega) = \hat{F}_{drive}(x|\omega) + \hat{F}_{thermal}(x|\omega) \quad (3.62)$$

$\hat{F}_{drive}(x|\omega)$ is a driving load that is applied to the cantilever to cause it to have some motion. $\hat{F}_{thermal}(x|\omega)$ represents the load that causes the cantilever to have some motion as a result of thermal energy. All objects that have a non-zero temperature will have a some vibration as a result. In this case the vibration is so large that it creates uncertainty in the measurements and is of importance to this analysis. Finally, $\hat{F}_{hydro}(x|\omega)$ is the hydrodynamic load which results from the surrounding fluid acting upon the beam. This force works by viscous effects and inertial effects. The viscous effects are caused by the fluid resisting motion caused by the motion of the beam. The inertial effects are the direct result of the beam pulling a mass of fluid along as it vibrates. This causes the cantilever to act as if it has a larger mass than it actually has. The effect of viscous effects and inertial forces will be discussed in more depth in Ch. 5.

Using Eq. (3.57) and Eq. (3.61), Eq. (3.60) can be rewritten as

$$\frac{d^4 \hat{W}(x|\omega)}{dx^4} - \frac{\mu \omega^2}{EI} \left(1 + \frac{\pi \rho b^2}{4\mu} \Gamma(\omega) \right) \hat{W}(x|\omega) = \hat{s}(x|\omega) \quad (3.63)$$

where

$$\hat{s}(x|\omega) = \frac{\hat{F}(x|\omega)}{EI}. \quad (3.64)$$

The elastic properties of Eq. (3.63) can be implicitly removed by substituting in the solution of Eq. (2.40) for μ/EI . Equation (2.40) applies to both the cantilever and the bridge and as a result the derivation remains valid for both beams as long as the values for C_n of the corresponding beam are used. $\omega_{vac,1}$, the first resonance frequency of the beam, can be determined by using C_1 for the respective beams and this result simplifies Eq. (3.63) to become

$$\frac{d^4 \hat{W}(x|\omega)}{dx^4} - \frac{B^4(\omega)}{l^4} \hat{W}(x|\omega) = \hat{s}(x|\omega) \quad (3.65)$$

where

$$B(\omega) = C_1 \sqrt{\frac{\omega}{\omega_{vac,1}}} \left(1 + \frac{\pi \rho b^2}{4\mu} \Gamma(\omega) \right)^{1/4}. \quad (3.66)$$

3.4 Green's Function Solution

The solution to Eq. (3.65) can be found using Green's function. First, the Green's function is defined as the solution to

$$\frac{\partial^4 G(x, x'|\omega)}{\partial x^4} - \frac{B^4(\omega)}{l^4} G(x, x'|\omega) = \delta(x - x') \quad (3.67)$$

The Green's function can then be used to obtain the general solution to Eq. (3.65) using

$$\hat{W}(x|\omega) = \int_0^l G(x, x'|\omega) \hat{s}(x'|\omega) dx'. \quad (3.68)$$

To solve for $\hat{G}(x, x'|\omega)$ we start by multiplying both sides by $\phi_n(x)\phi_m(x')$ and integrating with respect to x and x' , both from 0 to l , to obtain

$$\begin{aligned} \int_0^l \int_0^l \phi_n(x) \phi_m(x') \frac{\partial^4 \hat{G}(x, x' | \omega)}{\partial x^4} dx dx' - \frac{B^4(\omega)}{l^4} \int_0^l \int_0^l \phi_n(x) \phi_m(x') \hat{G}(x, x' | \omega) dx dx' \\ = \int_0^l \int_0^l \phi_n(x) \phi_m(x') \delta(x - x') dx dx'. \end{aligned} \quad (3.69)$$

The RHS evaluates to

$$\int_0^l \phi_n(x) \phi_m(x) dx = l \delta_{nm}. \quad (3.70)$$

The second term on the LHS of Eq. (3.69) can be used to create the definition

$$\hat{G}_{nm}(\omega) \equiv \frac{1}{l^2} \int_0^l \int_0^l \phi_n(x) \phi_m(x') \hat{G}(x, x' | \omega) dx dx'. \quad (3.71)$$

This definition allows Eq. (3.69) to be rewritten as

$$\int_0^l \int_0^l \phi_n(x) \phi_m(x') \frac{\partial^4 \hat{G}(x, x' | \omega)}{\partial x^4} dx dx' - \frac{B^4(\omega)}{l^2} \hat{G}_{nm}(\omega) = l \delta_{nm}. \quad (3.72)$$

The first term on the LHS can be solved using integration by parts. This integral requires the use of the boundary conditions for a cantilever,

$$\left[\phi(x) = \frac{d\phi(x)}{dx} \right] \Big|_{x=0} = 0$$

and

$$\left[\frac{d^2\phi(x)}{dx^2} = \frac{d^3\phi(x)}{dx^3} \right] \Big|_{x=l} = 0. \quad (3.73)$$

Thanks to the properties of the Green's function, $\hat{G}(x, x' | \omega)$ shares the same boundary conditions as ϕ . To simplify this process let us consider only the portion of the integral dependent on x . This leaves

$$\int_0^l \phi_n(x) \frac{\partial^4 \hat{G}(x, x' | \omega)}{\partial x^4} dx. \quad (3.74)$$

The process of integration by parts must be carried out four times to solve this integral. The result of integration by parts without evaluating at the limits is

$$\begin{aligned}
 & \int_0^l \phi_n(x) \frac{\partial^4 \hat{G}(x, x' | \omega)}{\partial x^4} dx \\
 &= \left[\phi_n(x) \frac{\partial^3 \hat{G}(x, x' | \omega)}{\partial x^3} \right] \Big|_0^l \\
 & - \left[\frac{d\phi_n(x)}{dx} \frac{\partial^2 G(x, x' | \omega)}{\partial x^2} \right] \Big|_0^l \\
 & + \left[\frac{d^2 \phi_n(x)}{dx^2} \frac{\partial G(x, x' | \omega)}{\partial x} \right] \Big|_0^l \\
 & - \left[\frac{d^3 \phi_n(x)}{dx^3} G(x, x' | \omega) \right] \Big|_0^l \\
 & + \int_0^l \frac{d^4 \phi_n(x)}{dx^4} G(x, x' | \omega) dx.
 \end{aligned} \tag{3.75}$$

Evaluation at the limits needs to be performed using the boundary conditions of the cantilever, Eqs. (2.30) and (2.31), and the bridge beam, Eq. (2.44). Evaluating the limits for both cases shows that the first four terms on the RHS are zero and only the final integral is left. Given that $\phi(x)$ is defined by Eq. (2.42) and Eq. (2.55) for the cantilever and bridge respectively, the derivative can be found and the integral becomes

$$\begin{aligned}
 \int_0^l \phi_n(x) \frac{\partial^4 \hat{G}(x, x' | \omega)}{\partial x^4} dx &= \int_0^l \frac{d^4 \phi_n(x)}{dx^4} \hat{G}(x, x' | \omega) dx \\
 &= \frac{C_n^4}{l^4} \int_0^l \phi_n(x) \hat{G}(x, x' | \omega) dx.
 \end{aligned} \tag{3.76}$$

This result can be substituted into Eq. (3.72) to obtain

$$\frac{C_n^4}{l^4} \int_0^l \int_0^l \phi_m(x') \phi_n(x) \hat{G}(x, x' | \omega) dx dx' - \frac{B^4(\omega)}{l^2} \hat{G}_{nm}(\omega) = l \delta_{nm}. \tag{3.77}$$

The first term can be simplified through the use of the definition of $\hat{G}_{nm}(\omega)$ to find

$$\frac{C_n^4}{l^2} \hat{G}_{nm}(\omega) - \frac{B^4(\omega)}{l^2} \hat{G}_{nm}(\omega) = l \delta_{nm}. \tag{3.78}$$

This result can now be solved algebraically to determine that $\hat{G}_{nm}(\omega)$ is

$$\hat{G}_{nm}(\omega) = \frac{l^3 \delta_{nm}}{C_n^4 - B^4(\omega)}. \quad (3.79)$$

The function $\hat{G}_{nm}(\omega)$ can be considered as an $n \times n$ diagonal matrix which determines the resonant structure for the cantilever or bridge.

$\hat{G}_{nm}(\omega)$ is not present in the general solution as given in Eq. (3.68) and a method to obtain $\hat{G}(x, x' | \omega)$ is required. By considering the definition in Eq. (3.71) and Eq. (3.70), it can be seen that $\hat{G}(x, x' | \omega)$ can be found by

$$\begin{aligned} \hat{G}(x, x' | \omega) &= \sum_n \sum_m \hat{G}_{nm}(\omega) \phi_n(x) \phi_m(x') \\ &= \sum_n \hat{G}_{nn}(\omega) \phi_n(x) \phi_n(x'). \end{aligned} \quad (3.80)$$

The second step makes use of the diagonal nature of $G_{nm}(\omega)$.

3.5 Frequency Response of the Beam

The beam's frequency response for some arbitrary driving load $\hat{F}(x' | \omega)$ is solved using the general solution to Eq. (3.67), which is given in Eq. (3.68).

Let us consider some arbitrary load that is being applied to the cantilever $\hat{F}(x | \omega)$ which is small in nature to ensure linearity. Due to the orthogonality of the cantilever's modes, this force can be expanded using $\phi_n(x)$ as a basis set,

$$\hat{F}(x | \omega) = \sum_n \hat{F}_n(\omega) \phi_n(x). \quad (3.81)$$

This result can be substituted into Eq. (3.68) using Eq. (3.64). Multiplying both sides of this result by $\phi_m(x)$ and integrating with respect to x from 0 to l we find

$$\begin{aligned}
 & \int_0^l \hat{W}(x|\omega) \phi_n(x) dx \\
 &= \frac{1}{EI} \sum_n \int_0^l \int_0^l \hat{G}(x, x'|\omega) \hat{F}_n(\omega) \phi_m(x) \phi_n(x') dx dx'.
 \end{aligned} \tag{3.82}$$

Given that $\hat{F}_n(\omega)$ is independent of both x and x' , it can be pulled out of the integrals and Eq. (3.71) can be used to simplifying the RHS of Eq. (3.82) to

$$\begin{aligned}
 & \frac{l^2}{EI} \sum_n \hat{G}_{nn}(\omega) \hat{F}_n(\omega) \\
 &= \frac{l^2}{EI} \hat{G}_{nn}(\omega) \hat{F}_n(\omega).
 \end{aligned} \tag{3.83}$$

In the same fashion that $\hat{F}_n(\omega)$ was expanded using $\phi_n(x)$ as a basis set, so too can $\hat{W}(x|\omega)$ to become

$$\hat{W}(x|\omega) = \sum_n \hat{W}_n(\omega) \phi_n(x). \tag{3.84}$$

This result can be substituted into the LHS of Eq. (3.82) to obtain

$$\begin{aligned}
 & \sum_n \hat{W}_n(\omega) \int_0^l \phi_n(x) \phi_m(x) dx \\
 &= \sum_n l \hat{W}_n(\omega) = \sum_n \frac{l^2}{EI} \hat{G}_{nn}(\omega) \hat{F}_n(\omega).
 \end{aligned} \tag{3.85}$$

Setting Eqs. (3.83) and (3.85) equal to each other, Eq. (3.82) becomes

$$\sum_n \hat{W}_n(\omega) = \frac{l}{EI} \sum_n \hat{G}_{nn}(\omega) \hat{F}_n(\omega). \tag{3.86}$$

Let us make the definition

$$\hat{W}_n(\omega) \equiv \hat{F}_n(\omega) \alpha_n(\omega) \tag{3.87}$$

This definition can be used to make Eq. (3.84) become explicitly dependent on $\hat{F}_n(\omega)$,

$$\hat{W}(x|\omega) = \sum_n \hat{F}_n(\omega) \alpha_n(\omega) \phi_n(x). \quad (3.88)$$

The function that is introduced, $\alpha_n(\omega)$, describes the susceptibility of the cantilever in a specific mode to a random driving load. $\alpha_n(\omega)$ can be easily solved for by substituting Eq. (3.87) and Eq. (3.79) into Eq. (3.86) to obtain

$$\begin{aligned} \alpha_n(\omega) &= \frac{l^4}{EI} \frac{1}{C_n^4 - B^4(\omega)} \\ &= \frac{3l}{k} \frac{1}{C_n^4 - B^4(\omega)} \end{aligned} \quad (3.89)$$

where the spring constant of the cantilever is

$$k = \frac{3EI}{l^3}. \quad (3.90)$$

The spring constant is related to the force that must be applied to the beam, F , to cause it to have a displacement of Δy ; from Hooke's law this is $F = -k\Delta y$.

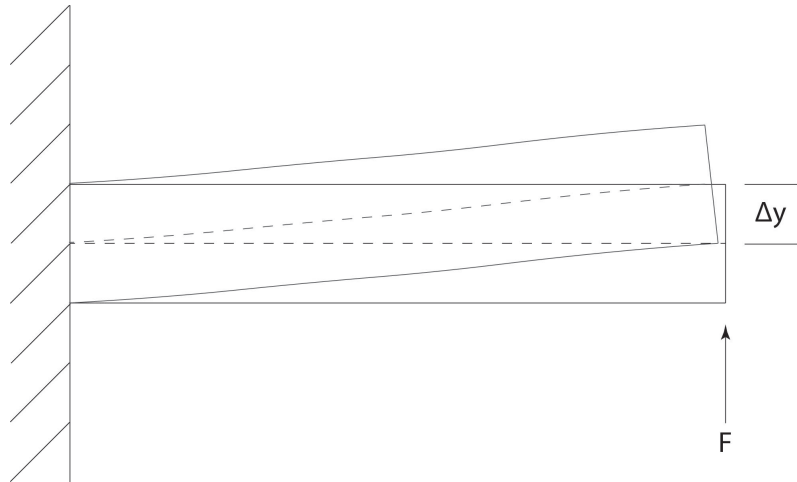


Figure 3.2: The spring constant of a beam is calculated based on the required force that must be applied to the beam such that it is deflected by a displacement of Δy .

3.6 Power Spectral Density for Fluctuating Loads

Consider a data set, $g(t)$, that was collected over a duration of time. Two possible methods for obtaining an average are a time average or an ensemble average. A time average is easily obtained by integrating over a duration of the data set and then dividing by that duration of time,

$$\langle g(t) \rangle = \frac{1}{2T} \int_{-T}^T g(t+t') dt'. \quad (3.91)$$

An ensemble average is calculated by dividing up the original data set into a subset, $g^k(t)$, each of duration T . The ensemble average for $g(t)$, where $0 \leq t \leq T$, is the sum of each subset at time t divided by the total number of subsets,

$$\{g(t)\} = \frac{1}{N} \sum_{k=1}^N g^k(t). \quad (3.92)$$

There are two important terms that must be outlined. First, a data set is referred to as stationary if there is no preferred time for $t = 0$. Secondly, a data set is called ergodic if over a sufficiently long duration of time the data set will pass through all possible values. If a data set is both stationary and ergodic, then the ensemble average is equal to the time average for that data set [53]. A data set which is a collection of purely noise measurements is an example of a stationary and ergodic set.

The correlation function for a random, stationary function is

$$K(s) = \{g(0)g(s)\}. \quad (3.93)$$

Exploiting the nature of stationary, ergodic functions it can be shown that the correlation function is the inverse Fourier transform of the PSD, $J(\omega)$, of the function $g(t)$,

$$K(s) = \frac{1}{2\pi} \int_{-\infty}^{\infty} J(\omega) e^{i\omega s} d\omega. \quad (3.94)$$

The time dependent solution to the EBBE, Eq. (3.58), that describes the displacement of the cantilever, $w(x, t)$, can be expanded using $\phi_n(x)$ as the basis set,

$$w(x, t) = \sum_n h_n(t) \phi_n(x) \quad (3.95)$$

where $h_n(t)$ is a function describing the time dependence of the cantilever. This analysis is interested in the spectral response of the cantilever which is the Fourier transform of $w(x, t)$. As a result of this relationship, if the inverse Fourier transform of Eq. (3.88) is computed, it can be found that

$$h_n(t) = \frac{1}{2\pi} \int_{-\infty}^{\infty} \hat{F}_n(\omega) \alpha_n(\omega) e^{i\omega t} d\omega. \quad (3.96)$$

For the following discussion let $\hat{F}_n(\omega)$ be a load that is random in nature, an example of which is noise. When the square of $w(x, t)$ is computed cross terms between the modes are introduced. However, if the ensemble average of $w^2(x, t)$ is found, it is expected that over a sufficiently long duration of time that $\{h_n(t)h_m(t)\} = 0$ when $n \neq m$ causing the cross terms to vanish. For such functions it can also be found that $\{h_n(t)h_n(t+s)\}$ becomes very small for large values of s . Using the result of Eq. (3.93), the auto-correlation of $h_n(t)$ is

$$K_n(t) = \{h_n(s)h_n(s+t)\}. \quad (3.97)$$

Using Eq. (3.95) the ensemble average of $w_n^2(x, t)$ can be written as

$$\begin{aligned} \{w^2(x, t)\} &= \sum_n \{h_n^2(t)\} \phi_n^2(x) = \sum_n K_n(s) \phi_n^2(x) \\ &= \sum_n \phi_n^2(x) \frac{1}{2\pi} \int_{-\infty}^{\infty} J_n(\omega) e^{i\omega t} d\omega. \end{aligned} \quad (3.98)$$

Given that the frequency response of the cantilever is the Fourier transform of $w(x, t)$, the PSD of $w(x, t)$ is

$$J_w(x|\omega) = \sum_n J_n(\omega) \phi_n^2(x). \quad (3.99)$$

Substituting the result of Eq. (3.99) into Eq. (3.98) this result can be rewritten as

$$\begin{aligned} J_x(x|\omega) &= \sum_n \{h_n^2(t)\} \phi_n^2(x) \\ &= \sum_n |\hat{F}_n(\omega)|^2 |\alpha_n(\omega)|^2 |\phi_n(x)|^2. \end{aligned} \quad (3.100)$$

The derivative of this PSD with respect to x is

$$J_{\frac{\partial w}{\partial x}} = \sum_n |\hat{F}_n(\omega)|^2 |\alpha_n(\omega)|^2 \left(\frac{d|\phi_n(x)|}{dx} \right)^2. \quad (3.101)$$

As a direct result of Eq. (3.95), the PSD can be written as a sum of the contribution of each mode,

$$J_w(x|\omega) = \sum_n J_{w,n}(x|\omega). \quad (3.102)$$

The PSD, which has units of m^2/Hz , can be integrated over the full frequency range and then square rooted to obtain the expectation displacement of the cantilever. By using the expanded form of $J_w(x|\omega)$ this can be done for individual modes,

$$\frac{1}{2\pi} \int_{-\infty}^{\infty} J_{w,n}(x|\omega) d\omega = K_n(0) \phi_n^2(x). \quad (3.103)$$

The motion can be considered to be driven by an arbitrary load that is yet to be defined. This load can be written in the general form of $f(x,t)$ or, expanding it using $\phi_n(x)$ as a basis set, as

$$f(x,t) = \sum_n \xi_n(t) \phi_n(x). \quad (3.104)$$

With $f(x,t)$ expanded, it is possible to determine the Fourier transform of $f_n(t)$ which is an

important term of Eq. (3.88), specifically

$$\hat{\Xi}_n(\omega) = \int_{-\infty}^{\infty} \xi_n(t) e^{-i\omega t} dt. \quad (3.105)$$

Let the contribution to the noise power spectral density for $f_n(x, t)$ be defined as

$$J_{f,n}(x|\omega) = J_{\xi,n}(\omega) \phi_n^2(x). \quad (3.106)$$

Let us assume that the force driving the motion of the cantilever is stochastic and uniform in nature such that it is independent of frequency, like white noise, and thus $J_{f,n}(x|\omega) = J_{f,n}(x|0)$. The power spectral density for w can then be written as

$$J_{w,n}(x|\omega) = |\alpha_n(\omega)|^2 J_{f,n}(x). \quad (3.107)$$

where $\alpha_n(\omega)$ is defined in Eq. (3.89). This result can be integrated over ω and through the use of Eq. (3.103) $J_{f,n}(x)$ can be determined,

$$J_{f,n}(x) = \frac{2\pi \{h_n^2(t)\} \phi_n^2(x)}{\int_{-\infty}^{\infty} |\alpha_n(\omega')|^2 d\omega'}. \quad (3.108)$$

$|\alpha_n(\omega)|^2$ is a symmetrical function allowing the integral in the denominator to be double that evaluated on the bounds of 0 to ∞ . This result can now be substituted into Eq. (3.107) to obtain

$$J_{w,n}(x|\omega) = \{h_n^2(t)\} \frac{\pi |\alpha_n(\omega)|^2}{\int_0^{\infty} |\alpha_n(\omega')|^2 d\omega'} \phi_n^2(x). \quad (3.109)$$

3.7 Cantilever Motion from Forces

The result of the previous sections determined the PSD of the beam in two forms. The first form described the PSD by $\{h_n^2(t)\}$, Eq. (3.109), while the other was dependent upon $|F_n(\omega)|^2$, Eq. (3.100).

The PSD of a beam will now be determined for a beam having a non-zero temperature and the resulting vibrations. This motion is a source of uncertainty that affects all measurements taken and must be considered for the Signal-to-Noise Ratio (SNR). In some cases the noise that is generated by equipment can be mitigated through the use of measuring techniques or improved equipment design. The noise that is generated by the beam is fundamental. The lock-in amplifier is used to reduce the bandwidth of the measurement to increase the SNR but the noise PSD cannot be reduced for a beam without cooling it.

As $w(x,t)$ is a function of the sum of each mode, if $w(x,t)$ is substituted into Eq. (2.29) then the potential energy equation becomes a function of the modes as well, that is

$$U_n(t) = \frac{EI}{2} h_n^2(t) \int_0^l \left(\frac{d^2 \phi_n(x)}{dx^2} \right)^2 dx. \quad (3.110)$$

For both the cantilever and the bridge beams the integral evaluates as

$$\int_0^l \left(\frac{d^2 \phi_n(x)}{dx^2} \right)^2 dx = \frac{C_n^4}{l^4} \int_0^l \phi_n^2(x) dx = \frac{C_n^4}{l^3}. \quad (3.111)$$

Making a substitution for the spring constant, $k = \frac{3EI}{l^3}$, the resulting expectation value for the potential energy of each mode, $\{U_n(t)\}$, is

$$\{U_n(t)\} = \frac{kC_n^4}{6} \{h_n^2(t)\}. \quad (3.112)$$

The equipartition theorem states that each degree of freedom that is quadratic in nature has an expectation energy of $\frac{1}{2}k_B T$ [54, 55]. As a result the expectation value of the potential energy for each mode is

$$\frac{1}{2}k_B T = \frac{kC_n^4}{6} \{h_n^2(t)\}. \quad (3.113)$$

This result can then be solved to for

$$\{h_n^2(t)\} = \frac{3k_B T}{kC_n^4}. \quad (3.114)$$

Using this result, Eq. (3.109) and Eq. (3.102) the noise power spectral density can be found to be

$$J_w(x|\omega) = \frac{3\pi k_B T}{k} \sum_n \frac{|\alpha_n(\omega)|^2}{C_n^4 \int_0^\infty |\alpha_n(\omega')|^2 d\omega'} \phi_n^2(x) \quad (3.115)$$

and its derivative is

$$J_{\frac{\partial w}{\partial x}}(x|\omega) = \frac{3\pi k_B T}{k} \sum_n \frac{|\alpha_n(\omega)|^2}{C_n^4 \int_0^\infty |\alpha_n(\omega')|^2 d\omega'} \left(\frac{d\phi_n(x)}{dx} \right)^2. \quad (3.116)$$

3.8 Conclusion

For the motion of the driven beam in a fluid to be determined the effects of the fluid were required. The hydrodynamic function and resulting load were derived from Stoke's equation. This result was used in conjunction with Green's function to solve the EBBE equation for the Noise Spectral Density (NSD) of the beam. The solution that was obtained applies to both the cantilever and bridge beams. This solution will be used to compare the cantilever and bridge beams to determine which will be the best candidate for the potential MOND experiment.

Finally, the noise PSD for the damped motion of a beam was determined as a function of temperature. Any object that has some temperature will have some energy and as a result will exhibit some vibration. This random vibration of the cantilever causes it to produce noise that can be measured and will affect experimental results.

Chapter 4

Vibrations of a Beam: C) with Prescribed Driving Forces

4.1 Introduction

The cantilever is subjected to loads that cause it to have motion beyond thermal vibration. To solve for the displacement of the cantilever requires an explicit solution to Eq. (3.58) using the Green's function and the form of the applied load to be defined. This chapter will consider two different types of loads that could be applied to the cantilever. The first load will be a load that is constant across the length of the beam and will be referred to as a uniform load. The driving laser that is used to drive the motion of the beam at a specific frequency will be assumed to be of this form. The second type of load will be a load that is applied at a point along the length of the beam.

4.2 Green's Function Solution

The Green's function is subject to the same boundary conditions as $\tilde{W}(x|\omega)$ is, namely:

$$\left[G(x, x'|\omega) = \frac{\partial G(x, x'|\omega)}{\partial x} \right] \Big|_{x=0} = 0 \quad (4.1)$$

and

$$\left[\frac{\partial^2 G(x, x'|\omega)}{\partial x^2} = \frac{\partial^3 G(x, x'|\omega)}{\partial x^3} \right] \Big|_{x=l} = 0. \quad (4.2)$$

The properties of the Green's function requires it to be continuous at $x = x'$ for G , $\partial G/\partial x$

and, $\partial^2 G/\partial x^2$. The final property that is required to solve this differential equation is:

$$\lim_{\varepsilon \rightarrow 0^+} \left[\frac{\partial^3 G(x, x' | \omega)}{\partial x^3} \right]_{x=x'-\varepsilon}^{x=x'+\varepsilon} = 1. \quad (4.3)$$

First the Green's function itself must be made. The Green's function is a piece wise function that is defined as $G_1(x, x' | \omega)$ for $0 \leq x \leq x' \leq l$ and $G_2(x, x' | \omega)$ for $0 \leq x' \leq x \leq l$. With appropriate terms based on Eq. (2.38), the Green's function can be made to fit the boundary conditions without any concern for what the coefficients may be. A combination of

$$\sin(B(\omega)x) - \sinh(B(\omega)x) \quad (4.4)$$

and

$$\cos(B(\omega)x) - \cosh(B(\omega)x) \quad (4.5)$$

will evaluate to 0 regardless of the coefficients and satisfy the boundary conditions of Eq.(4.1). The second set of primary terms that are required are:

$$\sin(B(\omega)(x-l)) + \sinh(B(\omega)(x-l)) \quad (4.6)$$

and

$$\cos(B(\omega)(x-l)) + \cosh(B(\omega)(x-l)). \quad (4.7)$$

These terms will then satisfy the second two boundary conditions of Eq. (4.2). A combination of these four terms will form the two piecewise parts of the Green's function,

$$\begin{aligned}
 G_1(x, x' | \omega) = & A \cdot (\sin(B(\omega)x) - \sinh(B(\omega)x)) \cdot (\sin(B(\omega)(x' - l)) + \sinh(B(\omega)(x' - l))) \\
 & + B \cdot (\sin(B(\omega)x) - \sinh(B(\omega)x)) \cdot (\cos(B(\omega)(x' - l)) + \cosh(B(\omega)(x' - l))) \\
 & + C \cdot (\cos(B(\omega)x) - \cosh(B(\omega)x)) \cdot (\sin(B(\omega)(x' - l)) + \sinh(B(\omega)(x' - l))) \\
 & + D \cdot (\cos(B(\omega)x) - \cosh(B(\omega)x)) \cdot (\sin(B(\omega)(x' - l)) + \sinh(B(\omega)(x' - l)))
 \end{aligned} \tag{4.8}$$

and

$$\begin{aligned}
 G_2(x, x' | \omega) = & A \cdot (\sin(B(\omega)(x - l)) + \sinh(B(\omega)(x - l)) \cdot (\sin(B(\omega)x') - \sinh(B(\omega)x')) \\
 & + B \cdot (\sin(B(\omega)(x - l)) + \sinh(B(\omega)(x - l)) \cdot (\cos(B(\omega)x') - \cosh(B(\omega)x')) \\
 & + C \cdot (\cos(B(\omega)(x - l)) + \cosh(B(\omega)(x - l)) \cdot (\sin(B(\omega)x') - \sinh(B(\omega)x')) \\
 & + D \cdot (\cos(B(\omega)(x - l)) + \cosh(B(\omega)(x - l)) \cdot (\sin(B(\omega)x') - \sinh(B(\omega)x'))
 \end{aligned} \tag{4.9}$$

where A , B , C and D are each some constant to be determined.

This combination of these terms also work to cause G_1 and G_2 to be continuous at $x = x'$ regardless of the values of the coefficients. The coefficients can be solved by evaluating the other properties of the Green's function at $x = 0$ and $x = l$. The first property to be considered here is the continuity of $\partial G / \partial x$ at $x = x'$ and will be evaluated at $x' = l$,

$$0 = \left. \frac{\partial G_2(x, x' | \omega)}{\partial x} \right|_{x=x'=l} - \left. \frac{\partial G_1(x, x' | \omega)}{\partial x} \right|_{x=x'=l} .$$

By evaluating this expression we obtain

$$\begin{aligned}
 0 = & A \cdot (\sin(B(\omega)) - \sinh(B(\omega)) - B \cdot (\cos(B(\omega)) - \cosh(B(\omega))) \\
 & + C \cdot (\cos(B(\omega)) - \cosh(B(\omega)) - D \cdot (-\sin(B(\omega)) - \sinh(B(\omega))).
 \end{aligned} \tag{4.10}$$

The second property requires $\partial^2 G / \partial x^2$ at $x = x'$ to be continuous,

$$0 = \left. \frac{\partial^2 G_2(x, x' | \omega)}{\partial x^2} \right|_{x=x'} - \left. \frac{\partial^2 G_1(x, x' | \omega)}{\partial x^2} \right|_{x=x'}.$$

This can be evaluated at $x = 0$ to obtain the relationship between C and D ,

$$C = D \cdot \frac{(\cos(B(\omega)) + \cosh(B(\omega)))}{(\sin(B(\omega)) + \sinh(B(\omega)))}. \quad (4.11)$$

If this property is evaluated at $x = l$ it can be found that

$$B = -D \cdot \frac{(\cos(B(\omega)) + \cosh(B(\omega)))}{(\sin(B(\omega)) + \sinh(B(\omega)))} = -C. \quad (4.12)$$

The final property is Eq. (4.3) which can be rewritten as

$$1 = \left. \frac{\partial^3 G_2(x, x' | \omega)}{\partial x^3} \right|_{x=x'} - \left. \frac{\partial^3 G_1(x, x' | \omega)}{\partial x^3} \right|_{x=x'}.$$

This can be evaluated at $x = 0$ to obtain

$$\frac{l^3}{2B^{-3}(\omega)} = -A \cdot (\sin(B(\omega)) + \sinh(B(\omega))) + B \cdot (\cos(B(\omega)) + \cosh(B(\omega))), \quad (4.13)$$

or if it is evaluated at $x = l$,

$$\frac{l^3}{2B^{-3}(\omega)} = B \cdot (\cos(B(\omega)) + \cosh(B(\omega))) - D \cdot (\sin(B(\omega)) - \sinh(B(\omega))). \quad (4.14)$$

Equations 4.10 to 4.14 can be used to algebraically solve for each coefficient. With each coefficient solved for and then substituted into the Green's function and simplified, the solution to the differential equation is

$$G(x, x' | \omega) = \frac{l^3}{4B^3(\omega)(1 + \cos(B(\omega)) \cosh(B(\omega)))}$$

$$\times \left\{ \begin{array}{l}
 \{ [\cos(B(\omega)) + \cosh(B(\omega))] [\cosh(B(\omega)x/l) - \cos(B(\omega)x/l)] \\
 + [\sin(B(\omega)) - \sinh(B(\omega))] [\sinh(B(\omega)x/l) - \sin(B(\omega)x/l)] \} \\
 \quad \times (\sin(B(\omega)(x' - l)/l) + \sinh(B(\omega)(x' - l)/l)) \\
 + \{ [\cos(B(\omega)) + \cosh(B(\omega))] [\sin(B(\omega)x/l) - \sinh(B(\omega)x/l)] \\
 - [\sin(B(\omega)) + \sinh(B(\omega))] [\cos(B(\omega)x/l) - \cosh(B(\omega)x/l)] \} \\
 \times (\cos(B(\omega)(x' - l)/l) + \cosh(B(\omega)(x' - l)/l)) \quad : 0 \leq x \leq x' \leq l \\
 \{ [\cos(B(\omega)) + \cosh(B(\omega))] [\cosh(B(\omega)x'/l) - \cos(B(\omega)x'/l)] \\
 + [\sin(B(\omega)) - \sinh(B(\omega))] [\sinh(B(\omega)x'/l) - \sin(B(\omega)x'/l)] \} \\
 \quad \times (\sin(B(\omega)(x - l)/l) + \sinh(B(\omega)(x - l)/l)) \\
 + \{ [\cos(B(\omega)) + \cosh(B(\omega))] [\sin(B(\omega)x'/l) - \sinh(B(\omega)x'/l)] \\
 - [\sin(B(\omega)) + \sinh(B(\omega))] [\cos(B(\omega)x'/l) - \cosh(B(\omega)x'/l)] \} \\
 \times (\cos(B(\omega)(x - l)/l) + \cosh(B(\omega)(x - l)/l)) \quad : 0 \leq x' \leq x \leq l
 \end{array} \right. \quad (4.15)$$

The result that is obtained for the Green's function can be tested by comparing the plot of the function with the conditions that were specified. The Green's function and its first three derivatives have been plotted in Figures 4.1 to 4.4. These plots were completed using a normalized axes for both x and x' , thus $x = x' = 1$ corresponds to $x = x' = l$. The Green's function is required to satisfy the same boundary condition as $\hat{W}(x|\omega)$, Eqs. (4.1) and (4.2), and, as it is being used to solve a 4th order differential equation, the third derivative is expected to have a discontinuity of 1 at $x = x'$, Eq. (4.3).

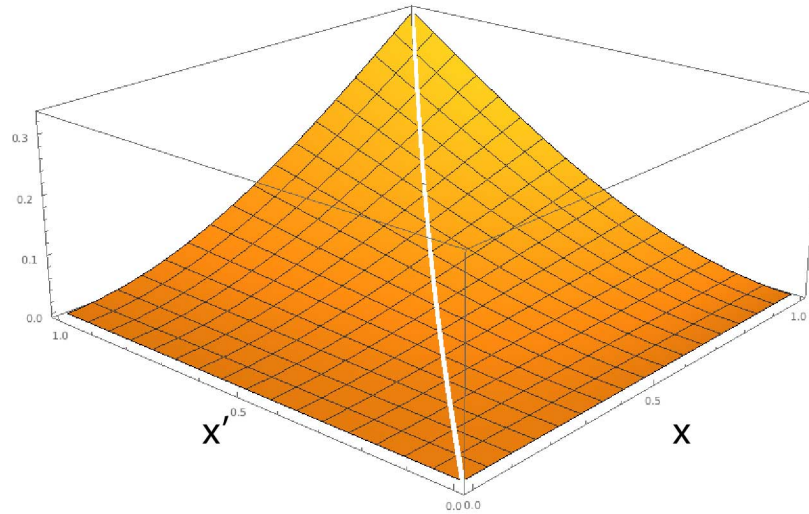


Figure 4.1: Plot of the Green's function. The axes for x and x' have been normalized such that $x = x' = 1$ corresponds to $x = x' = l$.

The boundary conditions required that the Green's function and its first derivative equal 0 at $x = 0$. The results of Fig. 4.1 and Fig. 4.2 show that these conditions are satisfied.

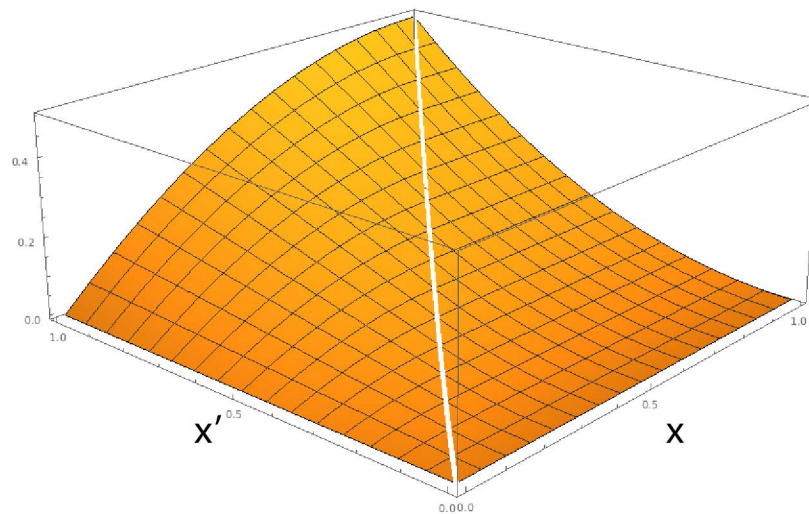


Figure 4.2: Plot of the first derivative of the Green's function with respect to x . The axes for x and x' have been normalized such that $x = x' = 1$ corresponds to $x = x' = l$.

From the boundary conditions it is expected that the second and third derivatives of the Green's function will equal 0 at $x = l$. Figures 4.3 and 4.4 are plots of these derivatives and show that these conditions are upheld.

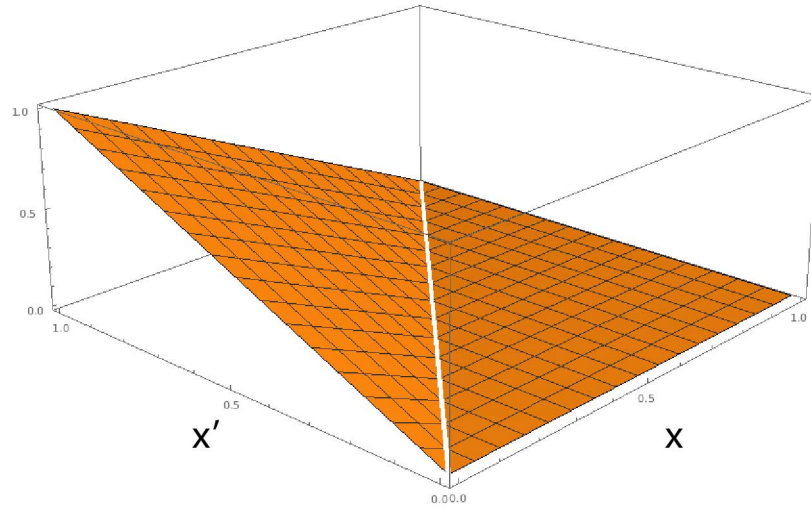


Figure 4.3: Plot of the second derivative of the Green's function with respect to x . The axes for x and x' have been normalized such that $x = x' = 1$ corresponds to $x = x' = l$.

The final condition that the Green's function is expected to satisfy is a discontinuity of 1. This, as with all previous boundary conditions, is satisfied. This indicates that the solution for the Green's function is correct and can be used to determine the displacement of the beam due to a load using Eq. (3.68).

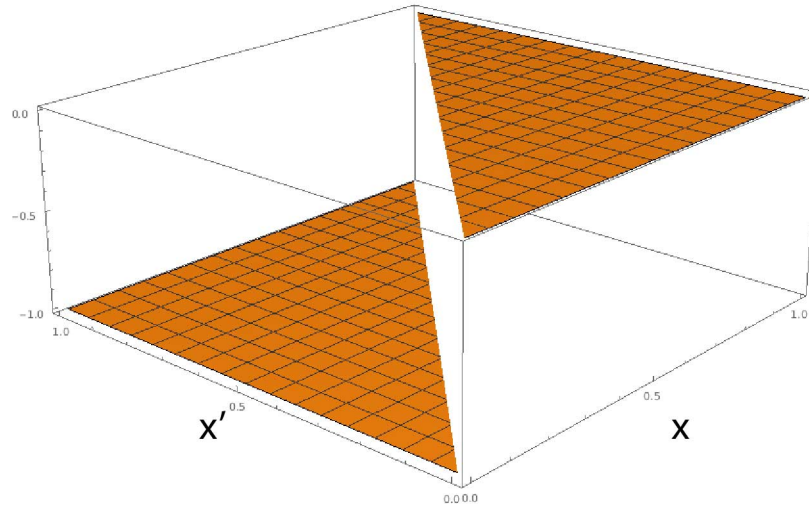


Figure 4.4: Plot of the third derivative of the Green's function with respect to x . The axes for x and x' have been normalized such that $x = x' = 1$ corresponds to $x = x' = l$.

The motion of the cantilever due to some driving load $\hat{F}(x|\omega)$ can now be determined through the use of Eq. (3.64) and Eq. (3.68). The laser that will be used to drive the motion of the cantilever has a near-Gaussian profile and can be described by

$$\hat{F}(x|\omega) = A(\omega)e^{-\frac{(x-x_0)^2}{2\sigma^2}} \quad (4.16)$$

where $A(\omega)$ is the peak power of the beam at a frequency of ω and σ^2 is the variance. Integration of Eq. (3.68) with a Gaussian function is sufficiently complicated that it should be evaluated numerically.

Two possible loads will be considered in light of the Gaussian profile. The laser can be moved such that the focal point of the laser is a large distance from the cantilever, causing σ to increase. The first case that will be considered is the extreme case where $\sigma \rightarrow \infty$ and the load can be considered to be uniform across the entire length of the beam. The second case to be considered here is when the cantilever is placed at the focal point of the beam. Here $\sigma \rightarrow 0$ and the load can be considered a point force on the beam.

4.3 Uniform Loads

The response of the cantilever to a uniform across the length of the beam, $\hat{F}(x|\omega) = \hat{F}(\omega)$, is an important case to this study. This case can be solved directly using Eq. (3.68). Substituting $\hat{F}(\omega)$ into Eq. (3.64), the integral solution for the displacement of the beam is

$$\begin{aligned}\hat{W}(x|\omega) &= \int_0^l G(x, x'|\omega) \hat{s}(\omega) dx' \\ &= \frac{\hat{F}(\omega)}{EI} \int_0^l G(x, x'|\omega) dx'.\end{aligned}\quad (4.17)$$

The frequency of the driving load that will be used for experimentation will be 25 rads^{-1} . At this frequency the value of $B(\omega)$ is 0.0285 and 0.0881 for the 225 μm and 500 μm cantilevers respectively. The result from integration can be simplified using the small value approximation for trig functions. This will give us the displacement of the cantilever for a uniform load at sufficiently low frequencies. From this it can be found that the displacement of the beam is

$$\hat{W}(x) = \frac{\hat{F}(x)}{24EI} (6x^2l^2 - 4x^3l + x^4). \quad (4.18)$$

Taking the derivative of this result the slope can be found,

$$\frac{d\hat{W}(x)}{dx} = \frac{\hat{F}(x)}{6EI} (2xl^2 - 2x^2l + x^3). \quad (4.19)$$

The detection point, the position along the beam that the detector is sensitive to, is located as close to the free end as possible. As will be discussed in Ch. 7, the detector measures the slope of the beam. To determine the displacement of the free end from the measured slope of the beam a conversion factor, ζ , will be necessary. ζ is defined as

$$\zeta(x) \equiv \frac{l}{\hat{W}(l)} \frac{d\hat{W}(x)}{dx} = \frac{1}{3} \left(12\frac{x}{l} - 12\frac{x^2}{l^2} + 4\frac{x^3}{l^3} \right). \quad (4.20)$$

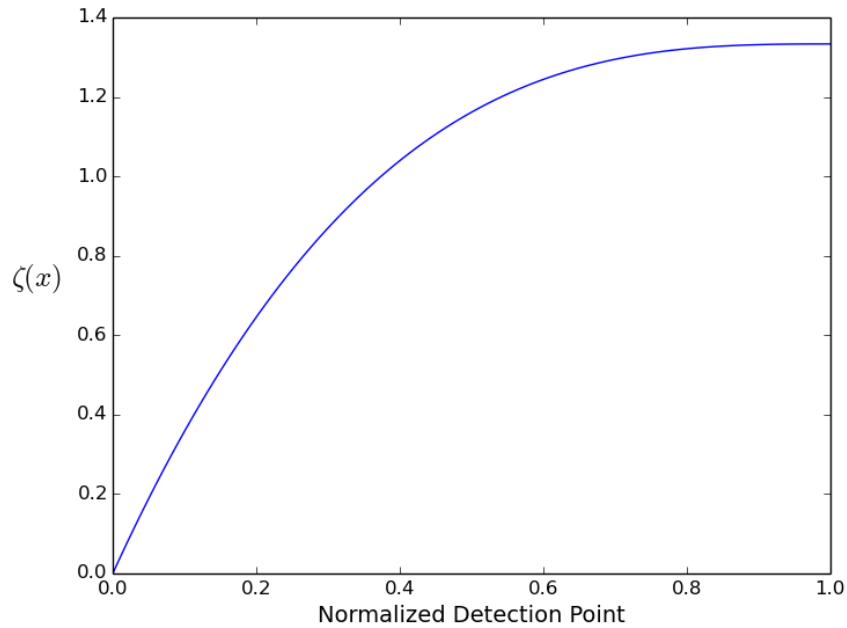


Figure 4.5: ζ describes the ratio of the slope of the cantilever at x with the displacement of the free end.

4.4 Point Loads

Loads that are applied at a point along the cantilever can be described by $\hat{F}(x|\omega) = \hat{F}(\omega)\delta(x - x_0)$. Solving for the displacement of the free end of the cantilever is determined by substituting this load into Eq. (3.64) and Eq. (3.68) to obtain

$$\begin{aligned}\hat{W}(l|\omega) &= \int_0^l G(l, x'|\omega)\hat{s}(\omega)dx' \\ &= \frac{\hat{F}(\omega)}{EI} \int_0^l G(l, x'|\omega)\delta(x' - x_0)dx'.\end{aligned}\tag{4.21}$$

The result of evaluating this integral is

$$W(l|\omega) = \frac{l^3 \hat{F}(\omega)}{2EIB^3(\omega)(1 + \cos(B(\omega)) \cosh(B(\omega)))} \times \begin{cases} \{[\cos(B(\omega)) + \cosh(B(\omega))] \\ \times [\sin(B(\omega)x_0/l) - \sinh(B(\omega)x_0/l)] \\ - [\sin(B(\omega)) + \sinh(B(\omega))] \\ \times [\cos(B(\omega)x_0/l) - \cosh(B(\omega)x_0/l)]\} \end{cases} \quad (4.22)$$

As this is a force applied at a specific point along the beam it is more convenient to express this in terms of the total force that is applied at that point as opposed to the applied load. In terms of the applied load the total force is $F(\omega) = l\hat{F}(\omega)$.

The displacement of a cantilever due to a point load is proportional to the Green's function, thus Fig. 4.1 shows the response of the beam due to a point load. This result demonstrates a benefit of driving the beam with a point load. As a point load is moved toward $x = 0$ the maximum displacement of the beam is reduced. This makes it possible to control the displacement of the beam by either moving the location of the point load or varying its intensity.

4.5 Laser Load

The load that is applied to the cantilever is assumed to be uniform across the length of the beam, allowing the previous result to be employed. For the laser to apply a force to the cantilever a small AC voltage was applied to the laser on top over a relatively large DC voltage. The resulting load of the laser can be expressed as

$$\hat{F}_{laser}(\omega) = \hat{f}_{DC}\delta(\omega) + \hat{f}_{AC}\delta(\omega - \omega_{AC}) \quad (4.23)$$

where \hat{f}_{DC} and \hat{f}_{AC} are the loads caused by the DC and AC components with units of Nm^{-1} , and ω_{AC} is the frequency of the AC component with units of $(\text{rad/s})^{-1}$. It can be seen that the load caused by the laser can be written as the sum of two loads of the same

form, $\hat{f}_n(\omega)\delta(\omega - \omega_n)$ where ω_n is the driving frequency and $\hat{f}_n(\omega)$ is the load at ω_n . The following derivation will continue using this generalized form.

$\hat{f}_n(\omega)$ is directly proportional to the magnitude of the radiation, p_n , at that frequency. The radiation pressure is

$$p_n = \frac{I_n}{c} \quad (4.24)$$

where I_n is the intensity of the beam at ω_n and c is the speed of light. From this the load that is applied to the cantilever is

$$\hat{f}_n(\omega) = \frac{I_n l w}{c l} = \frac{I_n w}{c}. \quad (4.25)$$

The derived result for $\hat{F}_n(\omega)$ does not account for the reflectivity of the beam. If the beam that is being driving is perfectly reflected and perpendicular to the beam, then a factor of 2 must be accounted for. This result can be substituted into Eq. (4.23) and then used to solve for the resulting deflection, Eq. (4.18), and slope, Eq. (4.19), of the beam.

4.6 Conclusion

The Green's function was solved explicitly in terms of trigonometric functions. The coefficients of the Green's function were then obtained by using the boundary conditions. The solution was then checked by plotting the Green's function and its first three derivatives. This allowed the plots to be compared with boundary conditions ensuring that the derivation was performed correctly and that the required discontinuity was present for the third derivative.

The response of a cantilever to a uniform load and a point load at x_0 have been determined. The case of a uniform load is of particular importance as the driving laser will be modelled as a uniform load. This allows for a simple and explicit result to be obtained which can be used to reduce the computation time of the model. This result allowed a con-

version function ζ to be determined which allows the displacement to be calculated from the measured slope of the beam. Point loads will not be used for further experimentation. They are of theoretical interest as they can be used to drive the motion of the cantilever. They also provide the benefit of allowing the maximum amplitude of the cantilever to be controlled by either the amplitude of the driving load or the position of the point load along the beam.

Chapter 5

Damped Harmonic Oscillator Model

5.1 Overview

In the past AFM cantilevers peaks have been modelled as if they were created by a DHO for calibration and analysis [51, 56, 57]. This model was used as it is relatively simple and can be applied to the first mode's peak, the dominant mode. The DHO model was used by Walters et al. in a study to determine the benefits of using short micro-cantilevers for AFM applications. They determined that the DHO model was sufficient for the simple case of studying the first resonant peak [58]. This method of fitting the data was done as it fits the resonant peaks individually while the EBBE model is a multi-peak fit. This model has the specific downfall that it does not rigorously account for the true geometry of the beam nor does it account for the higher order modes. The DHO model will be derived here from both the equation of motion for the DHO and the EBBE model and then compared with the EBBE model solution to ascertain the reliability of the DHO model. This final analysis will also include some discussion of the effects of the fluid on the motion of the beam. This analysis will be predominantly based on the EBBE model but will also show the resulting differences between the two models as the fluid starts to diverge from the assumptions used to derive the DHO model.

5.2 Damped Harmonic Oscillator

This section derives the DHO model from the equation of motion. The equation of motion will include both a dampening term along with a generic driving force. To determine

the motion of the DHO in the frequency domain, the Fourier transform of the equation of motion, a function of time, must be computed. This final result will be comparable with the EBBE model and the DHO model that will be derived from the EBBE using specific assumptions.

The equation of motion for a DHO is

$$m\ddot{x}(t) + \gamma\dot{x}(t) + kx(t) = F(t) \quad (5.1)$$

where m is the mass of the oscillator, $x(t)$ is the position of the oscillator as a function of time, γ is the dampening coefficient, k is the spring coefficient, $F(t)$ is the force driving the oscillators motion and dots imply a time derivative. The Fourier Transform of the equation of motion is

$$-m\omega^2 X(\omega) + i\gamma\omega X(\omega) + kX(\omega) = F(\omega). \quad (5.2)$$

This result can be solved to obtain

$$X(\omega) = \frac{F(\omega)}{m(\omega_0^2 - \omega^2 + i\beta\omega)}. \quad (5.3)$$

where

$$\beta = \gamma/m \quad \text{and} \quad \omega_0^2 = k/m. \quad (5.4)$$

The spectral density is simply the magnitude of Eq. (5.3),

$$|X(\omega)| = \frac{|F(\omega)|}{m\sqrt{((\omega_0^2 - \omega^2)^2 + \beta^2\omega^2)}}. \quad (5.5)$$

The PSD is defined as [59]

$$PSD(X(\omega)) = \lim_{T \rightarrow \infty} \frac{1}{2T} |X(\omega)|^2 \quad (5.6)$$

or in the case of the DHO

$$PSD(X(\omega)) = \frac{G(\omega)}{m^2} \frac{1}{\left((\omega_0^2 - \omega^2)^2 + \beta^2 \omega^2\right)} \quad (5.7)$$

where

$$G(\omega) = \lim_{T \rightarrow \infty} \frac{1}{2T} |F(\omega)|^2. \quad (5.8)$$

Parseval's Theorem can be used to determine the expectation value of $x(t)$,

$$\begin{aligned} \langle x(t)^2 \rangle &= \lim_{T \rightarrow \infty} \frac{1}{2T} \int_{-T}^T |x(t)|^2 dt = \lim_{T \rightarrow \infty} \frac{1}{2T} \int_{-\infty}^{\infty} |x(t)|^2 dt \\ &= \lim_{T \rightarrow \infty} \frac{1}{2T} \int_{-\infty}^{\infty} |X(\omega)|^2 d\omega = \int_{-\infty}^{\infty} PSD(X(\omega)) d\omega. \end{aligned} \quad (5.9)$$

Applying this and noting that thermal noise can be treated as white noise, we find:

$$\begin{aligned} \langle x(t)^2 \rangle &= \frac{G(\omega)}{m^2} \int_0^{\infty} \frac{d\omega}{\left((\omega_0^2 - \omega^2)^2 + \beta^2 \omega^2\right)} \\ &= \frac{G(\omega)}{m^2} \frac{\pi}{2\beta\omega_0^2}. \end{aligned} \quad (5.10)$$

Using the equipartition theorem from thermodynamics, the expectation energy is

$$m\omega_0^2 \langle x(t)^2 \rangle = k_B T. \quad (5.11)$$

The previous two results can be combined and solved for

$$G(\omega) = \frac{2k_B T \beta \omega_0^2 m^2}{\pi k} = \frac{2k_B T \omega_0^3 m^2}{\pi k Q} \quad (5.12)$$

where $Q = \omega_0/\beta$. Finally, this result can be substituted into Eq. 5.7 to obtain the PSD of the DHO, which will be referred to as the DHO model,

$$PSD(X(\omega)) = \frac{2k_B T \omega_0^3}{\pi k Q} \frac{1}{\left((\omega_0^2 - \omega^2)^2 + \frac{\omega_0^2 \omega^2}{Q} \right)}. \quad (5.13)$$

5.3 Small Dissipative Effects Model

The applicability of the DHO model for cantilevers can be tested for the case of small dissipative effects. In this case the imaginary component of $B(\omega)$, Eq. (3.66), is sufficiently smaller than its corresponding real part and each mode of the beam is weakly coupled and thus can be considered as independent. This will determine if and when the DHO model can be used for the purposes of understanding the behaviour of the cantilever and its corresponding noise in general.

Let us only concern ourselves with the frequency range in the vicinity of the resonant peaks and assume that the width of the peaks is much less than the separation between peaks. Equation (3.115) will be rewritten in the form

$$|\hat{W}(x|\omega)| \cong \left| \frac{a_n(x)}{C_n^4 - B^4(\omega)} \right| \quad (5.14)$$

where $|a_n(x)|$ is an rms term that is a function of x alone and defined as

$$a_n(x) = \left(\frac{27\pi k_B \Gamma l^2}{k^3 C_n^4 \int_0^\infty |\alpha_n(\omega')|^2 d\omega'} \right)^{1/2} \times |\phi_n(x)| \quad (5.15)$$

From Eq. (3.66) it can be seen that $B(\omega)$ varies as $O(\omega^2)$ while $\Gamma(\omega)$ varies as $O(\omega^{1/2})$, by Eq. (3.25) and Eq. (3.51). Due to the dominance of the $B(\omega)$ term it will be assumed for this case that $\Gamma(\omega)$ is a constant around the resonance peak frequency range. The most easily defined frequency that characterizes the region of interest is the resonance frequency. One of the limitations of the DHO model is that it only has 1 mode with a resonance peak located at ω_0 as defined in Eq. 5.4. This limitation of the DHO model can be addressed by considering each mode of the cantilever independently and defining the resonance fre-

quency for an arbitrary n^{th} mode of the cantilever as $\omega_{R,n}$.

Each mode of the cantilever can then be individually considered, or a sum of modes can be taken to obtain a result similar to Eq. 3.115 or Eq. 3.116. As a result of the previous argument $\Gamma(\omega)$ will be evaluated at $\omega_{R,n}$. Now that $\Gamma(\omega)$ has been considered for individual modes, a similar process should be applied to $B(\omega)$. A similar argument can be used for the need to rewrite $B(\omega)$ in a form for individual modes using the resonance frequency for the individual modes, $\omega_{vac,n}$, and it takes the form

$$B(\omega) \cong B_n(\omega) = C_n \sqrt{\frac{\omega}{\omega_{vac,n}}} \left[1 + \frac{\pi \rho_f b^2}{2\mu} (\Gamma_r(\omega_{R,n}) + i\Gamma_i(\omega_{R,n})) \right]^{1/4}. \quad (5.16)$$

For the case where there are not dissipative effects $Re \rightarrow \infty$ and $\Gamma \rightarrow 0$, thus at $\omega_{R,n}$ we have $B_n(\omega) \rightarrow C_n$. Using this result and the previously stated result that as dissipative effects become smaller $\Gamma_i(\omega)$ approaches 0, we find

$$\frac{\omega_{R,n}}{\omega_{vac,n}} = \left(1 + \frac{\pi \rho_f b^2}{4\mu} \Gamma_r(\omega_{R,n}) \right)^{-1/2}. \quad (5.17)$$

This result can be solved for $\omega_{vac,n}$ and then substituted into Eq. 5.16 to obtain

$$B_n(\omega) = C_n \sqrt{\frac{\omega}{\omega_{R,n}}} \left(1 + \frac{i}{Q_n} \right)^{1/4} \quad (5.18)$$

where

$$Q_n = \frac{\frac{4\mu}{\pi \rho_f b^2} + \Gamma_r(\omega_{R,n})}{\Gamma_i(\omega_{R,n})}. \quad (5.19)$$

The assumption of a small dissipative effect is fulfilled when the imaginary part of $\Gamma(\omega_{R,n})$ is much smaller than the real part. This is true when $Q_n \gg 1$, meaning that the DHO model cannot be applied if $Q_n \lesssim 1$. The assumption that the frequency range of interest is limited to the resonance peak can be used allowing approximation $\omega \cong \omega_{R,n}$ can be used.

Substituting Eq. 5.18 into Eq. 5.14 we find the Noise Amplitude Spectral Density (NASD) of the displacement to be

$$|\hat{W}(x|\omega)|_s \cong \sum_n \frac{a_n(x)\omega_{R,n}^2}{C_n^4} \frac{1}{\left((\omega^2 - \omega_{R,n}^2)^2 + \omega^2\omega_{R,n}^2/Q_n^2\right)^{1/2}}. \quad (5.20)$$

This result can then be used to determine the NASD of the slope,

$$\left|\frac{d\hat{W}(x|\omega)}{dx}\right|_s \cong \sum_n \frac{\omega_{R,n}^2}{C_n^4} \frac{1}{\left((\omega^2 - \omega_{R,n}^2)^2 + \omega^2\omega_{R,n}^2/Q_n^2\right)^{1/2}} \left|\frac{da_n(x)}{dx}\right|. \quad (5.21)$$

where

$$\frac{da_n(x)}{dx} = \left(\frac{27\pi k_B T l^2}{k^3 C_n^4 \int_0^\infty |\alpha_n(\omega')|^2 d\omega'} \right)^{1/2} \times \left| \frac{d\phi_n(x)}{dx} \right|. \quad (5.22)$$

Equation (5.21) will be referred to as the Small Dissipative Effects (SDE) model. This result can be compared with Eq. 5.13 to see that this is the PSD of the DHO with a different magnitude.

5.4 DHO Model Application

The EBBE model uses Eq. (3.116) which is related to Eq. (3.115), the equation the DHO model is based on. The optical lever method used for detecting the motion of the cantilever makes the equipment sensitive to the slope of the beam, which Eq. (3.116) describes. The ratio between these two equations is then accounted for by a fitting parameter in the DHO model. The EBBE model is computed using a program that was written for this purpose in Python [60]. The model is computed analytically with only the integral of $\alpha^2(\omega)$ using a numerical method. The function, `quad`, that was used is from the standard

Python package “scipy” [61].

The DHO model is derived for a specific system, a mass on a spring, that does not describe the geometry of the cantilever, how the spring system works, nor explicitly consider hydrodynamic effects. The previous result is limited to frequencies around the resonance frequency of the oscillator and in the case where the dissipative effects are small which requires $Q_n \gg 1$. The SDE model has the same form as the DHO model and they are both subject to the same limitations. It is derived direct from Eq. (3.115) using assumptions which limits both the frequency range and fluids that it can be applied in. This section serves to determine when the SDE model is applicable and if it accurately describes a cantilever. This will be treated as a model and not a fit. This is done as the SDE model is derived directly from Eq. (3.115) for a beam and it should have the correct amplitude for the resonance peaks while the DHO model is not expected to predict the amplitude of the resonance peaks.

For this comparison the DHO model will be used as a fitting function, DHO fit, using a least-squares fitting routine for the EBBE model to determine the quality factor and resonance frequency of the first three peaks. The first term of Eq. 5.13 determines the amplitude of the model but will be considered a fitting parameter along with ω_0 and Q . The EBBE model and SDE model can then be compared against each other using the fit results. For this analysis the NASD of the slope will be calculated for the first three resonant peaks of the 500 μm cantilever, using the ideal dimensions as outlined in Table 6.1 using both the EBBE and SDE models.

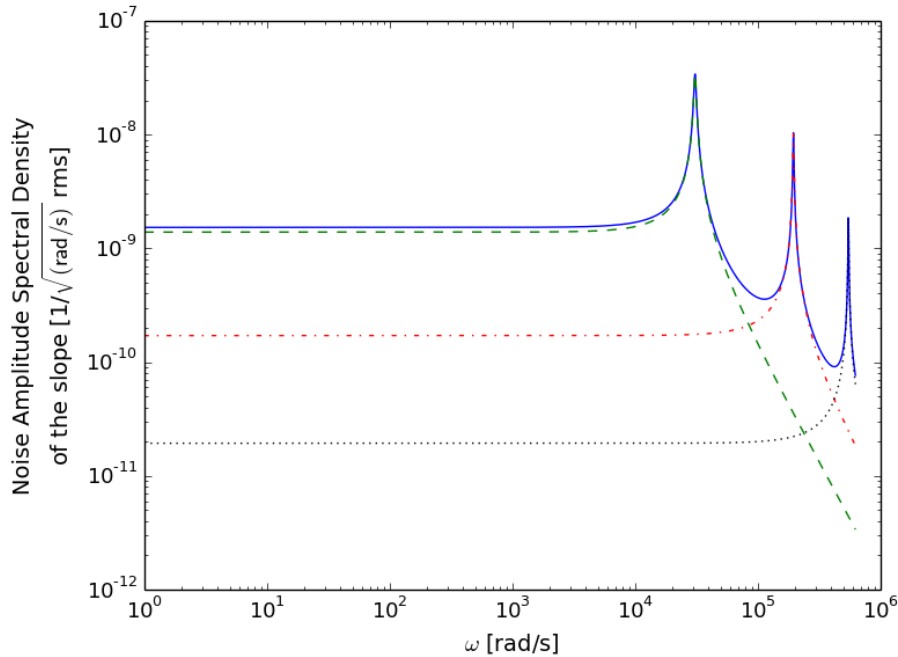


Figure 5.1: Plot of the NASD of the slope as calculated by EBBE model and DHO fits for 3 resonant peaks for a large frequency, ω , range. The solid blue line shows the results for the EBBE model as calculated for a $500 \mu\text{m}$ cantilever with ideal dimensions in air. The three other plots are results for the DHO fit of the first, dashed green line, second, dot dash red line, and third, dotted black line, peaks. See Table 5.1 for a summary of these results.

The calculated values for the first three resonant peaks of the $500 \mu\text{m}$ cantilever, EBBE model, and the resulting fit, DHO fit, are presented in Fig. 5.1. The blue curve of Fig. 5.1 was calculated using Eq. (3.116). The DHO fit was performed three times, once for each resonant peak. The results for the fits correspond well with the EBBE model at the resonant peaks. This is expected as the quality factor for all three peaks is well in excess of 1 and all variables were treated as fitting parameters. The results for the quality factor, the amplitude of the peak and the resonant frequency can be found from the results of the fit; these are the sources of the values in table 5.1. The noise of the cantilever at low frequencies is almost entirely accounted for by the noise of the first mode alone, demonstrating how this is the dominant mode at low frequencies. The higher order modes do not contribute significantly to low frequency noise. The frequency range of interest for work of this thesis is concentrated at low frequencies when considering the MOND experiment and thus the

higher order modes are sometimes ignored. The noise of the higher order modes only need to be accounted for if an experiment is being performed at frequencies higher than the first resonant peak.

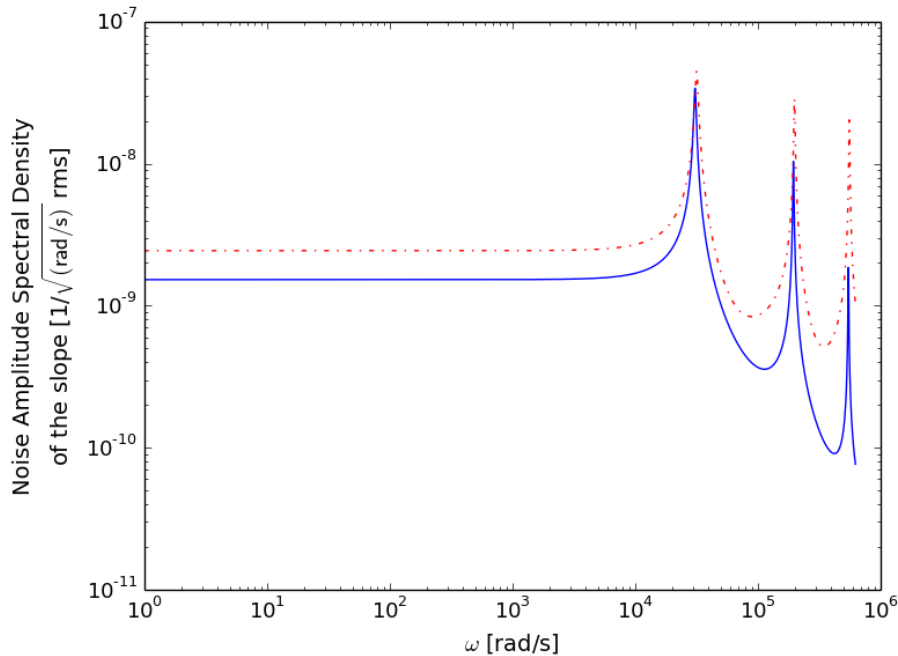


Figure 5.2: Plot of the NASD of the slope as calculated by the EBBE, blue solid line, and SDE, red dot dash line, models. The solid blue line is the EBBE model for a $500 \mu\text{m}$ cantilever with ideal dimensions. The dot dash red line shows the SDE model for the same cantilever. The SDE model can be seen as having larger deviations from the EBBE model as the peak number increases. See Table 5.1 for a summary of these results.

Figure 5.2 shows a comparison of the NASD of the slope for the first three resonant peaks as calculated by the EBBE model, blue curve and the same as in Fig. 5.1, and the SDE model, red dot-dash curve. The SDE model was derived from the EBBE model using the assumption of small dissipative effects. This allowed the EBBE to be solved in a form similar to that of the DHO. The noise of each resonant peak has not been treated as individuals as they were for the DHO since the SDE model is derived from the result for a cantilever. The results that are shown here are the models themselves and not a fit. From a qualitative analysis of Fig. 5.2 it can be seen that for low frequencies both of the models approach some constant value of noise and the value for the models are within a factor of

1.6 of each other. The amplitude of the noise is closest around the resonant peaks of the first mode which are within a factor of 1.3. The noise at large frequencies starts to differ significantly where the third resonant peaks differ by a factor of 11.

Table 5.1: Quantitative comparison of the the EBBE model, using values obtained using the DHO fit, and the SDE model.

		DHO Fit	SDE Model	
		Value	Value	Difference w.r.t. DHO Fit [%]
Peak 1	Peak Amplitude [$1/\sqrt{(\text{rad/s})}$ rms]	34.0	44.7	31%
	Frequency [rad/s]	31164	31923	2.4%
	Quality Factor	18.2	18.9	4.2%
Peak 2	Peak Amplitude [$1/\sqrt{(\text{rad/s})}$ rms]	10.2	29.1	185%
	Frequency [rad/s]	197984	200057	1.0%
	Quality Factor	42.8	50.7	20%
Peak 3	Peak Amplitude [$1/\sqrt{(\text{rad/s})}$ rms]	1.94	22.4	1050%
	Frequency [rad/s]	556479	560165	0.67%
	Quality Factor	81.0	84.3	4.1%

The deviations of the SDE model from the EBBE model follow general trends with the exception of the quality factor. The results for the percent difference of the peak amplitude show the SDE model predicting results very similar to that the of the EBBE model for the first peak and the difference increasing with increase mode number. The SDE model was derived using assumptions that limit it's application to the first couple of modes and as a

result this is the expected behaviour. The frequency of the first resonant peak is with 2.4% for all three peaks and with the percent difference decreasing with increasing mode number. The absolute difference between the resonant frequencies of the SDE and EBBE models are increasing with increasing mode number. The quality factor differs from this behaviour as the percent difference for the first and third peaks are approximately 4.1% while it is a significantly larger at 20% for the second peak. The source of this deviation is currently unknown.

The challenge of the SDE model for these peaks, specifically higher mode peaks, may be caused by one of the assumptions of the model. The cantilever is modelled as an infinitely long beam with a finite width. This model is applied using the condition that the real cantilever will have a significantly large aspect ratio of length/width. Due to this assumption the model is limited to a small number of modes, ideally one based on this analysis. This limitation is not a significant concern for the work of this study as low frequencies are of primary interest and the noise contribution from higher order modes at low frequencies is insignificant compared to the first mode.

5.5 Cantilever Calibration using the DHO Model

The EBBE DHO model and DHO fit can be used to determine the best values for the EBBE model. The values obtained by the DHO fit can be used as a starting value to give a good understanding of what is to be expected. Sader et al. [62] discusses a method that can be used for the purposes of calibrating an AFM cantilever. This paper is intended to determine the cantilever's spring constant for use with AFM. The method described by Sader et al. allows for one dimension of the cantilever to be calculated using information from the fit in conjunction with some properties of the cantilever and the fluid it is submerged in. The dimension of the cantilever that has the greatest effect on the resonant frequency of the cantilever is its thickness and thus it will be calculated here using the width and length as constants.

Sader et al. include an equation for fitting to the first resonance peak of the cantilever based on the PSD of a DHO, Eq. (5.13),

$$PSD(\omega) = A_{white} + \frac{B\omega_f^4}{(\omega^2 - \omega_f^2)^2 + \omega^2\omega_f^2/Q^2}. \quad (5.23)$$

The fitting parameters are A_{white} which is the noise of the system that contributes to the signal but is not generated by the DHO or cantilever itself, B which is related to the peak, the resonant frequency ω_f and, the quality factor Q . The values for ω_f and Q can be substituted into an equation provided by Sader et al. to obtain the thickness of the cantilever. The thickness of the cantilever is calculated by

$$h = \frac{\pi\rho_{fluid}b}{4\rho} (Q\Gamma_i(\omega_f) - \Gamma_r(\omega_f)) \quad (5.24)$$

where $\Gamma_r(\omega_f)$ and $\Gamma_i(\omega_f)$ and the real and imaginary components of $\Gamma_{rect}(\omega)$, Eq. (3.55), respectively.

5.6 Fluid Effects

The effects of fluids on resonance frequencies and quality factors for thermally driven cantilevers will now be considered. Each analysis will be generalized for a cantilever of arbitrary dimensions. The analysis will be carried out for values that are pertinent to AFM cantilevers and the fluids that they are generally immersed in. While experimental measurements must be made with the detection point not directly at the free end of the cantilever, the following results will be calculated for the end of the cantilever, $x = l$.

This analysis will use two scaling parameters. The first will be the Reynolds number evaluated at $\omega_{vac,1}$ and the second is based on Eq. (3.66) and the mass per unit length of the cantilever $\mu = \rho_{cant}bh$,

$$\overline{Re} = \frac{\rho_f\omega_{vac,1}b^2}{4\eta} \quad \text{and} \quad \overline{T} = \frac{\rho_f b}{\rho_c h}. \quad (5.25)$$

The value of \overline{Re} is the ratio of inertial forces to viscous forces at the resonance frequency. This can be solved in terms of the cantilever's properties by substituting the solution for $\omega_{vac,1}$ from Eq. (2.40) into the previous result to obtain

$$\overline{Re} = \frac{C_1^2 \rho_f}{8\sqrt{3}\eta} h \left(\frac{b}{l}\right)^2 \sqrt{\frac{E}{\rho_c}}. \quad (5.26)$$

As the cantilever moves in the fluid it will pull some mass of fluid with it, the value of \overline{T} is proportional to this mass. The mass that is moved by the cantilever has an effect due to the inertial forces in the fluid causing the cantilever to move as if it has a larger mass. From Eqs. (5.25) and (5.26) it is apparent that if a cantilever is uniformly scaled that \overline{T} will remain a constant but \overline{Re} will vary proportionally to the cantilever's thickness.

The values of \overline{Re} and \overline{T} are dependent on the properties of the fluid and the cantilever. For identical cantilevers, the values of \overline{Re} range over about 1 order of magnitude between gases and liquids as the kinematic viscosity, ρ_f/η , tends to vary over this range. The value of \overline{T} tends to vary significantly more, about 3 orders of magnitude, due to the large variation of densities between gases and liquids. An analysis will be included to show the different effects of gases and liquids.

The following plots show the effects of fluids on the quality factor and the frequency of the resonance peak. The x-axis of the plots is $\omega/\omega_{vac,1}$ as this analysis is intended for a cantilever with arbitrary dimensions. As a result it is expected that the resonant peak in a vacuum will be at 1. The shift of the resonance peak is compared to the expectation of the inviscid model, where viscous effects are minimal, that is $\overline{Re} \rightarrow \infty$. When the dissipative effects become minimal $\Gamma_r(\omega_{R,n}) \rightarrow 0$ and Eq. (5.17) becomes

$$\frac{\omega_{R,n}}{\omega_{vac,n}} = \left(1 + \frac{\pi \rho_f b^2}{4\mu}\right)^{-1/2}. \quad (5.27)$$

For Fig. 5.3, the quantity of interest for the plots is the normalized thermal amplitude spectra for the cantilever's displacement which is defined as

$$H \equiv \sqrt{\frac{k\omega_{vac,1}}{2k_bT} |\hat{W}(x|\omega)|_s^2}. \quad (5.28)$$

While it is a normalized value, from this analysis it will be possible to determine how fluids will qualitatively affect the noise that is measured for some generic cantilever.

Fluids can have an affect on the quality factor of the resonance peak as well. Consideration is required for this quantity as it will be shown that the quality factor has an influence at frequencies well beyond the resonance peak. The quality factor for each plot is calculated using a result from the SDE model derivation, namely,

$$Q_n = \frac{\frac{2\mu}{\pi\rho_f b^2} + \Gamma_r(\omega_{R,n})}{\Gamma_i(\omega_{R,n})}. \quad (5.29)$$

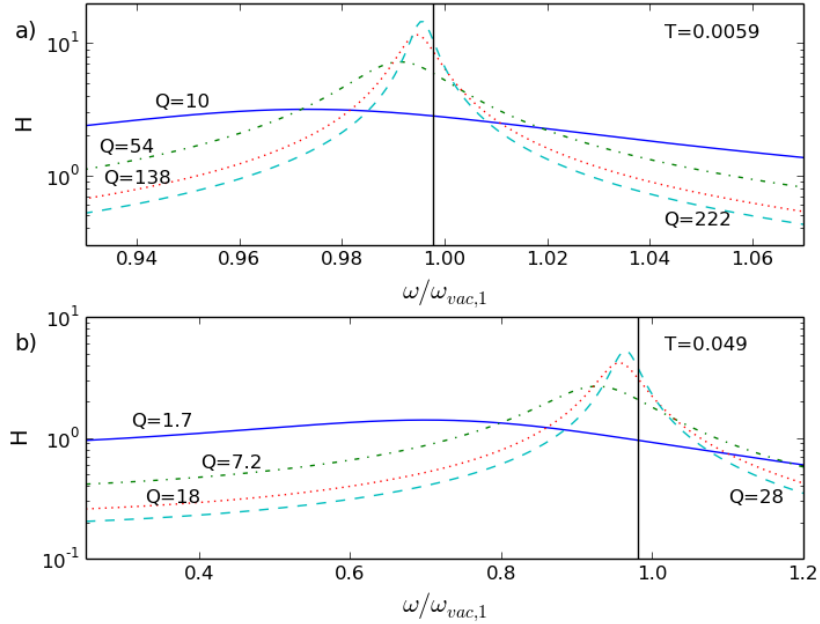


Figure 5.3: Normalized thermal displacement $NASD H = \sqrt{J_w(1|\omega)k\omega_{vac,1}/(2k_bT)}$ for the fundamental mode of a cantilever in a gas. The expected resonance frequency as calculated by the inviscid model, Eq. (5.27), is indicated by the black vertical line. The quality factor for each plot is shown with it's respective line. The plots are generated using $\overline{Re} = 0.1$ (blue solid line), $\overline{Re} = 1$ (green dot dash line), $\overline{Re} = 4.4$ (red dotted line) and, $\overline{Re} = 10$ (teal dashed line). Part a) is plotted using $\overline{T} = 0.0059$ and part b) $\overline{T} = 0.049$.

For a gas \overline{Re} and \overline{T} are on the order of $O(1)$ and $O(10^{-2})$ respectively. The inviscid equation does not account for any viscous effects meaning that as \overline{Re} is decreased, increasing the importance of viscous effects, the inviscid equation remains constant. The inviscid equation does show that the expected resonant frequency will decrease in a fluid due to some amount of added mass of the fluid being dragged by the cantilever but it does not fully account for the observed effects, Fig. 5.3 shows the effects of a gas on a cantilever. The resonant peak of an generic cantilever been plotted for a constant value of \overline{T} with four different values of \overline{Re} . There is only one accompanying predicted resonant frequency based on the inviscid model as it is the same for all three values of \overline{Re} . However, for the values of $\overline{T} = 0.0059$ and $\overline{T} = 0.049$ it can be seen that the inviscid model does predict two different resonant frequencies. This is a direct result of the inviscid model being dependent on \overline{T} and independent of \overline{Re} . The ratio of the resonant frequency in a fluid versus a vacuum can also be calculated using Eq. (5.17) from the SDE model. This equation also neglects any dissipative effects while increasing the effects from added mass due to the increase of the viscosity of the fluid. While not shown here, the discrepancy between the inviscid equation and the calculated resonance frequency is nearly entirely accounted for using the EBBE DHO model equation. While it is possible to varying \overline{Re} and \overline{T} independently, these results show that the effects of viscosity and inertial forces act together. The use of Eq. (5.17) helps to solve the discrepancy between the theoretical and inviscid model resonance frequencies by allowing the inertial effects to be increased as a direct result of the viscous effects of the fluid.

For the cases where \overline{T} is held constant and \overline{Re} decreases or \overline{Re} is held constant and \overline{T} increases, the resonance peak starts to broaden out and the resonance peak shifts to lower frequencies, the result of the increased importance of viscous effects. This broadening and shift are significant issues for the noise of the cantilever at low frequencies. As will be discussed later, the effects of the fluid cause the energy of the resonance peak to shift to lower frequencies. This causes the peak amplitude to decrease at the expense of increased

noise for frequencies less than the peak.

Liquids tend to have higher viscosities and densities than gases do, as a result typical values for \overline{Re} and \overline{T} for liquids are $O(10)$ [58, 63, 64]. The arguments that applied for gases apply to liquids as well, but, due to the larger viscosity and density of a liquid, the effects that are observed are much more dramatic. The results for the effects of liquids on cantilever vibration are shown in Fig. 5.4. The fundamental resonant peak and first harmonic are modelled in this case as very dense, viscous liquids can cause the second harmonic resonance frequency to shift to frequencies lower than the expected fundamental resonant frequency in a vacuum. This extreme shift is particularly prominent in Fig. 5.4b for the plot where $\overline{Re} = 1$ causing the first harmonic resonance peak frequency to be only about $0.6\omega_{vac,1}$. The shift of the resonance peak for the first harmonic is so extreme in some cases, like that where $\overline{Re} = 1$, that it starts to become indistinguishable from the fundamental mode, causing coupling of the modes. For this case the fundamental resonance peak has shifted to $0.1\omega_{vac,1}$ causing a significant noise increase at very low frequencies.

The previous results have used values for \overline{Re} that were specifically chosen for either liquids or gases. This served well to show general trends of large frequency ranges. The following analysis will allow \overline{Re} to vary over larger ranges with more continuity while \overline{T} has the values of 0.0059, 0.02 or 0.049 for gases and 5, 20 or 45 for liquids. The values that were used for these plots were calculated numerically. The noise spectra density of the cantilever was calculated using Eq. (3.116) over a large range for the resonant frequency. The resonance peak was found and then the frequency range was narrowed down and the process repeated until the resonance peak was known to within 0.16 rad/s. The value for the resonance frequency and peak energy were then recorded. The quality factor was calculated using Eq. (5.19) which was derived using the assumption that dissipative effects were small, that is $Q \gg 1$. Due to this assumption, the plots where $Q \lesssim 1$ should be considered as a qualitative assessment of the resonance peak. This region is where there is substantial broadening of the resonance peak and coupling of the modes becomes significant.

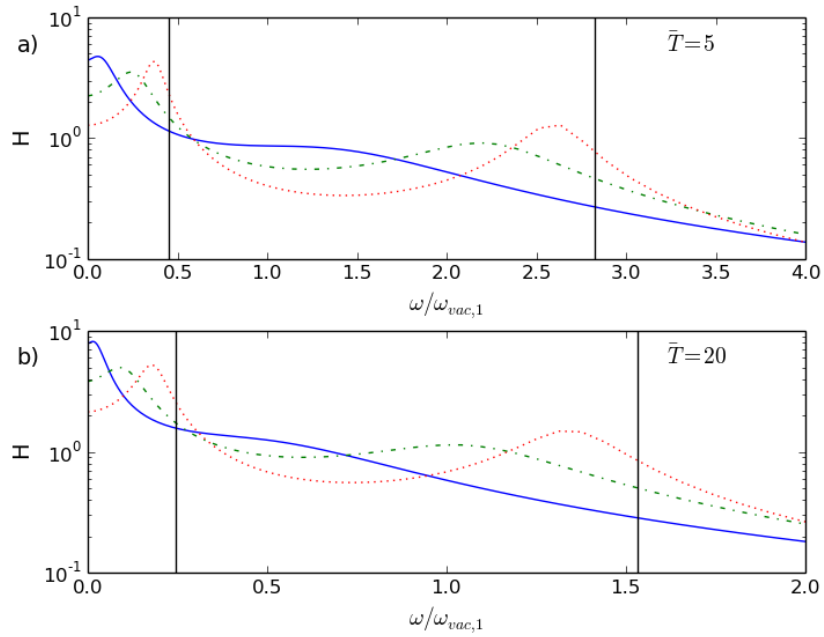


Figure 5.4: Normalized thermal displacement NASD $H = \sqrt{J_w(1|\omega)k\omega_{vac,1}/(2k_bT)}$ for the first two modes of a cantilever in a liquid. The expected resonance frequencies as calculated by the inviscid model, Eq. (5.27), are indicated by the black vertical lines. The quality factor for each plot is shown with its respective line. The plots are generated using $\overline{Re} = 1$ (blue solid line), $\overline{Re} = 10$ (green dot dash line) and, $\overline{Re} = 100$ (red dotted line). Part a) is plotted using $\overline{T} = 5$ and part b) $\overline{T} = 20$.

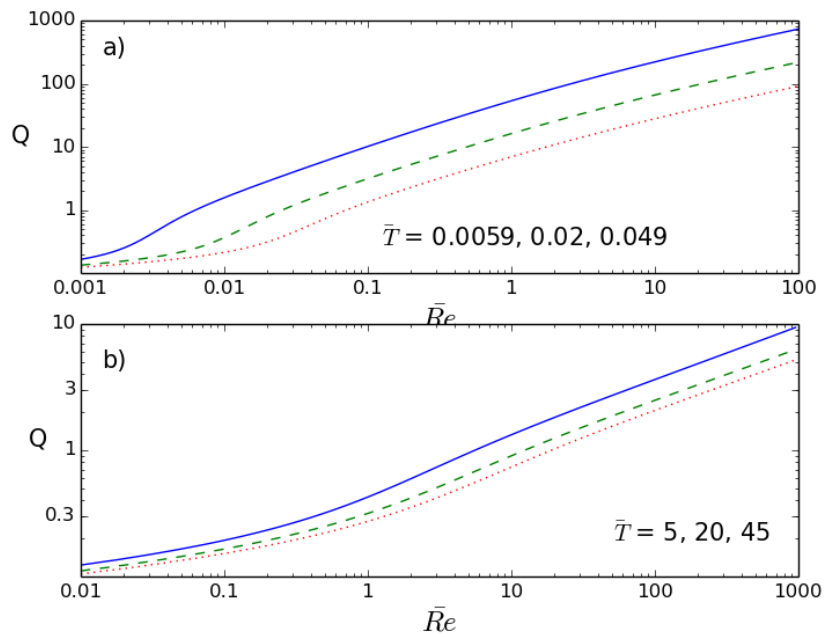


Figure 5.5: Plot demonstrating fluid effects on the quality factor the fundamental resonant peak, as calculated by Eq. (5.29). Plot a) generated using $\bar{T} = 0.0059$ (solid blue line), $\bar{T} = 0.02$ (green dashed line) and, $\bar{T} = 0.049$ (red dotted line). Plot b) generated using $\bar{T} = 5$ (solid blue line), $\bar{T} = 20$ (green dashed line) and, $\bar{T} = 45$ (red dotted line).

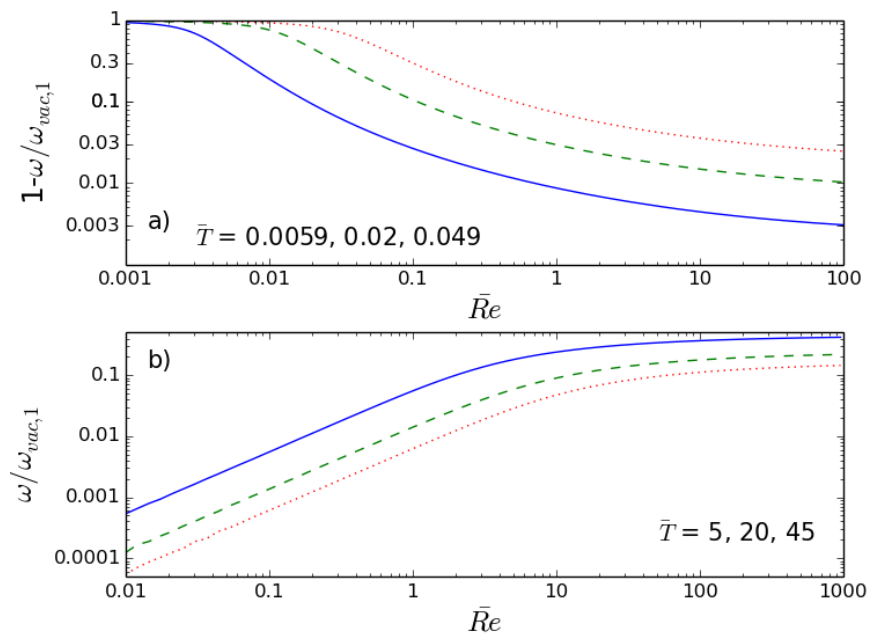


Figure 5.6: Relative fundamental resonance frequencies with respect to $\omega_{vac,1}$ for a broad range of \bar{Re} . Plot a) generated using $\bar{T} = 0.0059$ (solid blue line), $\bar{T} = 0.02$ (green dashed line) and, $\bar{T} = 0.049$ (red dotted line). Plot b) generated using $\bar{T} = 5$ (solid blue line), $\bar{T} = 20$ (green dashed line) and, $\bar{T} = 45$ (red dotted line).

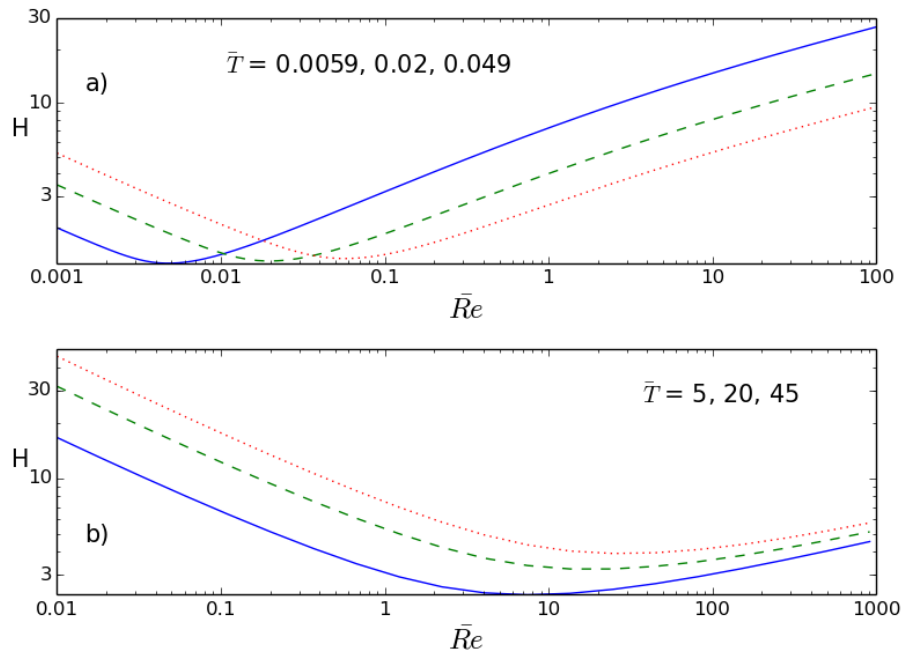


Figure 5.7: Normalized thermal displacement NASD $H = |J_w(1|\omega)|^2 k\omega_{vac,1} / (2k_b T)$, square root of Eq. (3.115), for the fundamental mode of a cantilever. Plot a) generated using $\bar{T} = 0.0059$ (solid blue line), $\bar{T} = 0.02$ (green dashed line) and, $\bar{T} = 0.049$ (red dotted line). Plot b) generated using $\bar{T} = 5$ (solid blue line), $\bar{T} = 20$ (green dashed line) and, $\bar{T} = 45$ (red dotted line).

The peak energy of the cantilever at the resonance frequency is observed as noise in the measurements. This can be a challenge as the cantilevers are occasionally driven around the resonance frequency. Figure 5.7 shows the results for the normalized peak energy and finds that a local minimum occurs about when $Q \simeq 1$ for varying \overline{Re} , compare with Fig. 5.5. This effect can be observed in Fig. 5.4. It is clear for a cantilever in a liquid that the peak energy is at a minimum when $\overline{Re} \simeq 10$. This response of the cantilever to the surrounding fluid can be used advantageously in the case of the AFM application as selecting the correct fluid for a given cantilever can reduce peak energy and thus the measured noise if measurements are taken around the resonant frequency.

The reduction of peak noise comes at the cost of low frequency noise. The fluid surrounding the cantilever causes the energy at the peak frequency to be shifted to lower frequencies. In the case where the quality factor is sufficiently large, $Q > 1$, significant shifting of the resonance frequency will not have occurred allowing the redistributed energy to be spread out across a large frequency range. In the case where the fluid causes large amounts of peak broadening and resonance frequency shift, $Q < 1$, the frequency range for energy redistribution to frequencies less than the resonant peak becomes small. Broadening and shifting will continue to occur as the fluid increases its effects on the cantilever. The redistribution of energy starts to become less significant, given that the bandwidth between 0 rad/s and the resonant peak becomes small, causing the resonance peak to start gaining peak energy. This is particularly problematic for the application of the potential MOND experiment. This experiment must be performed at very low frequencies where redistribution of energy causes a steady increase of noise at low frequencies as the fluid increases its effects. As a result of this, the MOND experiment should be performed in a vacuum as fluid can only have detrimental effects.

In Sec. 5.3 it was shown that in the case of small dissipative effects that the resonance peak can be described by the DHO model. Figure 5.8 is a comparison of the DHO model with the first mode of the more complex model derived for a beam. The comparison is

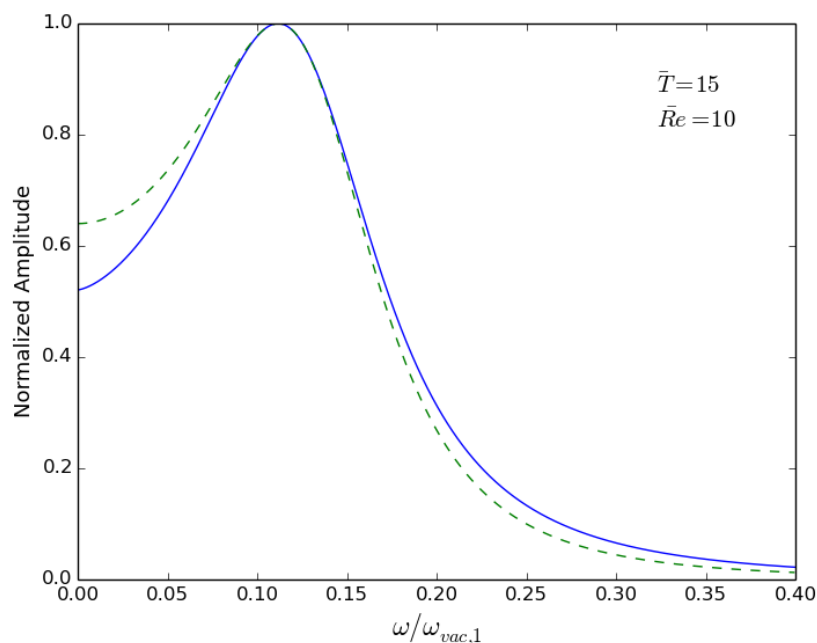


Figure 5.8: The EBBE model (solid blue line), square root of Eq. (3.115), is presented here using a normalized amplitude with respect to unity, $\overline{Re} = 10$ and $\overline{T} = 15$. The DHO model, square root of Eq. (5.10), is fit to this data (dashed green line).

computed using the values $\overline{Re} = 10$ and $\overline{T} = 15$ as this causes $Q \simeq 1$, where the assumption of small dissipative effects breaks down. This plot was created by fitting the DHO model to the beam model. From this fit it can be seen that the DHO model predicts that the measured noise will be larger at lower frequencies and less at higher frequencies. While the DHO model reasonably fits the beam model's resonant peak, there is significant deviations at both low and high frequencies. This makes the model inaccurate and not reliable. If a cantilever were being used in a case where $Q \lesssim 1$, for example if the fluid were a liquid like water or oil, the DHO model would not be sufficient and the beam model would be required.

5.7 Conclusion

The DHO PSD has been derived from the equation of motion for a DHO and also from the EBBE model of a cantilever, albeit with the assumption of small dissipative effects.

The derivation of the DHO PSD from the EBBE model shows that in specific cases it is possible to model a cantilever as a DHO. This fit showed that the DHO can be applied to the resonant peak when dissipative effects are sufficiently small, demonstrated by fitting the DHO model to the EBBE model.

The DHO model had been employed in the past for the purposes of calibrating AFM cantilevers. Over the years AFM has advanced and it is now possible for AFM imaging to work in a variety of different fluids, including liquids like oil. The DHO model was derived using the assumption of small dissipative effects which is reasonable in the atmosphere but is not necessarily true for viscous fluids like oil. The DHO is a system that has only one mode and as a result it cannot account for the higher order modes of the cantilever. This issue can be overcome by considering multiple different DHOs contributing to the signal, but the resonant frequency and quality factor of one mode cannot be predicted using the results of a different mode.

The effects of fluids on the NASD of a cantilever have also been studied. It was demonstrated that a beam in a fluid will have its resonance frequency shifted to a lower frequency and the resonance peak will become broadened. The shifting and broadening of the resonance peak causes energy from the resonance peak to become distributed to lower frequencies thus increasing low frequency noise and reducing high frequency noise. This could be used for a beneficial effect if a cantilever is being used to obtain an AFM image where the cantilever is driven at a very high frequency. With reduced noise at high frequencies it could be possible to increase the SNR. However, in the case of the MOND experiment this causes an issue. The cantilever is intended to be driven at a very low frequency, a frequency range with increased noise due to the fluid, as a result the ideal option is to perform the MOND experiment in a vacuum to minimize low frequency noise.

Chapter 6

Experimental Apparatus

6.1 Overview

This chapter discusses the equipment that is used for measuring the cantilever's motion and how individual components of the Lock-In Amplifier (LIA) influence the final measurement. The general layout of the equipment that is used for the experimental procedures will first be considered.

The experiments to measure the noise of a cantilever will be completed with two different cantilevers. The cantilevers that were chosen have different dimensions, most notably in their length and thickness, causing them to have resonant frequencies that vary by an order of magnitude. Given the small size of the cantilevers, sub-millimeter range, it is difficult to produce a type of cantilever where each cantilever has the ideal dimensions. As a result of this, cantilevers will be produced with dimensions that are within some range causing a range of possible spring constants and resonant frequencies within a production run. The effects of the range of possible dimensions will be analyzed to determine which dimension has the greatest effect on the resonance peak.

The other components of the experimental equipment that will be discussed are the driving and detection laser as well as the detector. The primary component that is used for data acquisition is the lock-in amplifier. This piece of equipment will also be discussed focusing on specific portions of its analysis processes that it uses for processing the input signal before returning a measurement value. The interest for the lock-in amplifier is to consider the important factors that directly influence the SNR and wait time required for

each measurement.

6.2 Equipment Overview

Figure 6.1 shows a top down view of the cantilever, detector and various lasers. The specifics for how each component works will be discussed in their respective sections; here we simply outline the position of each component and the path of the laser beams.

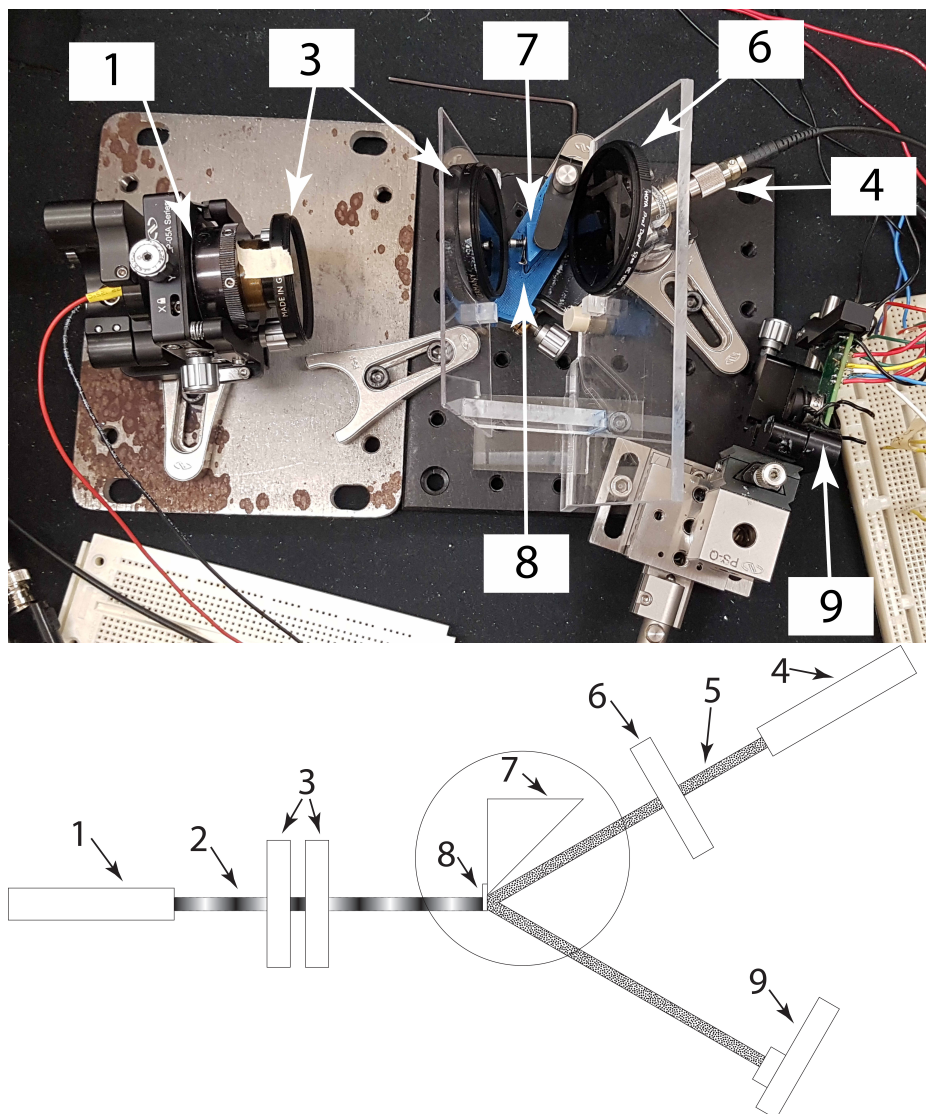


Figure 6.1: Schematic diagram of cantilever detection and driving setup. The individual components are: 1. driving laser, 2. pulsing laser beam to drive cantilever, 3. filter combination to reduce driving laser intensity, 4. detection laser, 5. detection laser beam at constant power, 6. filter to reduce power from detection laser, 7. mount used to hold the cantilever in place, 8. the cantilever, and 9. the detector.

Position detection of the cantilever is done using the optical lever method from atomic force microscopy. The optical level method uses a reflected laser off the cantilever. The cantilever's deflection will cause the angle of the reflected beam to vary. The deflection of the beam is then calculated based on the angular shift of the beam. Referencing Fig. 6.1, a laser with constant power, 4, is reflected off the cantilever, 8, towards a photo-diode detec-

tor, 9. The difference output of the detector, discussed in section 6.4, is used to measure the deflection of the beam which can then be used to calculate the cantilever's motion.

The driving laser, 1, is used for experiments which require the cantilever to be driven at a specific frequency. The pulsing laser causes the radiation pressure to drive the cantilever at the same frequency and phase of the driving laser. To measure the driven motion of the cantilever the X-output of the lock-in amplifier, subsection 6.8.4, is used.

6.3 Cantilevers

The cantilevers that will be used for the pertinent experiments are supplied by NanoWorld Innovative Technologies [65]. The following subsections will discuss the range of values that the two sets of cantilevers could have after production. Manufacturing of the cantilevers also includes some processes that are intended to help improve the signal obtained and the discussion will consider how this affects that cantilever and if it needs to be accounted for in the model. Finally, the EBBE model will be used to compute the expected noise and resonance frequency for the cantilevers if one of their dimensions is at the maximum or minimum value for the guaranteed range. This will demonstrate how the resonant frequency is affected by the dimensions and determine which dimension has the greatest effect on the cantilever's noise.

The cantilevers used for these experiments were manufactured by NanoWorld. The cantilevers are manufactured using a chemical or dry etching process [66]. The process of etching is performed by applying a protective coating that forms the pattern of the desired cantilever. The process of wet etching uses a liquid that is poured over the silicon substrate creating a soluble by-product that can be washed away. This process can also be performed using a gas which removes the substrate instead, this is dry etching. The protective coating prevents a portion of the substrate from being dissolved by the etching compound. This causes a remnant of silicon to be left behind in the shape of the protective coating [67]. The cantilevers have a thin coating that is applied that increases their reflectivity. This is

completed through the use of chemical vapor deposition. This process is often used to coat surfaces, such as metals or ceramics. The parts that are to be coated are heated and the material that is to be deposited is evaporated. The heat causes evaporated particles that come into contact with the surface to chemically react and bond to the surface, creating a thin layer [68].

In the case of chemical etching the silicon has a protective coating applied and then the etching chemical is poured over. The protective coating keeps a small part of the silicon from being removed during the etching process. The cantilevers are produced for AFM applications and thus have a small tip that is perpendicular to the length and width of the beam.

The cantilever has been designed with two features that are intended to help increase the reflectivity of the beam. The cantilever is designed with a trapezoidal cross section. The detection side of the cantilever is wider than the sample side, increasing the surface area that is reflecting the detection laser to the detector. The difference in size is small, $1.4 \mu\text{m}$, compared to the width of the beam [66]. It will be assumed that the tapered edges of the cantilever are small enough that they do not affect the dynamics of the cantilever and thus this will be ignored.



Figure 6.2: Cross-sectional schematic of cantilever. The cantilevers are manufactured such that they are slightly wider at the top where the detection laser is reflected off as compared to the sample side. This causes an increase of up to 30% of the reflecting surface, increasing the amount of the incident beam that is reflected toward the detector.

The detection side of the cantilever is also coated with gold, approximately 35 nm thick, to increase the reflectivity. The coating is applied using sputtering or evaporation. This process can be difficult to control and as a result the thickness and dispersion across the

cantilever cannot be known precisely. The coating is either gold [69] or PtIr5 [70], both of which have a higher density than the silicon that the cantilever is made of. As a result this coating has a notable effect on the density of the cantilever and must be accounted for. It will be assumed that the total thickness of the coating is thin enough that it will have no effect on the elastic properties of the cantilever despite it increasing the density of the cantilever.

The coating is very thin compared to the thickness of the cantilever, however, gold is over 8x denser than silicon and can affect the cantilever's dynamics. Equation (2.41) shows that the resonance frequency of the cantilever is proportional to $\mu^{-1/2}$. The density of the cantilever can be calculated using the density, ρ_{Si} , and thickness, h_{Si} of the silicon and the density, $\rho_{coating}$, and thickness, $h_{coating}$, of the coating as

$$\rho = \frac{\rho_{Si}h_{Si} + \rho_{coating}h_{coating}}{h_{Si} + h_{coating}}. \quad (6.1)$$

6.3.1 Ideal and Guaranteed Dimensions

The process that is used to produce the cantilevers is largely proprietary and thus this information is not shared with consumers. However, from the data sheets for the cantilevers and a NanoWorld brochure [71] some information about the general construction and guaranteed values can be determined.

Table 6.1: Manufacturer specified values for the 225 μm and 500 μm cantilevers.

	225 μm Cantilever		500 μm Cantilever	
	Ideal Value	Guaranteed Range	Ideal Value	Guaranteed Range
Length [μm]	225	220-230	500	495-505
Width [μm]	28	22.5-32.5	100	95-105
Thickness [μm]	3.0	2.5-3.5	1.0	0.5-2.5
Resonant Frequency [krad s^{-1}]	471	364-609	38	19-88
Force Constant [Nm^{-1}]	2.8	1.2-5.5	0.03	0.004-0.54

The first cantilever that will be discussed here will be referred to as the 500 μm cantilever [69]. This cantilever is made from highly doped, single crystal silicon, and has ideal values for the length of 500 μm , a width of 100 μm and a thickness of 1.0 μm ; see Table 6.1 for guaranteed values. This cantilever comes from the NanoWorld Arrow series and as a result it has a triangular tip that is intended to help position the tip over the area of interest for AFM experiments. This feature is not beneficial for this work as the model that will be developed to describe the motion of the cantilever will use the assumption that the cantilever is rectangular in nature with an abrupt tip. It will be assumed that this pointed tip has a trivial affect as the length of the cantilever is relatively large when compared to the short portion which is affected at the very end of the beam. The arrow tip affects approximately the last 10% of the beam where bending moments will be found to be very small compared to the rest of the beam.

The second cantilever [70], also made from single crystal silicon, will be referred to as the 225 μm cantilever. The ideal values for this beam are 225 μm for the length, 28 μm for the width and 3.0 μm for the thickness, see Table 6.1 for the guaranteed values. This



Figure 6.3: Zoomed in photograph of the 500 μm cantilever. This image shows the pointed tip which causes the last 10% of the tip to deviate from the expected rectangular shape.

cantilever is not part of the Arrow series and does not have a pointed tip at the end of the beam. It does, however, share the same trapezoidal cross section and have a coating, 25 nm PtIr5 coating in this case. The PtIr5 coating increases the reflectivity of the beam and it also makes electrical measurements a possibility; one that will not be explored in this work. The same assumptions that were made for the 500 μm cantilever for the trapezoidal shape and coating will be made for the 225 μm cantilever as well.

The resonance frequency of the 225 μm cantilever is expected to be 471 krad s^{-1} while the 500 μm cantilever is only 38 krad s^{-1} . This is due to the 225 μm cantilever being over 2x shorter, 3x thicker and having a spring constant nearly 100x larger than that of its 500 μm counter part.

6.3.2 Variation of Dimensions

This section investigates the effects of the dimensions of the cantilever on the resonant peak and the low frequency noise. The effects for both the 500 μm and the 225 μm can-

tilever will be considered here for the varied length, and thickness and width values for the manufacturer's guaranteed range (see Table 6.1). The analysis will assume that the fluid that each cantilever is subjected to remains a constant for all cases.

Let us start with the resonance frequency. The resonance frequency for the n^{th} mode can be solved by substituting Eq. (2.36) into a result for a rectangle beam in a fluid from Lindholm et al. [72],

$$\frac{\omega_{vac,n}}{\omega_{R,n}} = \left(1 + \frac{\pi\rho_f b}{4\rho_{cant} h} \right)^{1/2} \quad (6.2)$$

to find

$$\omega_{R,n} = \frac{C_n^2}{l^2} \sqrt{\frac{EI}{\mu}} \left(1 + \frac{\pi\rho_f b}{4\rho_{cant} h} \right)^{-1/2}. \quad (6.3)$$

The resonant frequency can be solved in terms of the cantilevers dimensions by using the area moment of inertia for a rectangle, $I = bh^3/12$, to obtain

$$\begin{aligned} \omega_0 &= \frac{C_1^2}{l^2} \sqrt{\frac{Ebh^3}{12\mu}} \left(1 + \frac{\pi\rho_{fluid} b}{4\rho_{cant} h} \right)^{-1/2} \\ &\propto \frac{\sqrt{bh^3}}{l^2}, \end{aligned} \quad (6.4)$$

where the final proportionality can be made as the term in brackets is on the order of 1. From this result, since all dimensional values are less than 1, the resonant frequency is dominated by an $O(l^{-2})$ term, and is influenced by an $O(h^{3/2})$ term while a variation of the width of the cantilever has a very small effect.

Figures 6.4 and 6.5 show the thermal NASD for the 500 μm and 225 μm cantilevers, respectively, if the dimensions are allowed to vary across the guaranteed range. For each of the figures, the results of varying the width, length and thickness of the cantilever across the guaranteed range are shown in the top, middle and bottom plots respectively. The width of the beam was found to have a minimal effect on the resonance peak of the cantilever. The lowest resonant frequency was found to occur when the cantilever was its either its

thinnest or its longest possible value. In both cases it can be seen that since the thickness of the cantilever is so small compared to the other dimensions, a 1-2 μm change causes a much larger shift in the resonance frequency. Due to the models increased sensitivity to this parameter it is treated as the primary dimension. The length and width of the cantilever are considered ideal and for the purposes of the model these two dimensions are given their ideal values. Section 5.5 derived a result that allows the thickness of the cantilever to be calculated based on some measured or fitted values and the width. The advantage of this method to determine the cantilever's thickness is its dependence only on width, the value that affects the resonance frequency the least, and is independent of the length.

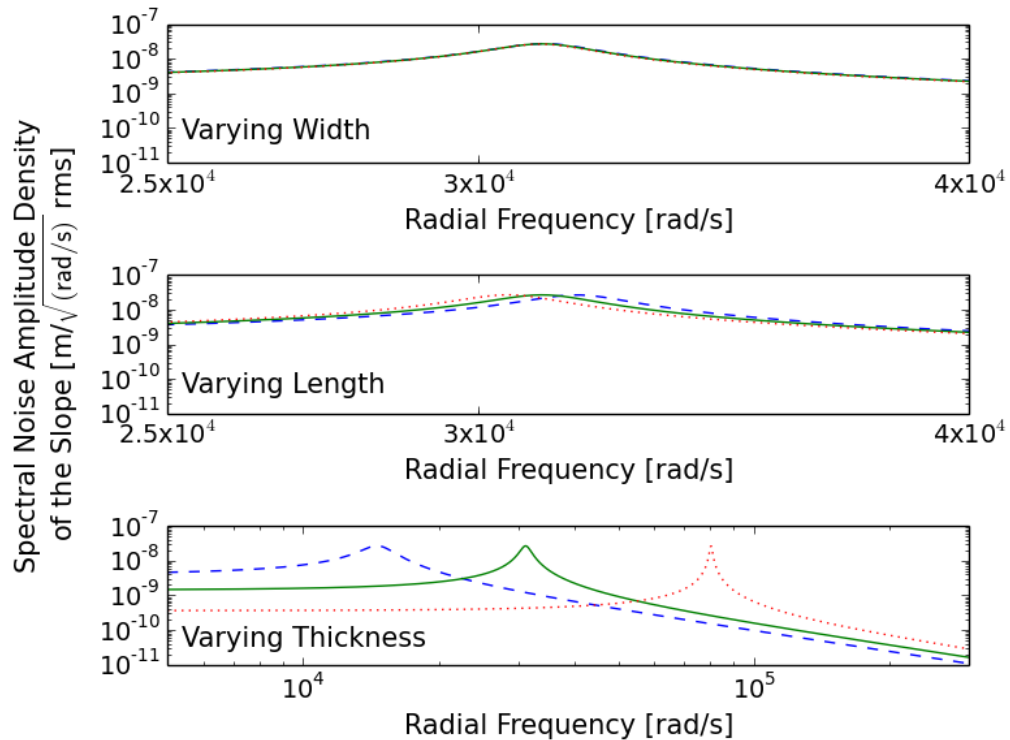


Figure 6.4: EBBE model results demonstrating the effects of varying the 500 μm cantilever's dimension on the fundamental resonant peak. Each subplot varies a different dimension as labelled on the subplot. The blue dashed line corresponds to the minimum guaranteed value, the solid green line is the ideal value and the red dotted line is the maximum guaranteed value. All values are based on Tab. 6.1.

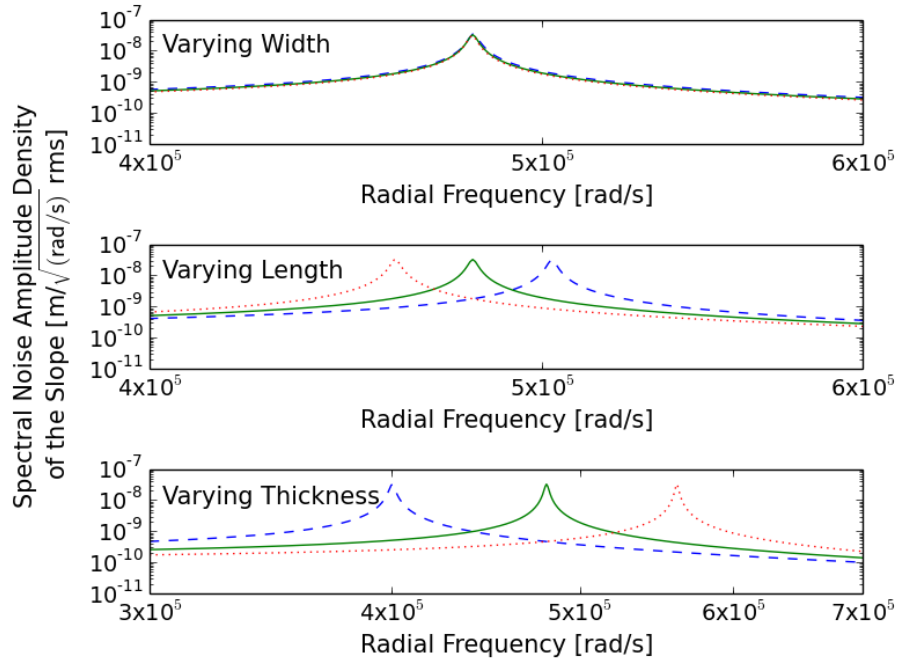


Figure 6.5: EBBE model results demonstrating the effects of varying the $225 \mu\text{m}$ cantilever's dimension on the fundamental resonant peak. Each subplot varies a different dimension as labelled on the subplot. The blue dashed line corresponds to the minimum guaranteed value, the solid green line is the ideal value and the red dotted line is the maximum guaranteed value. All values are based on Tab. 6.1.

The choice of cantilever for the future MOND experiment is highly dependent on the performance of the cantilever at very low frequencies, specifically low noise is best. Based on the previous analysis it can be determined that a thicker cantilever will have a resonance frequency that is shifted to higher frequencies. Due to the higher resonance frequency there can be significantly less noise at low frequencies. The $500 \mu\text{m}$ cantilever is an extreme example of this as the predicted noise for the low versus high resonance frequency is an order of magnitude larger. The $225 \mu\text{m}$ cantilever significantly out performs the $500 \mu\text{m}$ cantilever at low frequency noise levels thanks to the very high resonance frequency due to its increased thickness.

6.4 Detector

The detector uses a circular quadrant photo-diode array and has three different outputs. The first is the sum output which provides information about the total incident power striking the detector. The other two work on the same principle as each other. These outputs use a difference calculation based on a hemisphere on one side minus the other, either the top and bottom or left and right. The left minus right output is used for experiments and is referred to as the difference output.

The sum output is used to obtain a constant required for the detector model and contributes to determining the voltage to displacement conversion factor. The sum value is measured with a multimeter once at the beginning of the experiment and is assumed to be constant.

The Voltage To Displacement (VTD) conversion factor, C_{uv} with units of V/m, is the change of the difference output as a result of the laser shifting from one side to the other. The motion of the cantilever causes the laser to move back and forth between the left and right sides of the detector. All experiments that measure the cantilever motion use the LIA connected to the difference output.

The detector is composed of two different parts. First there is the circular silicon surface that is separated into four quadrants and outputs some voltage based on the total incident light striking each individual quadrant. The laser is aimed directly at this surface. The second component is the circuitry. There are three distinct circuits that determine the three outputs: sum total off all the quadrants, the difference between the left two quadrants versus the right two quadrants and, the difference between the top quadrants and the bottom quadrants. The two circuits dealing with the difference calculation use differential amplifiers for this calculation.

For simplicity let us consider the differential amplifier alone. It has two inputs, V_r and V_l , and a single difference output, V_d . The output is easily calculated as it is simply a difference, that is $V_d = V_r - V_l$. In the case where both inputs of the amplifier are increased

or decreased by a uniform amount, V_c , the new values for V_r and V_l will become $V_r + V_c$ and $V_l + V_c$ respectively. Substituting these values into the equation for V_d , it can be found that V_d does not change when both V_r and V_l are changed uniformly. A similar situation can also be considered where V_r and V_l are changed by some amount that is not equal for both inputs. Let V_r be increased by some value V_c to become $V_r + V_c$ while V_l is increased by some fraction, f , of V_c to be $V_l + fV_c$. In this case the output of the differential amplifier will be $V_d = V_r - V_l + (1 - f)V_c$. In the case where $f = 1$ it is clear that this result reduces to that where V_r and V_l are increased uniformly.

The following discussion will use the silicon surface of the detector as the voltage source which has an output that is directly proportional to the amount of incident light striking it. The left-minus-right circuit of the detector works by subtracting the output of the left hemisphere from the right hemisphere. If we call the voltage from the right hemisphere V_r and the voltage from the left hemisphere V_l we find that the output of the difference amplifier is $V_d = V_r - V_l$; the same result as found in the previous discussion.

If the laser is aimed such that there is an equal amount of light striking the left and right hemispheres of the detector it will be found that $V_r = V_l$. The output of the laser is not perfectly constant, it has noise. Let us assume that this noise causes the laser's output to vary by some factor that is constant across the entire beam. The noise will cause an equal increase of intensity on both hemispheres. From the previous discussion it was found that the output of the differential amplifier does not change in this case. However, if the laser is shifted over to the right hand hemisphere it will be found that $V_r > V_l$ and the variance of V_r will be greater than that of V_l . Noise that occurs equally at V_r and V_l is referred to as common mode noise. Due to how differential amplifiers work, they are capable of significantly reducing common mode noise. As a result of the concepts introduced here it is expected that the laser noise will reach a minimum value when $V_r = V_l$ and progressively increase to a maximum as the laser is shifted off center to one side or the other.

6.5 Detection Laser

The detection laser is a 635 nm low noise laser used to measure the motion of the cantilever and is powered by a constant voltage. The laser is passed down a fibre optic cable to a lens with a focal length of approximately 3.5 cm. The free end of the cantilever is placed at the focal point to maximize the intensity of light reflected to the detector. The detector has an amplifier which makes possible sensitive measurements but as a result issues of saturating occurred at very low laser power levels. In an effort to avoid saturation, the detection laser had to be at a minimal power level, so low its output was unstable causing measurement issues and excess noise. An optical filter was added between the fiber optic cable lens and the cantilever. This allowed the laser to be run at a higher, stable power level while reducing saturation.

The detection laser is aimed at the cantilever at an angle of incidence around 25° . This laser must be aimed at the cantilever at some angle of incidence for two reasons. First, the reflected beam from the laser must strike the detector to make a measurement. The laser and detector take up physical space and thus must be spread out. The angle that is used is intended to be as shallow as possible as the beam from the laser has a non-trivial diameter. If the angle of the laser is too large then the beam becomes “smeared out” across the cantilever and reduces the laser’s ability to illuminate a very small region of the beam. The second reason that the angle of incidence is beneficial is that this causes the detector to not be directly inline with the driving laser. A filter is placed in front of the detector to help block light from the driving laser. However, by having the detector off the axis of the driving laser beam, less of the driving laser’s intensity will influence the detectors output.

When the cantilever is deflected the angle of incidence increases or decreases depending on the direction of deflection. Due to the fact that the reflecting surface, the cantilever, is what moves, the change of the angle of reflection is twice the change of angle of incidence. This proves beneficial as it increases the laser’s displacement across the detector and improves the signal strength.

6.6 Driving Laser

The laser that drives the motion of the cantilever is a 405 nm laser diode and is not intended to directly influence the detector. The laser requires both an AC and DC signal for it to have a smooth and linear response to a varying voltage powering it. The DC signal causes the laser diode to have a constant power output in a power region that is known to have a linear response to the supply voltage. The AC component causes the power to vary and drive the cantilever's motion. An optical filter was added in front of the detector in an effort to keep this laser diode from influencing the detectors output. The filter allows approximately 87% of the detection laser to pass while nearly completely blocking the driving laser.

The driving laser beam is aimed such that it is nearly orthogonal with the cantilever's surface. The force due to the laser is proportional to $\cos^2(\theta)$ where θ is the angle of incidence. Since the derivative of $\cos^2(\theta) \rightarrow 0$ as $\theta \rightarrow 0$, aligning the laser orthogonal to the cantilever's surface maximizes the force the laser applies to the cantilever while minimizing the error caused if θ is varied.

The alignment procedure is intended to minimize θ while not actually making it zero. The laser is reflected off the cantilever and a piece of paper is used to find the reflected beam. The laser is then moved to cause the reflected beam to be nearly anti-parallel to the incident beam. There is a small angle of incidence, about 5° , that is maintained to avoid optical feedback at the diode.

The experiments that require the cantilever to be driven by the laser have shown that the laser over drives the cantilever causing the acceleration levels of the cantilever to be well outside of the MOND regime. To lower the acceleration levels of the cantilever the power of the laser must be reduced. This cannot be done sufficiently with the power supply used. Two methods have been employed to help with this issue. The first is the addition of an optical filter to reduce the intensity at the cantilever. The second method involved de-focusing the laser causing the total power of the laser to be spread out over an area of

approximately 1 cm^2 . This was beneficial for two reasons. Given the small size of the cantilever compared to the beam diameter and the reduced peak intensity, the total driving force of the laser was significantly reduced. Also, the mathematical model that is used to describe the motion of the cantilever as a result of the driving laser assumes that the power of the laser is uniform across the entire length of the cantilever. The driving laser's profile is Gaussian in nature; however, by increasing the beam diameter the value for sigma describing the profile was also increased causing a smaller variation across the length of the cantilever.

6.7 Equipment Mounts

The cantilever, detector and lasers were all mounted to a mounting plate. While this was very tight, it was found that this was possible to fit all the required equipment on this plate. It was later determined that this was not a viable option as it held the driving laser too close to the cantilever. The previous section discussed the need to pull the driving laser away from the cantilever to reduce the total driving force. To solve this issue a second plate was used to extend the mounting space and the driving laser was then moved. One of the spare C-holders was used to hold the two plates together such that the driving laser could not shift out of alignment.

The cantilever resides on a 3D printed prism that has a small notch for the base of the cantilever to seat into. It is held in place using a small strip of metal that is pressed down onto the cantilever using a spring. The prism is then set onto a Newport ULTIMA Gimbaled Three-Axis Optic Tilt Mount. This mount has a flat plate top with a single pillar and arm to hold prisms in place. To help reduce the alignment time a small guide plate was 3D printed. The guide plate had a triangular section cut out that the prism could be set into, thus forcing the cantilever to occupy nearly the same position relative to the equipment after it had been removed and placed back in. In general the cantilever would not be pulled out of the equipment until after the full gamut of experiments had been performed. However,

when a set of experiments were complete and it was time to work with a different cantilever, the cantilever could be swapped out for a second one in the prism and the prism set into the guide plate. The time required to correct the alignment for a second cantilever was reduced from potentially hours to a more common couple of minutes.

The pumping cavity and enclosure for the detection laser is located away from the experimental equipment and then the beam is transferred to the where it is required by a fibre optic cable. The fibre optic cable has a non-adjustable lens at the end. The only adjustment that can be made was via the mount used to hold the end of the fibre optic cable in position. The mount has screws that position the mount by pressing into the back of it. This allows the alignment of the laser to be adjusted both left/right or up/down. Due to the fixed lens the focal length of the laser cannot be changed. It was found that the focal point was at approximately 3.5 cm and thus the laser mount was bolted to the mounting plate at approximately this distance away from the cantilever. The position of the laser was moved until the focal point was as close as possible to the cantilever and then the screws on the plate holding the laser itself were adjusted to obtain a good alignment.

Using the original equipment setup that used only the one mounting plate, it was determined that a stand for the filters would be required that would hold the filters very close to the cantilever due to the cramped space between the two lasers and the cantilever. With the new system where the driving laser has been moved to a second plate there was more space and the filter for the driving laser could be moved significantly further away allowing space for two filters but this would require cutting up the mount. The filter stand is made out of acrylic that is welded together using acetone. The stand uses a back plate that is slightly sloped with two pegs to hold each filter in place. As a result the filters are not fixed to the stand but rather easily slide off the pegs that hold them in place. This allows filters to be easily changed without affecting any of the other equipment. For the purposes of driving the cantilever, it was found that a single filter did not reduce the intensity of the incident light enough and thus two were required. The space between the filter for the driving laser

and the cantilever is not enough to fit two filters. The first filter had to be hung from the face of the driving laser mount as a slight angle to reduce optical feed back effects while the second was placed on the stand.

The driving laser is a laser diode that is mounted within a Newport LP-05A along with a lens. The laser diode is held rigidly in place while the mount allows the lens to be adjusted in the X, Y and Z directions as well as rotationally about the X and Y directions. This mount also allows the focal length of the beam to be adjusted which proved essential for the driven cantilever experiments. This laser was moved to a second mounting plate to increase the distance between the laser and cantilever to reduce the total incident light from this laser on the cantilever.

The detector was mounted on a linear translation stage. This allowed the detector to be adjusted both vertically and left/right. The vertical alignment was used to adjust the detector such that the laser was aimed at either the lower or upper two quadrants. The detector has a small gap between each quadrant referred to as the “silicon gap” that is 0.2 mm wide. The laser is aligned such that it only strikes one set of quadrants to maximum amount of light incident upon the silicon detector surface maximizing the detectors output. The left/right adjustment was used to shift the detector for making measurements of the VTD conversion factor, a term that was discussed in more depth in section 6.4. The ability of shifting the detector left/right was also beneficial as it allowed the detection point to be moved to different positions along the cantilever. A significant portion of the cantilever was illuminated by the laser and while the detection point is only a thin section of the beam. Figure 6.6 shows a simple alignment. From this diagram it can be seen that as the detector is shifted to one side or the other, the section of the reflected beam that strikes the silicon gap of the detector will be reflected from a different position along the beam. The detector is sensitive to the position of the cantilever that reflects the laser beam that strikes the edges of the silicon gap.

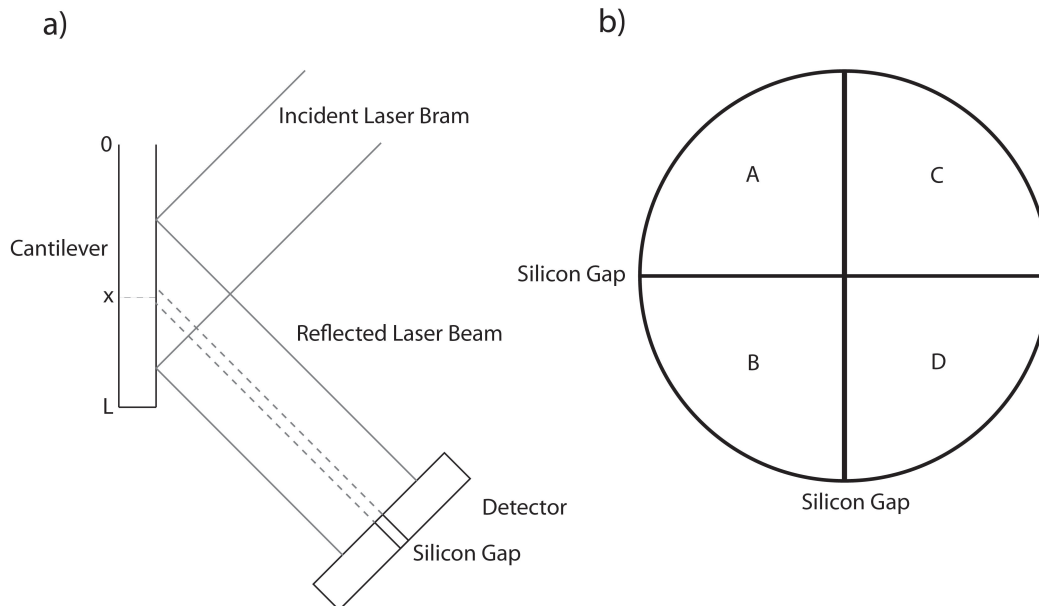


Figure 6.6: a) Diagram demonstrating the silicon gap between quadrants of the detector and its correlation to the detection point at x . As the cantilever moves the reflected beam will shift across the detector. The only portion of the reflected beam that transfers from a quadrant is the portion at the silicon gap. Any portion of the beam that strikes one quadrant and does not leave that quadrant due to laser shifting does not affect the output of the detector. b) Diagram showing the quadrant nature of the detector. Measurements for the displacement of the cantilever are collected from the left-minus-right output or $(A+B)-(C+D)$.

6.8 Lock-In Amplifier

The LIA is connected to the difference output of the detector, making it sensitive to the deflection of the cantilever. The LIA is effective at narrowing the Equivalent Noise Bandwidth (ENBW) that the measurement is dependent on which allows measurements of a small frequency range, reducing the uncertainty. The LIA uses a reference frequency which is provided by either the LIA itself or by some external source. The small frequency range that the measurement is subject to is centered about the reference frequency and determined by the ENBW, a concept to be discussed in subsection 6.8.2.

There are several different features of the lock-in amplifier which help to obtain the lowest SNR possible, albeit with some trade off. To increase the SNR the equivalent noise bandwidth must be reduced, or signals due to harmonics must be attenuated, which re-

quires time and extends the duration required for a statistically independent and accurate measurement.

This section is not an in-depth discussion of the LIA or its features. The discussion here is limited to a couple of features of the LIA that are pertinent to the data acquisition process and the primary interest here is the effect they have on the SNR and time required for measurement. Further discussion about these effects on the potential future MOND experiment will be discussed in chapter 9. The primary source for this discussion is the SR830 Lock-In Amplifier manual [1].

6.8.1 Phase Sensitive Detector

A phase sensitive detector is a linear multiplier used to multiply the reference signal with the input. If the frequency for the reference and signal are ω_{ref} and ω_{sig} respectively, the mathematical operation occurring is

$$\cos(\omega_{ref}) \times \cos(\omega_{sig} + \phi) = \frac{1}{2} [\cos(\omega_{ref} - \omega_{sig} - \phi) + \cos(\omega_{ref} + \omega_{sig} + \phi)] \quad (6.5)$$

where ϕ is the phase difference between the reference and input signals. In the case where $\omega_{ref} = \omega_{sig}$ the output of the phase sensitive detector will include a DC and an AC voltage. Over a significantly long enough duration of time all signals will average out to 0 except for the DC signal. The output of the phase sensitive detector proceeds to the low pass filter which continues the analysis.

The LIA uses two phase sensitive detectors, one with the reference signal directly and the other uses the reference signal with a $\pi/4$ phase shift. This allows the LIA to determine the magnitude and phase of the input signal with respect to the reference signal.

6.8.2 Low Pass Filter

After the phase sensitive detector, the LIA uses a Low Pass Filter (LPF) to reduce the effects of non-DC signals. The LPF is a series of RC type filters which each have a -6 dB/octave roll off. The time constant, τ , determines the cutoff frequency, $\omega_{co}=1/\tau$ rad/s, where the attenuation of the individual RC filters is -3 dB. The LPF can be modelled using the concept of a brick wall filter. Brick wall filters are described by a Heaviside step function with a cut off frequency of ω_{ENBW} ; that is, there is no attenuation of the signal from DC to ω_{ENBW} and then all other frequencies are perfectly blocked. The ENBW of the LPF is defined as the cutoff frequency of a brick wall filter that has the same ENBW as the LPF. Although an actual brick wall filter is not possible and they are used for modelling and conceptual use only, there are some filters that are designed to work like a brick wall filter and a combination of filters can be used to produce similar behaviour.

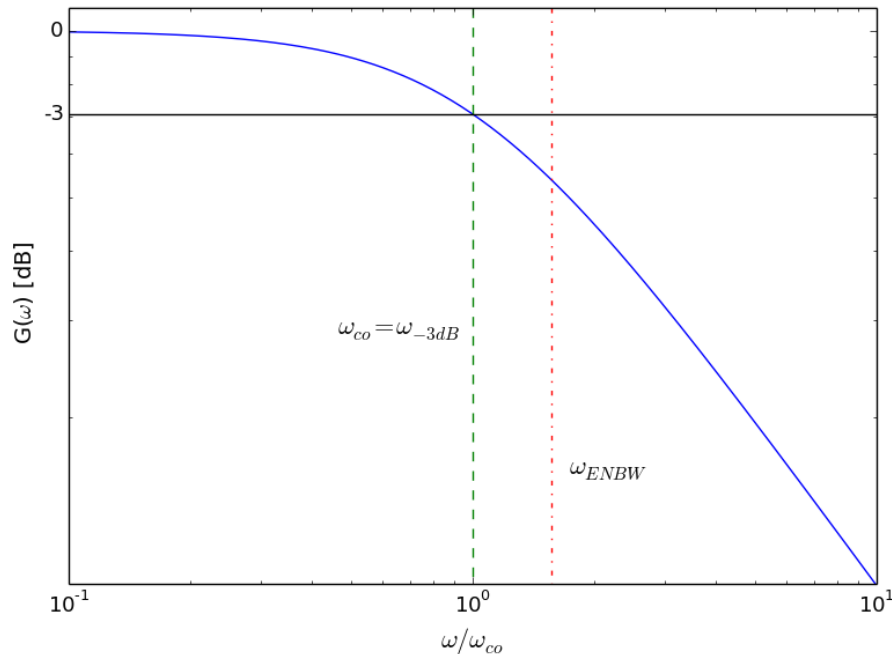


Figure 6.7: Plot showing the response of an arbitrary low pass filter, $G(\omega)$. LPF have minimal attenuation at low frequencies and completely pass DC signals. As the frequency increases the signal becomes attenuated. At the frequency ω_{co} the filter attenuates the signal to -3 dB, symbolized by the green dash line.

Figure 6.7 is a plot of the gain of an arbitrary LPF, $G(\omega)$ as specified by Eq. (6.6). This simple filter allows low frequencies to pass and DC signals to pass completely. As frequencies increase the filter starts to block the signal and at ω_{co} the signal has been attenuated to -3 dB. The ENBW of a brick wall filter, ω_{ENBW} , can be found by integrating $|G^2(\omega)|d\omega$ from $\omega = 0$ to ∞ . A common time constant that will be used for experiments is 0.3 seconds which corresponds to a cutoff frequency of $\simeq 3.33$ rad/s. This relatively short time constant allows data to be obtained quickly. If the 1st order pole filter were used the resulting ω_{ENBW} would be 5.23 rad/s.

The number of RC filters that are used in the LIA's LPF is called the filter pole order. The LIA can use up to four RC filters sequentially which is referred to as a 4th order pole. The use of multiple RC filters in series increases the roll off of the LPF to $-6n$ dB/octave and the attenuation at ω_{co} to $-3n$ dB, where n is the number of RC filters, as demonstrated in Fig. 6.8.

The magnitude of the gain for any given frequency ω across the capacitor of a 1st order pole filter is:

$$\begin{aligned} G(\omega) &= \frac{1}{\sqrt{1 + (\omega\tau)^2}} \\ &= \frac{1}{\sqrt{1 + (\omega/\omega_{co})^2}}. \end{aligned} \tag{6.6}$$

The LPF is used for its gain response alone. Its effect on the phase of the signal is not relevant. Any phase change that the LPF may have at this point does not affect the output of the LIA. The ENBW for the LPF is equal to the integral across all frequencies of the magnitude of the gain squared. This is solved by using the substitution $\omega/\omega_{co} = \tan(x)$. For higher order poles the ENBW for any given frequency is the magnitude of the gain of a 1st-order pole filter to the power of $2n$, assuming all filters have the same ω_{co} . The generic integral in this case is

$$\begin{aligned}
 ENBW &= \int_0^{\infty} |G(\omega)|^{2n} d\omega \\
 &= \omega_{co} \int_0^{\pi/2} \cos^{2n-2}(x) dx.
 \end{aligned} \tag{6.7}$$

In the case of a 1st-order-pole filter the $\cos^{2n-2}(x)$ term equals 1 and the integral is easily solved to obtain $\pi/2\tau$. For the higher order poles this integral can be solved by using

$$\int \cos^m(x) dx = \frac{1}{m} \sin(x) \cos^{m-1}(x) + \frac{m-1}{m} \int \cos^{m-2} dx. \tag{6.8}$$

Since m in this case will always be an even number, all terms will either be dependent on a $\sin(x) \cos^{m-1}(x)$ term or will be some factor times $\int dx$ which, for these limits, evaluates to $\pi/2$. The $\sin(x) \cos^{m-1}(x)$ term when evaluated between 0 and $\pi/2$ will always be 0. The result of the integral will be a constant times $\pi/2$. This constant can be solved as a product of terms for a n^{th} order filter pole. As a result, the ENBW for any n^{th} order-pole, where $n > 1$, is:

$$\begin{aligned}
 ENBW &= \omega_{co} \frac{\pi}{2} \prod_{r=1}^{n-1} \frac{2r-1}{2r} \\
 &= \frac{\pi}{2\tau} \prod_{r=1}^{n-1} \frac{2r-1}{2r}.
 \end{aligned} \tag{6.9}$$

Increasing the time constant or the filter pole order of the LPF will cause a reduction of the ENBW, each by their own way. Increasing the time constant lowers the cutoff frequency for each filter while adding increasing the filter pole order increases the attenuation of higher frequency signals. These have the effect of reducing the ENBW which reduces noise and variation of the LIA's output signal. However, increasing τ and the filter pole order causes the LPF to respond slower to input changes and as a result a longer duration of time is required for the LIA to reach 99% of the final value, this is referred to as the wait time.

Table 6.2: Equivalent noise bandwidth and required wait time based on the filter pole order and time constant, τ [s] [1].

Filter Pole Order	ENBW [rad/s]	Wait Time [s]
1	$2\pi/(4\tau)$	5τ
2	$2\pi/(8\tau)$	7τ
3	$6\pi/(32\tau)$	9τ
4	$10\pi/(64\tau)$	10τ

The use of higher order poles and longer time constants helps to reduce the ENBW at the expense of wait times. Short time constants are beneficial in situations where the experiment can not be run for extended durations of time. There is a penalty to pay beyond increased uncertainty in measurements for short time constants. Due to ω_{co} being relatively large, the LIA becomes sensitive to 2^{nd} harmonic noise at higher frequencies. The output of the phase sensitive detector includes a non-trivial signal at harmonics of the reference signal. The most troublesome of these signals is that at $2\omega_{ref}$ which can equal or exceed the magnitude of the desired DC component depending on the phase. If the time constant is too short the $2\omega_{ref}$ component will not be attenuated significantly, causing it to influence the final output of the LIA.

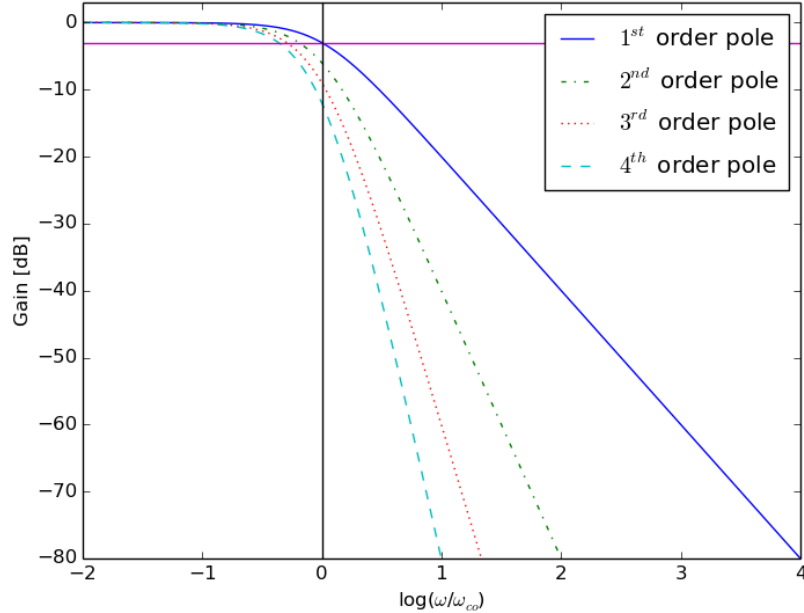


Figure 6.8: Theoretical low pass filter gain for multiple pole orders. The purple line corresponds to -3 dB.

6.8.3 Synchronous Filters

The synchronous filter, sync filter, can be used to solve the issue of harmonic noise. The sync filter calculates the average of the output of the second RC filter over the period of the reference signal, this average is updated 128 times over the period and then used as the input for the third RC filter. This process does not attenuate broadband noise in general, it only works as a notch filter for the harmonics of the reference frequency. As the sync filter performs averaging over one period of the reference signal this process adds $2\pi/\omega_{ref}$ seconds to the wait time.

6.8.4 Lock-In Amplifier Output Channels

The LIA has multiple different values that it can provide but there are only two pertinent here, the X and R values. The R output is the magnitude of the signal without dependence on the phase difference between the source and reference signal. The phase of noise is random and for pure noise measurements we are only interested in the magnitude, thus noise

measurements are made from the R output. The X-output of the LIA gives the magnitude of the signal that is in phase with the reference signal. For the acceleration experiments an AC signal is used to power a laser to drive the motion of the cantilever. The signal that is used to power the laser is used as the reference signal and the cantilever's motion is measured based on the X-output. This allows the motion of the cantilever, which is expected to be in phase with the driving force, to be accurately measured while reducing the uncertainty in the measurement as noise is unlikely to be in phase with the reference signal.

6.9 Conclusion

This chapter has given a brief outline of how the pertinent components of the equipment operate. The discussion started by providing an understanding of how the equipment was oriented and will interact with the cantilever to either drive or detect its motion. This discussion also provides the reasoning behind the decisions of how the equipment would be setup, either for alignment ease or fidelity of measurement.

The LIA was also considered, with its process broken down to the effect of the individual components. The intent was to help the reader understand how the LIA reduces the bandwidth of measurements to increase the SNR and the concept of the required wait time. A derivation was provided where possible to establish a theoretical basis for the components. The theory also helps to shed light on how noise from harmonic frequencies of the reference frequency can be introduced if the time constant is too short, the resulting effect of the harmonic frequencies and the process to remove them.

Chapter 7

Response Analysis

7.1 Overview

This chapter derives several different results related to the detector and the model describing the LIA's output, and also the two calculation processes that are used for the bulk of the future analysis. The model describing the detector's output is based predominantly upon the properties of the laser beam and the detector itself, with little concern for how the LIA works. The functionality of important components of the LIA was covered in Ch. 6 and is not required here. The final result that is obtained is a simple relation that incorporates the ENBW model, the geometry of the equipment and a factor describing the detector's response to the shifting of the laser beam between the left and right side.

The analysis sections derive the relations between the cantilever's motion and the LIA's three outputs to obtain the cantilever's noise, as well as the relation between the LIA's raw output to obtain the cantilever's acceleration. The cantilever's noise will be used in a later chapter to determine which cantilevers produce the least amount of noise. The acceleration analysis will be used to determine the acceleration of the cantilever as a result of some driving force. Both of these results will be used to determine which cantilevers and frequency ranges are the ideal candidates for the potential MOND experiment.

7.2 Detector Output Model

We have a model that describes the motion of the cantilever as a result of thermal energy. The next step is to develop a model that will describe what the output of the lock-in amplifier

will be as a result of a laser reflecting off the cantilever. In order to simplify the problem the system will be considered in two dimensions, the property of height will not be included. With the exception of the laser, the entire system has symmetry from top to bottom. The detector is outputting a left minus right difference and the response will be the same across its height, as a result only the motion of the cantilever along its length is considered and any torsion of the cantilever is wholly ignored. The incident laser for this experiment has a 2D-Gaussian profile. However, it will be assumed that the variance across the cantilever's height is small such that the profile can be considered constant across the cantilever's height and only varying along its length.

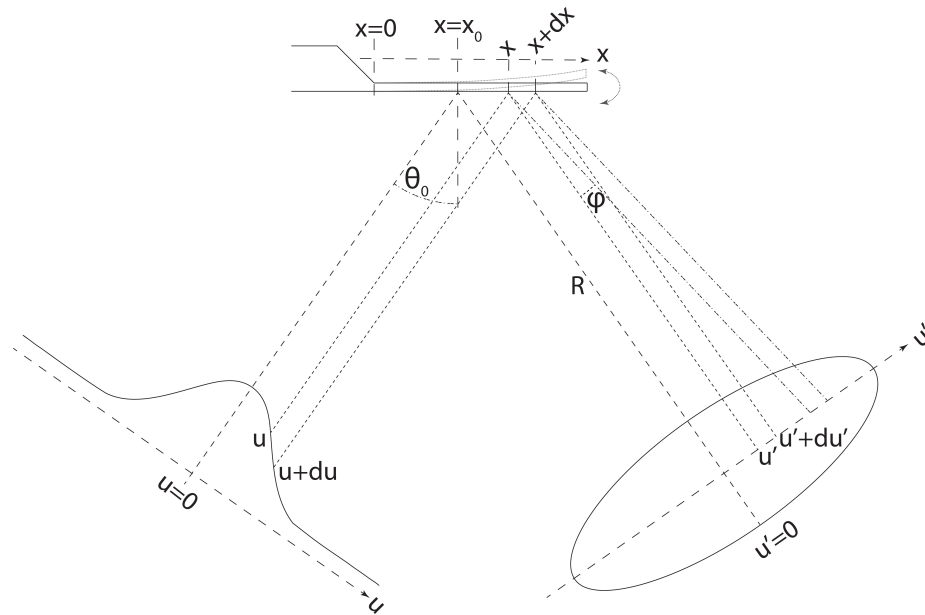


Figure 7.1: A schematic diagram showing the geometry and the various coordinate systems being employed. The u -coordinate system describes the incident beam, the x -coordinate system describes the cantilever and finally the u' -coordinate system describes the detector surface. θ_0 is the angle between the norm of the cantilever and the incident beam or the norm of the detector. ϕ is equal to the angle of deflection caused by the motion of the cantilever bending from center.

As can be seen in figure 7.1 there are three different coordinate systems in use. The x -coordinate system is used to describe the position along the cantilever with $x = 0$ defined as the point where the cantilever starts at the main body and x_0 is the point where a ray

from $u = 0$ will strike. This is referred to as the detection point and it is this point that the detector is sensitive to. The u -coordinate system is used to describe the incident laser profile before striking the cantilever and $u = 0$ is located in the center of the laser beam. Finally, the u' -coordinate system describes the position across the detector where $u' = 0$ is located at the dividing line separating the left and right quadrants of the cantilever. The angle from the normal of the x -coordinate system to the normal of the u - or u' -coordinate systems is defined to be θ_0 . The u' -coordinate system is defined in such a manner that if the cantilever were a flat, stationary mirror then any ray that is emitted from the laser at the position u would strike the detector at $u' = u$. The real cantilever will have motion that causes an incident ray emitted at u to be reflected to the position $u' + du'$ on the detector.

The relation between the x - and u -coordinate systems and the resulting differential relation are

$$x = x_0 + \frac{u}{\cos(\theta_0)} \quad (7.1)$$

and

$$dx = \frac{du}{\cos(\theta_0)}. \quad (7.2)$$

The incident laser beam is described by the optical power profile function $P_{inc}(u)$. As a practical example this model will be developed using a laser with a Gaussian profile, specifically

$$P_{inc}(u) = P_0 G_{beam}(u) \quad (7.3)$$

where

$$G_{beam}(u) = \frac{1}{\sqrt{2\pi\sigma_{beam}^2}} \exp\left(\frac{-u^2}{2\sigma_{beam}^2}\right) \quad (7.4)$$

and σ_{beam} describes the standard deviation of the laser profile across u .

The laser profile that strikes the detector itself is $P_{det}(u')$ and in the special case where the cantilever is a flat, stationary mirror we expect $P_{det}(u')du' = P_{inc}(u')du'$, where $u = u'$, as a result of how the three coordinate systems are defined.

The position of the cantilever as a function of time is given by Eq. (3.95),

$$w(x, t) = \sum_{n=1}^{\infty} h_n(t) \phi_n(x) \quad (7.5)$$

where ϕ is defined by Eq. (2.42) for the cantilever or Eq. (2.55) for the bridge beam and $h_n(t)$ is the inverse Fourier transform of $\hat{F}_n(\omega) \alpha_n(\omega)$. The ensemble average of $h_n^2(t)$ can be found using the Plancherel theorem [73] and was determined in a previous section, Eq. (3.114), these two results are

$$\langle h_n^2(t) \rangle = \frac{1}{2\pi} \int_{-\infty}^{\infty} |\hat{F}_n(\omega)|^2 |\alpha_n(\omega)|^2 d\omega = \frac{3k_B T}{kC_n^4}. \quad (7.6)$$

While $h_n(t)$ follows the Gaussian probability distribution:

$$P(h_n(t)) = \frac{1}{\sqrt{2\pi\sigma_{full, n}^2}} \exp\left(\frac{-h_n^2(t)}{2\sigma_{full, n}^2}\right), \quad (7.7)$$

where

$$\sigma_{full, n}^2 = \frac{3k_B T}{kC_n^4} = \langle h_n^2(t) \rangle, \quad (7.8)$$

k_B is Boltzmann's constant, T is the cantilever's temperature in Kelvin, and k is the spring constant for the cantilever.

The value that the lock-in amplifier returns is not the result across all frequencies. The lock-in amplifier is only sensitive to a narrow bandwidth of frequencies. Let us assume that a brick-wall filter is used which allows the frequencies from ω' to $\omega' + \Delta\omega'$ with bandwidth $\Delta\omega'$. The probability of the value $h_n(t)$ can be determined using Eq. (7.7) where $\sigma_{full, n}^2$ is

replaced by

$$\begin{aligned}\sigma_{cant,n}^2 &= \frac{1}{2\pi} \int_{\omega'}^{\omega'+\Delta\omega'} |\hat{F}(\omega)|_s^2 |\alpha_n(\omega)|^2 d\omega \\ &\simeq \langle h_n^2(t) \rangle \Delta\omega' = \frac{3k_B T}{kC_n^4} \Delta\omega'.\end{aligned}\quad (7.9)$$

Next we need to introduce the motion of the cantilever. The position of the cantilever is described by $w(x,t)$ and the slope of the cantilever is

$$q(x,t) = \frac{\partial w(x,t)}{\partial x}.\quad (7.10)$$

The actual displacement and angle of the cantilever is very small and as a result we can employ the small angle approximation. A ray which is emitted from the point u will strike the detector at

$$\begin{aligned}u'(t) &= u + 2R \left. \frac{\partial w(x,t)}{\partial x} \right|_{x=x_0+u/\cos(\theta_0)} \\ &= u + 2Rq(x,t) \Big|_{x=x_0+u/\cos(\theta_0)}.\end{aligned}\quad (7.11)$$

Likewise, a ray starting out at $u + du$ will then strike the detector at

$$u'(t) + du' = u + du + 2Rq(x,t) \Big|_{x=x_0+(u+du)/\cos(\theta_0)}.\quad (7.12)$$

The relation between du and du' can be found by subtracting equation (7.11) from (7.12) to obtain

$$du' = du + du \frac{2R}{\cos(\theta_0)} \left. \frac{\partial q(x,t)}{\partial x} \right|_{x=x_0+u/\cos(\theta_0)}.\quad (7.13)$$

Since the total deflection of the beam is very small it can be said that

$$du' \approx du.\quad (7.14)$$

A ray that is emitted at some time t and position u will, as a result of the cantilever's motion, strike the detector at

$$u'(t) = u(t) + 2R \sum_{n=1}^{\infty} h_n(t) \left. \frac{\partial \phi_n(x)}{\partial x} \right|_{x=x_0+u/\cos(\theta_0)}. \quad (7.15)$$

This is the point where the detector and its response starts to become of fundamental importance. There are two constants that are required to describe this response. For the first constant lets consider the sum output on the detector. If there is an incident beam on the detector with some constant power then the sum output will output a constant voltage. The relation between the incident power and the sum output is linear in nature and related by the factor C_{pv} , that is

$$V_0 = C_{pv}P_0. \quad (7.16)$$

This constant can be determined through the use of semi-conductor physics and an understanding of the circuitry of the detector itself. However, for simplicity this constant factor can be determined experimentally by aiming a laser at the detector and recording the sum output voltage as the laser power changes.

The second factor is related to the first but it deals with the difference output instead. As a laser with constant power shifts from the one side of the detector to the other the left-minus-right output, also referred to as the difference output, will also change in voltage. For short distances, $\sim 0.25\text{mm}$ either way from center for the laser used in this experiment, the relation between the distance traversed to change in voltage is approximately linear, as shown in section 8.3, and proportional to the constant C_{uv} .

Using the first factor we can determine the output of the detector by the use of

$$V_{diff} = C_{pv} \left(\int_{-\infty}^0 P_{det}(u') du' - \int_0^{\infty} P_{det}(u') du' \right). \quad (7.17)$$

The detector does not follow what individual rays across its width are doing. Instead it

gives a value based on what is happening at $u' = 0$, the boundary between the two sides. That is to say, the output of the detector is not based on $-\infty$ to ∞ but some narrow $2\Delta u'$ centred at $u' = 0$. $\Delta u'$ is the distance the laser can shift due to the cantilever's deflection from center and it is a function of time since the cantilever's position changes with time. If $\Delta u'(t) \ll \sigma_{beam}$ then this can be restated as

$$\begin{aligned} V_{diff}(t) &\simeq C_{pv}2\Delta u'(t)P_{det}(0) \\ &= 4RC_{pv}P_0G_{beam}(0) \sum_{n=1}^{\infty} h_n(t) \frac{\partial \phi_n(x)}{\partial x} \Big|_{x=x_0}. \end{aligned} \quad (7.18)$$

From equation 7.18 it can be seen that the dependence of V_{diff} on $h_n(t)$ is linear and as a result since $\langle h_n(t) \rangle = 0$ then $\langle V_{diff,n}(x,t) \rangle = 0$. The LIA measures the Root Mean Square (RMS) value of a signal over time, and since $\langle h_n^2(t) \rangle \neq 0$, then $\langle V_{diff,n}(x,t) \rangle \neq 0$ as well. For a signal across the bandwidth ω' to $\omega' + \Delta\omega'$, the expectation voltage squared is

$$\langle V_{diff,n}^2 \rangle = \left(4RC_{pv}P_0G_{beam}(0) \frac{\partial \phi_n(x)}{\partial x} \right)^2 \langle h_n^2(t) \rangle_{\Delta\omega'} \quad (7.19)$$

where

$$\langle h_n^2(t) \rangle_{\Delta\omega} = \sigma_{cant}^2 = \frac{3k_B T}{kC_n^4} \Delta\omega'. \quad (7.20)$$

In order to obtain the output value of the lock-in amplifier across all modes a sum must be taken across n , mathematically

$$\begin{aligned} \langle V_{diff}^2 \rangle &= \sum_{n=1}^{\infty} \langle V_{diff,n}^2 \rangle \\ &= \sum_{n=1}^{\infty} \left[4RC_{pv}P_0G_{beam}(0) \frac{\partial \phi_n(x)}{\partial x} \Big|_{x_0} \right]^2 \frac{3k_B T}{kC_n^4} \Delta\omega'. \end{aligned} \quad (7.21)$$

The beam of the laser is shifted across the detector as a result of the angle of the beam and not due to its deflection, see Fig. 7.2. As a result the detector is sensitive to the angle of the beam and from Eq. (3.116) the derivative of the PSD of the beam at $x = x_0$ is

$$J_{\frac{\partial w}{\partial x}}(x_0|\omega) = \frac{3\pi k_b T}{k} \sum_{n=1}^{\infty} \frac{|\alpha_n(\omega)|^2}{C_n^4 \int_0^{\infty} |\alpha_n(\omega')|^2 d\omega'} \left(\frac{\partial \phi_n}{\partial x} \right)^2. \quad (7.22)$$

To obtain the RMS voltage that the lock-in amplifier will return all that is required is to substitute eq. 7.22 into 7.21 and take the square root of this result

$$(V_{diff})_{rms} = \frac{2V_0}{\pi} \frac{R}{\sigma_{beam}} \sqrt{J_{\frac{\partial w}{\partial x}}(x_0|\omega) \Delta\omega'}. \quad (7.23)$$

If we continue with the previous result, it can be stated that

$$\begin{aligned} (V_{diff})_{rms} &= \frac{V_0}{\pi\sigma_{beam}} \Delta u' \sqrt{J_{\frac{\partial w}{\partial x}}(x_0|\omega) \Delta\omega'} \\ &\equiv C_{uv} \Delta u' \sqrt{J_{\frac{\partial w}{\partial x}}(x_0|\omega) \Delta\omega'} \end{aligned} \quad (7.24)$$

where

$$C_{uv} \equiv \frac{V_0}{\pi\sigma_{beam}}. \quad (7.25)$$

The final result for the RMS voltage is

$$(V_{diff})_{rms} = 2RC_{uv} \sqrt{J_{\frac{\partial w}{\partial x}}(x_0|\omega) \Delta\omega'}. \quad (7.26)$$

7.3 Noise Calculation

Noise is generally reported in terms of its NASD, and often has the units of V/\sqrt{Hz} [48] or $V/\sqrt{rad/s}$. An alternative way to represent noise is as a noise spectral density, NSD, which is simply the NASD squared and thus has units of $V^2/(rad/s)$. The unit is related to the quantity of interest and Eq. (3.115), which describes the frequency response of the square of the magnitude of the displacement of the cantilever, has units of $m^2/(rad/s)$.

The definition of a Fourier transform was provided in Eq. (3.59),

$$\hat{X}(\omega) = \int_{-\infty}^{\infty} x(t)e^{-i\omega t} dt. \quad (7.27)$$

As a result of this definition, the inverse Fourier transform is

$$x(t) = \frac{1}{2\pi} \int_{-\infty}^{\infty} \hat{X}(\omega)e^{i\omega t} d\omega. \quad (7.28)$$

As was determined in the previous section, the LIA is sensitive to the slope of the cantilever and not the displacement, see Eq. (7.13). Let there be a function which represents the slope of the beam as a function of time, $y'(x, t)$. If a measurement of the slope of the beam is taken over a duration of time from $-T$ to T then the time average of the slope of the beam over this duration of time is

$$\{y'(x, t)\} \equiv \frac{1}{2T} \int_{-T}^T y'(x, t) dt. \quad (7.29)$$

The limits of this integration can be extended to ∞ if a new function, $y'_T(x, t)$, is defined that is identical to $y'(x, t)$ in the region of $-T$ to T and 0 elsewhere. Let the inverse Fourier transform of $y'_T(x, t)$ be $\hat{Y}(x|\omega)$.

The correlation between some ergodic function and itself at a later time is

$$\begin{aligned} K(s) &= \langle x(0)x(s) \rangle = \{x(0)x(s)\} \\ &= \frac{1}{2T} \int_{-T}^T x(t)x(s+t) dt \end{aligned} \quad (7.30)$$

where $\langle \rangle$ denotes an ensemble average. The correlation function for $y'_T(x, t)$ is

$$\begin{aligned} K(s) &= \frac{1}{2T} \int_{-T}^T y'_T(x, t)y'_T(x, s+t) dt \\ &= \frac{1}{2T} \int_{-\infty}^{\infty} y'_T(x, t)y'_T(x, s+t) dt. \end{aligned} \quad (7.31)$$

Using the definition of an inverse Fourier transform this can be rewritten as

$$\begin{aligned}
K(s) &= \frac{1}{8\pi^2 T} \int_{-\infty}^{\infty} \int_{-\infty}^{\infty} \hat{Y}'(x|\omega_1) e^{i\omega_1 t} d\omega_1 \int_{-\infty}^{\infty} \hat{Y}'(x|\omega_2) e^{i\omega_2(s+t)} d\omega_2 dt \\
&= \frac{1}{8\pi^2 T} \int_{-\infty}^{\infty} \hat{Y}'(x|\omega_1) d\omega_1 \int_{-\infty}^{\infty} \hat{Y}'(x|\omega_2) e^{i\omega_2 s} d\omega_2 \int_{-\infty}^{\infty} e^{i(\omega_1+\omega_2)t} dt.
\end{aligned} \tag{7.32}$$

It should be noted at this point that the output of the LIA is proportional to

$$\hat{F}(x|\omega) = \frac{1}{4\pi T} \int_{-\infty}^{\infty} \hat{Y}'(x|\omega) d\omega \int_{-\infty}^{\infty} e^{i(\omega_1+\omega_2)t} dt \tag{7.33}$$

where $\frac{1}{2T}$ is the ENBW, $\Delta\omega_{enbw}$. Specifically, the LIA has three different outputs, $X \propto \text{Real}(\hat{F}(x|\omega))$, $Y \propto \text{Imag}(\hat{F}(x|\omega))$ and $R \propto |\hat{F}(x|\omega)|$. Let us assume that the duration of the measurement is sufficiently large that it can be considered infinite, that is $2T \gg \omega_1$. If this is true then

$$\int_{-\infty}^{\infty} e^{i(\omega_1+\omega_2)t} dt = 2\pi\delta(\omega_1 + \omega_2). \tag{7.34}$$

This integral result can be used to rewrite $\hat{F}(x|\omega)$ as

$$\hat{F}(x|\omega) = \Delta\omega_{enbw} \hat{Y}'(x|\omega). \tag{7.35}$$

$\hat{Y}(x|\omega)$ is a real and symmetrical function, thus $\hat{Y}(x|\omega) = \hat{W}(x|-\omega)$. Using this relation and $\Delta\omega_{enbw}$, Eq. (7.32) becomes

$$K(s) = \frac{\Delta\omega_{enbw}}{2\pi} \int_{-\infty}^{\infty} |\hat{Y}'(x|\omega_1)|^2 e^{i\omega_1 s} d\omega_1. \tag{7.36}$$

The correlation function, like any other function of time, can be expressed as an inverse Fourier transform. For the special case of the correlation function the inverse Fourier transfer function is a power spectral density,

$$K(x|s) = \frac{1}{2\pi} \int_{-\infty}^{\infty} \hat{J}_{diff}(x|\omega) e^{i\omega s} d\omega. \tag{7.37}$$

From a comparison of Eqs. (7.36) and (7.37), it can be seen that the power spectral density of the cantilever is

$$\hat{J}_{diff}(x|\omega) = \Delta\omega_{enbw} |\hat{Y}'(x|\omega)|^2. \quad (7.38)$$

This can be expressed in terms of the LIA's output using Eq. (7.35) as

$$\hat{J}_{diff}(x|\omega) = \frac{|\hat{F}(x|\omega)|^2}{\Delta\omega_{enbw}}. \quad (7.39)$$

This result shows that the NSD of the measured noise of the cantilever is the output of the LIA squared and divided by the ENBW at the time of measurement.

The output of the LIA is a voltage measurement, V_{diff} , which is measured for some point x on the cantilever and some frequency ω . To obtain the NSD, V_{diff} is squared and divided by the ENBW,

$$\hat{J}_{diff}(x|\omega) = \frac{V_{diff}^2(x|\omega)}{\Delta\omega_{ENBW}}. \quad (7.40)$$

The output of the LIA, V_{diff} , is equal to the RMS output of the detector, $(V_{diff})_{rms}$, which was calculated in Eq. (7.26). This result can be squared and substituted into Eq. (7.40) to obtain

$$\hat{J}_{diff}(x|\omega) = 4R^2 C_{uv}^2 \hat{J}_{slope}(x|\omega) \quad (7.41)$$

where $\Delta\omega_{ENBW} = \Delta\omega'$ and $x = x_0$. In the ideal case where the only source of noise is due to the thermal motion of the cantilever, it would be found that $\hat{J}_{slope}(x|\omega)$ is equal to $J_{\frac{\partial w}{\partial x}}(x|\omega)$, Eq. (3.116). This result can now be solved to obtain the NSD of the slope of the beam,

$$\hat{J}_{slope}(x|\omega) = \frac{\hat{J}_{diff}(x|\omega)}{4R^2 C_{uv}^2}. \quad (7.42)$$

This result is the experimentally determined value for the NSD of the slope of all the mea-

sured noise while its theoretical counter part, Eq. (3.116), is for the noise of the beam alone. The RMS of the noise amplitude spectrum of the slope of the beam, $\left(\frac{\partial W(x|\omega)}{\partial x}\right)_{rms}$ is calculated using

$$\left(\frac{\partial W(x|\omega)}{\partial x}\right)_{rms} = \sqrt{\hat{J}_{slope}(x|\omega)\Delta\omega} \quad (7.43)$$

7.4 Acceleration Calculation

A quantity of particular interest is the acceleration of the cantilever as well as the acceleration noise from the equipment. The calculation process for the cantilever acceleration and the acceleration noise is the same but they start with difference values and units. The cantilever acceleration starts with the raw voltage measurement that is recorded by the LIA, having units of V, while the acceleration noise is calculated based on the NASD, $V/\sqrt{rad/s}$. The units used to outline the following process are for acceleration noise; however, the units for cantilever acceleration are the same with the $1/\sqrt{rad/s}$ being absent.

The displacement of the cantilever is calculated based on the slope measurements and the function $\zeta(x)$ from section 4.3. The EBBE model can be use to show that the dominant mode at low frequencies is the first mode, thus the noise will be calculated as if it is the only mode present.

Figure 7.2 shows the physical layout and the variables used. The process to calculate the acceleration NASD, $\sqrt{\hat{J}_{acc}(x|\omega)}$, is:

1. divide the NASD by the voltage-to-displacement conversion factor, C_{uv} , giving the distance the laser has shifted across the detector, s ,

$$s = \frac{\sqrt{\hat{J}_{diff}(x_0|\omega)}}{C_{uv}};$$

2. using the small angle approximation the laser's displacement is divided by the distance between the cantilever and detector, R , to obtain the laser's angle shift, β ,

$$\beta = \frac{s}{R};$$

3. the cantilever's angular deflection is half of that of the laser thus the previous angle is divided by two, θ ,

$$\theta = \frac{\beta}{2};$$

4. the displacement of the beam, w , is calculated by multiplying the angular deflection of the beam by the conversion factor $l/\zeta(x_0)$, Eq. (4.20),

$$w = \frac{\theta l}{\zeta(x)};$$

5. finally, the acceleration of the cantilever is related to its displacement by the frequency of its oscillations squared. Combining the previous results, the NASD of the acceleration is

$$\sqrt{\hat{J}_{acc}(x|\omega)} = \frac{l\omega^2}{\zeta(x)} \frac{\sqrt{\hat{J}_{diff}(x_0|\omega)}}{2C_{uv}R}. \quad (7.44)$$

The RMS acceleration of the beam, a_{rms} , can be calculated by substituting Eqs. (7.41) and (7.42) into Eq. (7.44) to obtain

$$a_{rms} = \frac{l\omega^2}{\zeta(x)} \left(\frac{\partial W(x|\omega)}{\partial x} \right)_{rms}. \quad (7.45)$$

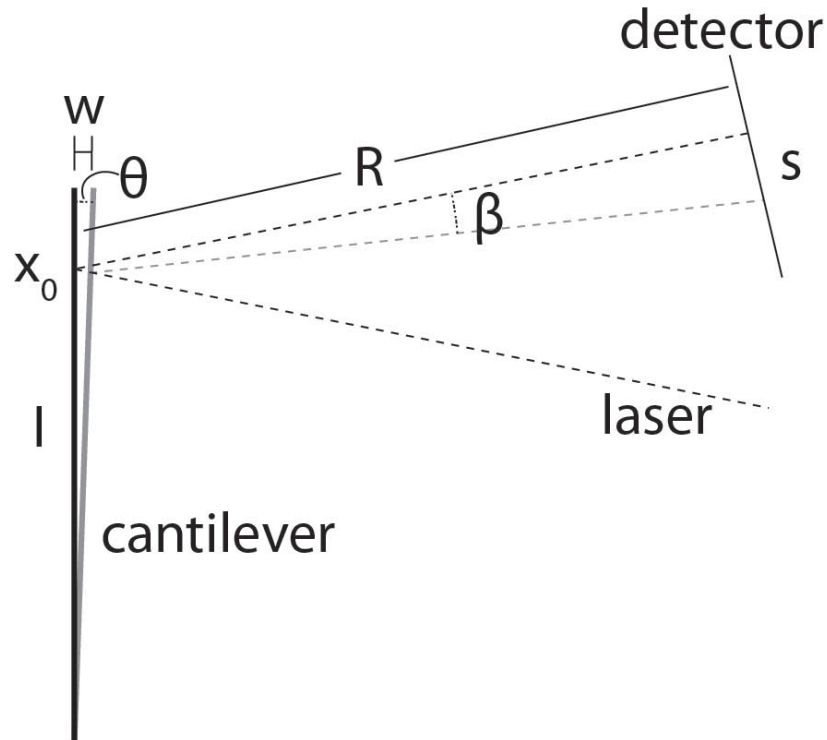


Figure 7.2: Diagram showing single light ray response to cantilever motion.

7.5 Conclusion

In Ch. 6 the equipment setup was covered along with some theory detailing how some individual components of the LIA work. This chapter was dedicated to the derivation of a model that describes the output of the LIA based on the displacement of a laser beam across the detector. This derivation is heavily dependent upon the process of how the detector works and not the LIA.

Unlike the derivation of the EBBE model, the profile of the laser was treated using its actual profile, Gaussian, as opposed to being uniform across the length of the beam. It was possible to make this assumption for the EBBE model as the beam diameter could be enlarged to such a degree that the beam distribution across the cantilever would become nearly continuous. In this case, however, this is not possible as the cantilever is located as close to the focal point of the laser as possible and thus the laser's intensity does vary across the length of the beam.

Later sections dealt with issues relating the LIA's three outputs, X, Y and R, to the cantilever's noise and the process of calculating the NASD of the cantilever from the LIA's output. This can be computed theoretically and incorporates the ENBW of the LIA but does not concern itself with any of the LIA's processes required to obtain that ENBW.

The final section of the chapter outlines the process to obtain the cantilever's acceleration and acceleration noise. The process uses geometry to obtain the desired result. This process can be used to determine both the acceleration noise of the cantilever, based on experiments measuring the cantilever's NASD, or the cantilever's acceleration, based on experiments where the cantilever is driven.

Chapter 8

Experimental Results

8.1 Overview

There were primarily two different sets of experiments that were performed with the various cantilevers. The first set of experiments were intended to determine the NASD of the system as a whole, including the cantilever, over a large frequency range. This helps to determine the best frequency to use for the acceleration experiments and verify the EBBE of the model. The second set of experiments were to determine the cantilever's response to a driving force and is specifically interested in the cantilever's acceleration.

This chapter will also explain the process used to obtain two important factors. The voltage-to-displacement conversion factor is a factor relating the measured voltage to the displacement of the beam across the detector. While this factor could be determined theoretically using semi-conductor physics, it is simpler to obtain it by an experiment. The second factor is for the RMS width of the laser's profile. The voltage-to-displacement factor is used to calculate the acceleration of the cantilever while the RMS width of the beam is required for the detector output model.

During the alignment process the laser and detector are aligned such that the detection point, the position of the cantilever that the detector is sensitive to, is as close as possible to the free end of the beam. Experimental data was collected for four different detection points along a cantilever's length, with particular interest given to the first harmonic peak. These results will be explained with the help of the theoretical model and mode shape. Using the results from the cantilever it will be possible to determine if the bridge beam could be a

candidate for MOND experiment.

The experimental PSD of the cantilever will be used to obtain the limits of a measurement. Specifically, these results will be used to determine the expected uncertainty of a measurement of the acceleration of the cantilever. This will be used to assess the amount of uncertainty that will accompany the low acceleration levels required for the MOND experiment. These results can then be used to ascertain the best equipment settings and driving frequency.

8.2 Harmonic Noise

The noise of a 50 ohm resistor was measured using a time constant of 30 ms, Fig. 8.1, and 1 s, Fig. 8.2, for all four possible filter pole orders. The noise was also measured using a time constant of 10 s and a 4th order pole filter to use as a reference for the expected noise at low frequencies. The noise was also measured using time constants of 10 ms and 30 ms. For both the 10 ms and 30 ms data sets it was found that the noise would reach a constant value for very high frequencies but as the reference frequency decreased the measured noise would suddenly increase. The LIA uses a reference frequency of ω_{ref} and the increase of the noise is the result of inadequate attenuation of the noise at harmonics of ω_{ref} . The frequency where the harmonic noise becomes significant is dependent on both the time constant and the filter pole order. Based on a comparison of these two plots and Fig. 6.8, it is clear that the harmonic signal is much louder than the desired result.

One method to minimize the harmonic noise is to reduce the ENBW of the measurement. This can be accomplished by increasing the time constant, reducing the cut off frequency, or increasing the filter pole order, increasing the roll off. Both of these methods can have the disadvantage of increasing the required wait time for a measurement to be obtained. In order for measurements to be obtained at frequencies as low as 25 rad s^{-1} , a 1 second time constant and fourth order pole are necessary, requiring a wait time of 10 s. This is an issue when measurements must be obtained quickly.

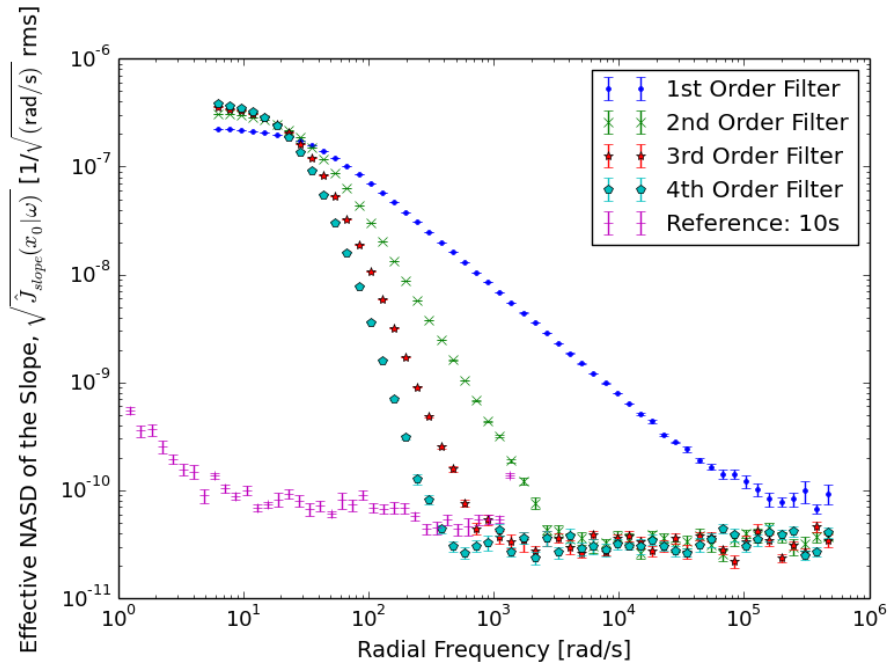


Figure 8.1: Noise Measurements of a 50 ohm resistor for different filter pole orders and using a time constant of 30 ms. Noise measurements were obtained using a 10 s time constant has been included to show what is the expected noise at frequencies below 1 krad/s.

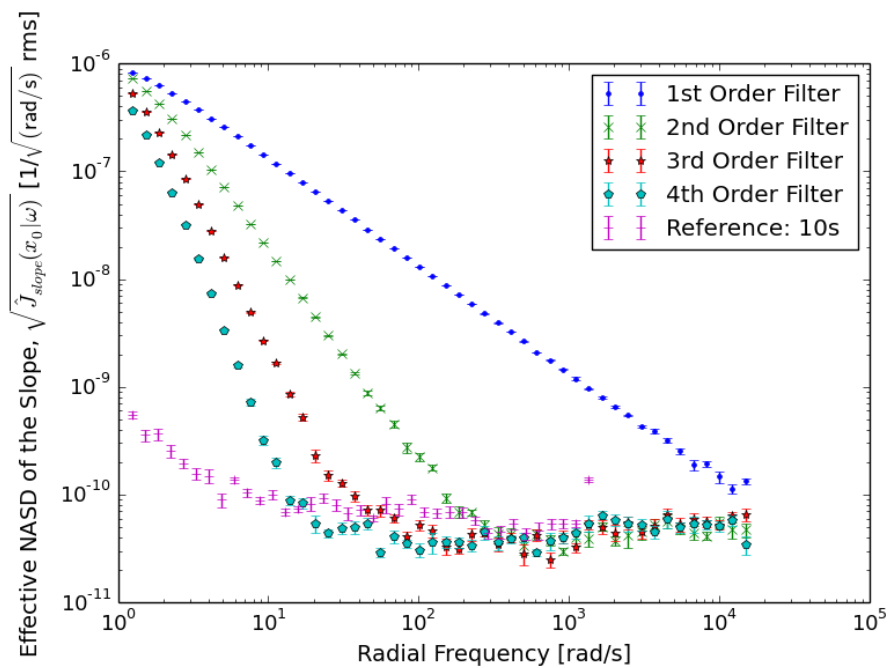


Figure 8.2: Noise Measurements of a 50 ohm resistor for different filter pole orders and using a time constant of 1 s. Noise measurements were obtained using a 10 s time constant has been included to show what is the expected noise at frequencies below 1 krad/s.

An alternative method to reduce harmonic noise is to use the sync filter feature of the LIA. This uses digital processing to average the signal 128 times over the period of the reference frequency, adding $2\pi/\omega_{ref}$ seconds to the wait time. This does not eliminate noise in general but does act as a notch filter for harmonics of ω_{ref} . This allows short time constants and low filter pole orders to be used without issues of harmonic noise.

Figure 8.3 demonstrates the improvements provided by the sync filter. A 50 ohm resistor was used as the source of the noise as it was known to provide less noise than all other pieces of equipment. Data was collected for a large range of frequencies, from 6 rad/s to 600 krad/s, using a time constant of 30 ms, 4th order pole filter and the sync filter off. At 500 rad/s there is a sudden increase in the measured noise due to the second harmonic. The experiment was repeated with the sync filter turned on over the low frequencies where the harmonic noise was an issue. These results found the measured noise level for the short 30 ms time constant were consistent with results using a 3 s time constant which was found to be reliable at low frequencies.

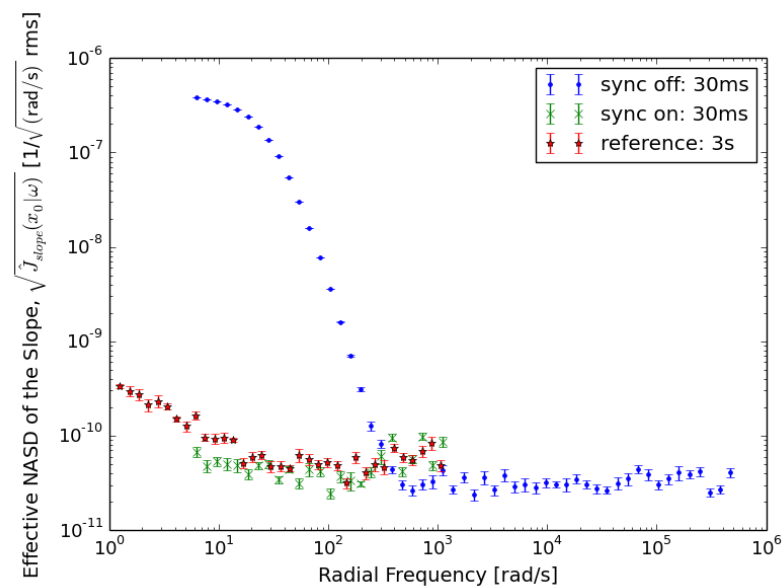


Figure 8.3: Comparison of the measured noise of a 50 ohm resistor with the synchronous filter on, green, or off, blue, with time constant of 30 ms and a 4th order pole. Measurements were made from 1 to 1000 rad/s with a time constant of 3 second and 4th order pole, red, to determine the expected noise at lower frequencies.

The sync filter also increases the wait time for a measurement; however, in some cases the increase of time is less than that of changing the time constant and filter pole order. The time required to make a measurement at 25 rad s^{-1} using a 30 ms time constant, fourth order pole and the sync filter is 0.55 seconds. Of the 0.55 seconds, the sync filter requires 0.25 seconds for it to average over a full cycle.

For all of the results shown below, the sync filter was utilized. This allowed a time constant of 300 ms to be used across the entire frequency range of the experiment. This helped to reduce the total amount of time that was required to acquire data.

8.3 Detector Model Factors

The VTD factor determines the ratio of the detector voltage, from the difference output, to the displacement shift of the laser across the detector. This factor is used to determine the displacement of the cantilever based on the detector's output and is defined as C_{uv} in Eq. (7.25). It is determined experimentally by reflecting the detection laser off the cantilever and onto the detector. The detector is positioned such that the laser is primarily striking one side of the detector and the output of the detector's difference output is recorded. The detector is moved in $50 \mu\text{m}$ increments such that the red dot for the laser progresses to the other side of the detector. Measurements are made from the difference output after each step, for a total distance of 4 mm. The final results are then analyzed to find a small region, about $200 \mu\text{m}$, that is reflected from near the free end of the cantilever and has a constant slope. This region is fit with a linear function to determine the VTD factor which has units of V/mm. An example of these results for the $500 \mu\text{m}$ cantilever are shown in Fig. 8.4.

The beam has a near-Gaussian profile. We expect the results from the difference output, which outputs the integral of the left side minus the integral of the right, to resemble the error function. This is confirmed by Fig. 8.4. Fitting the data with the Error function provides a value for the RMS width of the beam, σ_{beam} , a term introduced in the detector model in Eq. (7.4).

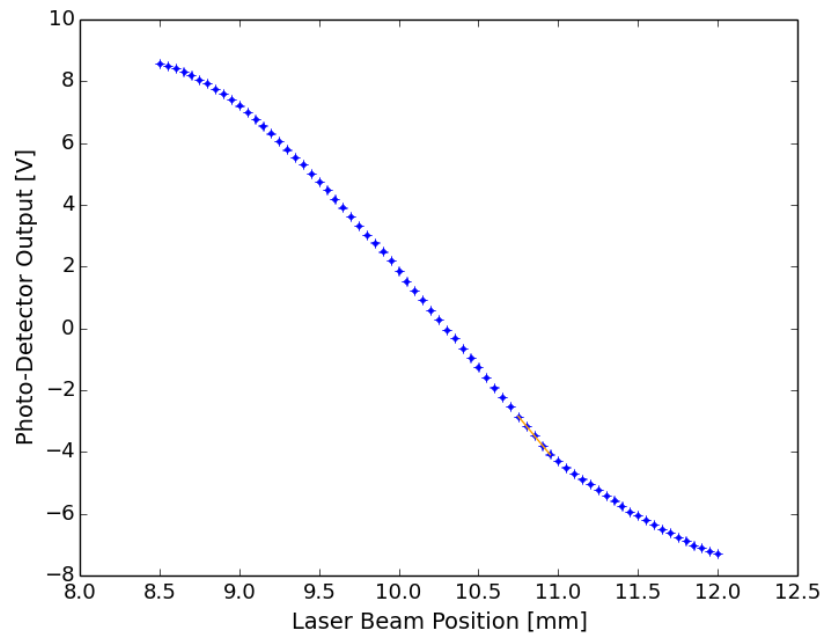


Figure 8.4: Experimental results for determining voltage to displacement factor for a cantilever and the RMS width of the laser's profile.

The detection point shifts toward the free end as the detector approaches 12 mm. For this example the region that was selected was from 10.75 mm to 10.95 mm, see Fig. 8.5, and the VTD factor was found to be (6.21 ± 0.07) V/mm. The detector was then set to 10.85 mm for the experiments that followed.

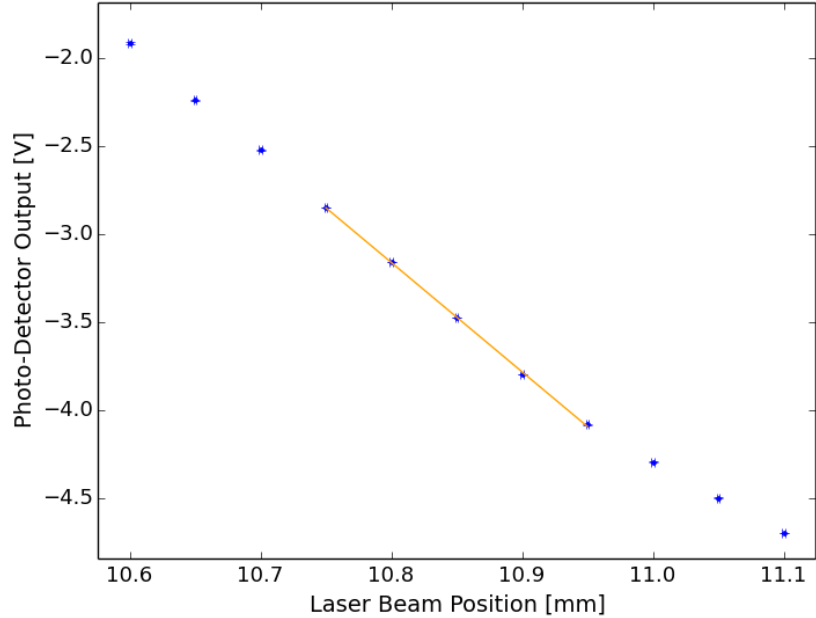


Figure 8.5: A selected portion of the voltage to displacement factor data (dots) and the resulting linear fit (line).

8.4 Driving Laser Calibration

The power output of the driving laser was measured using a power meter. The voltage that was used to power the laser started at 0 V and was progressively turned up to 5 V in 0.025 V increments. The results were then plotted to determine the minimum voltage required for the laser to turn on and obtain a range where a change of voltage caused a linear increase of the power output. The results of this experiment are presented in Fig. 8.6.

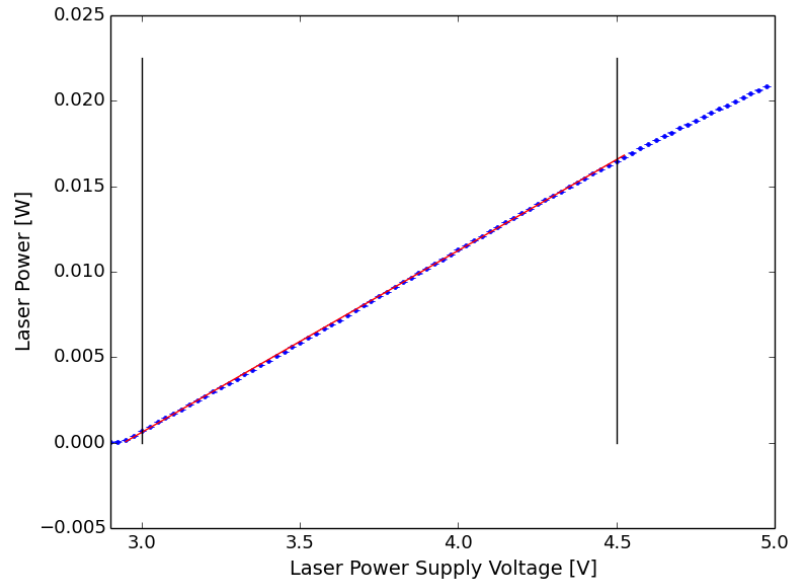


Figure 8.6: Driving laser output response to power supply voltage. Calibration of the driving laser was performed by measuring the laser's power output, blue dots, over a range of voltages. The marked off region, two black bars, indicate the region where the laser has a linear response to the supply voltage. The red line is a linear fit to this region.

The driving laser was found to turn on at a voltage of ~ 2.95 V and has a linear response range from 3 V to 4.5 V. The linear response range was determined by fitting the data with a linear function, using the least squared method, and clipping off data points until a linear region was identified. From these results it was determined that a DC voltage of 3.75 V should be used to ensure that the laser remained in the linear response range while a maximum of $1.5 V_{pp}$ variation could be used for the AC component.

8.5 Common Mode Noise and Photon Shot Noise

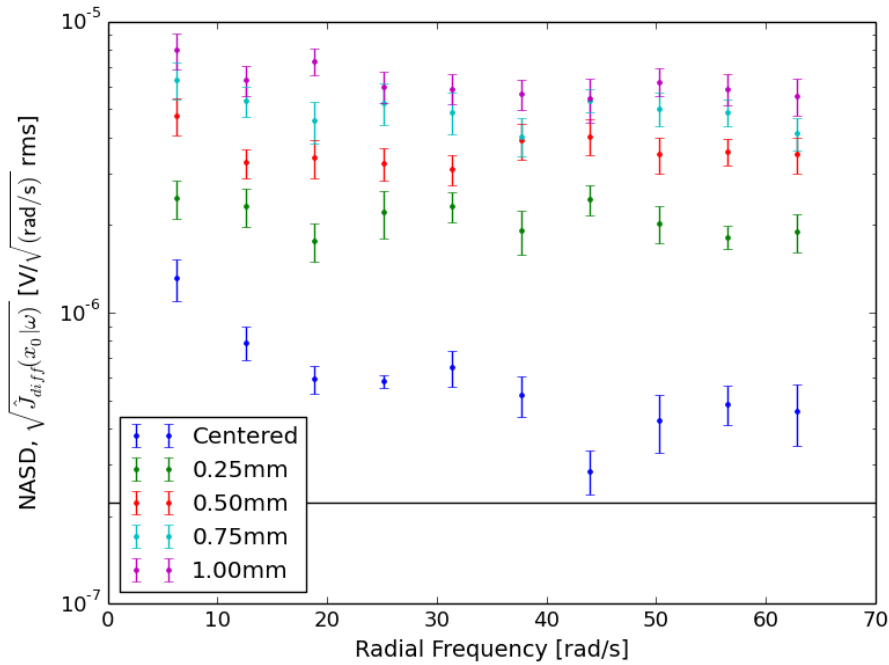


Figure 8.7: Effective NASD of the slope for the detection laser aimed directly at the detector. Detection laser noise centered (blue) is where the difference output reads 0 volts and 0.25 mm (orange) is the average of the noise when the laser is shifted 0.25 mm either left or right of centered. The same is true for the 0.50 mm (green), 0.75 mm (red) and, 1.00 mm (purple) results. The black line indicates the expected shot noise of the laser.

Figure 8.7 shows the effects of shifting the laser to cause uneven light distribution across the detector. First the laser was positioned such that the difference output was ~ 0 volts, meaning there was an even distribution of light across the detector. The noise was then measured for a small number of frequencies using the difference output. The experiment was then repeated with the laser shifted some distance to the left and then to the right. The results from these two experiments were averaged to determine the expected noise if the laser were shifted that distance off center. The noise was found to increase as the laser was shifted further from center. It is thought that this is the result of common mode noise as discussed in Sec. 6.4.

The process of centering the beam allows for noise that is common across the laser and not fundamental to be reduced, until only fundamental noise remains which cannot be

removed. Lasers produce shot noise which is caused by statistical fluctuations of photons as a result of the discrete nature of light. The PSD of optical shot noise is

$$S(\omega) = \frac{h\nu\bar{P}}{\pi} \quad (8.1)$$

where h is Planck's constant, ν is the frequency of the light and \bar{P} is the average power of the laser [74]. From this equation it can be seen that the PSD of optical shot noise is independent of the measurement frequency. The theoretical shot noise was converted to an expected detector voltage by taking the square root of the shot noise and then multiplying by a volts/watt conversion factor. This noise has been plotted in Fig. 8.7 as the horizontal black line.

It is not always possible to position the detector such that the laser is centered. To obtain the largest signal for the experiments to measure cantilever noise and acceleration, the detection point of the cantilever must be near the free end. While the cantilever is placed as close as possible to the laser's focal point, about 200 μm of the cantilever's body reflects laser light at the detector. The detector is moved such that the detection point is as close to the free end as possible causing the a majority of the light reflected off the cantilever's body to strike one side of the detector and reducing the cancellation of noise.

8.6 Cantilever Dimension Estimates

In section 5.5 it was proposed that the DHO model could be used to determine the thickness of the cantilever. It was found in Sec. 6.3.2 that the resonance peak location was most significantly impacted by variations of the thickness of the cantilever. The approximate thickness of the cantilever can be calculated using Eq. (5.24). Manufacturer ideal values can be used to evaluate Eq. (5.24), using the guaranteed range to calculate the expected variation.

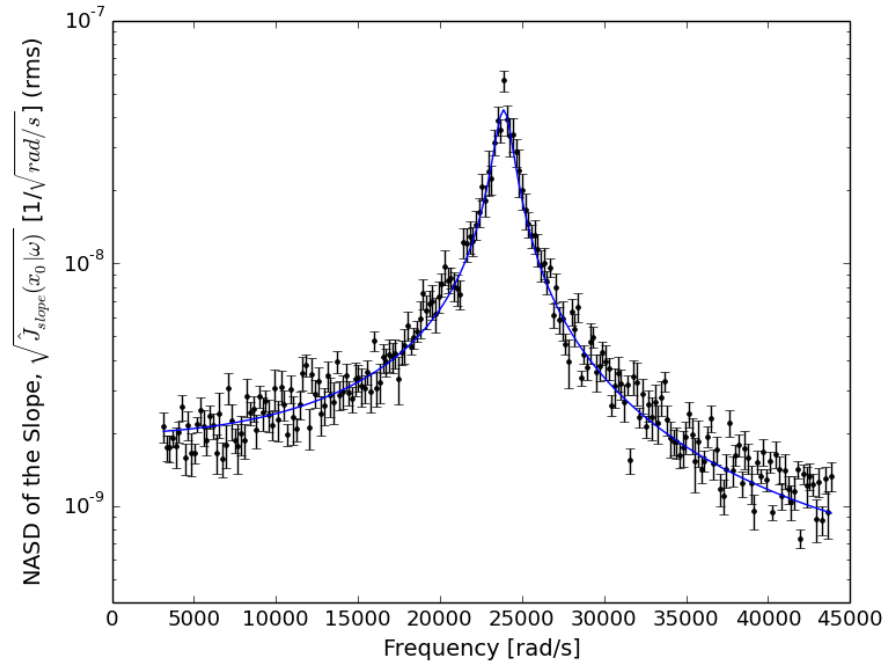


Figure 8.8: Fit of the DHO model to experimental data collected for the 500 μm cantilever. The values required to calculate the thickness of the cantilever are the resonant frequency, ω_f , and the quality factor, Q . Fit results for Q and ω_f were 22.09 ± 0.06 and $(23894.843 \pm 0.0007) \text{ rad s}^{-1}$ respectively.

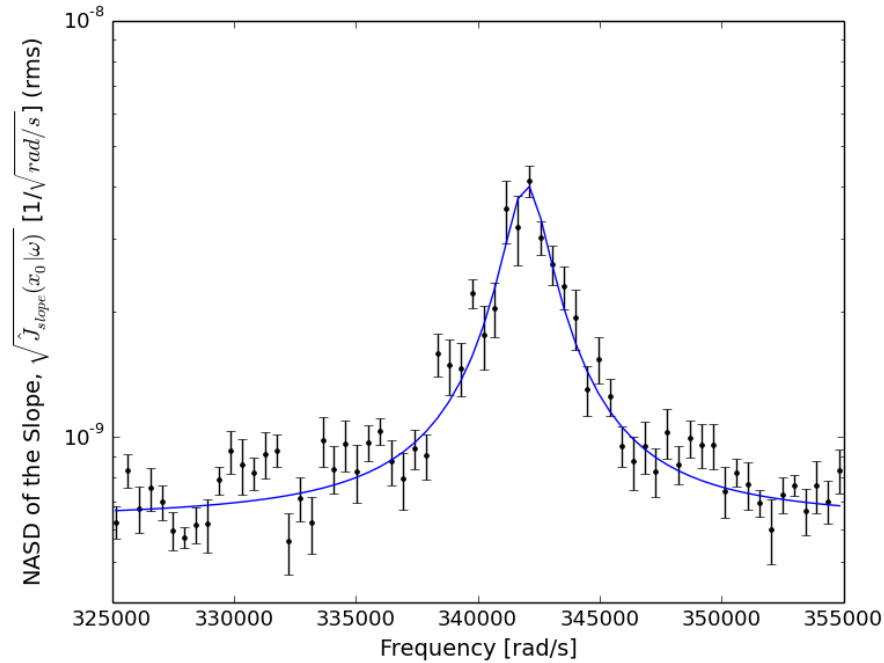


Figure 8.9: Fit of the DHO model to experimental data collected for the 225 μm cantilever. The values required to calculate the thickness of the cantilever are the resonant frequency, ω_f , and the quality factor, Q . Fit results for Q and ω_f were 180.0 ± 0.4 and $(341999.0 \pm 0.0.1) \text{ rad s}^{-1}$ respectively.

Let us assume that the cantilever is made out of pure silicon, which has a density of 2330 kg/m^3 . The fluid that the cantilever is submerged in is air which has a density of 1.225 kg/m^3 . Substituting the appropriate values from Table 5.1 and the results of Fig. 8.8 into Eq. (5.24) the thickness of the 500 μm cantilever is $(1.4 \pm 0.1) \mu\text{m}$. This process can be repeated using the results of Fig. 8.9 to calculate the thickness of $(3.3 \pm 1.1) \mu\text{m}$ for the 225 μm cantilever.

The cantilevers have a reflective coating added to one side. The coating is intended to be 35 nm thick and is applied using evaporation. Gold is 8 times more dense than silicon and the coating is very thin. It is possible that the coating will be a slightly different thickness than intended which could cause a significant change of the cantilever's density.

For the purposes of these calculations it will be assumed that the thickness of the coating, h_{coating} , is 35 nm as stated by the manufacturer since the thickness of the coating on the real cantilevers cannot be determined on a cantilever to cantilever basis. The densities

of gold and PtIr5 are $19,300 \text{ kg/m}^3$ and $21,500 \text{ kg/m}^3$ respectively. The values for the thickness of the cantilevers are obtained by fitting the cantilever's NASD noise data with the EBBE model. The fit was performed by eye, using calculated values for the density of the cantilever, leaving the width and length constant at their ideal values, see Table 6.1, while varying the thickness of the cantilever until the model fit the data at the peaks. From these results it was determined that the thickness of the cantilevers, h_{Si} , was $(0.87 \pm 0.01) \mu\text{m}$ for the $500 \mu\text{m}$ cantilever and $(2.25 \pm 0.01) \mu\text{m}$ for the $225 \mu\text{m}$ cantilever. Substituting these values into Eq. (6.1), the calculated values for the densities of the cantilevers are $(2,986 \pm 7) \text{ kg/m}^3$ for the $500 \mu\text{m}$ and $(2,624 \pm 2) \text{ kg/m}^3$ for the $225 \mu\text{m}$ cantilever. The $500 \mu\text{m}$ cantilever is over 2.5 times thinner than the $225 \mu\text{m}$ cantilever causing the added mass due to the coating to have a larger effect on the density of the cantilever. As an example, the density of the $500 \mu\text{m}$ cantilever is calculated by

$$\begin{aligned} \rho &= \frac{\rho_{Si}h_{Si} + \rho_{Au}h_{Au}}{h_{Si} + h_{Au}} \\ &= 2,986 \text{ kg/m}^3. \end{aligned} \quad (8.2)$$

Using the results of Fig. 8.8 and Fig. 8.9, the thickness of the $225 \mu\text{m}$ and $500 \mu\text{m}$ cantilevers, respectively, can be calculated. The calculated thickness of the $225 \mu\text{m}$ cantilever is $(2.8 \pm 1.0) \mu\text{m}$ and the $500 \mu\text{m}$ cantilever is $(1.1 \pm 0.1) \mu\text{m}$.

The results for the cantilever's thickness as calculated from the DHO fit are outlined in Table 8.1. The thickness was calculated for the realistic case where the cantilever has a coating and also the simpler case of no coating. A comparison of the cases with and without a coating demonstrate the importance of accounting for the coating as the error in the thickness of the beam is about half of that when the coating is ignored.

The calculated thickness of the cantilever is significantly different than the value used for the EBBE model when fitted to the same data as that used for the DHO fit. As a result, the values that are obtained through this method are not reliable and should be used as starting values for a fit of the EBBE model itself.

Table 8.1: Calculated values for the 225 μm and 500 μm cantilevers based on DHO fits. The thickness of the 225 μm and 500 μm cantilevers were calculated using the values of the quality factor and resonant frequency from the DHO fit of the first resonant peak for each cantilever. The columns indicating with or without a coating allow the thickness of each cantilever to be calculated with the added mass of the coating. The EBBE thickness is the required thickness for the EBBE model to fit the data that was used for the DHO fit.

		With Coating	Without Coating
225 μm Cantilever	EBBE Thickness [μm]	2.27 \pm 0.02	2.14 \pm 0.02
	DHO Calculated Thickness [μm]	2.8 \pm 1.0	3.3 \pm 1.1
	% Difference	23%	54%
500 μm Cantilever	EBBE Thickness [μm]	0.87 \pm 0.03	0.79 \pm 0.03
	DHO Calculated Thickness [μm]	1.1 \pm 0.1	1.41 \pm 0.1
	% Difference	23%	79%

8.7 Fluid Effects

The 500 μm cantilever that was used for these results and all that follow is a different one than that used for the results of sections 8.4 and 8.6. A change of cantilevers was necessary as the first cantilever broke. The results for the first cantilever were used for the DHO fit as the peak was found to be very well defined and good results were obtained from using that data set.

The experiments to measure the noise of these cantilevers were completed with the cantilevers in the air of the laboratory. The air that surrounds the cantilevers is expected to have an effect on the cantilever's motion and its NASD. \overline{Re} and \overline{T} will be calculated for

both the 225 μm and 500 μm cantilevers while Q was determined in the previous section and these results will be compared with the figures of section 5.6 which discusses the theory for fluid effects.

\overline{Re} and \overline{T} can be obtained using Eq. (5.25). \overline{T} is dependent upon the density of the cantilever, ρ_{cant} , which must be calculated using Eq. (6.1) to account for the thickness of the coating. An example of the calculation for the density of a cantilever with a coating was given in Section 8.6. The quality factor of a cantilever can be obtained by fitting the DHO model to the cantilever's first resonance peak. This fit was performed in the previous section with a quality factor of 22.0 for the 500 μm cantilever, Fig. 8.8, and 180.0 for the 225 μm cantilever, Fig. 8.9.

Table 8.2: Summary of the properties of the 225 μm and 500 μm cantilevers. The values for for Q and ω_f were obtained from the DHO fits from Figures 8.9 and 8.8. ρ_{cant} is calculated using Eq. (6.1) and values provided in this section. Calculated values for \overline{Re} and \overline{T} , Eq. (5.25), for the 225 μm and 500 μm cantilevers. The values of these parameters determine how the motion of the beam will be affected by the fluid the beam is submerged in.

	Q	ω_f rad/s	ρ_{cant} kg/m ³	\overline{Re}	\overline{T}
225 μm cantilever	180.0 \pm 0.4	341999.0 \pm 0.1	2,580 \pm 10	4.6 \pm 0.6	0.006 \pm 0.001
500 μm cantilever	22.09 \pm 0.06	23894.843 \pm 0.001	2,902 \pm 9	4.25 \pm 0.04	0.049 \pm 0.002

\overline{T} is related to the added mass that is dragged along with the cantilever as it vibrates. The 500 μm cantilever has a much larger value for \overline{T} , 0.049, 225 μm cantilever, 0.0059. This is largely the result of the 500 μm cantilever being over twice as long, increasing its surface area, and having a thickness of nearly 2.6 times thinner than the 225 μm cantilever. From Eq. (3.90) it can be seen that the spring constant of a cantilever beam is inversely proportional to the length of the beam cubed. The 500 μm cantilever has a vary small

spring constant compared to the 225 μm cantilever, allowing the 500 μm cantilever to have a larger displacement from an applied force causing it to pull the fluid a greater distance and increasing the effects due to the fluid.

Figures 5.3 and 5.6 to 5.7 were generated using \bar{T} values of 0.0059 and 0.049 as these correspond to the 225 μm and 500 μm cantilevers, respectively. Using the corresponding \bar{Re} values from Table 8.2 the theoretical effects of the fluid on the cantilever's fundamental resonance peak can be found in Fig. 5.3. The resonant frequency of the cantilever in a vacuum is unknown, however, values for the quality factor are known from the analysis of the previous section. The fluid effects theory using the appropriate \bar{Re} values for each cantilever predicts a quality factor of 141 for the 225 μm and 17 for the 500 μm cantilever compared with the DHO model results of 180 and 22.0 respectively. This corresponds to an error of 28% for the 225 μm cantilever and 29% for the 500 μm cantilever.

Figure 5.5 is a plot demonstrating the effects of varying \bar{Re} on the quality factor while maintaining a constant \bar{T} value. Both the 225 μm and 500 μm cantilevers have a very similar \bar{Re} . The two cantilevers have a large difference in their \bar{T} values causing the fluid to have a significantly larger affect on the 500 μm cantilever's quality factor. The reduced quality factor will have caused the amplitude of the fundamental resonance peak to have been decreased, as shown in Fig. 5.7, causing energy to be redistributed to lower frequencies.

8.8 Effects of Varying the Detection Point

Cantilever Beam

The method used to determine the displacement of a beam, and thus its acceleration, makes the assumption that the beam moves like a rigid beam pivoting about a point. This assumption allows for simple trigonometry to be used and is a reasonable assumption for the first mode of a cantilever, Figure 8.10, due to the mode shape and small deflection. As was shown in Section 7.2, by Eq. (7.13) it can be seen that the detector is sensitive to the angle of the beam and not the deflection of the beam.

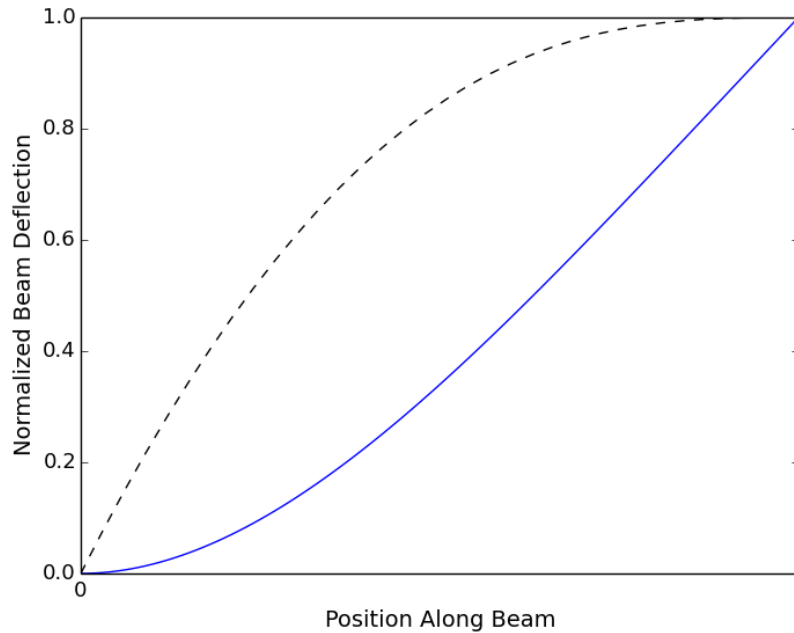


Figure 8.10: Diagram of the normalized deflection for the first mode of a cantilever (blue line) with length l and the normalized slope of the first mode (black dashed line). Calculated using Eq. 2.42.

The first mode of the cantilever has a normalized slope of 0.8 at $0.45l$ and the second derivative of the first mode becomes small close to the free end. It is incredibly difficult to align the detector such that it is sensitive to the very tip of the cantilever. If the alignment is such that the detection point is at $0.8l$, the normalized slope of the cantilever is 0.989 and the results can be considered as if they were obtained at the free end.

The first derivative of the first mode remains relatively large across the entire length of the beam compared to the second mode. This can be seen by comparing Figures 8.10 and 8.11 respectively. The first derivative starts to approach a constant value like the first mode but not until after $0.8l$. This makes it more challenging to determine what the displacement of the free end is as the alignment must be such that the detection point is as close to l as possible.

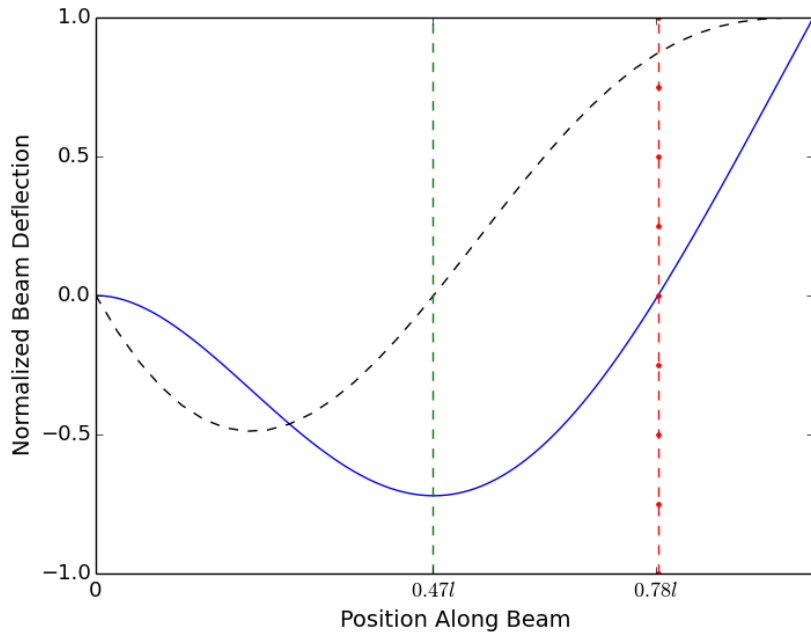


Figure 8.11: Diagram of the normalized deflection for the second mode of a cantilever with length l (blue line) and the normalized slope of the second mode (black dashed line). The green dashed vertical line at $0.47l$ indicates where the slope is 0 and the red dot-dashed vertical line at $0.78l$ indicates where the deflection of the cantilever is 0.

The alignment challenge is not the greatest issue that arises as a result of the equipment detecting the slope of the beam as opposed to its displacement. Consider the shape and slope of the second mode. Figure 8.12 shows the expected peak noise for the second mode for varying positions along the length of the $500 \mu\text{m}$ cantilever. There are two vertical lines, a green dashed line and red dot dash line, that correspond to the lines shown in Fig. 8.11. This result shows that the expected noise goes to zero at $0.47l$ despite the fact that the cantilever has a non-zero displacement at that point.

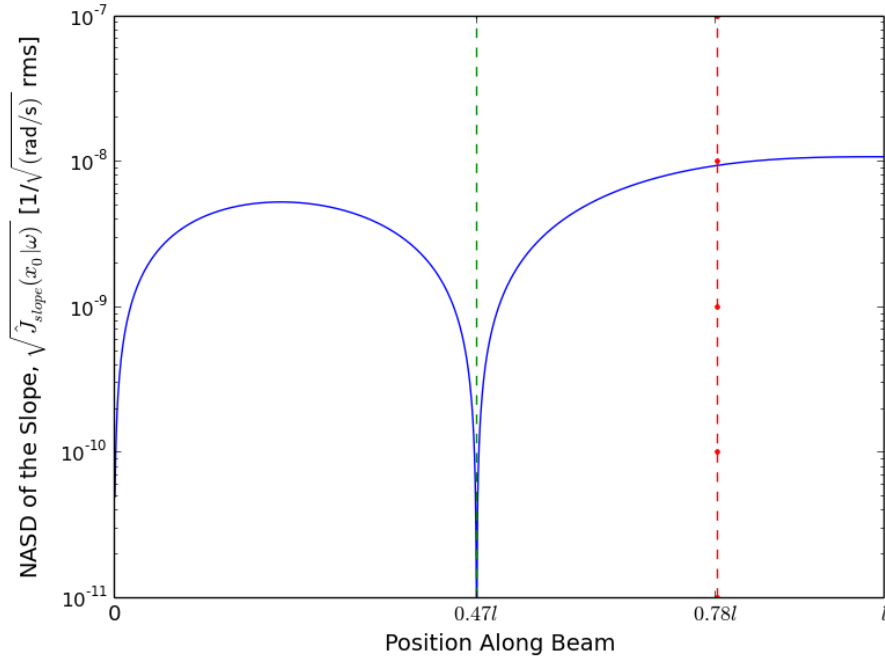


Figure 8.12: NASD of the slope of the beam. EBBE model prediction for the measured noise of the second mode of a cantilever beam (blue line). The green dashed line and red dot-dashed line correlate to those in Fig. 8.11 indicating where the slope and displacement are 0 respectively.

The noise of the cantilever was measured at four different positions along the length of the beam, based on the predicted noise of Fig. 8.12. The result of this experiment are presented now. Figure 8.13 shows the experimental result for $J_{slope}(x|\omega)$ when the detection point is at $0.8l$ while the spectrum $J_{slope}(x|\omega)$ is calculated from the raw data using Eq. (7.42). The peak for both the first and second modes can be clearly identified. The model, for reasons unknown, is large by a factor of 2.

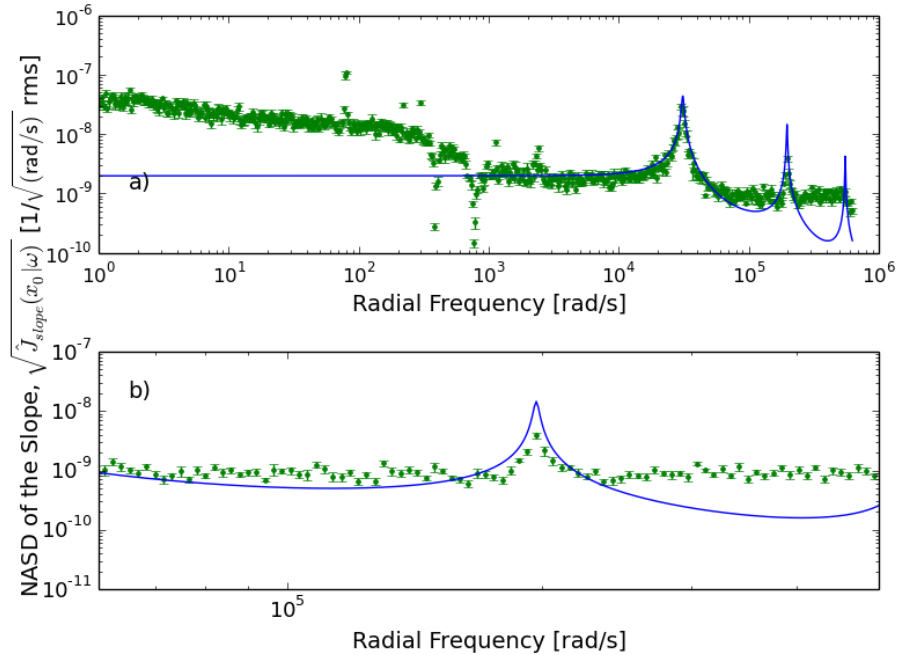


Figure 8.13: Measured noise of the 500 μm cantilever when the detection point is approximately at $0.8l$ where $\zeta(x) = 1.32$. Plot a) shows the measured noise across the full range of 0.16 rad s^{-1} to 628 krad s^{-1} . Plot b) shows a zoomed in image of the second harmonic peak. The second resonance peak is easily found in both plot a) and b) without the EBBE model showing where it is located.

Without knowledge of the detectors response to the cantilever's slope it would be reasonable to guess that, based on normalized displacement of the second mode, that the peak for the second mode would not be identifiable if the detection point were at $0.78l$ as the displacement of the beam is 0. However, the second derivative of this mode is non-trivial and thus, based on the detector's response to the slope of a beam, a peak is expected to be observed. Figure 8.14 shows these results and a peak is found despite the cantilever having no deflection at this point.

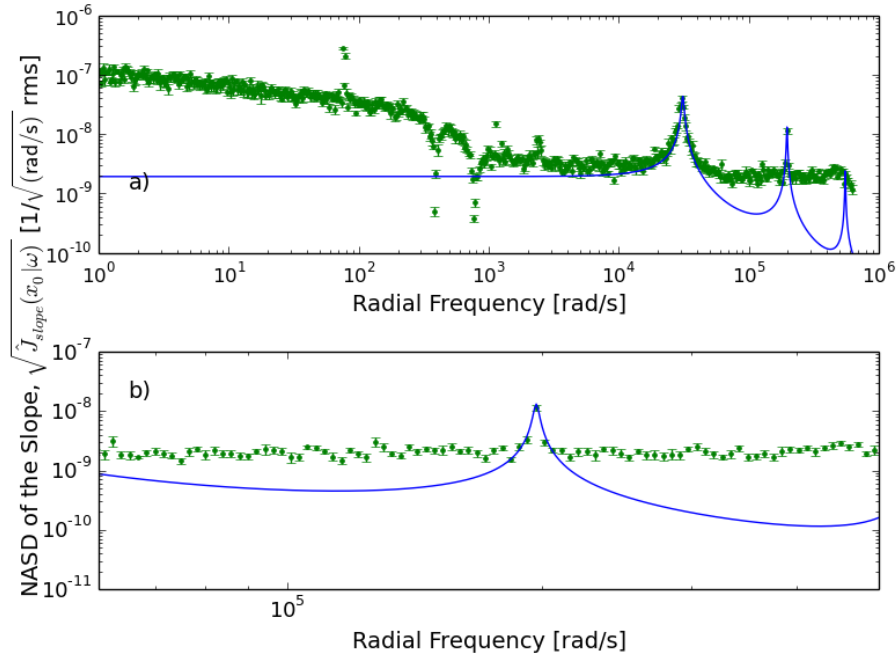


Figure 8.14: Measured noise of the $500\ \mu\text{m}$ cantilever when the detection point is approximately at $0.78l$ where $\zeta(x) = 1.32$. Plot a) shows the measured noise across the full range of $0.16\ \text{rads}^{-1}$ to $628\ \text{krads}^{-1}$. The resonance peak for the first mode is easily detected and there is a notable data point where the second resonance peak is expected to be. The displacement of the beam at this point is 0 while the slope is not. Plot b) shows a zoomed in image of the second harmonic peak. The location of the second resonance peak can only be found using the EBBE model and could easily be mistaken for a random, high noise data point. The location of the peak is indicated by a single data point as the peak is largely hidden by the noise of the system.

At the point $0.47l$ the cantilever has a normalized displacement of 0.72 while the slope is 0. The results of Fig. 8.15 shows that the resonance peak for the second mode at the point $0.44l$ and the peak is indistinguishable from the noise of the rest of the system. The model shows that there should be a small peak detected by the equipment if the system noise were quiet enough. Between the two quadrants of the detector is a small gap of $0.2\ \text{mm}$ causing the detector to be sensitive to two points slightly separated apart. In an attempt to obtain a measurement as close as possible to the point $0.47l$, the detector was slowly shifted back and forth until a minimum noise level was found around the point $0.47l$. As a result of this slight gap the peak could not be wholly eliminated; however, it can be seen that it does vanish into the system noise.

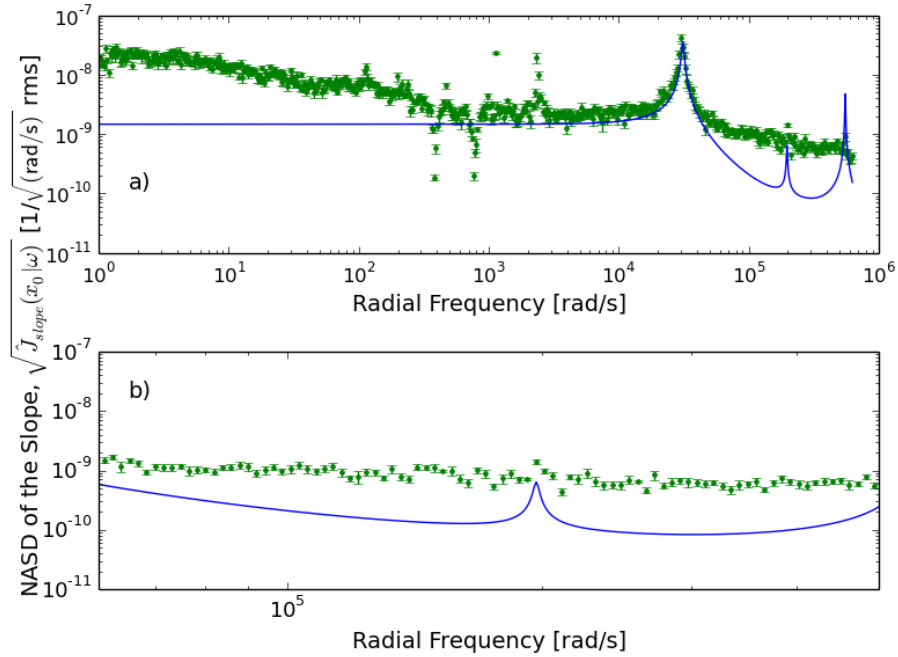


Figure 8.15: Measured noise of the $500\ \mu\text{m}$ cantilever when the detection point is approximately at $0.47l$ where $\zeta(x) = 1.13$. Plot a) shows the measured noise across the full range of $0.16\ \text{rad s}^{-1}$ to $628\ \text{krad s}^{-1}$. Plot b) shows a zoomed in image of the second harmonic peak. The slope of the second mode is 0 at this point while the displacement is not. The location of the second resonance peak is indicated by the EBBE model but the peak is not notable as it is completely hidden by the noise of the rest of the system.

The detector was then shifted such that detection point would move much closer to the base of the cantilever. It was hoped that the detector point would be around $0.2l$ where there is a local maximum of the first derivative of the mode. Unfortunately this point proved difficult to find and it was determined that the detector was sensitive to the point $0.045l$ instead.

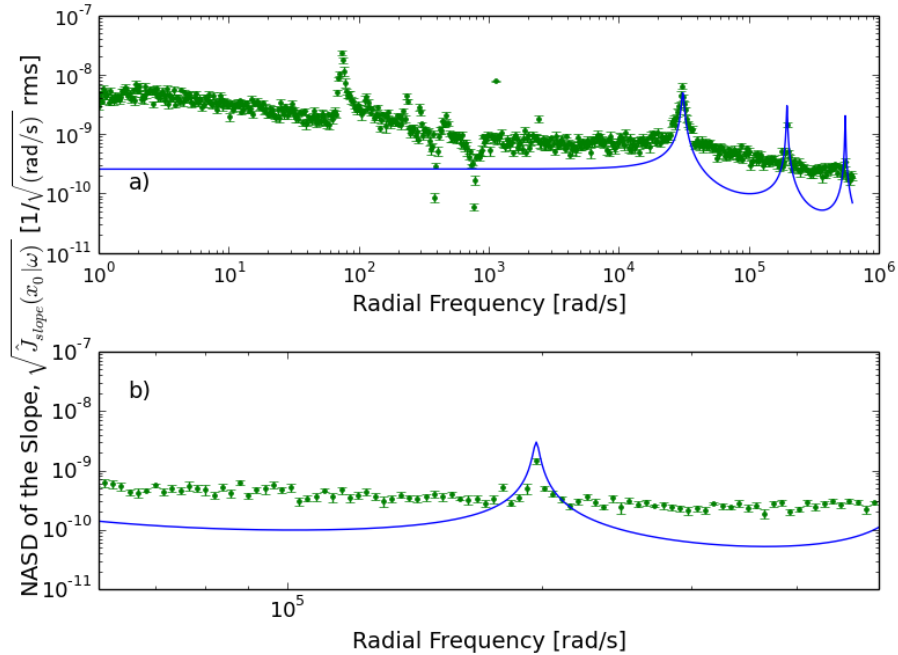


Figure 8.16: Measured noise of the $500\ \mu\text{m}$ cantilever when the detection point is approximately at $0.45l$ where $\zeta(x) = 1.11$. Plot a) shows the measured noise across the full range of $0.16\ \text{rad s}^{-1}$ to $628\ \text{krad s}^{-1}$. The amplitude of the resonance peak, as calculated using the EBBE model, for the first mode is about the same as the second mode's peak. Plot b) shows a zoomed in image of the second harmonic peak. The amplitude of the noise peak for the second mode has increased from the previous plot as the slope is greater, despite the fact that the displacement is smaller.

A contributing factor to this variation is likely to be the process used to determine the position that the detector is sensitive to. Obtaining a good alignment with good knowledge of the point the detector is sensitive to is challenging at best. The equipment is aligned such that the first mode's resonance peak can be detected and then the detector is shifted until it is believed that the detector is sensitive to the correct location of the cantilever based on the image of the reflected laser on the detector. The exact point of sensitivity cannot be determined at this time of the experiment. The data is collected and then the model is fit to the data and the point of sensitivity is then obtain from this result. The fitting process is done by eye based on the amplitude and position of the resonant peak. This process is not done using a fitting routine as the noise over large frequency ranges may not be caused predominantly by the cantilever and, as seen in Fig. 8.13, the amplitude of the models

noise can be significantly different than the data causing other fitting issues. Fitting by eye introduces other difficulties that may be contributing to inaccuracies of the position of sensitivity. However, these errors are not expected to be significant as these fits were done with two peaks in mind and a change of position of a few percent can be found to make large changes to the model, especially with regards to the second mode's resonance peak.

Bridge Beam

The interest of the bridge beam is to determine if the cantilever is the best option for the MOND experiment. This consideration is purely theoretical and no data has been acquired for a bridge. The validity of the bridge can be determined based on the detector's response to the deflection of a beam and the results found for the cantilever. The dominant mode at low frequencies is the first mode and as a result this is the mode that will be considered here.

The first mode of the cantilever has both the largest deflection and largest slope at the free end of the beam. As a result the optimal point to make measurements of the beam is at the free end. This deflection and slope is possible as the free end of the beam is unrestricted and by the boundary conditions of the cantilever at the free end, Eq. (2.31), neither the deflection nor slope are constrained at this point. The bridge beam is rigidly mounted at both ends causing both the displacement and slope to be zero at both ends, see the boundary conditions in Eq. (2.44). From these boundary conditions the first mode was determined and it is shown in Fig. 8.17.

Based on the results of the previous section and the shape of the bridge beam's first mode, it is expected that the point where the beam has its maximum deflection, $0.5l$, will also produce a trivial amount of noise due to it having zero slope at this point. In the same fashion that the noise was determined along the length of a cantilever beam in Fig. 8.12, so too has the noise been found for the bridge, Fig. 8.18. The results found for the bridge theoretically confirm what was expected at $0.5l$ where the noise becomes trivial. Given that the maximum displacement cannot be accurately measured for the dominant mode at

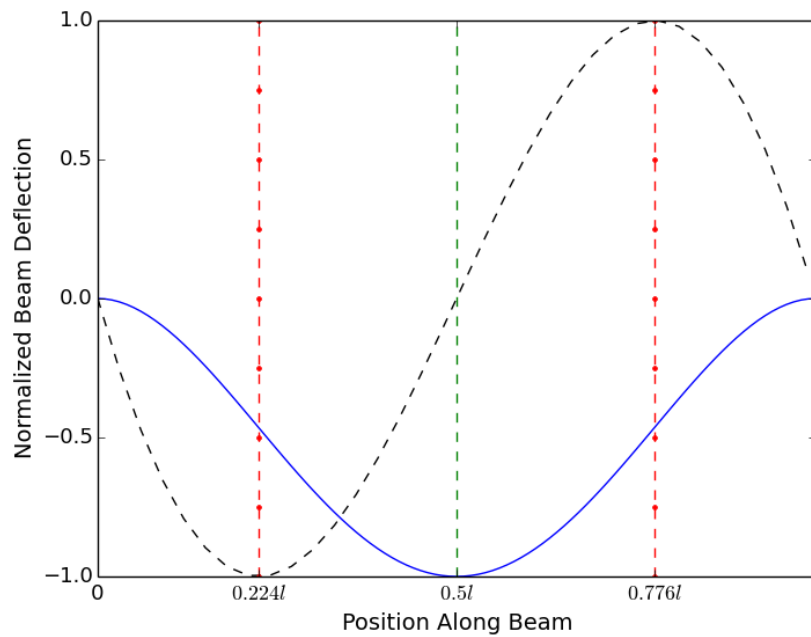


Figure 8.17: Diagram of the normalized deflection for the second mode of a bridge beam with length l (blue line) and the normalized slope of the first mode (black dashed line). The green dashed vertical line at $0.5l$ indicates where the slope is 0 and the red dot-dashed vertical lines at $0.224l$ and $0.776l$ indicates where the deflection of the cantilever is 0.

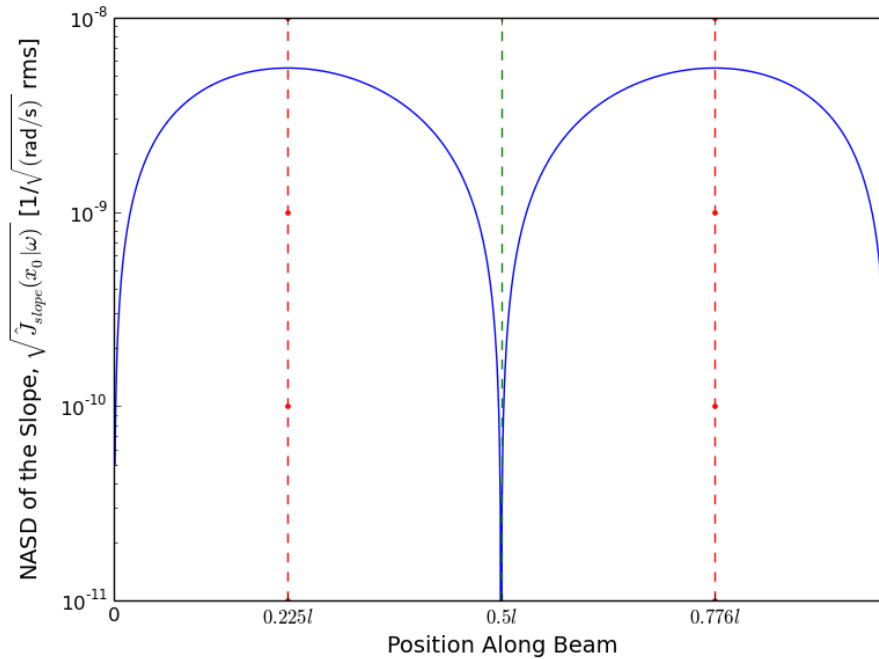


Figure 8.18: NASD of the slope of the beam. EBBE model prediction for the measured noise of the first mode of a bridge beam (blue line). The green dashed line and red dot-dashed lines correlate to those in Fig. 8.17 indicating where the slope and displacement are 0 respectively.

low frequencies where the potential MOND experiment is intended to be performed means that the bridge beam cannot be used. A potential method to solve this issue is by using an interferometer aimed perpendicularly to the beam at $0.5l$. While this method would work for measuring the noise of the beam, issues arise when a second laser is introduced to drive the beam's motion. It is possible that the beam from the driving laser could interfere with the interferometer which would, at best, introduce noise or, at worst, interfere with the signal completely making the measurement unreliable.

8.9 Instrument Noise

Each piece of equipment contributes to the total noise of the system. A careful study of the each component's noise levels can help to determine which component is the noisiest and requires improvement or replacement. The same experimental procedure used to determine the NASD of the cantilever is repeated with the equipment component of inter-

est connected to the LIA. The only exception to this is the detection laser, an issue to be discussed later.

The noise measurements that are presented from this section to 8.10 are noise measurements for the cantilever. Section 7.2 discusses the relationship between the motion of the cantilever and the measured result, Eq. (7.26). The measurements that are obtained for one setup to the next will vary, even for the same cantilever. Each time the equipment is setup it is likely that the VTD factor or distance between the cantilever and detector will change. The results presented here are intended to eliminate potential changes between setups by presenting the NASD of the slope of the beam, calculated using

$$\sqrt{J_{\frac{\partial w}{\partial x}}(x_0|\omega)} = \frac{(V_{diff})_{rms}}{2RC_{uv}\sqrt{\Delta\omega'}}. \quad (8.3)$$

For the cases where instrument noise was being measured, LIA, detector and laser noise, the values used for Eq. (8.3) were based on values for when the 500 μm cantilever was in place. This was chosen as measurements of the detection laser's noise were obtained while the sum and difference output of the detector were as close as possible to the case where the 500 μm cantilever was being measured. Based on typical values for $2RC_{uv}$ of the 500 μm and 225 μm cantilevers, it is expected that the reported noise values for instrument noise alone to be twice as large as it would be if values for the 225 μm were used. Noise of this type is referred to as effective noise.

All of the noise in Fig. 8.19 is equipment noise with the exception of the spike at ~ 1130 rad/s which is the third harmonic of the input power. The total noise of the LIA and detector are several orders of magnitude quieter than any of the other components and thus this noise is not a significant contributor and will be wholly ignored.

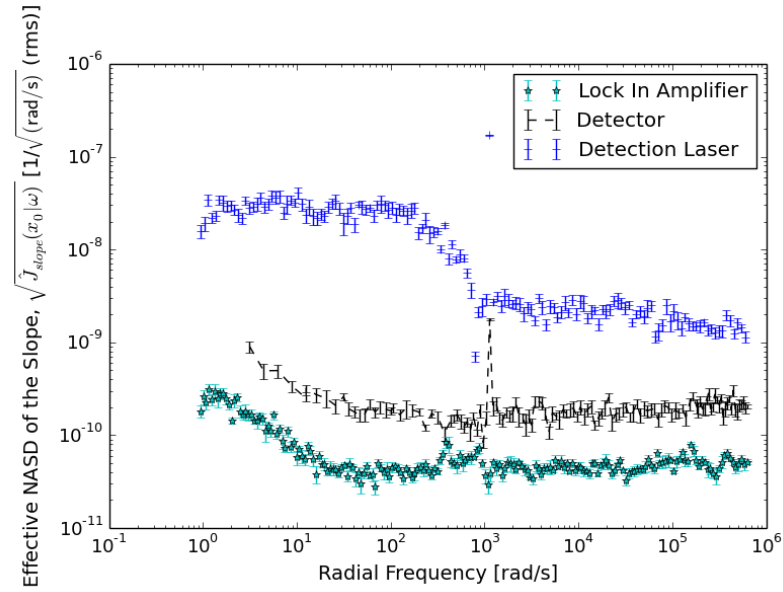


Figure 8.19: Effective NASD of the slope noise for the LIA, detector and detection laser. The noise of the LIA (cyan stars), detector (black dashes) and detection laser (blue pluses). These results show that the LIA, connected to a 50 Ohm resistor, generates less noise than any other piece of equipment. The detection laser also generates more noise than the LIA and detector combined and thus only the laser needs to be considered for future analysis.

Figure 8.20 shows the noise results for the detection laser and the 225 μm and 500 μm cantilevers. The noise of the 225 μm cantilever is consistently quieter than that of the 500 μm cantilever except for the fundamental resonance peak of the 225 μm cantilever.

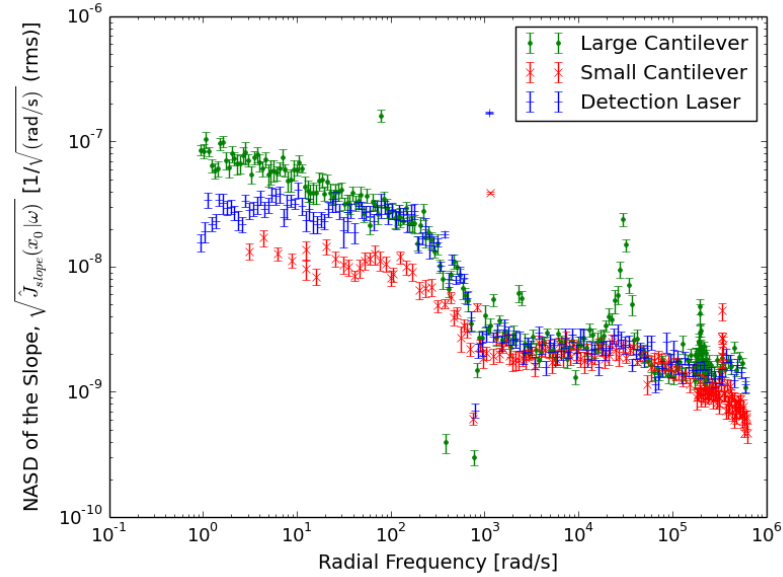


Figure 8.20: NASD comparisons for the detection laser (blue pluses), the 225 μm cantilever (red x) and the 500 μm cantilever (green dots). The detection laser was measured using the difference output of the detector using an alignment that gave the same sum and difference output as that with the 500 μm cantilever.

As mentioned earlier, determining the actual noise of the driving laser when attempting to measure the cantilever’s noise is challenging. The noise is measured using a similar method as that of the cantilevers. For this measurement the cantilevers are removed from the system and the laser is aimed directly at the detector. The noise reported for the laser in Figures 8.19 and 8.20 were collected while the output of the laser was set such that the sum and difference output of the detector were the same as they were for the experiment measuring the 500 μm cantilever’s noise. This method was chosen as it would give a good understanding of the noise of the laser during the 500 μm cantilever measurement experiment. These results show that the total noise that is measured for the 500 μm cantilever was affected by the detection laser, especially in the range of 25 to 900 rad/s. This could be a potential issue for the future MOND experiment as results will show that the ideal frequency range is between 6 and 60 rad/s.

The noise of the detection laser could not be determined for the 225 μm cantilever. The surface area of this cantilever is very small making the reflected portion of the beam that

strikes the detector cover a much smaller area than in the case of the 500 μm cantilever or the laser directly on the detector. The output response of the detector is dependent on both the intensity of the beam that strikes it and the area over which the beam is spread. In order to get the beam to strike a small enough area an object would be required for blocking which would be incredibly difficult to get the right shape to reproduce the 225 μm cantilever result.

8.10 Cantilever Noise Results

NASD is the square root of the power per unit of bandwidth and is a general term that applies to many different noise and power sources. The NASD is calculated based on the raw output of the LIA using the method outlined in section 7.3. The NASD for each system or individual equipment pieces can be measured by connecting them to the LIA and recording the resulting noise across a large range of frequencies.

This section discusses the NASD calculated from the LIA output for the equipment as a whole but the dominant source of noise, especially at high frequencies, is the displacement of the laser across the detector caused by the motion of the cantilever.

8.10.1 500 μm Cantilever

The cantilever was found to have a fundamental frequency of 31.3 krad/s (See Fig. 8.21). There are four notable data points that do not conform to the expected trends of the data based on the model. The first two are at 75 and 80 rad/s where the source of the sudden spikes of noise at these two points is unknown. There are no known features or sources of noise that are expected to cause large amounts of noise at these two frequencies. The other two are at 380 and 750 rad/s. These two sudden drops in noise are located at the fundamental frequency and first harmonic of the power line. The LIA uses a filter at these frequencies causing measurements in this region to be lower than expected.

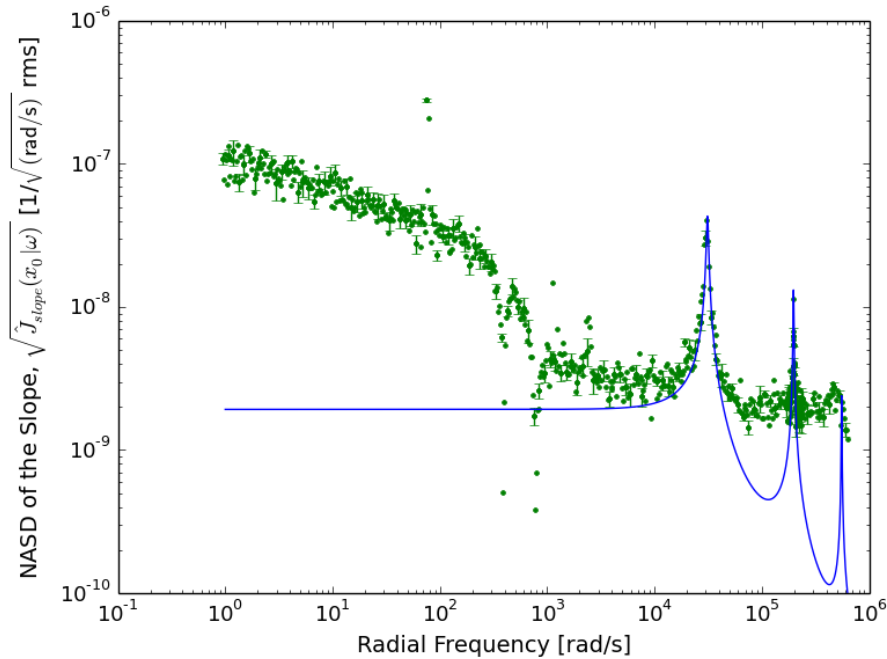


Figure 8.21: NASD of the slope of the 500 μm cantilever with the theoretical EBBE model (blue line) and experimental results (green dots). The theoretical model does not account for any noise sources except for the expected cantilever noise. This data was collected using a detection point of $0.75l$.

The measured noise fits the model at the resonant peaks of the first two modes well for both the resonant frequency and amplitude. The values for the resonant frequency of the EBBE model and the DHO fit for the two peaks are different by 1%. The third peak as calculated by the EBBE model is expected to be less than the noise of the system, confirmed by the data as this peak is not present. There is more noise in the experimental data than is expected from the model. This noise is louder than the third resonant peak causing it to be hidden. From the results of Fig. 8.20 this source of this noise is expected to be from the detection laser. The largest variation between the EBBE model and the data is at low frequencies, specifically the experimental results diverge from the model at 5 krad s^{-1} and the data has a large increase in the noise at frequencies below 1 krad s^{-1} . The source of the low frequency noise is expected to be the result of the detection laser, based on the results of Fig. 8.20.

8.10.2 225 μm Cantilever

The 225 μm cantilever has a very high fundamental frequency, 341.9 krad/s (See Fig. 8.22), which is close to the maximum frequency that the lock-in amplifier is capable of measuring, 640 krad/s . All of the higher order resonance frequencies are well above what can be measured and as a result cannot be used to help obtain a good fit of the EBBE model of the experimental results. The detection point, based on the EBBE model, is at $0.25l$. This is very close to the base of the cantilever. The detector and lasers were realigned in an attempt to obtain better results but the resonant peak could not be found. These results provided a well defined resonant peak that could easily be fit and thus have been used for this analysis.

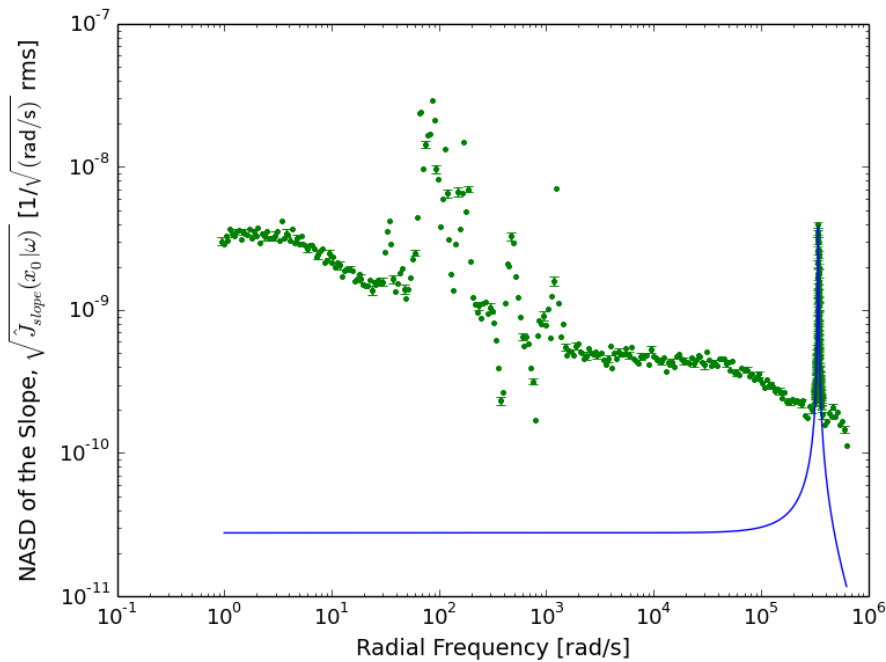


Figure 8.22: NASD of the slope of the 225 μm cantilever with the theoretical EBBE model (blue line) and experimental results (green dots). This data was collected using a detection point of $0.25l$.

The experimental results for the instrumental noise of the 225 μm cantilever is 29 times quieter than that of the 500 μm cantilever at 25 rad/s while the theoretical model for the thermal noise is 70 times quieter. As a result the 225 μm cantilever is a better candidate for

the MOND experiment. However, due to the small amount of noise, the cantilever thermal noise can easily be drowned out by other sources. For the small cantilever to be a candidate for the MOND experiment the detection system would need to be improved, potentially by converting to an interferometer setup as opposed to the optical lever detection system used currently or a laser with less noise. The $225 \mu\text{m}$ cantilever also has the advantage of a very high quality factor compared to the $500 \mu\text{m}$ cantilever. As a result, the thermal energy driving the vibrations of the cantilever is concentrated in the resonant peak which reduces low end noise.

The discrepancies between the model and the data make it difficult to use the model for any useful understanding at the lower frequencies that could be used for a future MOND experiment. Frequencies below 70 rad s^{-1} are shown in Fig. 8.23 where the model and data differ by up to 2 orders of magnitude. Any efforts to try and determine the uncertainty for acceleration measurements must be done from the data alone.

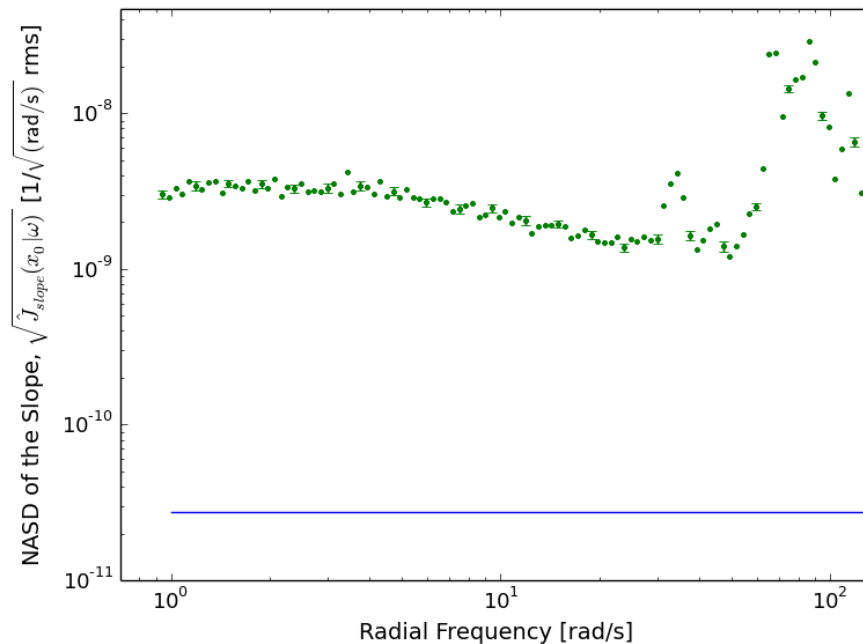


Figure 8.23: Plot of the theoretical (blue line) and experimental (green dots) NASD of the slope of the $225 \mu\text{m}$ cantilever. This data was collected using a detection point of $0.25l$.

Walters et al. [58] studied micro-cantilevers to determine the advantages of using short

cantilevers, $200\ \mu\text{m}$ and shorter, for AFM experiments. They studied the noise spectra of the cantilevers in air and water. Their results found that the fluids caused a shift and broadening of the resonance peak. However, their results showed that for two cantilevers in the same fluid, the shorter one would have less noise at lower frequencies. The study that they performed was interested in micro-cantilevers and their application for AFM applications. The noise spectrum that they obtained were at higher frequencies and they did not study frequencies below $1\ \text{krads}^{-1}$. At the time of writing the author is unaware of any study of the noise spectrum of micro-cantilevers at frequencies below $1\ \text{krads}^{-1}$.

8.11 Noise in the Cantilever's Slope

The total noise contribution to a measurement is dependent upon the time constant and filter pole order that are used for the measurement, dictating the ENBW. Table 6.2 lists the equations to calculate the ENBW and required wait time for a measurement for the first four pole orders. The duration of time for an experiment to be performed while the apparatus is in free fall on Earth in a drop tube or air plane is very short. The noise contribution will be considered for three different time constants, all using a 4^{th} order pole, they are: 0.03 seconds, 1 second (reasonable for Earth based experiments), and 1000 seconds (for satellites).

Table 8.3: ENBW for measurements using a 0.003 s, 1 s and 1000 s time constant, each using a 4^{th} order pole

	0.003 s	1 s	1000 s
ENBW [rads^{-1}]	16	0.49	4.9×10^{-4}
$\sqrt{\text{ENBW}}$ [$\sqrt{\text{rads}^{-1}}$]	4.0	0.70	2.2×10^{-2}

The expected contribution of the noise of the slope to a measurement can be calculated by multiplying the NASD of the slope by the ENBW of the measurement. This has been computed using the results from the previous section, Sec. 8.10, and the aforementioned

time constants. These results are plotted in Fig. 8.24 for the 500 μm cantilever.

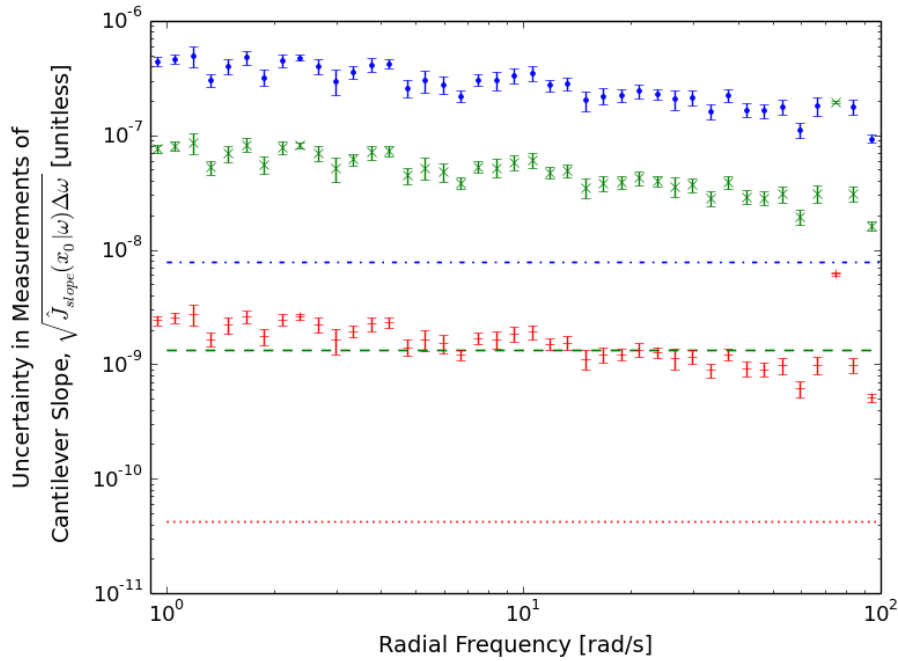


Figure 8.24: Contribution of the noise to a measurement of the slope of the beam for the 500 μm cantilever using three different time constants, each using a 4th order pole. The time constants are: 0.03 second time constant (data: blue dots, model: blue dot dash line), 1 second (data: green x's, model: green dashed line), and 1000 seconds (data: red pluses, model: red dotted line).

Table 8.3 gives the square root of the ENBW for the three different time constants being considered here. The relative difference of the uncertainty of a measurement for two time constants can be determined by taking the ratio of the square root of their respective ENBW. From this we expect that the 0.03 s time constant will have ~ 5.7 times larger uncertainty than the 1 s time constant, while the 1000 second time constant will have ~ 32 less uncertainty than the 1 s time constant. These ratios are confirmed by the results of Fig. 8.24. When choosing a time constant for experiments it is ideal to use one that is as large as possible. This reduces the uncertainty of a measurement, increasing the SNR.

8.12 Cantilever Acceleration Noise Spectral Density

The noise measurements presented in this section is the acceleration NASD of the cantilever. It is calculated using the results of the previous section and the process outlined in section 7.4.

The NASD experiments help to determine the ideal frequency for the acceleration experiment. For the MOND experiment, it is beneficial to use a frequency that is as small as possible as this allows the amplitude of the cantilever and the signal to be as large as possible. Extra considerations will be made for the 3 to 60 rad s^{-1} range as this has been determined to be the ideal range for the MOND experiment.

At frequencies below 500 rad/s the LIA NASD tends to increase with decreasing frequency. The acceleration NASD of the cantilever has a linear dependence on the beam's displacement but is related to ω^2 , see section 7.4. Since ω^2 increases at a much faster rate than the LIA NASD decreases, the acceleration NASD increases with frequency.

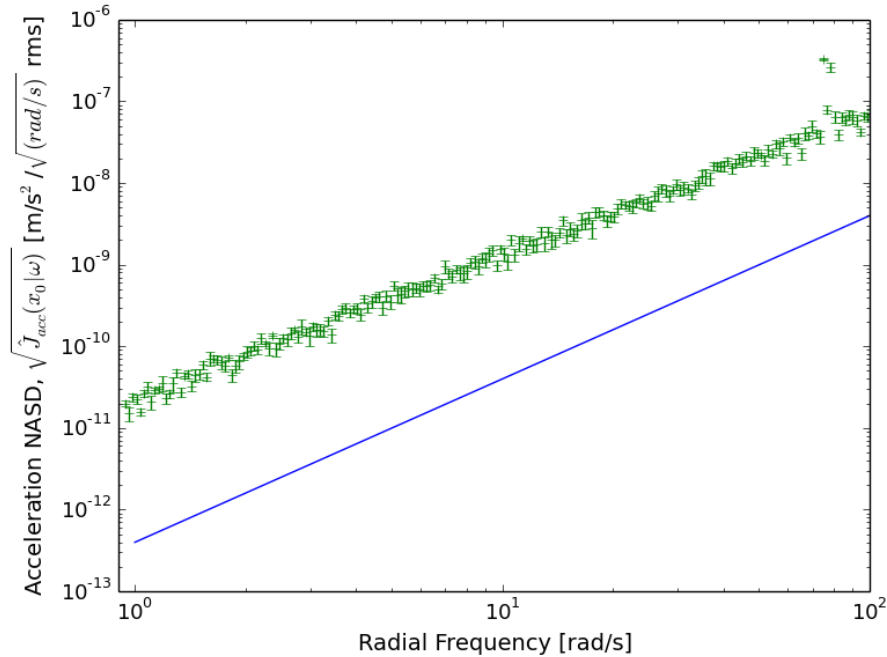


Figure 8.25: Plot of the theoretical (blue line) and experimental (green dots) acceleration NASD of the 500 μm cantilever.

Figure 8.25 shows the acceleration NASD, calculated from the slope NASD using Eq.

(7.44), for the 500 μm cantilever while Fig. 8.26 shows the acceleration NASD for the 225 μm cantilever. The NASD results for the 500 μm cantilever is about 10x larger than that of the 225 μm cantilever and this continues with the acceleration NASD. This reduction in noise is an argument for the use of the 225 μm cantilever for the potential MOND experiment.

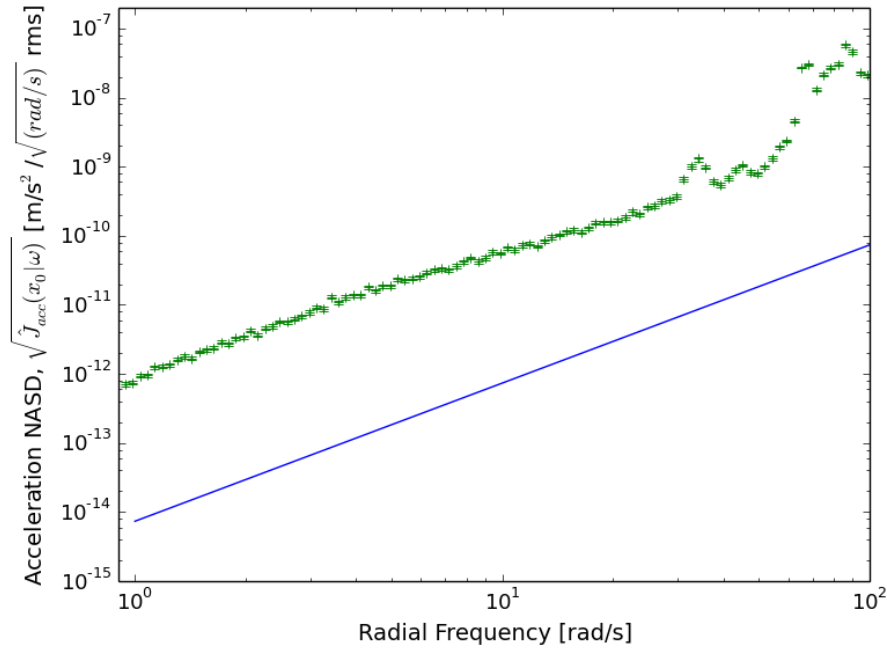


Figure 8.26: Plot of the theoretical (blue line) and experimental (green dots) acceleration NASD of the 225 μm cantilever.

From these results it would appear that the optimal frequency to use for the MOND experiment is the lowest possible frequency as the acceleration NASD and frequency are proportional. Selection of the measurement frequency for the MOND experiment is also dependent upon the choice of settings used with the LIA. As discussed in Sec. 8.2, harmonic noise becomes an issue if too short of a time constant or low of a filter pole order are chosen. The sync filter option of the LIA, section 6.8.3, can be used to remove harmonic noise at the expense of extending the measurement time by $2\pi/\omega$ seconds, where ω is the measurement frequency.

8.13 Rms Acceleration Noise

Experimental results for a_{rms} will now be presented and compared with a_0 . This will allow for different equipment settings to be considered for the purposes of reducing the acceleration uncertainty to be about a_0 , or even better, to just $0.1a_0$. Uncertainty levels of this magnitude will allow for the MOND experiment to be performed, at least in principle, in a suitable environment with low drag, free fall.

The expected acceleration uncertainty of a measurement, a_{rms} , can be calculated from the acceleration NASD, $J_{acc}(x|\omega)$, by using Eq. (7.45). The ENBW will be calculated using the a 4^{th} order pole and the time constants specified in section 8.11. This has been computed using the data from Fig. 8.25 to produce Fig. 8.27 using the previously mentioned time constant and filter pole order pairs.

Figures 8.27 and 8.28 show the expected acceleration uncertainty for three different time constants: 0.03 seconds, 1 second, and 1000 seconds. From Fig. 8.27 for the 500 μm cantilever, the maximum possible frequency where the acceleration uncertainty will be equal to a_0 can be found for a given time constant. The uncertainty is proportional to the frequency and thus this maximum frequency can always be found. For the listed time constants the frequency is (1.1 ± 0.06) rad/s, (2.8 ± 0.1) rad/s, and (21 ± 1) rad/s, respectively. If the duration of the experiment can be extended then the uncertainty can be reduced to just $0.1a_0$. For this small uncertainty the maximum frequency is (1.19 ± 0.06) rad/s for the 1 second time constant and (5.9 ± 0.3) rad/s for the 1000 second time constant. The data does not extend to a low enough frequency for a value to be obtained for the 0.03 second time constant option. The results that are obtained here are very encouraging for the MOND experiment. The uncertainty can also be reduced by increasing the time constant and allowing the experiment to run longer. This aspect along with the benefits of repeated measurements will be discussed in more depth in Ch. 9.

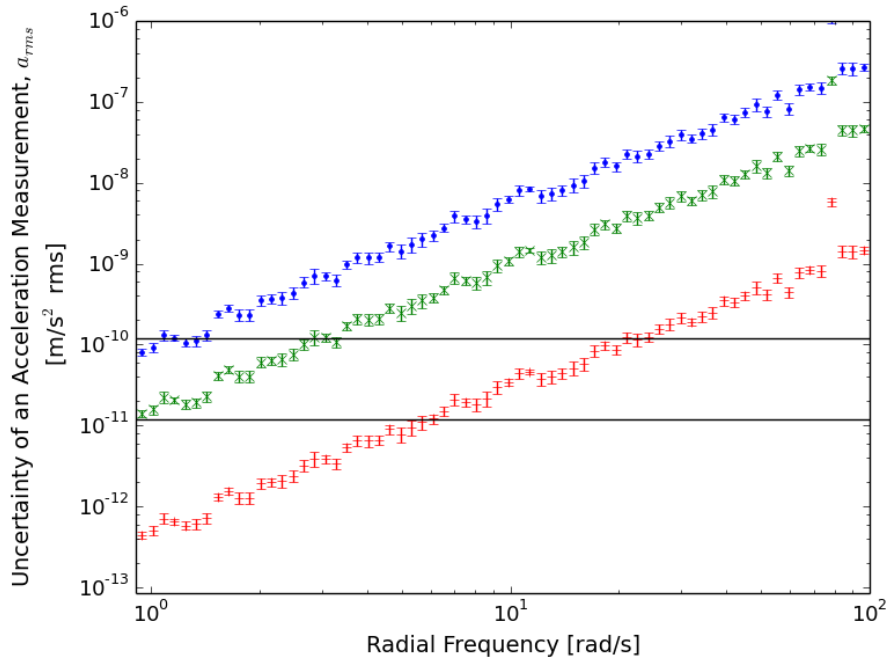


Figure 8.27: Contribution of the noise to a measurement of the acceleration of the 500 μm cantilever using three different time constants, each using a 4th order pole. The time constants are: 0.03 second time constant (data: blue dots, model: blue dot dash line), 1 second (data: green x's, model: green dashed line), and 1000 seconds (data: red pluses, model: red dotted line). The solid, black, horizontal line indicates a_0 and the black, dashed, vertical line indicates 10 rad/s.

Figure 8.28 is a plot of the expected uncertainty of an acceleration measurement for the 225 μm cantilever. These results are calculated using the same time constants as those used for the 500 μm cantilever: 0.03 seconds, 1 second, and 1000 seconds. The maximum frequency for a measurement with an expected uncertainty of a_0 for the 225 μm cantilever for these time constants are (6.2 ± 0.3) rad/s, (20 ± 1) rad/s, and (63 ± 3) rad/s, respectively. The uncertainty can be reduced further to just $0.1a_0$ if the maximum frequency for each time constant is reduced to (1.77 ± 0.08) rad/s, (4.4 ± 0.2) rad/s and (38 ± 2) rad/s, respectively. The increased maximum frequencies is the result of the 225 μm cantilever having less noise at low frequencies than the 500 μm cantilever.

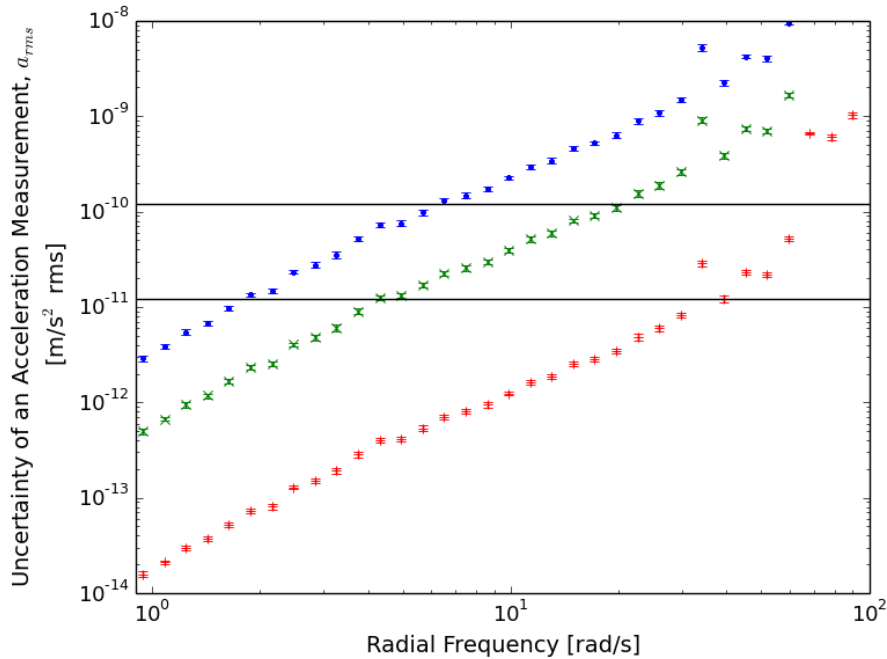


Figure 8.28: Contribution of the noise to a measurement of the acceleration of the 225 μm cantilever using three different time constants, each using a 4th order pole. The time constants are: 0.03 second time constant (data: blue dots, model: blue dot dash line), 1 second (data: green x's, model: green dashed line), and 1000 seconds (data: red pluses, model: red dotted line). The solid, black, horizontal line indicates a_0 and the black, dashed, vertical line indicates 55 rad/s.

The results of Figs. 8.27 and 8.28 for the maximum frequencies are presented in Table 8.4. These results show that the frequency ranges that can be used for both the 225 μm and 500 μm cantilevers extend to relatively large frequencies for an uncertainty on the order of a_0 . This shows that both cantilevers can be used for the MOND experiment. For example, if the 225 μm cantilever were used with a 1 second time constant at 20 rad/s, the required experimental time for the MOND experiment is just 10.3 seconds. This duration is comprised of 10 seconds required for the LPF and 0.3 seconds for the sync filter. It is possible to reduce the uncertainty to well below a_0 if there is sufficient time. If the experiment is performed at a frequency of 4.4 rad/s the sync filter will required 1.4 seconds. In this case the time for the experiment will be 11.4 seconds and the uncertainty will be $0.1a_0$. For an increased experimental time of just 1.1 seconds the uncertainty can be reduced

by an order of magnitude.

Table 8.4: Comparison of the frequency where acceleration noise is equal to a_0 and $0.1a_0$ for the 225 μm and 500 μm cantilevers. The results are presented for a LPF using a 4th order pole filter and time constants of 0.03 s, 1 s and 1000 s. The frequency for $0.1a_0$ for the 500 μm cantilever has not been included as the data does not extend to a low enough frequency.

Time Constant [s]	225 μm Cantilever		500 μm Cantilever	
	Frequency for a_0 [rad/s]	Frequency for $0.1a_0$ [rad/s]	Frequency for a_0 [rad/s]	Frequency for $0.1a_0$ [rad/s]
0.03	6.2 \pm 0.3	1.77 \pm 0.08	1.1 \pm 0.06	-
1	20 \pm 1	4.4 \pm 0.2	2.8 \pm 0.1	1.19 \pm 0.06
1000	63 \pm 3	38 \pm 2	21 \pm 1	5.9 \pm 0.3

8.14 Driven Acceleration Results

The MOND experiment requires the cantilever to be driven at a specific frequency and the cantilever's resulting deflection to be measured. The driven acceleration experiment uses the same detection system as before with the only equipment change being the addition of a laser aimed at the cantilever to drive the cantilever's motion. Unlike the detection laser, the driving laser's intensity is pulsed at a frequency of 25 rad/s and variation of the radiation pressure causes the cantilever to move.

8.14.1 500 μm Cantilever

The 500 μm cantilever is very thin, 1 μm , and has a small spring constant, 0.03 N/m, compared to the 225 μm cantilever, 2.5 μm and 2.8 N/m respectively. The 500 μm cantilever is highly susceptible to small forces making it difficult to reach low accelerations. In an effort to help minimize the acceleration, the cantilever was placed a large distance away from the focal point of the driving laser and a filter was used on the laser resulting in about 0.01% of the emitted light to strike the cantilever.

Figure 8.29 shows the results of the laser driven experiment for the 500 μm cantilever. The measurements were obtained using a 3 second time constant, fourth order pole filter and the sync filter. The laser was set to a given power and then 49 samples were obtained for that load.

From these results it can be seen that the 500 μm cantilever can be driven at acceleration levels around a_0 . As the 500 μm cantilever is so thin it is very susceptible to small loads which can make it difficult to reach very low acceleration levels. The acceleration of the detection point on the cantilever can be modelled as a simple harmonic oscillator. The magnitude of the acceleration of a simple harmonic oscillator is $|a| = A\omega^2$ where A is the amplitude and ω is the frequency of oscillation. The acceleration of the oscillator can be held constant while increasing the amplitude if the frequency is reduced appropriately. If the driving frequency were reduce to 10 rad/s then the amplitude of oscillation would be increased by a factor of 6.25. This would make it easier to drive the cantilever at lower accelerations and could provide a significant improvement for the 500 μm cantilever.

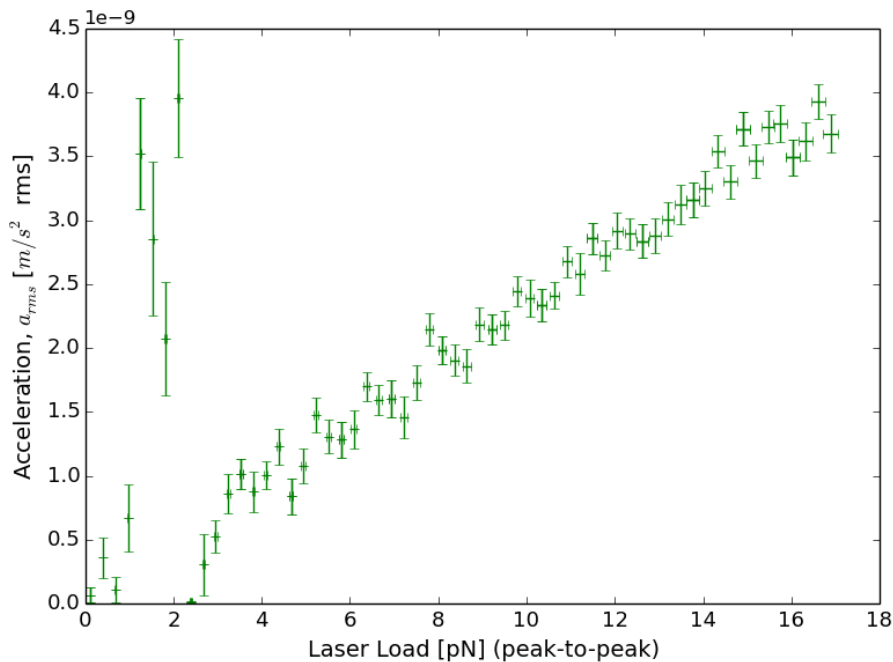


Figure 8.29: Plot of the experimental acceleration of the 500 μm cantilever driven by a laser. These results were obtained with the cantilever driven at 25 rad/s, using a 3 second time constant and 4th order pole filter. The error of the laser load is 0.1%.

8.14.2 225 μm Cantilever

It is easier to reach acceleration levels below a_0 with the 225 μm cantilever than it was with the 500 μm cantilever due to its increased thickness and spring constant. The 225 μm cantilever also has a surface area that is $8\times$ smaller than that of the 500 μm cantilever allowing smaller driving loads to be achieved.

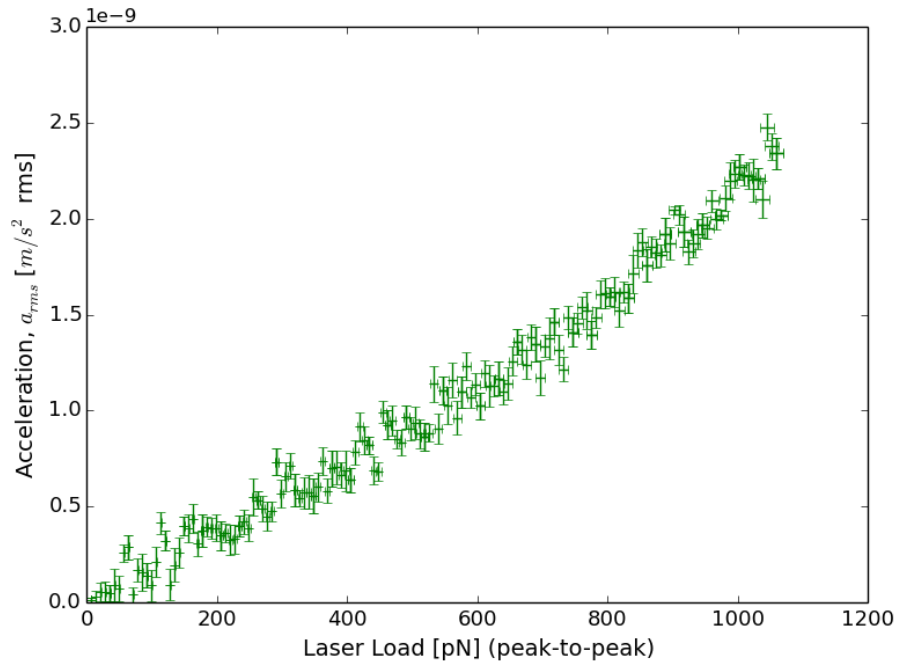


Figure 8.30: Plot of the experimental acceleration of the 225 μm cantilever driven by a laser. These results were obtained with the cantilever driven at 25 rad/s, using a 3 second time constant and 4th order pole filter. The error of the laser load is 0.1%.

Figure 8.30 shows the results of the laser driven experiment for the 225 μm cantilever. The measurements were obtained using a 3 second time constant, fourth order pole filter and the sync filter. The laser was set to a given power and then 49 samples were obtained for that load.

The 225 μm cantilever was capable of being driven at very low acceleration levels. The results presented in Fig. 8.30 focus on the acceleration of the cantilever in the Newtonian regime, accelerations greater than a_0 . As with the 500 μm cantilever, it has been found that the 225 μm cantilever can be driven at very small accelerations approaching the MOND

regime.

The same results displayed on a log-log scale in Fig. 8.31 show that it is possible to reach acceleration levels below 10^{-10} m/s², that is, within the MOND regime. At these low acceleration levels the noise contribution to the measurement becomes significant. The error of these measurements could be reduced by increasing the time constant or filter pole order. This plot is included to show transition from the Newtonian regime to accelerations within MOND regime. The experiment is performed in the Earth's gravitational field and no MOND effects are expected to be observed. However, this cantilever has been successfully driven at accelerations within the MOND regime.

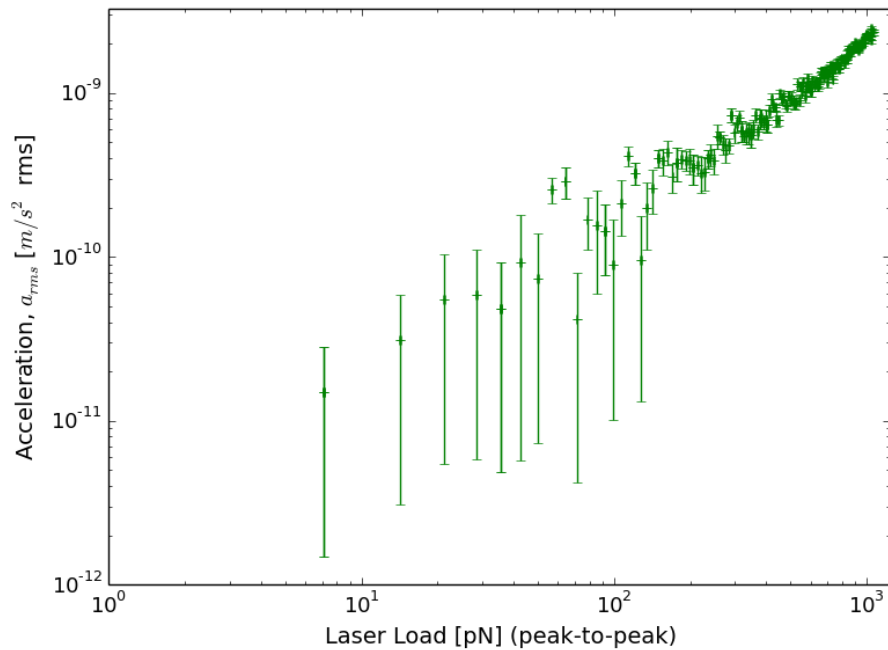


Figure 8.31: Plot of the experimental acceleration of the 225 μm cantilever driven by a laser. These results show the driven acceleration level of the cantilever to be within the MOND regime. The error of the laser load is 0.1%.

The 225 μm cantilever would benefit from a lower driving frequency, just like the 500 μm would. The results for the 225 μm cantilever found that there was a notable increase in the relative uncertainty of the acceleration measurements as the acceleration dropped below 3.5×10^{-10} m/s². Reducing the frequency and increasing the amplitude of oscillation for

the 225 μm cantilever could reduce the measured noise at these low accelerations.

8.15 Conclusion

The MOND experiment must be performed at low frequencies as this is where the noise is the smallest. The measurements must be recorded in a short amount of time, a few seconds, as the duration of time that an object can be in free fall is limited by the size of the drop tube. As a result harmonic noise becomes an issue. Harmonic noise can be limited through the use of the sync filter. The sync filter works as a notch filter to eliminate harmonic noise at the expense of extending the wait time required for a measurement. The sync filter will be required for the MOND experiment due to its restrictions but a careful consideration of the frequency will be required to ensure that the wait time does not become excessively long.

The methods used to determine important factors for the model were discussed. The VTD factor can be found by taking measurements of the detectors output as the laser beam shifts from one hemisphere to the other. This method is used to obtain the VTD factor and determine a small region where the VTD factor can be described as linear. The driving laser was calibrated using the simple method of measuring the power output of the laser with respect to the voltage used to power it. These results were fitted with a linear function such that a range could be found where the power output of the laser is linear with respect to the applied voltage. This will determine the range that is used to power the laser for the experiments which require the cantilever to be driven. Finally, the DHO model was used to obtain values for the thickness of the cantilever. These results were found to vary significantly from the EBBE model but could be used as initial values for a fit.

The noise effects of shifting the laser across the detector has been demonstrated. These results found that the noise is minimized when the laser is centered, such that the mean output of the detector is 0 V. It is expected that this is the result of common mode noise. This allows noise that is common across the laser beam to be cancelled by the detectors

left-minus-right operation. If the laser is off center the noise contribution on one side of the detector will be greater than that of the other, which will be measured as increased noise.

The common mode noise is minimized by centering the laser but this does not eliminate the measured noise. Shot noise is fundamental and randomly distributed across the laser beam. This means that it cannot be eliminated and, due to its randomness, will not be affected by the position of the laser on the detector.

The values for \overline{Re} and \overline{T} were calculated for both the 225 μm and 500 μm cantilevers. From these results it is expected that the fluid will have an effect on the motion of the cantilevers. This will result in broadening and shifting of the resonance peaks, leading to an increase of the noise at low frequencies. Due to the larger value of \overline{T} , it is expected that the noise of the 500 μm cantilever will be affected by the fluid to a greater extent than the 225 μm cantilever.

The detector is sensitive to the slope of the beam and not the displacement. It was found that the detection point was an important factor when measuring the noise for the second mode. The second mode has a slope of zero at $x = 0.47l$ which causes the noise to go to zero for this mode at this detection point. This is not an issue for the first mode as the only location that it has a slope of zero is at the beams mounting point and the measurements are obtained using a detection point as close to the free end as possible.

The EBBE model was fit to experimental NASD of the slope data for the cantilevers to determine if the measured noise of the equipment was excessively loud. The results found that the noise generated at high frequencies was predominately generated by the cantilever. This can be concluded based on the comparison of the EBBE model with the data at frequencies around the resonance peaks of the cantilever. However, there was significant instrumentation noise at low frequencies. This is an issue as it increases the noise at low frequencies where the MOND experiment will be performed by a factor of 55 times for the 500 μm cantilever and 125 times for the 225 μm cantilever. The source of this noise has not been confirmed but it is likely caused by the detection laser. Improvements may

be possible changing detection lasers or by switching the detection system from the optical level method to an interferometer. The comparison of the instrumentation noise found that the detection laser is also much louder than the noise generated by the LIA and the detector. As a result it is reasonable to consider the noise of the LIA and detector as insignificant to the noise. Any improvements of the detection system will have to come from improving the laser or detection method.

The NASD of the slope of the cantilevers were measured and used to calculate the noise of the cantilever's acceleration. It was found that, by optimizing the equipment for low frequency measurements, that the both cantilevers generate a small amount of noise and that it is possible to make measurements of the acceleration within the MOND regime.

Both of the cantilevers were driven at acceleration levels near the MOND regime. This demonstrates that both cantilevers are potential candidates to be used for the MOND experiment. It was difficult to drive the 500 μm cantilever at accelerations within the MOND regime. This is an issue that could be solved by driving the cantilever at a low frequency. The results for the 225 μm cantilever showed that it could be driven at acceleration levels within the MOND regime at 25 rad/s but the relative uncertainty of these measurements were larger than those when the cantilever was driven at accelerations larger than 2×10^{-10} m/s². This cantilever would benefit from reducing the driving frequency as well, likely reducing the relative uncertainty at low accelerations.

Chapter 9

Future MOND Experiments

9.1 Overview

This thesis has explored if an experiment to test MOND is possible in an Earth based laboratory using an AFM cantilever. This chapter will use the experimentally determined results from Ch. 8 to address this issue.

The MOND experiment is designed to be performed on Earth and with the equipment in free fall which places significant restrictions on the duration of the experiment. Results with higher SNR can be obtained with longer time constants and a larger filter order pole for the LPF but the total time an object can spend in free fall is limited by the experiment duration. There are two Earth based and one satellite experiments that will be considered.

9.2 Evaluation of RMS Acceleration

The acceleration of the cantilever can be solved by modelling the free end as a simple harmonic oscillator, as in Sec. 7.4. Using this model the RMS acceleration, a_{rms} , of the free end is $a_{rms} = A_{rms}\omega^2$ where A_{rms} is the RMS amplitude and ω is the frequency of oscillation. The LIA output is proportional to the slope of the cantilever and the conversion function $\zeta(x)$, Eq. (4.20), is used to obtain the cantilever's displacement.

For a white NSD, J , with a magnitude of J_0 and a narrow bandwidth $\Delta\omega$, the RMS of the noise amplitude spectrum of the slope of the beam is

$$\left(\frac{\partial W(x|\omega)}{\partial x}\right)_{rms} = \sqrt{J_0\Delta\omega}. \quad (9.1)$$

Using the function $\zeta(x)$ this result can be used to determine the acceleration of the free end as a simple harmonic oscillator,

$$\begin{aligned} a_{rms} &= \frac{l\omega^2}{\zeta(x)} \left(\frac{\partial W}{\partial x} \right)_{rms} \\ &= \frac{l\omega^2}{\zeta(x)} \sqrt{J_0 \Delta\omega}. \end{aligned} \quad (9.2)$$

The bandwidth and wait time for the LPF can be calculated using

$$\Delta\omega = \xi_T \tau^{-1} \quad (9.3)$$

and

$$T_w = \xi_w \tau \quad (9.4)$$

where τ is the time constant. ξ_T and ξ_w are dimensionless quantities that are dependent upon the filter pole order used. Their values can be determined from the results of Table 6.2.

The sync filter can be used to reduce harmonic noise allowing shorter time constants to be used at low frequencies. The sync filter requires one period of the measurement frequency, ω , and adds $T_s = 2\pi/\omega$ to the wait time. The total wait time that is required for the LPF and sync filter is

$$T = T_w + T_s. \quad (9.5)$$

The previous three results can be used to express Eq. (9.2) as

$$a_{rms} = \frac{l\sqrt{J_0} (2\pi)^2}{\zeta(x) T_s^2} \sqrt{\frac{\xi_T \xi_w}{T_w}} \quad (9.6)$$

The duration of time that can be used for the MOND experiment is determined by the experimental parameters. However, T_w and T_s are variable and must sum to T . The

derivative of this result, Eq. (9.6), with respect to T_s and T_w can be used to determine that the minimization of a_{rms} occurs when

$$T_s = 4T_w = \frac{4}{5}T. \quad (9.7)$$

This result can be substituted into Eq. (9.6) to obtain the minimum value of a_{rms} for an experimental time of T ,

$$a_{rms} = \frac{25l\pi^2}{4T^{2.5}} \frac{1}{\zeta(x)} \sqrt{5\xi_T\xi_w J_0}. \quad (9.8)$$

Let us consider the example for the 500 μm cantilever and use the NASD from Fig. 8.13. If a time constant of 0.1 s, a fourth order pole and a detection point of $0.8l$ are used, then the values of the pertinent constants are:

$$\begin{aligned} \xi_T &= \frac{10\pi}{64} \\ \xi_w &= 10 \\ \xi_T\xi_w &= 4.9087 \\ \zeta(0.8l) &= 1.32 \\ \sqrt{J_0} &\simeq (3.6 \pm 2.4) \times 10^{-8} \quad 1/(\text{rad/s}). \end{aligned} \quad (9.9)$$

The values for $\xi_T\xi_w$ for 1st, 2nd and 3rd order pole filters expressed to 5 decimal places are 7.85398, 5.49779, and 5.30144, respectively. This allows for a 1 second measurement and the expected uncertainty is $1.15 \times 10^{-8} \text{ m/s}^2$ or, dividing by $a_0 = 1.2 \times 10^{-10} \text{ m/s}^2$, $35a_0$. Equation (9.8) can be used to express the ratio of acceleration uncertainty with respect to a_0 as

$$\frac{a_{rms}}{a_0} = \left(\frac{4.1 \pm 2.1}{T} \right)^{2.5}. \quad (9.10)$$

when T is expressed in units of seconds. This ratio allows us to easily determine the ex-

pected acceleration uncertainty for any duration of time of an experiment or solve for the required time based on the desired uncertainty level.

The drop tube at the Bremen facility allows for a maximum free fall time of 4.5 seconds with a free fall distance of 146 meters [75]. If the experiment were performed at a facility such as Bremen then the expected uncertainty, by Eq. (9.10), would be $(0.6 \pm 0.4)a_0$. Bremen also offers the use of a “catapult” which is used to toss the equipment straight up in the air to nearly the top of the 146 meter tube resulting in a 9.3 second free fall time [76]. Using the catapult system the uncertainty would be reduced to $(0.13 \pm 0.09)a_0$.

Suppose that we are interested in reducing the uncertainty to $0.1a_0$. This will require a measurement time, in seconds, of

$$T = \frac{(4.1 \pm 2.1)}{0.1^{1/2.5}} = 10 \pm 7. \quad (9.11)$$

NASA has a KC-135 that flies parabolic paths between 24,000 and 32,000 feet creating a short period of zero-g for 20-25 seconds [77, 78]. If we consider the longest duration possible then it would be possible to reduce the uncertainty to just $0.011 \pm 0.007a_0$.

Let us now consider the case of extremely long time constants. Satellites allow the experiment to always be in an inertial frame of reference meaning data can be collected for as long as the equipment remains reliable. A recent experiment of the equivalence principle was performed on board a satellite. The satellite was placed in a circular, sun-synchronous orbit and used cold gas thrusters to control and maintain the orbit. Using this system the experiment was capable of running for 120 orbits or roughly 8 and a quarter days allowing for a difference of accelerations to be measured on the order of 10^{-15} m/s^2 , an order of magnitude better than previous measurements [79]. A satellite could be used to reduce the uncertainty to well below a_0 . The time required for a measurement with a uncertainty level of $a_0 \times 10^{-5}$ is (410 ± 280) seconds.

The experiment can be performed in a custom made or very short vacuum chamber such that the duration of the experiment becomes very small. If a vacuum chamber were

designed such that it is 1 meter tall and has an apparatus at the bottom that is capable of catching and tossing the experiment, then the experiment duration is 0.9 s. The uncertainty for this duration is $(44 \pm 30)a_0$. To reduce the uncertainty down to a_0 , using multiple measurements and statistics, a total of $44^2 = 1936$ trials will be required. If we assume that each trial takes 1 second from the initial toss to catching and preparing to toss again this will require 33 minutes.

This experiment could be performed with the $225 \mu\text{m}$ cantilever instead. In this case the value for J_0 would be $3.5 \times 10^{-9} \text{ 1/(rad/s)}$. Repeating the experiment in the short vacuum chamber of the previous example, the uncertainty of this measurement will be $3.38a_0$ which will require just 12 trials, based on theory.

9.3 Differentiating forms of $\mu(x)$

MOND modifies Newtonian gravity through the use of the function $\mu(x)$. The form of $\mu(x)$ is as yet undetermined, however, there are several different forms that have been proposed. Two examples are used in literature are [80]:

$$\begin{aligned}\mu_1(x) &= \frac{x}{1+x} \\ \mu_2(x) &= \frac{x}{\sqrt{1+x^2}}\end{aligned}\tag{9.12}$$

Each of these functions have been used to obtain fits of observational data. $\mu_1(x)$, the “simple” interpolating function, has been utilized for the purpose of fitting galactic rotation curves with some positive results. Due to the slow transition from the Newtonian to MOND regime it has not provided satisfactory results for solar system observations [81]. The second potential form, $\mu_2(x)$, is referred to as the “standard choice.” This form transitions between the MOND and Newtonian regimes much quicker [82], Fig. 9.1 demonstrates this.

Figure 9.1 shows a comparison of the expected acceleration of the cantilever due to a laser driving source. This plot demonstrates how $\mu_2(x)$ approaches the Newtonian expectation at much smaller acceleration levels. It is possible that the results of the MOND

experiment in an Earth based laboratory will not provide a result that is considered strong evidence for MOND. However, the experimental results may be help to determine if one form of $\mu(x)$ is a candidate and which is not.

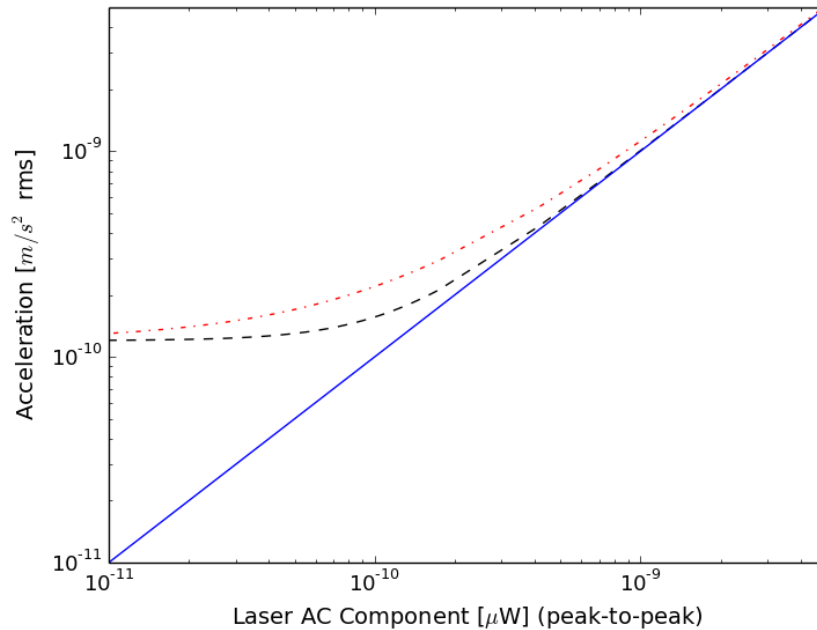


Figure 9.1: A comparison of the expected acceleration for the Newtonian regime, blue line, and the MOND regime using $\mu_1(x)$, red dot dash line, and $\mu_2(x)$, black dash line.

9.4 Conclusion

This analysis has found that it is possible to reduce the uncertainty of the measurements low enough that the experiment is possible in an Earth based drop tube. The uncertainty can be reduced to less than a_0 using the Bremen catapult system. These experiments could also be performed in a small vacuum tube. The uncertainty of such a system is an order of magnitude or two greater than a_0 , thus this method would required a large number of trials. Satellites can be used to reduce the uncertainty to several orders of magnitude below a_0 . Satellites could be used to obtain a collection of results for a range of frequencies. This would allow for the results to be compared with different forms of $\mu(x)$ to determine if they were potential candidates or not.

Chapter 10

Conclusion

This thesis has considered the potential application of using an AFM cantilever for the purposes of measuring the driven accelerations within the MOND regime.

A theoretical model was developed to describe the thermal noise of the cantilever. The EBBE was derived from first principles. This result was then solved for a cantilever in a vacuum, from which the shape of the modes could be determined. The experiments performed for this thesis were completed with the cantilever submerged in air. The effects of a fluid on a beams motion were solved using the hydrodynamic function, which was derived from Stokes' equation. Finally, the thermal noise of the cantilever was calculated using thermodynamics. From this a model was developed which could be used to calculate the NASD for the thermal noise of a cantilever in a fluid.

The EBBE model of the thermal noise of a cantilever in a fluid was used primarily for two purposes. The first purpose was to study the effects of the fluid on the thermal noise by varying the properties of the fluid. The fluid was found to affect the resonant peak, both its frequency and width, as well as the noise at low frequencies. Secondly, the model was also used to fit to the experimental data to determine if the measured noise was predominantly generated by the cantilever or some other noise source. The cantilever thermal noise was found to be the primary source at frequencies around the resonant peak but not at very low frequencies.

The EBBE model was also used to assess the DHO model which has been used in the past to calibrate AFM cantilevers. DHO model predicts similar trends around the resonance

peaks, but since it does not incorporate the true shape of the beam it is not capable of calculating the expected noise or position of the resonance peaks on its own. The DHO was used to fit and obtain both the quality factor and resonance frequency of the fundamental mode of the cantilever. These values can then be used to calculate the thickness of the cantilever by assuming ideal values for the width and length of the beam. It was demonstrated that the DHO model can be used to fit the resonant peak of a cantilever. However, the calculated value for the thickness of the beam using the quality factor and resonant frequency from this fit was found to vary significantly from the EBBE.

Green's function was used with the *EBBE* model to determine the response of a beam to loads that are uniformly applied along the length of the beam and for point loads. The case of a uniform load is of particular interest as the load caused by the driving laser is uniform. This result will be necessary for the MOND experiment as deviations from this result could indicate MOND effects.

The equipment used for the noise and driven cantilever experiments were discussed. The manufacturer cannot produce the cantilevers to exact specifications and provide both ideal values and a guaranteed range for the cantilevers. The guaranteed range was used to demonstrate the effects of varying the dimension on the resonant peak. It was found that varying the thickness of the cantilever has the greatest effect, thus it was used as the varying parameter when fitting the EBBE model to the experimental data.

Important features of the LIA were also explained. The gain response of the LPF was discussed and from this the ENBW was calculated. The LIA uses the LPF to reduce the ENBW; this is what makes it possible for the LIA to detect very small signals in relatively large amounts of noise. Harmonic noise can be introduced to the signal. This is an issue that can be rectified through the use of the sync filter which serves as a notch filter for harmonic noise. The sync filter is an important component as it allows the use of short time constants at low frequencies, reducing the wait time for a measurement.

A model was then derived to describe the response of the equipment to the motion of

the cantilever. This model allows for the NASD of the slope to be calculated. An important constant is for this model is C_{uv} . This constant is measured experimentally and the process to obtain this constant was demonstrated. The alignment process is used to try and get the detection point, x_0 , as close to the tip of the beam as possible. The NASD is experimentally obtained and then x_0 is found using a fit of this model to the data. If the detection point is found to be too close to the mounted end of the cantilever the alignment process is repeated and the experiment repeated. The cantilever experiences the greatest amount of deflection and acceleration at the free end of the beam, thus the equipment is aligned such that x_0 is as close to the free end as possible. A process was then developed that allows the acceleration of the free end of the beam to be calculated using x_0 .

The advantages of the sync filter were shown using experimental data. If a short time constant is used to make measurements at very low frequencies harmonic noise can become an issue. This was demonstrated using multiple different data sets collected using different time constants and filter pole orders with the sync filter on and off. These results showed that the sync filter acts as a notch filter and removes the harmonic noise.

A limitation of the optical lever method is that it is sensitive to the slope of the beam and the displacement of the beam must then be calculated. The model for the equipment response was used to determine the expected NASD of the slope for the 500 μm cantilever for four different positions along the beam for the second mode. The second mode was chosen as it has a node where the deflection is zero but the slope is non-zero and an anti-node where the slope is zero and the deflection is not. The model and the experimental results found that the resonant peak for the second mode could be found for the node. However, the resonant peak could not be identified at the anti-node, where the beam is deflected.

Experimental measurements of the noise for both cantilevers were collected. These results showed that there is significantly more low frequency noise than is expected as calculated by the EBBE model. The source of this excess noise is thought to be from

the detection laser, based on its noise measurements. It may be possible to reduce the noise at low frequencies by using a detection laser that has less low frequency noise or by improving the detection system over all. If this can be done then the low frequency noise could be reduced by over an order of magnitude for each cantilever, a significant benefit for the MOND experiment. This may be possible by switching to a detection laser that exhibits less low frequency noise or changing to an interferometer detection system. The current system for detection is the optical level method, which is sensitive to the slope of the beam forcing the deflection to be calculated from this value. If the detection system were changed to an interferometer setup, then the equipment would be sensitive to the displacement of the beam.

The acceleration noise of the cantilevers can be calculated from the NASD of the slope. These results show that the acceleration noise is quiet enough that, with the correct equipment settings, measurements of the cantilever's acceleration can be made with an uncertainty less than a_0 . This result shows positive results for the application of a micro-machined cantilever to test MOND and has been the goal of this research project. If the experiment is performed using a 4th order pole and 1 second time constant the acceleration uncertainty, a_{rms} is expected to be a_0 at (2.8 ± 0.1) rad/s or $0.1a_0$ at (1.19 ± 0.06) rad/s for the 500 μm cantilever. For the 225 μm cantilever a_{rms} is expected to be equal to a_0 at (20 ± 1) rad/s or $0.1a_0$ at (4.4 ± 0.2) rad/s.

The acceleration uncertainty is related to the ENBW of the measurement and thus the duration of the experiment. If the experimental duration must be kept very short, causing the acceleration uncertainty to exceed a_0 , the uncertainty of the measurements can be reduced using statistics and multiple measurements. Even in the case where the experimental duration is only 1 second and the uncertainty is $44a_0$, the experiment can be repeat 1936 times and reduce the uncertainty to be on the order of a_0 .

Using a driving laser, the cantilever were tested to determine if they could be driven at acceleration levels around or below a_0 . The 500 μm cantilever was found that it could

be driven at acceleration levels of $3 \times 10^{-10} \text{ m/s}^2$ but it was difficult to achieve less. It is possible that this cantilever needs to be driven at a low frequency than what was used, 25 rad/s. This would allow the cantilever to be driven at a larger amplitude causing it to not become over driven as easily. It was found, at the same 25 rad/s, that the 225 μm cantilever could be used to detect acceleration levels within the MOND regime. The 225 μm cantilever was found that it could be driven at acceleration levels within the MOND regime. The 225 μm cantilever, similarly to the 500 μm cantilever, would likely benefit from being driven at a lower frequency as well.

Adding in the condition of low-drag free-fall, the drop tube method can be used for both very short time durations, 0.3 seconds, or a moderate duration of time, 4.5 seconds. The duration of time that is possible is dependent upon the length of the drop tube. The cost of the experiment can be reduced if the experiment is performed on location where there is a sizable drop tube already constructed, like the Bremen facility with its 146 m drop distance. This facility also provides the benefit of a very long drop distance and the catapult system, increasing the free fall time. While this incurs the cost of travel, the benefits are significant as a drop tube designed specifically for this experiment does not need to be built and the number of trials that are required will be reduced.

The toss and catch method can be used to eliminate one of the main disadvantages of the drop tube method, i.e., the length of the tube tube is only utilized for one direction of travel. By tossing the experiment up and then catching the total duration of time for the experiment is increased by a factor of two. This allows for data to be collected over a larger amount of time and less trials to be required. This can pose a technical challenge as an apparatus must be designed which can toss the equipment up smoothly, straight up, and then catch it upon its return. A facility like Bremen is ideal for this method as they already have an apparatus that is designed for this in their drop tube. This long duration of time for the experiment allows for the equipment to use a small ENBW, increasing the SNR, and the cantilever can be driven at a lower frequency, increasing the signal.

A technical challenge that arises for both the drop tube and toss and catch method is that the equipment needs to be reset after each run. For the drop tube the equipment will need to be hoisted back to the top. The toss and catch system will require the equipment to be re-centered in the tossing mechanism. This will ensure it does not collide with the wall during flight.

The toss and catch method is the best method as it allows for the longest duration of experimental time. There is also no need to build a specialized drop tube for the experiment as there are drop tubes that already have the toss and catch ability. This makes the experiment easily repeatable and the duration of time allows for a SNR greater than 1. The two benefits can allow the experiment to be repeated multiple times using several different driving frequencies in a short time for all the required experiments. Even if these results do not provide conclusive evidence for MOND, having measurements for multiple different driving frequencies may allow for the experiment to determine if some forms of $\mu(x)$ are better candidates than others.

Bibliography

- [1] SRS Stanford Research Systems. *Model SR830 DSP Lock-In Amplifier*.
- [2] J. C. Kapteyn. First attempt at a theory of the arrangement and motion of the sidereal system. *Astrophys. J.*, 55:302–328, 1922.
- [3] F. Zwicky. Die rotverschiebung von extragalaktischen nebeln. *Helvetica Physica Acta*, 6:110–127, 1933.
- [4] M. Milgrom. A modification of the newtonian dynamics as a possible alternative to the hidden mass hypothesis. *Astrophys. J.*, 270:365–370, 1983.
- [5] Peter Eaton and Paul West. *Atomic Force Microscopy*. Oxford University Press, Oxford, England, 2010.
- [6] G. Binnig, Quate C.F., and Ch. Gerber. Atomic force microscope. *Physical Review Letters*, 56(9):930–933, 1986.
- [7] The Nobel Foundation. The nobel prize in physics 1986. https://www.nobelprize.org/nobel_prizes/physics/laureates/1986/.
- [8] Gerhard Meyer and Nabil M. Amer. Novel optical approach to atomic force microscopy. *Appl. Phys. Lett.*, 53:1045–1047, Sept. 1988.
- [9] Theodorus Maria Nieuwenhuizen. How Zwicky already ruled out modified gravity theories without dark matter. *Fortschr. Phys.*, 65, 2017.
- [10] F. Zwicky. On the masses of bevulae and of clusters of nebulae. *Astrophysical Journal*, 86, 1937.
- [11] F. Zwicky. Republication of: The redshift of extragalactic nebulae. *Gen Relativ Gravit*, 41:207–224, 2008. Translated by Anita Ehlers.
- [12] J. G. de Swart, G. Bertone, and J. van Dongen. How dark matter came to matter. *Nature Astronomy*, 2017.
- [13] D. H. Rogstad and G. S. Shostak. Gross Properties of Five Scd Galaxies as Determined from 21-Centimeter Observations. *ApJ*, 176:315, September 1972.
- [14] W. K. Huchtmeier. Rotation-curves of galaxies from 21 cm-line observations. *A&A*, 45:259–268, December 1975.
- [15] D. T. Emerson and J. E. Baldwin. The rotation curve and mass distribution in M31. *MNRAS*, 165:9P–13P, 1973.

- [16] J. E. Baldwin. *M/l Ratios in Galactic Disks*. In A. Hayli, editor, *Dynamics of the Solar Systems*, volume 69 of *IAU Symposium*, page 341, 1975.
- [17] M. S. Roberts. *Radio Observations of Neutral Hydrogen in Galaxies*, page 309. the University of Chicago Press, January 1975.
- [18] N. J. Woolf. On the Stabilization of Clusters of Galaxies by Ionized Gas. *ApJ*, 148:287, April 1967.
- [19] A. Finzi. On the validity of Newton's law at a long distance. *MNRAS*, 127:21, 1963.
- [20] W. R. Forman. A Reduction of the Mass Deficit in Clusters of Galaxies by Means of a Negative Cosmological Constant. *ApJ*, 159:719, February 1970.
- [21] J. C. Jackson. The dynamics of clusters of galaxies in universes with non-zero cosmological constant, and the virial theorem mass discrepancy. *MNRAS*, 148:249, 1970.
- [22] S. Hawking. Gravitationally collapsed objects of very low mass. *MNRAS*, 152:75, 1971.
- [23] R. Cowsik and J. McClelland. An Upper Limit on the Neutrino Rest Mass. *Physical Review Letters*, 29:669–670, September 1972.
- [24] G. O. Abell. *Clusters of Galaxies*, page 601. the University of Chicago Press, January 1975.
- [25] Robert H. Sanders and Stacy S. McGaugh. Modified newtonian dynamics as an alternative to dark matter. *Annu. Rev. Astron. Astrophys.*, 40:263–317, 2002.
- [26] M. Milgrom. A modification of the newtonian dynamics-implications for galaxies. *Astrophys. J.*, 270:371–389, 1983.
- [27] R. H. Sanders. The cirial discrepancy in clusters of galaxies in the context of modified newtonian dynamics. *Astrophys. J.*, 512, 1999.
- [28] R. H. Sanders. Neutrinos as cluster dark matter. *Monthly Notices of the Royal Astronomical Society*, 380(1):331–338, 2007.
- [29] B. Famaey, G.W. Angus, G. Gentile, and Zhao H.S. Shan, H.Y. The wedding of modified dynamics and non-exotic dark matter in galaxy clusters. *Dark Matter in Astroparticle and Particle Physics*, pages 393–401, 2008.
- [30] G. Gentile, B. Famaey, F. Combes, P. Kroupa, H. S. Zhao, and O. Tiret. Tidal dwarf galaxies as a test of fundamental physics. *A&A*, 472:L25–L28, September 2007.
- [31] M. Milgrom. MOND and the Mass Discrepancies in Tidal Dwarf Galaxies. *ApJ*, 667:L45–L48, September 2007.
- [32] Mordehai Milgrom. Galaxy groups and modified dynamics. *Astrophys. J.*, 496, 1998.

- [33] R. H. Sanders. Clusters of galaxies with modified newtonian dynamics. *Mon. Not. R. Astron. Soc.*, 342:901–908, 2003.
- [34] D. Gerbal, F. Durret, M. Lachieze-Rey, and G. Lima-Neto. Analysis of X-ray galaxy clusters in the framework of modified Newtonian dynamics. *A&A*, 262:395–400, September 1992.
- [35] Anthony Aguirre, Joop Schaye, and Eliot Quataert. Problems for mond in clusters and the ly-alpha forest. *Astrophys. J.*, 561, 2001.
- [36] D. Clowe, M. Bradač, A. H. Gonzalez, M. Markevitch, S. W. Randall, C. Jones, and D. Zaritsky. A Direct Empirical Proof of the Existence of Dark Matter. *ApJ*, 648:L109–L113, September 2006.
- [37] G. W. Angus, H. Y. Shan, H. S. Zhao, and B. Famaey. On the Proof of Dark Matter, the Law of Gravity, and the Mass of Neutrinos. *ApJ*, 654:L13–L16, January 2007.
- [38] H. Meyer, E. Lohrmann, S. Schubert, W. Bartel, A. Glazov, B. Lohr, C. Niebuhr, E. Wunsch, L. Jonsson, and G. Kempf. Test of the law of gravitation at small accelerations. *General Relativity and Gravitation*, 44(10):2537–2545, 2012.
- [39] Alex Abramovici and Zeev Vager. Test of newton’s second law at small accelerations. *Phys. Rev. D*, 34(10):3240–3241, 1986.
- [40] J. H. Gundlach, S. Schlamminger, C. D. Spitzer, K.-Y. Choi, B. A. Woodahl, J. J. Coy, and E. Fischbach. Laboratory test of newton’s second law for small accelerations. *Phys. Rev. Lett.*, 98:150801, Apr 2007.
- [41] Jonas Pereira, James Overduin, and Alexander J. Poyneer. Satellite test of the equivalence principle as a probe of modified newtonian dynamics. 117, 08 2016.
- [42] Alex Ignatiev. Is violation of newtons second law possible? 98:101101, 04 2007.
- [43] V. A. de Lorenci, M. Faúndez-Abans, and J. P. Pereira. Testing the Newton second law in the regime of small accelerations. *A&A*, 503:L1–L4, August 2009.
- [44] Saurya Das and S. N. Patitsas. Can mond type hypotheses be tested in a free fall laboratory environment? *Phys. Rev. D*, 87, 2013.
- [45] Lawrence Kinsler, Austin Frey, Alan Coppers, and James Sanders. *Fundamentals of Acoustics*. John Wiley and Sons, 1982.
- [46] J. Stewart. *Calculus*. Cengage Learning, 2015.
- [47] E.B. Magrab. *Vibrations of Elastic Systems: With Applications to MEMS and NEMS*. Solid Mechanics and Its Applications. Springer Netherlands, 2012.
- [48] Wilhelm Flugge. *Handbook of Engineering Mechanics*. McGraw-Hill.

- [49] Sir George Gabriel Stokes. *Mathematical and Physical Papers*. Cambridge University Press, London, 1901.
- [50] L. Rosenhead. *Laminar Boundary Layers*. Oxford University Press, Oxford, England, 1963.
- [51] John E. Sader. Frequency response of cantilever beams immersed in viscous fluids with application to the atomic force microscope. *Journal of Applied Physics*, 84(1):64–76, 1998.
- [52] Chia-Shun Yih. *Fluid Mechanics*. McGraw-Hill, 1969.
- [53] F. Reif. *Fundamentals of Statistical and Thermal Physics*. Waveland Press, 2009.
- [54] B. D. Hauer, C. Doolin, K. S. D. Beach, and J. P. Davis. A general procedure for thermomechanical calibration of nano/micro-mechanical resonators. *Annals of Physics*, 339:181–207, December 2013.
- [55] D.V. Schroeder. *An Introduction to Thermal Physics*. Addison Wesley, 1999.
- [56] H.J. Butt, P. Siedle, K. Seifert, K. Fendler, T. Seeger, E. Bamberg, A. L. Weisenhorn, K. Goldie, and A. Engel. Scan speed limit in atomic force microscopy. *Journal of Microscopy*, 169(1):75–84, 1993.
- [57] Jeffrey L. Hutter and John Bechhoefer. Calibration of atomic force microscope tips. *Review of Scientific Instruments*, 64(7):1868–1873, 1993.
- [58] D. A. Walters, J. P. Cleveland, N. H. Thomson, P. K. Hansma, M. A. Wendman, G. Gurley, and V. Elings. Short cantilevers for atomic force microscopy. *Review of Scientific Instruments*, 67(10):3583–3590, 1996.
- [59] Alan V. Oppenheim and George C. Verghese. *Signals, Systems & Inference*. Pearson, 2017.
- [60] Welcome to python.org. <https://www.python.org/>.
- [61] Scipy.org. <https://www.scipy.org/>.
- [62] J. E. Sader, J. W. M. Chon, and P. Mulvaney. Calibration of rectangular atomic force microscope cantilevers. *Review of Scientific Instruments*, 70:3967–3969, October 1999.
- [63] H. J Butt, P. Siedle, K. Seifert, K. Fendler, T. Seeger, E. Bamberg, A. L. Weisenhorn, K. Goldie, and A. Engel. Scan speed limit in atomic force microscopy. *Journal of Microscopy*, 169(1):75–84, 1993.
- [64] Deron A. Walters Barney Drake Erik K. Runge Jason P. Cleveland Mark A. Wendman Paul K. Hansma Tilman E. Schaeffer, Mario Viani. Atomic force microscope for small cantilevers, 1997.

- [65] NanoWorld AG. Home. <http://www.nanoworld.com/>.
- [66] Michaela Author NanoWorld. personal communication.
- [67] Sofia de Lemos Henriques Ferreira. *Microelectromechanical Systems - Fabrication and Characterization of Microcantilevers*. PhD thesis, 2014.
- [68] Andrew W. McFarland. *Production and Analysis of Polymer Microcantilever Parts*. PhD thesis, 2004.
- [69] NanoWorld AG. Arrow t11au afm probe. <http://www.nanoworld.com/tipless-gold-coated-afm-tip-arrow-t11au>.
- [70] NanoWorld AG. Efm afm probe. <http://www.nanoworld.com/pointprobe-electrostatic-force-microscopy-afm-tip-efm>.
- [71] NanoWorld. Nanoworld spm and afm probes. http://www.nanoworld.com/lang/en/NanoWorld_Product_Brochure.pdf.
- [72] Ulric S. Lindholm, Daniel D. Kana, Wen-Hwa Chu, and H. Norman Abramson. Elastic vibration characteristics of cantilever plates in water. *Journal of Ship Research*, pages 11–36, June 1965.
- [73] K.F Riley, M.P Hobson, and S.J Bence. *Mathematical methods for physics and engineering*. Cambridge University Press, 2015.
- [74] Dr. Rudiger Paschotta. Shot noise. https://www.rp-photonics.com/shot_noise.html.
- [75] <https://www.zarm.uni-bremen.de/en/drop-tower/general-information.html>.
- [76] Zarm: What is the catapult system? <https://www.zarm.uni-bremen.de/en/drop-tower/general-information/what-is-the-catapult-system.html>.
- [77] Thomas J. Rathz and Michael B. Robinson. The nasa/marshall space flight center drop tube user’s manual. Technical Report NASA TM - 100392, NASA/Marshall Space Center, March 1990.
- [78] Brian Dunbar. “as the stomach turns” on the kc-135. <https://www.nasa.gov/missions/research/kc135.html>.
- [79] P. Touboul, G. Métris, M. Rodrigues, Y. André, Q. Baghi, J. Bergé, D. Boulanger, S. Bremer, P. Carle, R. Chhun, B. Christophe, V. Cipolla, T. Damour, P. Danto, H. Dittus, P. Fayet, B. Foulon, C. Gageant, P.-Y. Guidotti, D. Hagedorn, E. Hardy, P.-A. Huynh, H. Inchauspe, P. Kayser, S. Lala, C. Lämmerzahl, V. Lebat, P. Leseur, F. Liorzou, M. List, F. Löffler, I. Panet, B. Pouilloux, P. Prieur, A. Rebray, S. Reynaud, B. Rievers, A. Robert, H. Selig, L. Serron, T. Sumner, N. Tanguy, and P. Visser. MICROSCOPE Mission: First Results of a Space Test of the Equivalence Principle. *Physical Review Letters*, 119(23):231101, December 2017.

- [80] Luc Blanchet and Jrme Novak. External field effect of modified newtonian dynamics in the solar system. *Monthly Notices of the Royal Astronomical Society*, 412(4):2530–2542, 2011.
- [81] Benoit Famaey and James Binney. Modified newtonian dynamics in the milky way. *Monthly Notices of the Royal Astronomical Society*, 363(2):603–608, 2005.
- [82] K. G. Begeman, A. H. Broeils, and R. H. Sanders. Extended rotation curves of spiral galaxies: dark haloes and modified dynamics. *Monthly Notices of the Royal Astronomical Society*, 249(3):523–537, 1991.